TiO2 photocatalysts prepared via a sol-gel route assisted by P- and F- containing additives : applications to the degradation of MEK and to the elimination of bacteria on surfaces

Yige Yan

UNIVERSITÉ DE STRASBOURG

ÉCOLE DOCTORALE DES SCIENCES CHIMIQUES

ICPEES CNRS/UMR 7515 et IS2M CNRS/UMR 7361

THÈSE présentée par :

YAN Yige

soutenue le : **25 octobre 2016**

pour obtenir le grade de : **Docteur de l'université de Strasbourg**

Discipline/ Spécialité : Chimie/Chimie des matériaux et photocatalyse

TiO_2 photocatalysts prepared *via* a sol-gel route assisted by P- and F- containing additives. Applications to the degradation of MEK and to the elimination of bacteria on surfaces.

THÈSE dirigée par :
Mme KELLER Valérie — Directrice de Recherche, CNRS/Université de Strasbourg

Co-encadrante :
Mme Lydie PLOUX — Chargée de Recherche, CNRS

RAPPORTEURS :
M. HOCHEPIED Jean-Francois — Chargé de Recherche, MINES ParisTech et ENSTA ParisTech
M. JOUENNE Thierry — Directeur de Recherche, CNRS

EXAMINATEURS :
M. KELLER Nicolas — Chargé de Recherche, CNRS
Mme GUILLARD Chantal — Directrice de Recherche, CNRS

Remerciements

Je tiens à remercier Madame Valérie Keller de l'ICPEES, directrice de ma thèse, de m'avoir confié ce sujet de thèse. J'apprécie la confiance et la liberté nécessaire qu'elle m'a donné tout au long de mes travaux. Je la remercie aussi pour sa compréhension, son écoute, et sa grande personnalité de prévoyance qui cherchait toujours à mener ce projet à sa valeur maximale.

Un grand merci à Monsieur Nicolas Keller de l'ICPEES, également directeur de ma thèse, pour sa contribution qui consistait à la fois en des explications scientifiques très promoteurs, et en des nombreuses conseils en regard de l'esprit de recherche, qui m'ont beaucoup inspiré. Il a toujours montré une attitude scientifique rigoureuse, et je suis sur que les discussions passionnées et scientifiques que nous avons eues me manqueront.

Je tiens à remercier profondément Madame Lydie Ploux, directrice de ma thèse, qui m'a accueilli chaleureusement dans son laboratoire de microbiologie à l'IS2M. Je la remercie vivement pour ses conseils avisés, pour son grand esprit de partage et pour nos éclats de rire qui font surmonter notre relation à un nouveau niveau, au-delà de celle de prof-élève. Grace à tout cela, mon entrée dans le monde de la microbiologique s'est fait de manière aisée.

Ma reconnaissance va également à l'Institut MICA Carnot pour le financement de ma thèse dans le cadre du projet R&D CLEANCOAT.

Je suis très sensible à l'honneur que m'ont fait Madame Chantal Guillard, Monsieur Jean-François Hochepied et Monsieur Thierry Jouenne en acceptant d'être membres du jury de ma thèse. J'éprouve un profond respect pour leurs travaux et leurs parcours.

Je remercie Madame Sara Mercado et Monsieur Mostafa NAJMI du CRITT Matériaux Alsace, Madame Marie-Hélène Desmonts et Monsieur Bernard Hezard du CRITT Aérial pour ces travaux dédiés dans le cadre du projet CLEANCOAT.

Je remercie sincèrement mes collègues de l'IS2M, Charline Sorahu et Jules Valentin pour leur aide chaleureuse et leurs travaux délicats réalisés pour une partie des expériences microbiologiques dans le cadre de ce travail.

Je tiens également à manifester ma gratitude à tout le « staff » technique de l'ICPEES, en particulier à Monsieur Alain Rach et Michel Wolf, à la fois pour leurs talents électro-mécaniques (niveau Thomas Edison) grâce auxquels la mise en place du pilote de test photocatalytique a été possible, et pour nos discussions avec bonne humeur. Je tiens à remercier Messieurs Pierre Bernhardt, Vaso Papaefthymiou de l'ICPEES et Madame Samar Garreau de l'IS2M pour les analyses XPS, ainsi que Monsieur Thierry Dintzer de l'ICPEES pour ses conseils techniques en DRX. Mes remerciements vont également à Monsieur Loic Vidal de l'IS2M pour les images TEM et à Monsieur Aissam Alroudj de l'IS2M pour les analyses AFM.

Je remercie Messieurs Mohamad El Roz, Philippe Bazin et Frederic Thibault-Starzyk du Laboratoire de Catalyse et Spectrochimie (LCS) de Caen pour leur collaboration, malgré la quantité limitée des résultats relatifs présentés dans ma thèse.

Je remercie Véronique Verkruysse et Francine Jacky pour leurs démarches administratives effectuées qui couvrent mon contrat de travail et aussi mes déplacements fréquents entre ICPPES et IS2M.

Je n'oublie pas tous mes collègues, particulièrement Romain Masson, mon prédécesseur et mon tuteur lors de ma phase de démarrage. Je pense aux bons moments passés avec Clément Marchal, Marvin Motay, Pauline Barrois, Loic Michel, Thomas Favet, Cérise Robert, Claire Holtzinger, Pablo Jimenez Calvo, Armelle Sengele et Quentin Minetti de l'ICPEES. Et avec Adeline Marguier, Charline Sorahu, Jules Valentin, Jessica Hinostroza-Ramos, Caroline Steinmetz, Mathieu Veuillet de l'IS2M. Je n'oublie pas non plus mon bon souvenir international avec Kinga Ostojska, Klaudia Zbudniewek, Joanna Wojciechowska, Christoforidis Konstantions et Marek Twardoch. Mais aussi les autres membres des deux laboratoires: Valérie Caps, Thomas Cottineau, Laurent Pieuchot et Tatiana Bourgade. Grâce à toutes ces personnes, je garde de très bons souvenirs à la fois de l'ICPEES et de l'IS2M.

Je pense enfin à ma communauté chinoise, surtout Qinqin Ji, qui m'a soutenu tout au long de ces 4 ans de thèse. Mes remerciements doivent être aussi adressés à mes parents pour leur soutien moral malgré la distance.

Résumé de la thèse

I. Introduction et bibliographie

L'homme passe environ 70% de son temps en environnement intérieur confiné, dans lequel l'air est souvent plus pollué qu'à l'extérieur. Les sources de pollution et de contamination environnementales sont multiples : elles peuvent être de nature chimique (pesticides, composés organiques volatils (COVs)...) ou biologique (bactéries, moisissures, virus). La plupart des solutions actuellement existantes contre ces pollutions (adsorption, dégradation chimique, traitements à l'ozone et antibiotique...) possèdent un certain nombre d'inconvénients : beaucoup d'entre elles sont consommatrices en énergie, certaines ne sont que des solutions de stockage ou de transfert de la pollution, d'autres mettent en œuvre ou génèrent des composés chimiques nuisibles à l'homme et à l'environnement. La plupart ne permettent pas une action conjointe sur les pollutions chimiques et biologiques.

L'oxydation photocatalytique hétérogène est un procédé d'oxydation avancée, considérée comme une technologie prometteuse avec un spectre d'applications potentielles ou déjà existantes, très large, et qui bénéficie notamment d'une mise en oeuvre douce (à température ambiante et pression atmosphérique), propre et verte (lumière UV comme seule source d'énergie, absence de produits chimiques toxiques et de rejets polluants), et peu coûteuse. De plus, il s'agit d'une technologie de destruction de la pollution chimique et biologique conduisant souvent à une minéralisation totale. Lorsqu'un semiconducteur est illuminé par des rayonnements possédant une énergie au moins égale à sa bande interdite, il y a génération de paires trou / électron au sein du matériau. Si ces charges photogénérées arrivent à atteindre la surface du semi-conducteur, sur laquelle peuvent s'adsorber les réactifs, et si les bandes de conduction et de valence du semi-conducteur sont convenablement disposées par rapport aux couples redox des réactifs, ces charges peuvent conduire à des réactions redox permettant la destruction (par oxydation) de composés organiques. De plus, les microorganismes étant un assemblage des molécules organiques elles-même plus ou moins complexes, ils peuvent également être dégradés par photocatalyse d'oxydation à température ambiante.

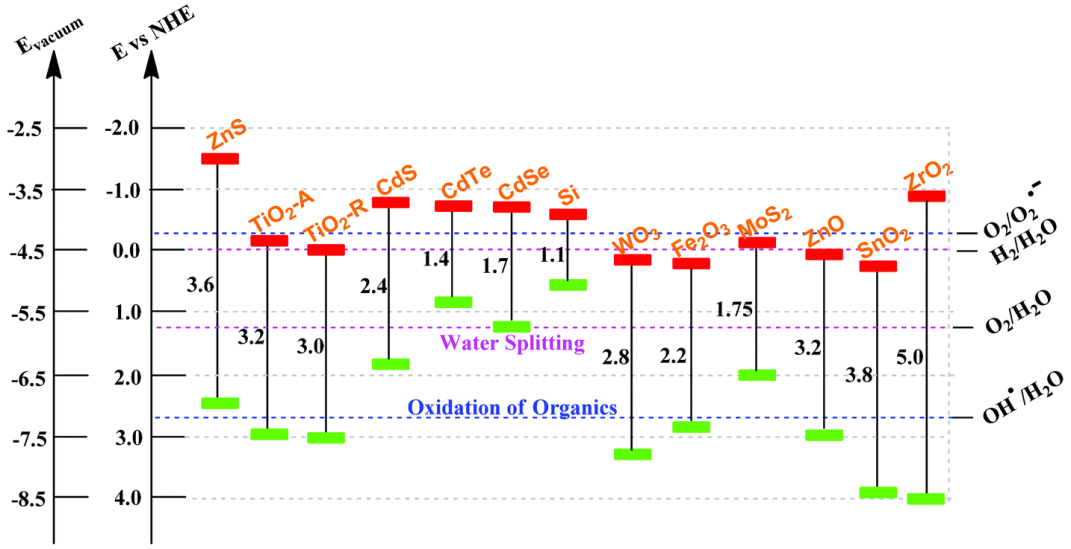

Figure 1 : Les semi-conducteurs les plus utilisés et leurs positions de band-gap. (Au pH = 1-2)

Parmi les semiconducteurs les plus utilisés et les plus performants en photocatalyse, TiO_2 (de structure cristallographique anatase) a été choisi dans ce travail comme matériau de base pour la réalisation de solutions (revêtements photocatalytiques épurants et bactéricides) pour décontaminer les surfaces et l'air. Sa bande interdite d'environ 3,2 eV nécessite une activation par des longueurs d'onde UV-A, typiquement inférieures à 390 nm.

Il existe plusieurs façons de produire TiO_2 en nanoparticules. TiO_2 P25 (Evonik), le photocatalyseur de référence commerciale de-facto, est préparé *via* le procédé chlorine en échelle industrielle. Ici dans cette thèse, on focalise notamment sur la méthode sol-gel pour synthétiser nanomatériaux de TiO_2 photocatalytiques en échelle laboratoire. Une stratégie appliquée pour améliorer la performance photocatalytique de TiO_2 est de contrôler la morphologie des matériaux en TiO_2, ceci peut être réalisé par varier les paramètres de synthèse ou par additionner les additives en petite quantité. Yang *et al.* ont mise en évidence le rôle de HF sur le changement de morphologie des cristaux de TiO_2, la facette {001} du anatase exposée a été proposé comme un factor positive vis-à-vis l'amélioration de l'efficacité photocatalytique. Zhao *et al.* ont investi le rôle d'un liquide ionique $BmimBF_4$ sur le changement de morphologie des cristaux de TiO_2, il a conclu que les ions $Bmim^+$ et F^- issues de ce liquide ionique est responsable de la croissance favorisée de la facette {100} et {001} des cristaux d'anatase. Yoo *et al.* ont utilisé un autre liquide ionique : 1-Butyl-3-methylimidazolium hexafluorophosphate ($BmimPF_6$) comme additive dans la synthèse sol-gel de TiO_2, ils ont observé que le produit TiO_2 présente une taille des particules plus petites et une meilleur cristallinité par rapport l'échantillon synthétisé sans additive. Pourtant, il manque des études sur le mécanisme et le rôle de structuration de ce liquide ionique durant la synthèse.

L'objectif de ce travail consistait à étudier les propriétés de matériaux photocatalytiques à base de TiO_2 obtenus par synthèse sol-gel assistée par liquide ionique $BmimPF_6$ et d'identifier le rôle et l'impact des différents constituants élémentaires du liquide ionique sur les propriétés physico-chimiques et photocatalytiques des matériaux.

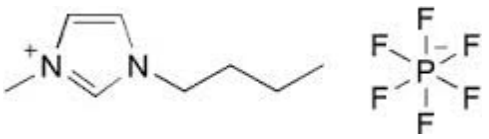

Figure 2 : Structure moléculaire de 1-Butyl-3-methylimidazolium hexafluorophosphate (BmimPF6)

Ensuite, en parallèle au développement de photocatalyseurs, les activités photocatalytiques en dégradation d'un polluant chimique modèle Méthyl ethyl Cétone (MEK) en phase gazeuse et de différentes espèces bactériennes (*E. coli*, *S. epidermidis* et *P. fluoresences*) dans liquide par rapport à la référence commerciale usuelle ont été réalisés. Ceux-ci sont suivi par l'étude de corrélation entre les propriétés physico-chimique de nanomatériaux en TiO_2 et leur propriétés photocatalytiques ; et par l'étude des mécanismes à l'interface bactérie (et biofilm)/matériaux qui n'est encore que partielle, alors qu'elle est nécessaire pour conduire *in fine* à de nouvelles stratégies de prévention.

Enfin, l'objectif ultime de cette thèse consistait à intégrer ces nanocharges actives dans des formulations pour élaborer des revêtements épurants et antibactériens destinés à l'assainissement des surfaces et de l'air intérieur. Pourtant ici dans ce manuscrit, on focalise sur les premiers trois taches.

Cette thèse a été réalisée dans le cadre d'un projet financé par l'Institut Carnot MICA d'Alsace en collaboration entre l'ICPEES et l'IS2M, et en partenariat avec le CRITT Matériaux Alsace et le CRITT Aérial.

II. Préparation et caractérisation des échantillons TiO_2

II.1. TiO_2 obtenu par synthèse sol-gel modifiée par ajout de $BmimPF_6$ en milieu HAc

Dans ce travail, inspiré de l'étude faite précédemment par K.S.Yoo *et al*, les nanomatériaux à base de TiO_2 ont été obtenus *via* un procédé de synthèse sol-gel modifiée par l'assistance d'un liquide ionique, le $BmimPF_6$. Brièvement pour une synthèse typique, 5 g de $Ti(O^iPr)_4$ est mélangé avec 10 g de propan-2-ol, auquel 0,09 g, 0,49 g ou 2,02 g de $BmimPF_6$ est ajouté correspondant un ratio molaire $BmimPF_6$/Ti de 0,03, 0,1 et 0,4 respectivement. Une émulsion $BmimPF_6$/solvant organique est formée après 30 min de mélange de celui du précédent. Ensuite, 6,2 g de solution acide acétique en 2,2 mol/L est ajouté de façon goute à goute, et une précipitation blanche se forme tout de suite lors de l'hydrolyse. L'ensemble de solution est agité pour encore 1 h avant d'être laisser murir sans agitation en faisant varier le temps de mûrissement (de 18 h, 72 h, 6 jours). Enfin, le produit solide blanc est obtenu par filtration, lavage et calcination successivement.

Nous avons mis en évidence l'impact de ces paramètres expérimentaux sur certaines caractéristiques des matériaux obtenus, comme la taille des cristallites de TiO_2 et la surface spécifique. Il a été montré en utilisant plusieurs méthodes de caractérisation (DRX, XPS, BET, TEM, etc.) que la synthèse par ajout de $BmimPF_6$ conduit à des tailles de cristallites plus réduites et à des surfaces spécifiques plus importantes (même à des températures de calcination de 550 °C), ceci en comparaison avec le catalyseur commercial Aeroxide® TiO_2 P25 et les matériaux synthétisés par voie sol-gel mais sans ajout de liquide ionique (Tableau 1).

Sample name	*$BmimPF_6$/Ti molar ratio*	*Aging duration*	*BET surface area/T-plot surface area (m^2/g)*		*Mean crystallite size (nm)*		*BET-derived calculated particle size (nm)*	
			Dried samples	*Calcined samples*	*Dried samples*	*Calcined samples*	*Dried samples*	*Calcined samples*
P25	-	-	-	55	-	22[a]		
IL0 6d	0	6 days	286/312	50/44	6	19	5	31
IL0.03 18h	0.03	18 h	294/283	110/107		10		14
IL0.03 72h	0.03	72 h	238/208	104/107		10		15
IL0.03 6d	0.03	6 days	251/250	97/100	8	11	6	16
IL0.1 18h	0.1	18 h		101/96		10		15
IL0.1 72h	0.1	72 h	242/298	113/136		10		14
IL0.1 6d	0.1	6 days		109/127	8	10		14
IL0.4 18h	0.4	18 h	273/268	118/214		7		13
IL0.4 72h	0.4	72 h	266/264	114/231		8		14
IL0.4 6d	0.4	6 days	237/232	96/190	7	12	7	16

Tableau 1 : Surface spécifique (BET) et taille de cristallite (DRX) des TiO_2 synthétisés avec des ratios molaires de BmimPF6/Ti et des temps de mûrissement différents. La température de calcination pour l'ensemble de ces échantillons est 550 °C. TiO_2 P25 est la référence commerciale d'Evonik.

Constaté par les spectres DRX des échantillons en TiO_2 synthétisés avec un ratio molaire $BmimPF_6$/Ti de 0 à 0,4 et un temps de murissement de 6 jours fixé avant et après calcination (Figure 3), la présence de $BmimPF_6$ favorise la cristallisation en TiO_2 anatase durant le murissement. En plus, sa présence limite la croissance des cristaux de TiO_2 au cours de calcination, autrement dit : la présence de $BmimPF_6$ peut donner TiO_2 une résistance thermique contre calcination. Sans $BmimPF_6$, l'échantillon synthétisé montre une croissance brutale de la taille de cristallite de 6 nm à 19 nm (une taille proche à celle de P25), alors qu'avec $BmimPF_6$, cette croissance est limitée de 7-8 nm à 10-12 nm. L'augmentation du temps de murissement ne permet pas d'avoir une croissance de taille de cristallite plus importante sauf dans le cas où le ratio molaire de $BmimPF_6$/Ti est de 0,4.

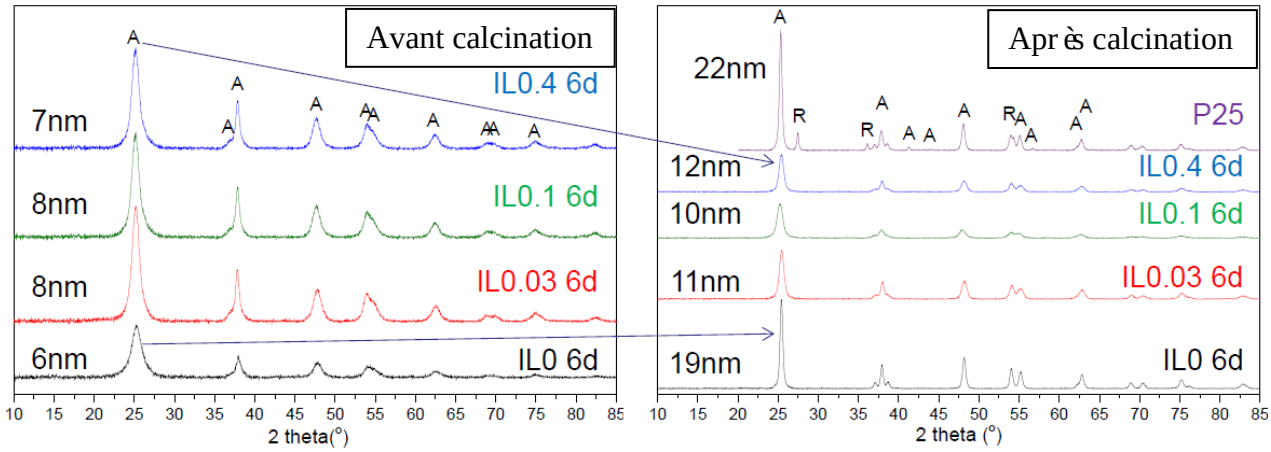

Figure 3 : XRD des échantillons en TiO_2 synthétisés avec un ratio molaire $BmimPF_6$/Ti de 0 à 0,4 et un temps de murissement de 6 jours fixé avant calcination (gauche) et après calcination (droite).

L'étude des différents échantillons en TiO_2 *via* TEM (Figure 4) et BET (Tableau 1, aussi la forme des courbes isothermes et la distribution de la taille de pore) confirme que la présence de $BmimPF_6$ dans la synthèse augmente la surface spécifique de TiO_2 après calcination tout en inhibitant la croissance de la taille des cristaux durant ce dernier. Ici, les observations sont cohérentes avec celles obtenues par DRX précédemment, puisqu'une surface spécifique élevée est généralement le résultat d'une taille de particule petite pour les matériaux non-poreux.

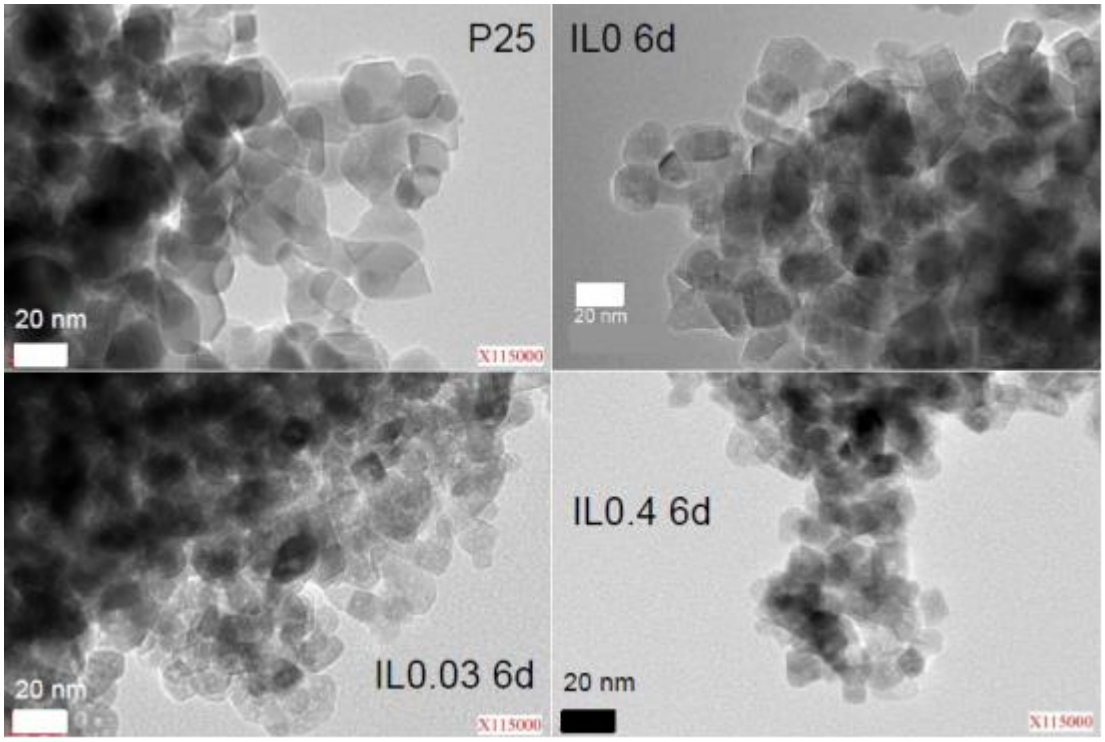

Figure 4 : Images de TEM montrant l'influence de la quantité de $BmimPF_6$ sur la taille des cristaux de TiO_2. Sauf pour P25, le temps de murissement est fixé à 6 jours et la température de calcination est fixée à 550 °C.

La durée de murissement augmenté n'a pas un effet significatif sur la taille de cristallite sauf pour le cas ou le ratio molaire de $BmimPF_6$/Ti est 0.4, pour lequel la taille de cristallite de TiO_2 augmente de 7 nm to 12 nm si la durée de murissement passe de 18h à 6 jours. Ceci est également accompagné d'un gain au niveau de la cristallinité de la phase anatase. (Figure 5)

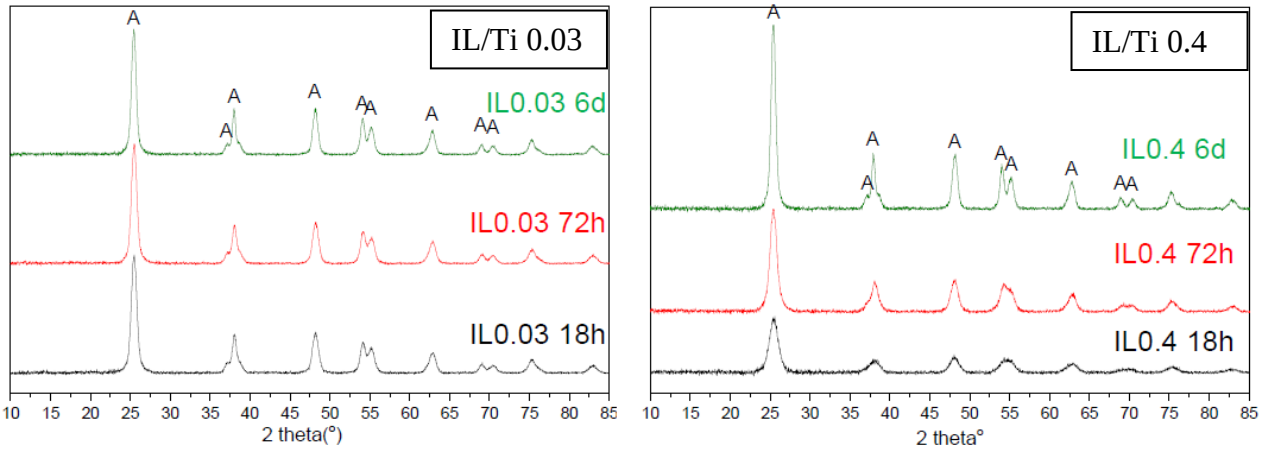

Figure 5 : Influence de la durée de murissement dur la cristallinité de TiO_2 synthétisé avec un ratio molaire $BmimPF_6$/Ti 0.03 et 0.4 après calcination à 550 °C.

Figure 6 et 7 montrent les spectres de XPS de Ti_{2p}, O_{1s} et P_{2p} des échantillons séchés et calcinés de TiO_2 synthétisés avec différents ratios de $BmimPF_6$/Ti (0, 0,03 and 0.4) utilisés dans la synthèse sol-gel.

Avant calcination, la région Ti_{2p} montre les doublets typiques de $Ti_{2p}3/2$-$Ti_{2p}1/2$, avec un constant de couplage spin-orbite de 5,7 eV, qui sont assignés aux Ti^{4+} (Ti-O) dans une coordination octaédrique avec les oxygènes dans une structure de TiO_2 cristalline typique. Et la région O_{1s} montre les spectres soit de O^{2-} dans les liaisons O-Ti de TiO_2, soit des oxygènes dans les liaisons O-H des groupes hydroxyles de surface. On n'a pas pu mettre en évidence la présence de phosphore à cet instant, mais on a pu détecter la présence de fluor adsorbé sur la surface des matériaux mais pas celle de phosphore, même si le ratio $BmimPF_6$/Ti (donc P /Ti également) est de 0,4.

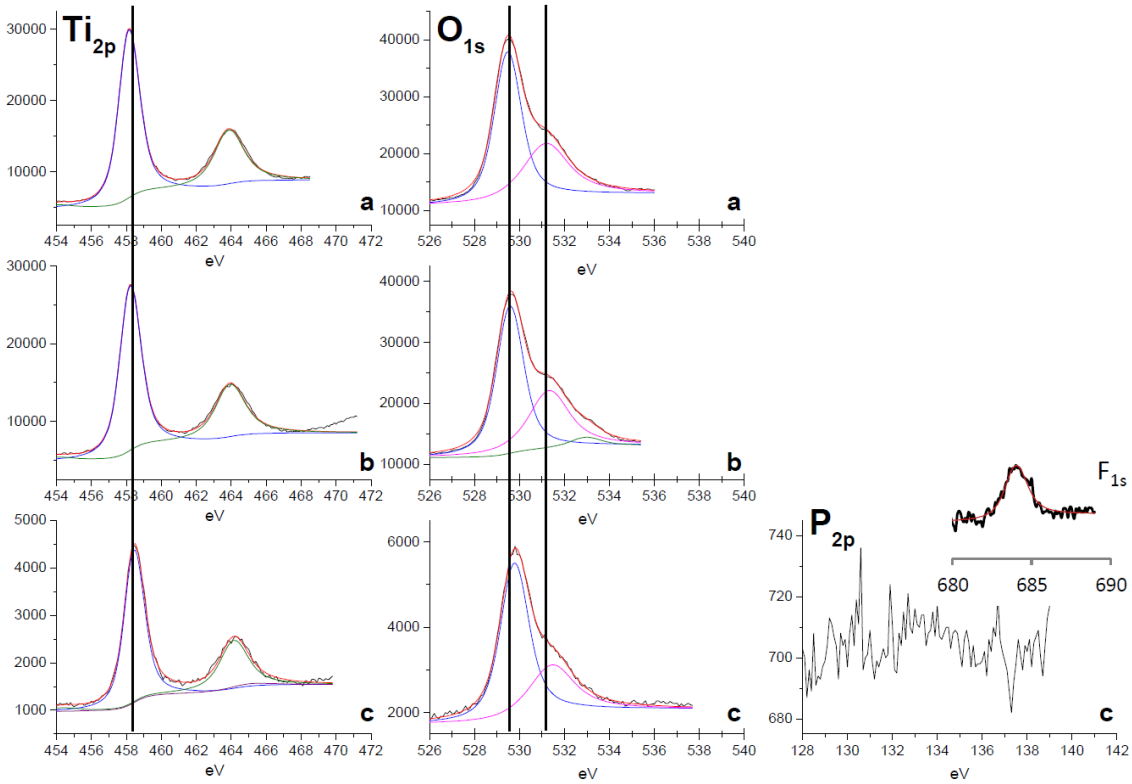

Figure 6 : Spectres de XPS de Ti_{2p}, O_{1s} et P_{2p} des échantillons séchés de TiO_2 synthétisés avec différents ratios de $BmimPF_6$/Ti dans la synthèse sol-gel : 0(a), 0.03(b) and 0.4 (c). L'acide utilisé est HAc et la durée de murissement est fixée à 6 jours.

Après calcination à 550 °C pour les mêmes échantillons, les spectres de Ti_{2p} et O_{1s} montrent des contributions similaires que ceux d'avant calcination, malgré la quantité de liquide ionique utilisé. Par contre, pour l'échantillon synthétisé avec un ratio $BmimPF_6$/Ti 0,4, l'apparition d'un doublet $P_{2p}3/2$-$P_{2p}1/2$ avec un constant de couplage spin-orbite de 0,87 eV indique la présence de phosphore en état d'oxydation pentavalent (P^{5+}) généralement dans les groupes phosphates. On suppose que les phosphate ont été formé *via* hydrolyse de $BmimPF_6$ à condition acide et ils sont très dispersés dans le bulk de TiO_2 avant calcination, ce qui rende une quantité faible de ceux derniers en surface d'échantillon même si le teneur en $BmimPF_6$ été élevé. Alor qu'après calcination, il y aurait une migration partielle des phosphates vers la surface, qui conduit à l'augmentation de l'intensité de pic de P_{2p}. L'absence des contributions de Ti-O-P dans les spectres de Ti_{2p} ou de O_{1s} est probablement dû au teneur faible de phosphore dans les échantillons de TiO_2. Enfin, le teneur de fluor a été fortement diminué, qui est dû à la désorption de fluor de la surface de TiO_2 à une température élevée.

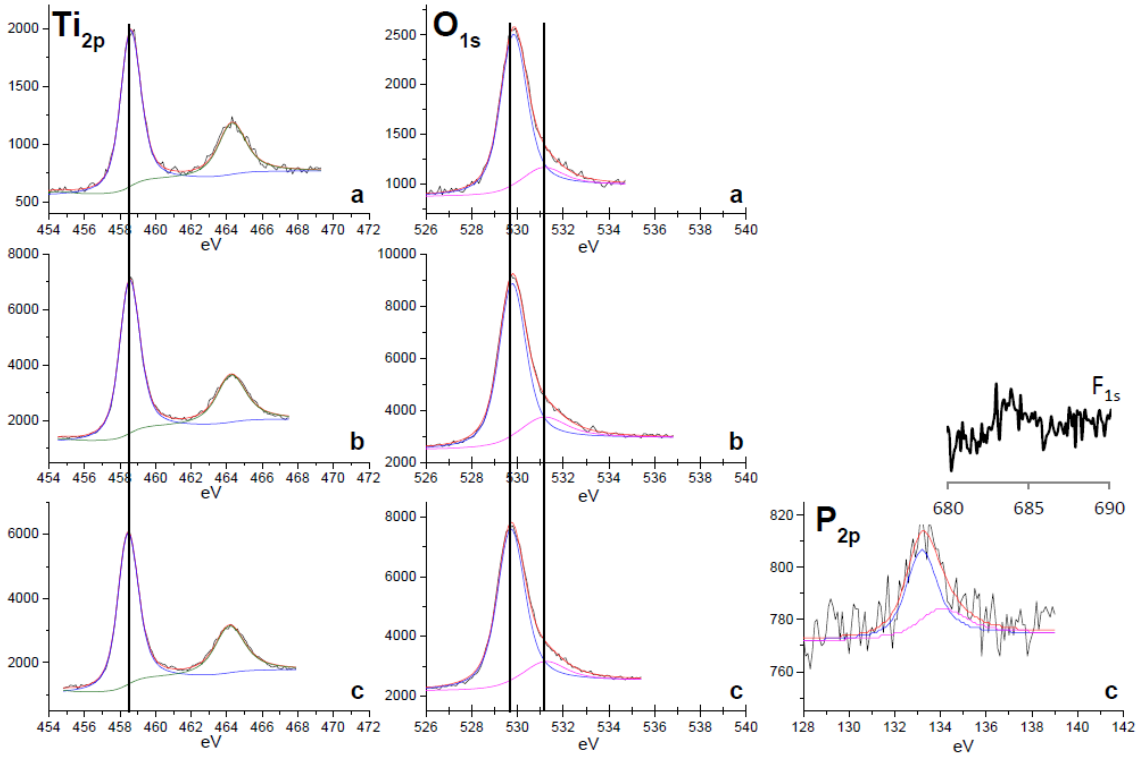

Figure 7 : Spectres de XPS de Ti_{2p}, O_{1s} et P_{2p} des échantillons calcinés de TiO_2 synthétisés avec différents ratios de $BmimPF_6$/Ti dans la synthèse sol-gel : 0(a), 0.03(b) and 0.4 (c). L'acide utilisé est HAc et la durée de murissement est fixée à 6 jours.

II.2. Etude mécanistique de synthèse

Dans un second temps, après l'étude paramétrique, nous avons mené une étude fondamentale permettant de comprendre et d'expliquer l'impact de l'ajout du liquide ionique $BmimPF_6$ sur la nucléation et la croissance des cristaux de TiO_2. Pour ce faire, les différents éléments constituants $BmimPF_6$ ($Bmim^+$, PO_4^{3-} et F^-) ont été ajoutés séparément (les additives de remplacement sont sous forme de BmimCl, H_3PO_4 et NaF) lors de la synthèse sol-gel afin d'identifier les éléments/ions responsables de l'impact sur les modifications de structure et de surface relevées dans la première phase de l'étude lorsque la synthèse est réalisée avec le liquide ionique. Pour cela, trois combinassions des deux additives de remplacement de liquide ionique ont été utilisées à la place de $BmimPF_6$, qui sont BmimCl + NaF, BmimCl + H_3PO_4 et H_3PO_4 + NaF. Ces échantillons correspondants sont notés «BCNaF», «BCPA» et «PANaF». Les autres paramètres sauf la durée de murissement (18h ou 6 jours) sont identique à ceux utilisés dans la synthèse sol-gel de TiO_2 réalisée avec le liquide ionique.

L'influence des différents constituants du liquide ionique (notamment F^- et P^{5+}) a été étudiée par DRX, BET, XPS et TEM sur :

- La cristallinité et la nature cristallographique de TiO_2,
- La surface spécifique de TiO_2,
- La taille des cristallites,
- La morphologie de TiO_2,
- La chimie de surface de TiO_2.

La figure 8 montre les spectres de DRX et les tailles de cristallite des échantillons « BCNaF », « BCPA » et « PANaF » avant et après calcination. D'ici, l'influence de la présence de phosphore (dans le cas de « BCPA » et « PANaF ») sur l'inhibition de la croissance de taille de cristallite durant calcination a été mise en évidence. En plus, ces derniers échantillons ont une surface spécifique élevée grâce à la petite taille de cristallite, autour de 100 m^2/g *via* analyse BET. Ces propriétés intéressantes des échantillons synthétisés en présence de phosphore sont similaires à celles des échantillons synthétisés avec $BmimPF_6$.

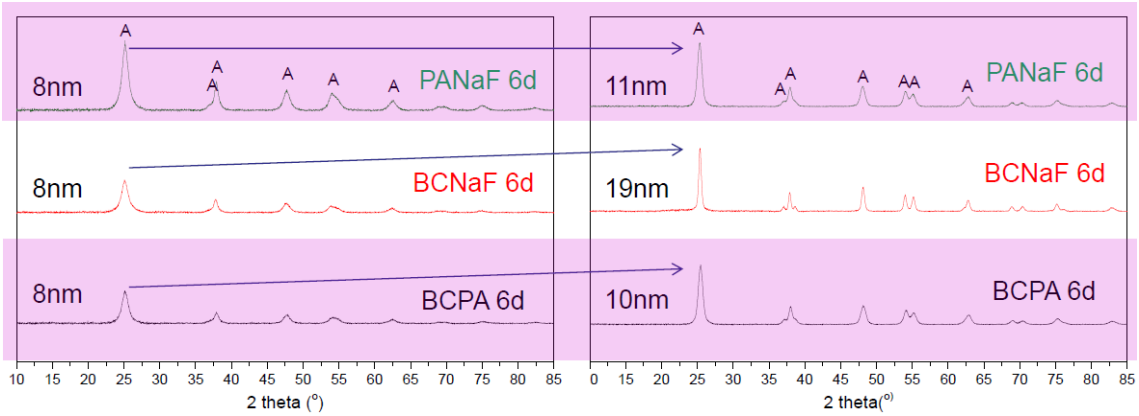

Figure 8 : Spectres de DRX et les tailles de cristallite des échantillons « BCNaF », « BCPA » et « PANaF » avant (gauche) et après calcination (droite). Le temps de murissement est fixé à 6 jours. Ceci montre l'influence de la présence de phosphore (dans le cas de « BCPA » et « PANaF » qui sont marqués en violet) sur l'inhibition de la croissance de taille de cristallite durant calcination.

L'analyse XPS des échantillons de TiO_2 synthétisé avec la présence de phosphore, donc l'échantillon « BCPA » et « PANaF » (Figure 9), permet de mettre en évidence la présence de phosphore sous forme de phosphate (contribution P^{5+}-O dans les spectres de P_{2p}) sur la surface de TiO_2, même si le teneur en phosphore est relativement faible (le ratio P/Ti est 0,03). Ayant le même ratio molaire de P/Ti à 0,03, l'absence de pic de phosphore dans l'échantillon synthétisé avec liquide ionique précédemment indique probablement qu'une différence entre la quantité de phosphore décomposé de $BmimPF_6$ *via* hydrolyse et celle intervenue par H_3PO_4 directement. Mais similaire que l'utilisation de $BmimPF_6$, l'acide phosphorique utilisé dans la synthèse de l'échantillon « BCPA » et « PANaF » conduit à un augmentation de ratio molaire calculé de P/Ti durant calcination à 550 °C, ce qui adapte l'hypothèse d'une migration partielle de phosphate vers la surface de TiO_2 à une haute température.

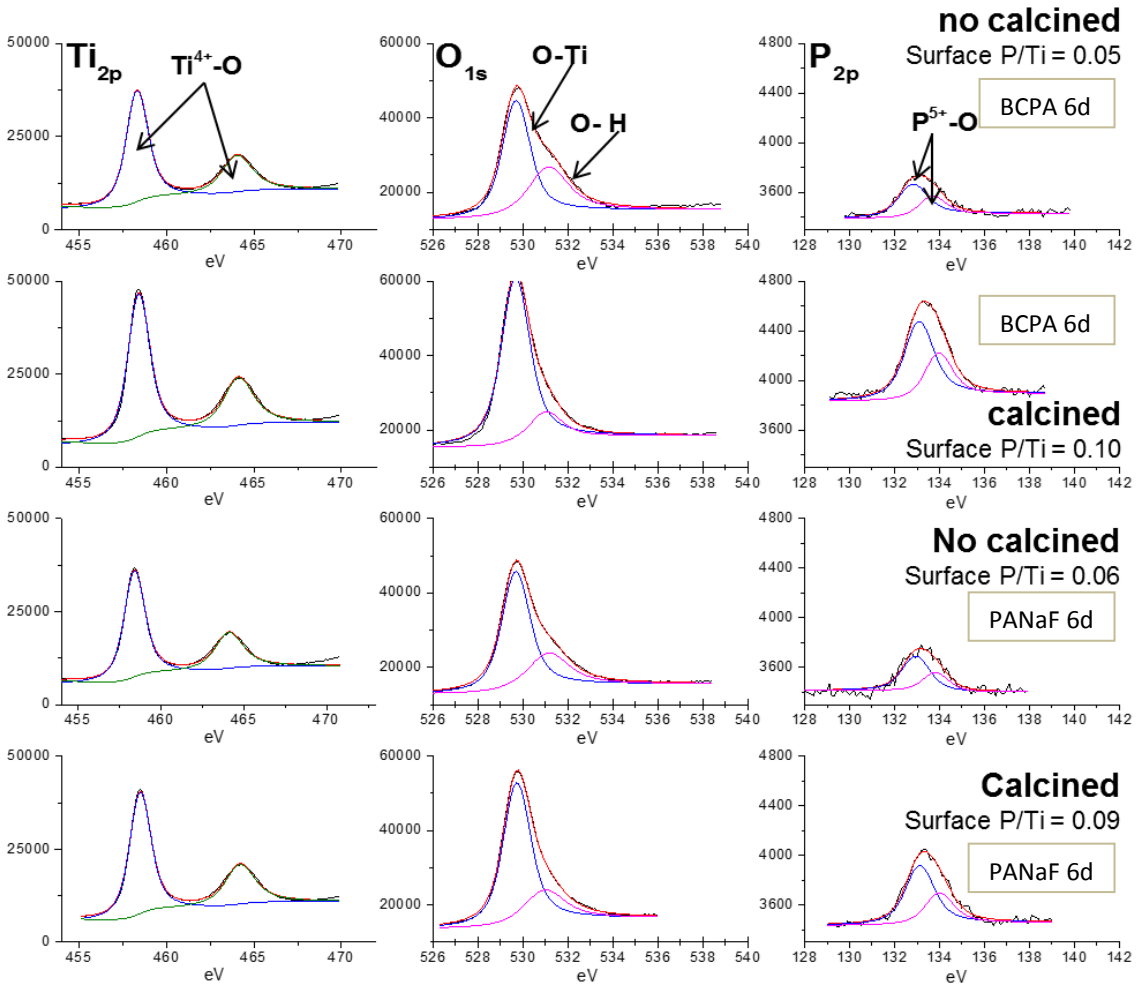

Figure 9 : Spectres de XPS de Ti_{2p}, O_{1s} et P_{2p} et le ratio molaire calculé de P/Ti des échantillons non calcinés et calcinés de « BCPA » et « PANaF » synthétisés avec un ratio fixé de P/Ti (0,03) dans la synthèse sol-gel. L'acide utilisé est HAc et la durée de murissement est fixée à 6 jours.

Si le ratio molaire de P/Ti augmente à 0,4 (dans le cas de « PANaF »), les spectres de XPS de Ti_{2p}, O_{1s} et P_{2p} des échantillons non calciné ou calciné (Figure 10) sont beaucoup plus compliqués. Dans le spectre Ti_{2p}, un second doublet attribué à liaison Ti-O-P (Ti-PO_4) a été observé à part celui de Ti^{4+}-O de TiO_2. La grande valeur de shift au niveau d'énergie de liaison vers plus haute énergie met en évidence l'interaction forte de Ti avec PO_4^{3-}, probablement grâce à une polarisation importante de la densité électronique autour des atomes de Ti vers les phosphates qui sont électron-attracteurs. Dans le spectre de O_{1s}, une enveloppe de pic très élargie a été observé dans ce cas. Cet élargissement de pic peut être causé par l'ajout d'oxygène supplémentaire apporté par les phosphate. Alors pour le spectre de P_{2p}, un second doublet a été observé et a été contribué à phosphore sous forme de polyphosphate, conforment à l'apparition d'un second doublet dans le spectre de Ti_{2p}.

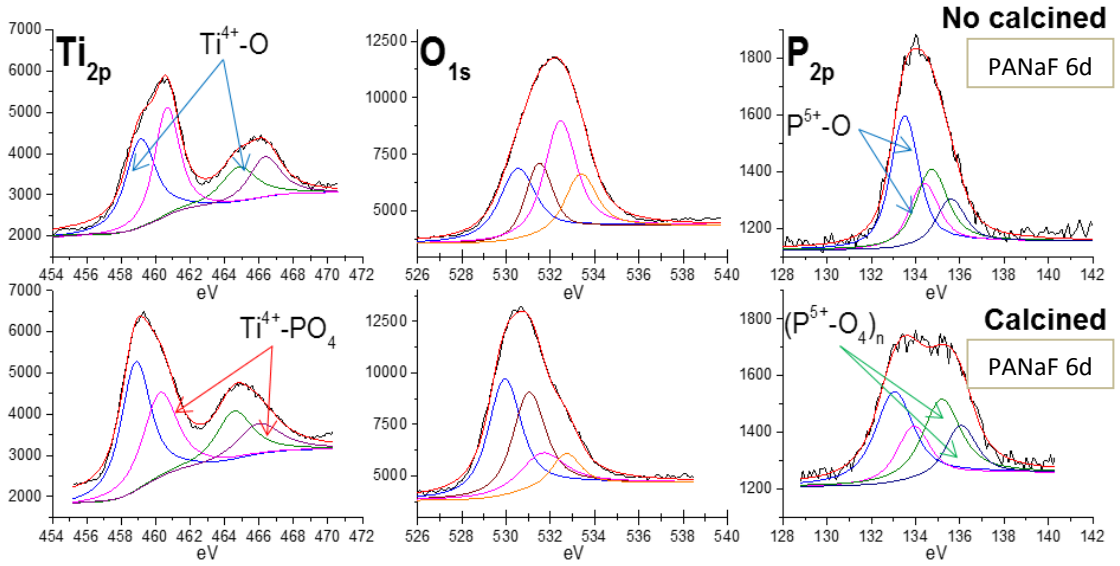

Figure 10 : Spectres de XPS de Ti_{2p}, O_{1s} et P_{2p} des échantillons non calcinés et calcinés de « PANaF » synthétisés avec un ratio fixé de P/Ti (0,4) dans la synthèse sol-gel. L'acide utilisé est HAc et la durée de murissement est fixée à 6 jours.

La présence de phosphate et la formation de liaison Ti-PO_4 a été aussi mise en évidence par analyse DRX (Figure 11), si le ratio molaire de P/Ti augmente à 0,4 (dans le cas de « PANaF ») et si la température de calcination est 800 °C. Une quantité élevée de phosphore utilisée dans la synthèse et une température de calcination élevée sont nécessaire pour voir les phases cristallisées de phosphate de titane. Néanmoins à un faible ratio molaire de P/Ti (0,03), l'existence de la formation de Ti-PO_4 peut être quand même spéculé, sous forme amorphe et en l'état très dispersé. En fin, il faut aussi noter que l'anatase est la seule phase formée pour l'échantillon « PANaF » avec un ratio molaire de P/Ti de 0,03, même calciné à 800 °C. Ce dernière observation confirme que la présence de phosphore (même en faible quantité) inhibite la transformation de de phase anatase-rutile, comme ce que $BmimPF_6$ fait.

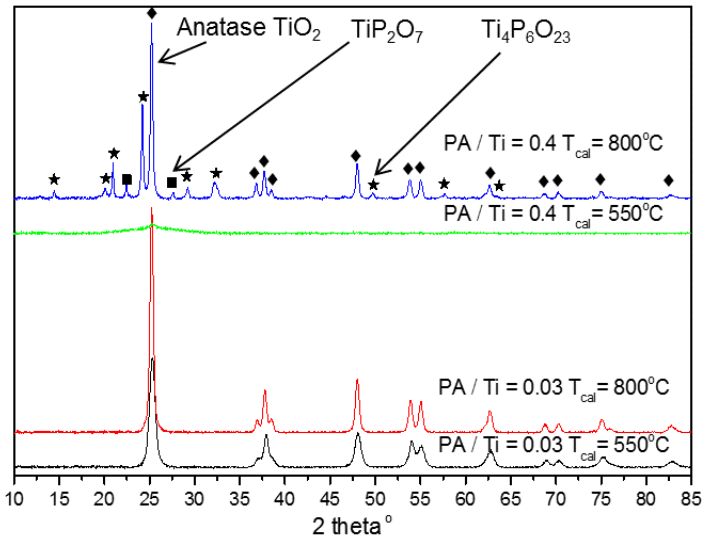

Figure 11 : Spectres de DRX de l'échantillon « PANaF » ayant diffèrent ratio molaire de P/Ti (0,03 ou 0,4) et différentes températures de calcination (550 °C ou 800 °C). Le temps de murissement est fixé à 6 jours.

Images TEM de l'échantillon « PANaF » no calciné muries à 6 jours ayant un ratio molaire de P/Ti de 0,03 (Figure 12) montrent nanocristaux relativement bien cristallisés, mais avec un forme anisotropique par rapport à celle obtenue par synthèse classique de TiO_2. Ceci peut être lié à la présence des ions fluor en milieu de synthèse, qui a été connu comme un agent de modification

structurale d'anatase. Plus d'information concernant son influence à la performance photocatalytique de TiO_2 vont être discuté prochainement.

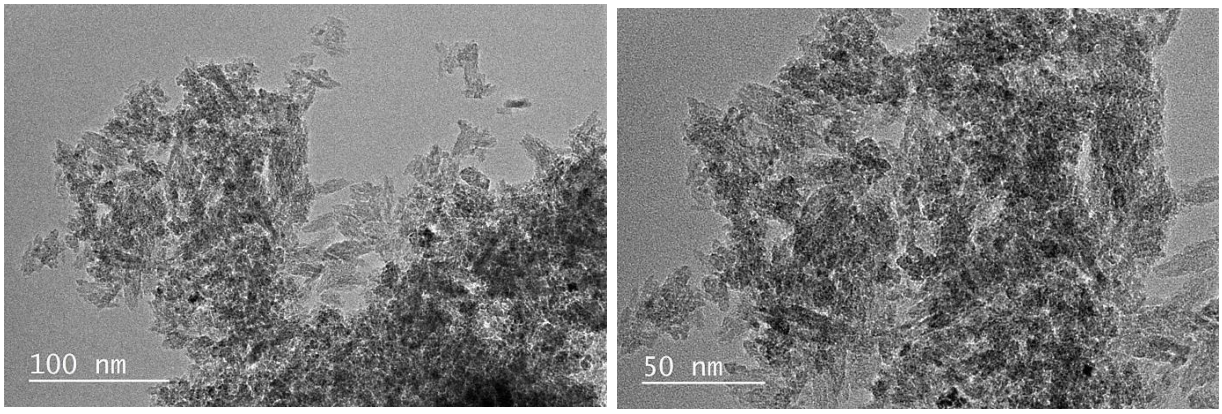

Figure 12 : Images TEM de l'échantillon « PANaF » no calciné ayant un ratio molaire de P/Ti de 0,03. Le temps de murissement est de 6 jours.

Parallèlement au changement de $BmimPF_6$ par des additives, l'acide utilisé dans la synthèse sol-gel de TiO_2 a été changé par HCl aussi pour mieux comprendre le mode d'action de P et F sur les propriétés physico-chimique de TiO_2. Les résultats ne sont pas présentés ici mais seront totalement démontrés dans la version originale de thèse.

L'interprétation des résultats issus des caractérisations nous a permis d'avancer les hypothèses suivantes :

- La durée de murissement a un effet direct sur la taille des cristallites et sur la surface spécifique.
- La présence de fluor sous forme de F^- semble agir, après nucléation, par adsorption privilégiée sur les certaines faces (celles de {001}) de TiO_2 anatase, résultant ainsi en une croissance anisotropique des cristallites (vérifiée par MET).
- La présence de phosphore sous forme PO_4^{3-} (mise en évidence par DRX et XPS) semble intervenir lors du murissement et permet de former la liaison Ti-PO_4 avec les atomes de Ti, qui est lié d'une manière ou d'une autre à limitation la taille des cristallites, même après traitement thermique à 550 °C.

Sachant les rôles primordiaux du phosphore et du fluor lors de la synthèse par voie sol-gel, une synthèse alternative a été mise en œuvre avec succès en remplaçant le liquide ionique $BmimPF_6$ par ces constituants les plus impactants, noté « PANaF ». Ce photocatalyseur TiO_2 a été caractérisé et possède des propriétés physico-chimiques similaires à celles des TiO_2 synthétisés en présence de liquide ionique, en termes de cristallinité et de nature cristallographique, de surface spécifique, de taille des cristallites, de morphologie et de chimie de surface. Avec des rapports atomiques P/Ti = 0,03 et F/Ti = 0,03, une surface spécifique élevée de 130 m^2/g avec une taille de cristallite limitée à 11 nm est notamment maintenue après calcination.

III. L'activité photocatalytique des nanomatériaux à base de TiO_2 vis-à-vis de la dégradation d'un Composé Organique Volatile (COV) modèle, et de l'élimination des bactéries en surface

III.1. Tests de photooxydation de la MéthylEthylCétone (MEK)

Tous les matériaux photocatalytiques synthétisé avec $BmimPF_6$ ou avec les additives de remplacement de $BmimPF_6$ ont ainsi pu être comparés en termes d'activité de photooxydation de la MEK sous flux (RH 50%, MEK 100 ppmv, débit total 227 ml/min, température contrôlée à 25℃) avec une illumination UV-A de 30 W/m^2 à 365 nm. Les matériaux, en suspension dans l'éthanol, ont été déposés par drop-casting sur une plaque de verre à une densité de 1 mg/cm^2. Les tests photocatalytiques ont été menés sur le dispositif expérimental décrit sur la Figure 13, et le réacteur a été conçu d'après la norme série ISO 22197.

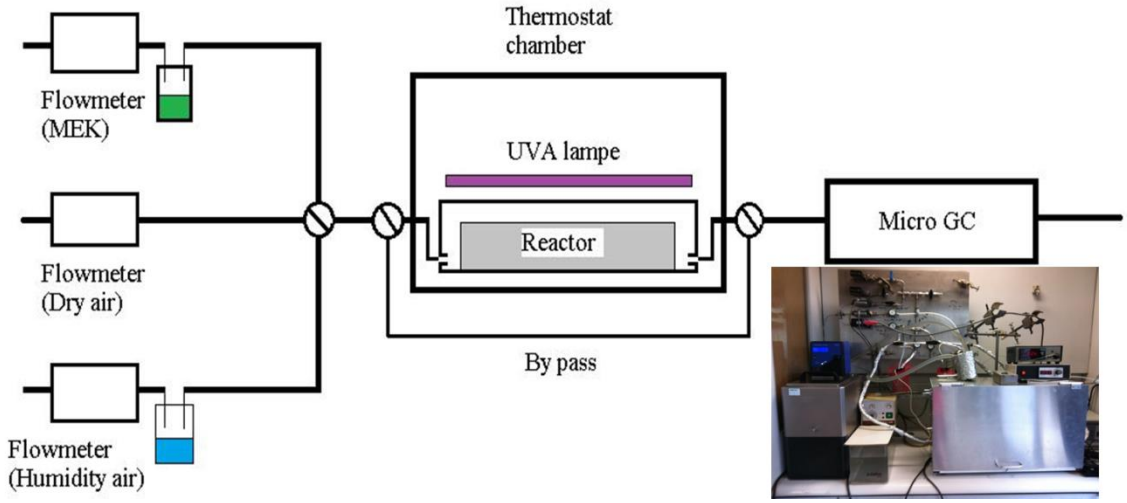

Figure 13 : Pilote de test photocatalytique de dégradation de la MEK.

L'activité photocatalytique des échantillons est exprimée par la conversion de MEK (C_{MEK}), la sélectivité en CO_2 et celle en acétaldéhyde (S_{CO2} et S_{Ac}), et enfin le taux de minéralisation en CO_2 (Y_{CO2}).

$$C_{MEK}(\%) = \frac{([MEK_{dark}] - [MEK_{UV}])}{[MEK_{dark}]} * 100$$

$$S_{CO_2}(\%) = \frac{[CO_{2\,out}]}{([MEK_{dark}] - [MEK_{UV}]) * 4} * 100$$

$$S_{Ac}(\%) = \frac{[Ac_{out}]}{([MEK_{dark}] - [MEK_{UV}]) * 2} * 100$$

$$Y_{CO_2}(\%) = \frac{[CO_{2\,out}]}{[MEK_{dark}] * 4} * 100$$

On observe (Figure 14) que l'activité photocatalytique des photocatalyseurs calcinés synthétisés par voie sol-gel en présence de $BmimPF_6$ ($BmimPF_6$ / Ti = 0,03 ou 0,4) sont bien plus élevée en termes de taux de minéralisation que celle du TiO_2 P25 commercial (Evonik). L'échantillon IL0,03 muri de 6 jours présente une activité deux fois plus élevés termes de taux de minéralisation que celle du TiO_2 P25, ce qui résulte à la fois d'une conversion de la MEK ou d'une sélectivité en CO_2 plus élevées.

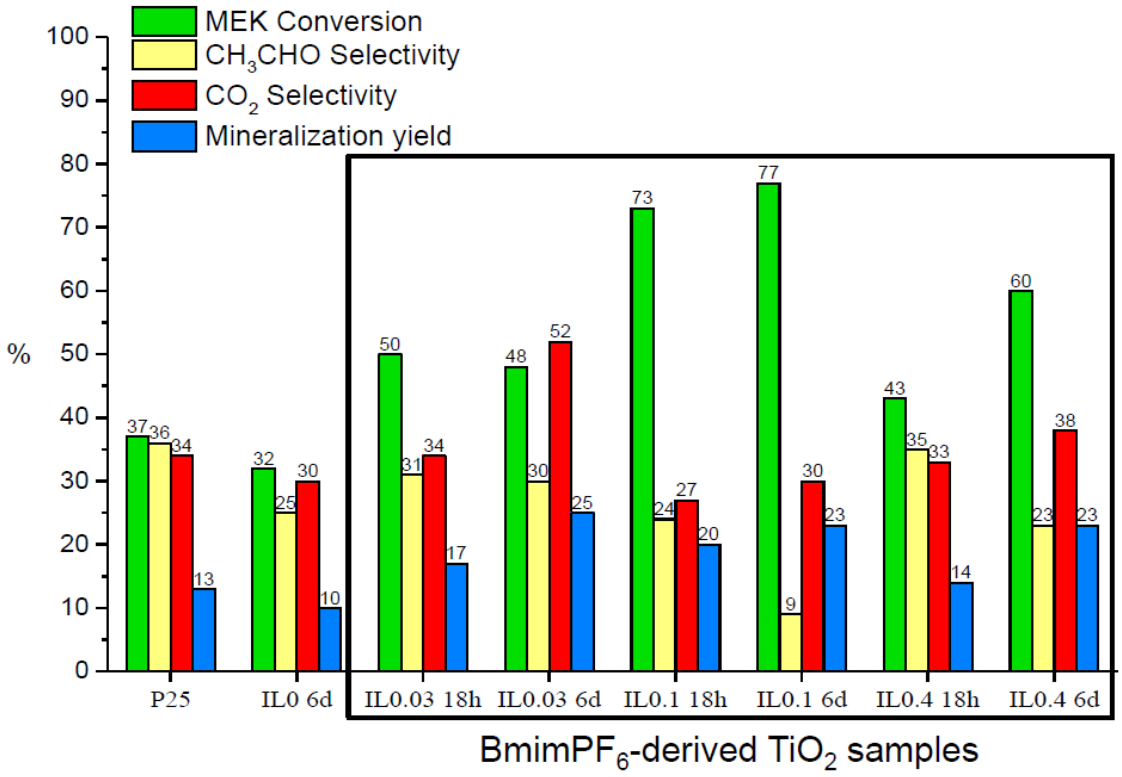

Figure 14 : Activité de photooxydation de la MEK exprimée en termes de conversion de la MEK, sélectivité en CO_2 et taux de minéralisation pour les échantillons synthétisés avec $BmimPF_6$ (entourés). Le TiO_2 P25 commercial (Evonik) et le TiO_2 synthétisé sans additive sont pris comme références.

En changeant le $BmimPF_6$ par des combinassions des additives de remplacement (Figure 15), on peut noter que la présence de P semble favoriser la conversion de MEK et la présence de F semble améliorer la sélectivité en CO_2. Seule la combinaison des constituants d'influence sous forme d'acide phosphorique et de fluorure de sodium (« PANaF » avec P/Ti = 0,03, F/Ti = 0,03) présente une performance analogue, voire légèrement supérieure à celle de meilleur obtenue avec TiO_2 synthétisée en présence de liquide ionique, grâce à la fois à une conversion de la MEK et à une sélectivité en CO_2 la plus élevée.

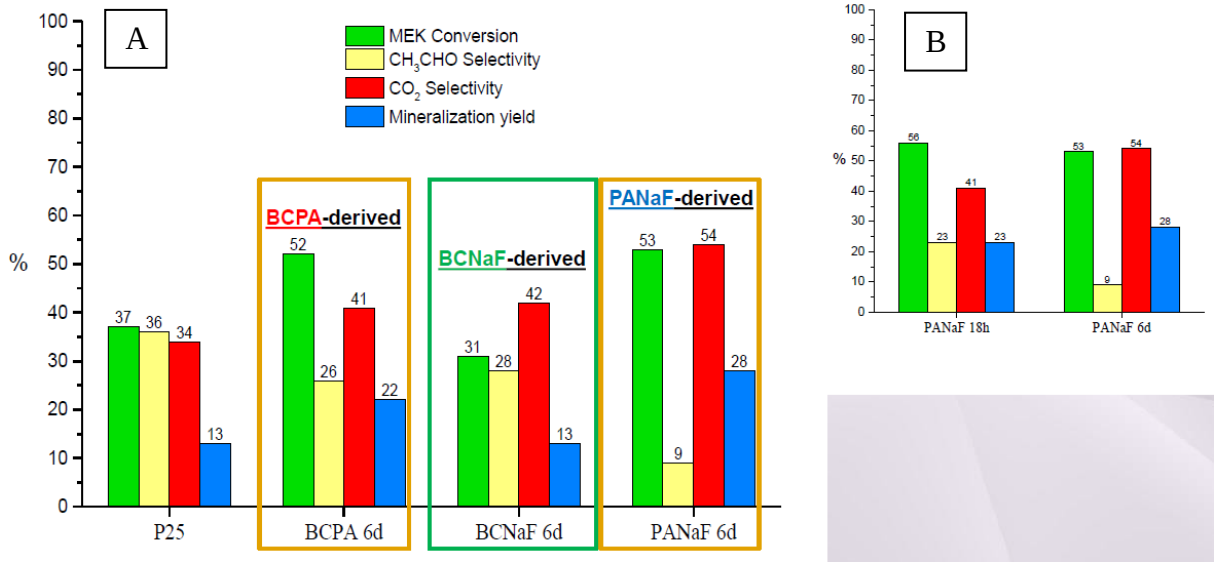

Figure 15 : Activité de photooxydation de la MEK exprimée en termes de conversion de la MEK, sélectivité en CO_2 et taux de minéralisation pour les échantillons « BCPA », « BCNaF » et « PANaF », les ratios molaire des additive/Ti sont fixés à 0,03 (A) ; Activité de photooxydation de la MEK exprimée en termes de conversion de la MEK, sélectivité en CO_2 et taux de minéralisation pour l'échantillon « PANaF » en fonction de la durée de murissement (18h ou 6jours), le ratio molaire de additive/Ti est fixés à 0,03. Le TiO_2 P25 commercial (Evonik) est pris comme références.

Enfin, il est noté que la performance photocatalytique dépende au temps de murissement, pour les photocatalyseurs synthétisés avec $BmimPF_6$ ou avec les additives de remplacement de $BmimPF_6$. Plus un échantillon est muri (6 jours maxi), plus il est performant.

Cette amélioration de performance photocatalytique de TiO_2 (en présence de liquide ionique ou pour TiO_2 «PANaF ») résulterait, tout en maintenant une bonne cristallinité de la phase anatase du TiO_2, d'une augmentation du nombre des sites réactionnels sur l'ensemble des nanocristaux de TiO_2, associée :

D'une part à une taille de particules adéquate grâce à la présence de P, qui augmente la surface spécifique des échantillons de TiO_2. Ce qui favorise la quantité de MEK adsorbée par unité en masse de photocatalyseur, donc la conversion de MEK.

D'autre part à une modification de morphologie des cristaux de TiO_2 probablement grâce à la présence de F durant le murissement, qui améliore plutôt la sélectivité en CO_2.

Ces propriétés résultent donc directement de la présence du phosphore et du fluor lors de la synthèse de TiO_2. Il est également important de noter que le photocatalyseur «PANaF » est le plus performant de l'ensemble des photocatalyseurs synthétisés lors de ce travail, tout en maintenant le coût de production le plus faible en raison de la substitution du liquide ionique, onéreux, par des précurseurs classiques de la chimie de synthèse.

Discussion : Modification des propriétés de TiO_2 par les additives et la corrélation avec l'activité photocatalytique

P et F ont été mis en évidence comme les 2 éléments qui jouent un rôle important dans la synthèse sol-gel des nanomatériaux à base de TiO_2. D'où on a noté trois impacts majeurs de la présence de P et F de $BmimPF_6$ ou des additives de remplacement de liquide ionique sur les propriétés physico-chimiques et l'activité photocatalytique de TiO_2.

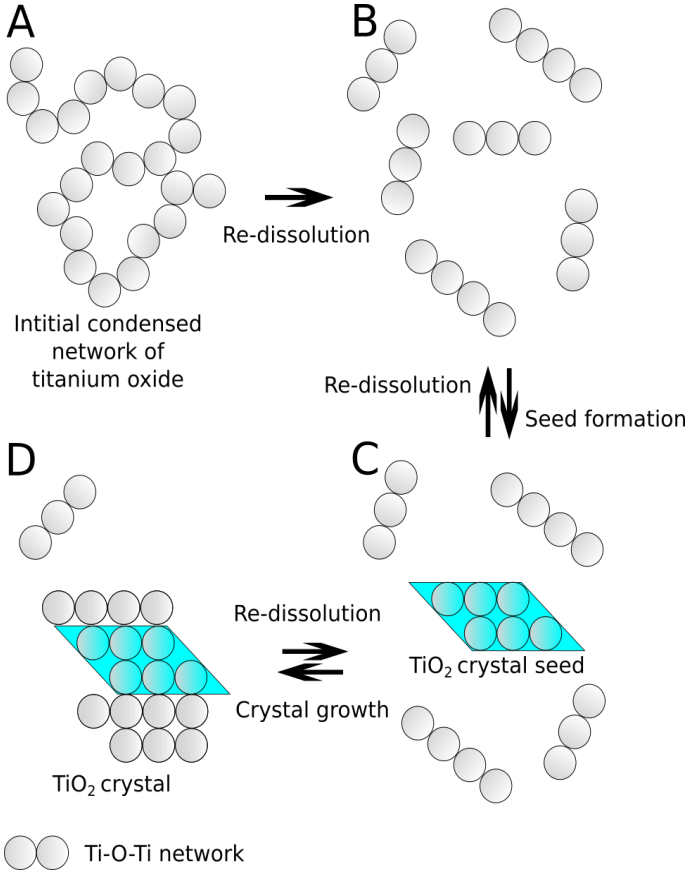

Figure 16 : Illustration schématique du mécanisme de cristallisation de TiO_2 en température ambiante sans l'aide des additives durant le murissement.

1 : L'activité photocatalytique de TiO_2 avec la présence de P et F est **dépendante de la durée de murissement**. Généralement ce phénomène se manifeste par une augmentation de l'activité photocatalytique de TiO_2, accompagné d'une diminution de la surface spécifique, une augmentation de taille de cristallite et l'intensité de pic DRX, en fonction du temps de murissement. On suppose que les variations autour des cristaux de TiO_2 résultent d'un processus de s'auto-cristallisation en solution durant le murissement en température ambiante, qui est proposé dans Figure 16. A) Polymérisation des chaines Ti-O-Ti issue de condensation ; B) Ré-dissolution des chaines aux segments plus petits à condition acide ; C) Formation des nucléides par l'arrangement ordonné des

petits segments ; D) Cristallisation de TiO_2 à partir des nucléides stabilisés par réarrangement ordonné des petits segments. Il nous semble que l'utilisation de $BmimPF_6$ ou des additifs contenants P permet d'accélérer la vitesse de cristallisation et de maintenir une petite taille des cristaux avant et après calcination (résistance à calcination). Ce qui est un facteur très important pour améliorer l'activité photocatalytique de TiO_2. L'effet de phosphore durant murissement sera discuté prochainement.

2 : L'activité photocatalytique de TiO_2 avec la présence de P et F, surtout la sélectivité en CO_2, est influencée par **un effet de modification structurale des cristaux de TiO_2 induit par la présence de F**. F a été connu de s'adsorbe sélectivement sur la face {001}, cela permet donc de diminuer l'énergie de cette face et de favoriser la croissance préférentielle de cette dernière. L'activité photocatalytique serrait plus élevée pour les cristaux de TiO_2 en forme bipyramide après modification structurale par F, grâce aux deux raisons : a) Une séparation de charge spatiale, dont les trous photogénérés migrent vers les faces {001} et les électrons photogénérés migrent vers les faces {101} ; b) L'adsorption des certaines molécules issus de la dégradation intermédiaire d'un COV est plus favorisée sur les faces {001} que sur autres faces, ceci permet d'augmenter la sélectivité en CO_2. On n'a pas pu mettre en évidence une forme bipyramide des cristaux de TiO_2 dans notre cas quel que soit la synthèse. Néanmoins, une forme en nanobâtonnet des cristaux de TiO_2 avant calcination pour l'échantillon « PANaF » a été observée, qui serait probablement dû à un effet de modification structurale atypique par la présence de F selon des études précédentes.

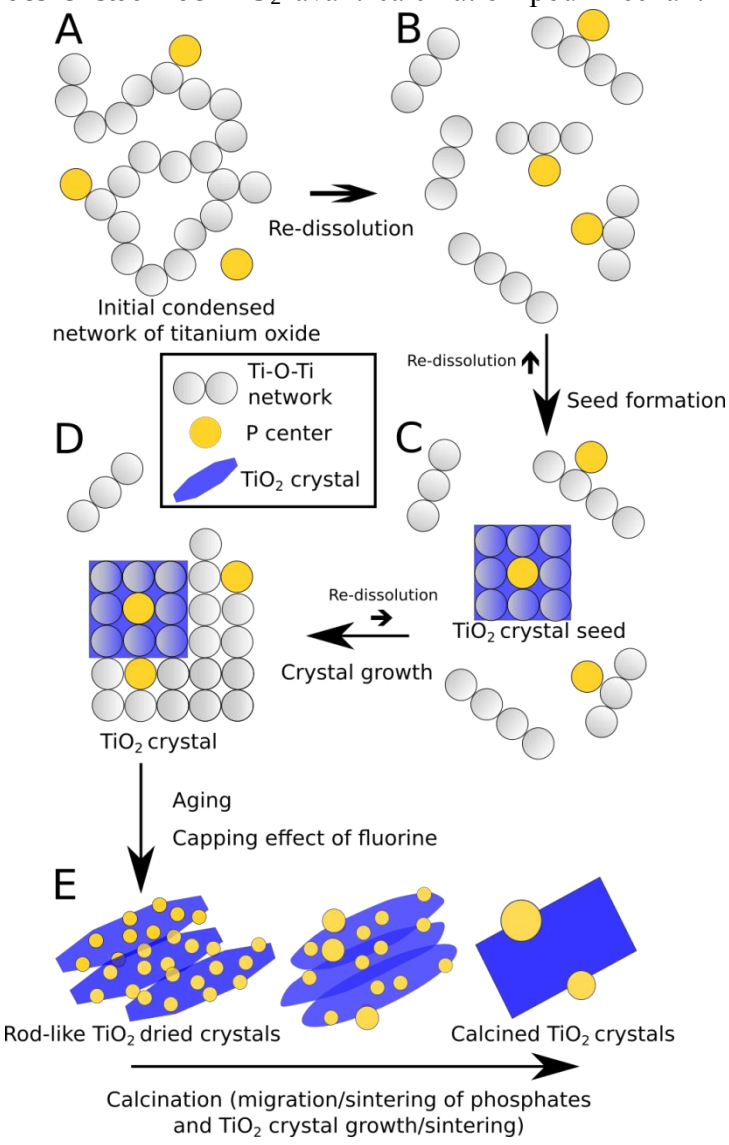

Figure 17 : Proposition de l'action complète de phosphore (ratio molaire de P/Ti faible) sur TiO_2 synthétisé dans milieu acide. acétique

3 : L'activité photocatalytique de TiO_2 avec la présence de P et F, surtout la conversion de MEK, bénéfice à **un effet de modification de la taille de particule de TiO_2 induit par la présence de P**. Les phosphates (de l'hydrolyse de $BmimPF_6$ ou de H_3PO_4 directement) forment des liaison intimes avec des petits chaines de réseau Ti-O-Ti une fois après hydrolyse de précurseur de Ti (Figure 17 A-B) ; la formation des nucléides et la croissance des cristaux à partir de ces derniers sont plus favorisées, à cause de l'inhibition de re-dissolution des nucléides qui s'est produit souvent au course de murissement dans la synthèse sans présence de phosphore, et un plus grand nombre des cristaux, encore plus cristallisés, est donc formé, ce qui est l'origine de la petite taille des cristaux (Figure 17 C-D) ; les cristaux de TiO_2 bien cristallisés sous forme de nanobâtonnet (*via* l'action de F) contient des phosphate en état très dispersé, possiblement plus en surface qu'en bulk de TiO_2 avant calcination ; et il y a eu une migration/frittage des phosphates vers la ou en surface accompagné d'une croissance légère de taille des cristaux par attachement préférentiel des

nanobâtonnets selon la direction de largeur ; les phosphates après calcination sont concentrés en surface de TiO_2 dans une zone limité (Figure 17 E).

Deux avantages fournis par la présence de phosphore sont marqués ici : a) la petite taille des cristaux en anatase maintenue après calcination conduit à une surface spécifique élevée, ce qui favorise adsorption de MEK donc la conversion de MEK ; b) la présence des phosphate (en petite quantité) concentrés en surface de TiO_2 conduit à un effet de séparation de charge, qui favorise l'activité photocatalytique de TiO_2 grâce à la propriété électron attracteur de phosphate.

Enfin, les rôles combinés de phosphore et fluor dans la synthèse sol-gel de TiO_2 en milieu acide acétique, ainsi que leur contribution à l'activité photocatalytique augmentée a été proposés dans la Figure 18.

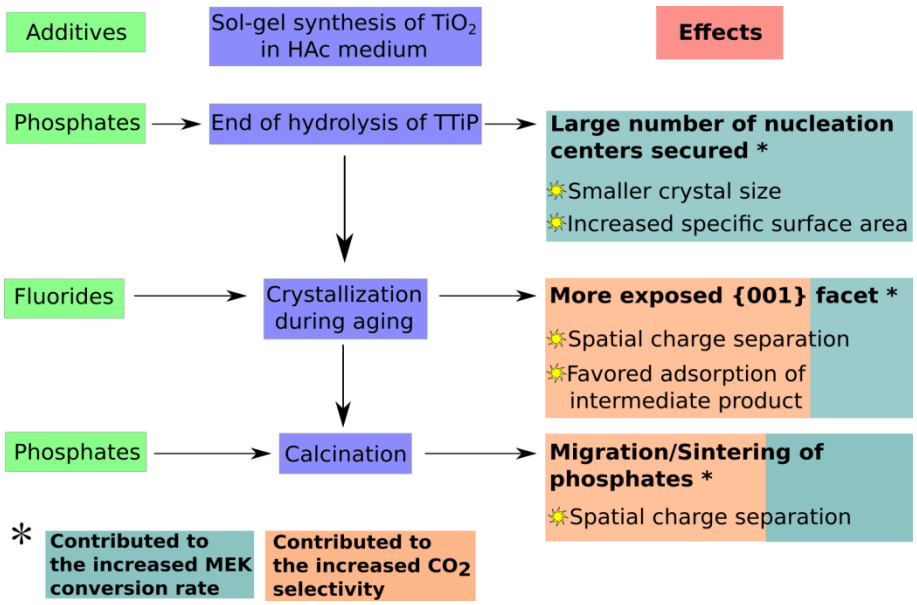

Figure 18 : Explication schématique des rôles combinés de phosphore et fluor dans la synthèse sol-gel de TiO_2 en milieu acide acétique, ainsi que leur contribution à l'activité photocatalytique augmentée.

III.2. Evaluation et étude des propriétés biocides des nanomatériaux de TiO_2

Les performances antibactériennes du nouveau photocatalyseur PANaF ont été étudiées en comparaison du photocatalyseur commercial P25. Dans cette optique, des tests photocatalytiques ont été réalisés en phase liquide, dans un milieu physiologique constitué d'une solution de NaCl à 9g/L, sur des dépôts de TiO_2 identiques à ceux utilisés pour les tests de dégradation de MEK (densité de TiO_2 de 1 mg/cm^2 sur plaques de verre). L'étude microbiologique a été complétée par une caractérisation par AFM de la topographie de surface, qui a révélé une différence significative de morphologie entre les dépôts de PANaF et P25 (Figure 5), différence potentiellement responsable de différences d'adhésion et de surface de contact entre les microorganismes et la surface des nanomatériaux déposés.

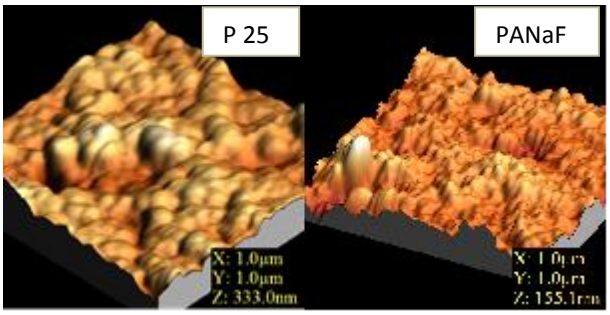

Figure 19 : Topographie des dépôts de P25 et PANaF, analysée par AFM.

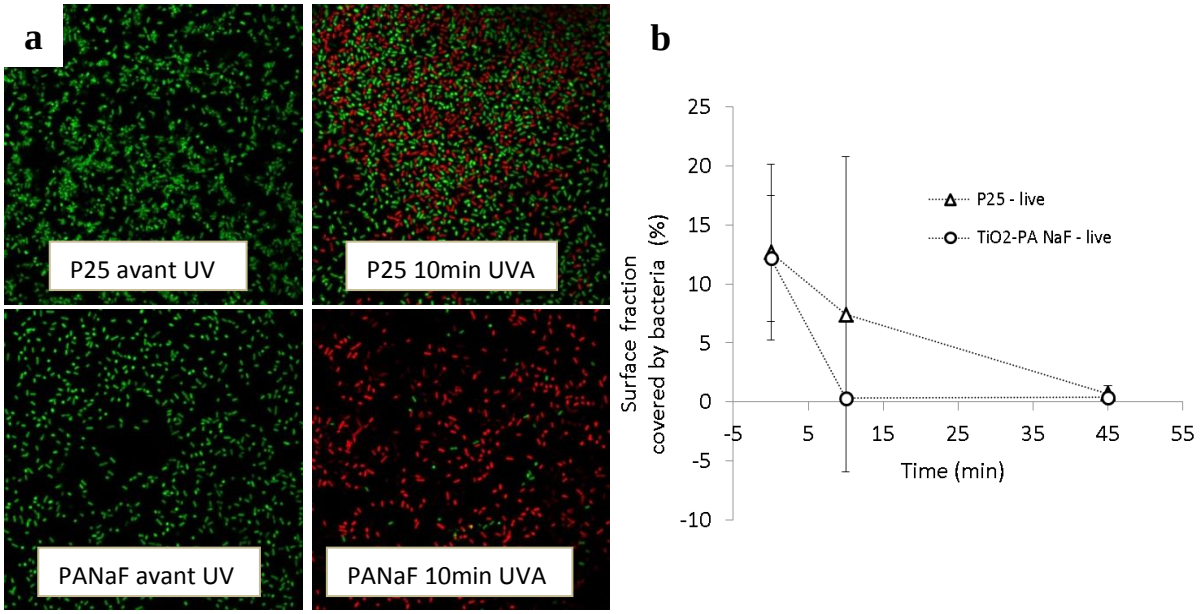

Figure 20 : (a) Images microscopiques confocales de bactéries *E.coli* sur échantillons TiO_2 P25 et PANaF, avant et après 10 min de traitement UVA (en vert, les bactéries actives; en rouge, les bactéries dont la membrane est endommagée). (b) Fraction de surface couverte par les bactéries *E.coli* avant et après 10 min et 45 min de traitement UVA, sur échantillons TiO_2 P25 et PANaF.

Les tests photocatalytiques antibactériens ont été conduits avec plusieurs espèces bactériennes aux caractéristiques membranaires différentes, susceptibles d'influer leur sensibilité au traitement photocatalytique (*Escherichia coli –E. coli-*, *Staphylococcus epidermidis –S. epidermidis-*, *Pseudomonas fluroescens –P. fluorescens-*). La souche SCC1 de *E.coli*, génétiquement modifiée pour exprimer une protéine fluorescente GFP, a été utilisée comme bactérie de référence. Les bactéries non fluorescentes par GFP ont été marquées au Syto9® pour déterminer la population bactérienne totale. Toutes les bactéries ont de plus fait l'objet d'un marquage à l'iodure de propidium (IP) afin de déterminer l'état d'intégrité de leur membrane. L'observation *in situ* par microscopie confocale des populations bactériennes adhérées sur les dépôts de TiO_2 a permis de montrer une efficacité très significativement plus élevée des TiO2 PANAF en comparaison des P25. En particulier, une diminution de plus de 95% de recouvrement des surfaces par des bactéries *E.coli* intactes est obtenue dès 10 min d'une illumination UV-A de 30 W/m^2 sur le produit PA-NaF alors que, dans le même temps, seul un effet faible et variable est observé sur les dépôts P25. Une telle dégradation quasi-complète des populations d'*E. coli* adhérées n'est observée sur les dépôts de P25 qu'après 45 min d'illumination (Figure 5). Les performances antibacteriennes très significativement plus élevées des nanomatériaux PANaF en comparaison des P25 ont été confirmées sur toutes les espèces bactériennes précédemment citées, ainsi que sur une souche de *Listeria monocytogenes* (*L. monocytogenes*) (expérience complémentaire réalisée par le partenaire CRITT Aérial). Toutefois, une efficacité variable selon les espèces a été constatée, selon l'ordre décroissant *E. coli* > *S. epidermidis* > *P. fluorescens*, sans lien direct avec la constitution membranaire des bactéries. Après respectivement 45 min et 3h d'illumination,

cependant, la dégradation quasi-totale des populations de *S. epidermidis* et *P. fluorescens* était atteinte sur les dépôts PANaF, alors qu'elle n'était que très partielle sur les dépôts de nanomatériaux P25.

Afin d'évaluer l'efficacité à long-terme du traitement photocatalytique antibactérien, les populations bactériennes traitées ont ensuite été placées pendant plusieurs heures (jusqu'à 15h) en conditions nutritives favorables à leur réparation et à la reprise de croissance de la population. Les analyses par microscopie confocale ont montré que, bien que capable de reconstituer une population bactérienne, les bactéries endommagées par le traitement photocatalytique ne pouvaient reproduire une densité de population similaire à celle observée sans traitement. De plus, l'efficacité antibactérienne significativement plus élevée des nanomatériaux PANaF a abouti à une réduction plus forte de la reprise de croissance sur ces matériaux, en comparaison des populations reconstituées sur les dépôts de nanomatériaux P25.

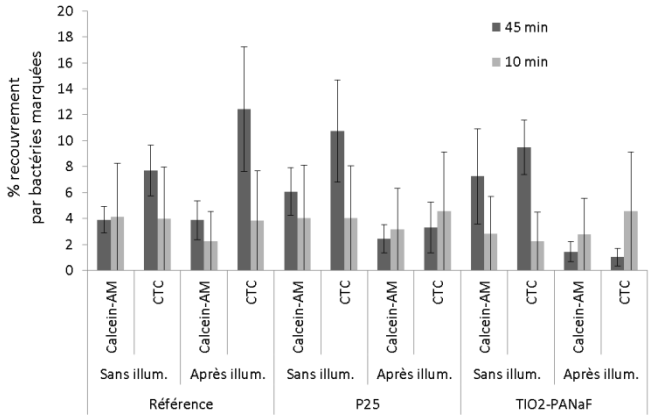

Figure 21 : Effets photocatalytiques sur l'activité enzymatique (marquée par Calceine AM) et l'acivité de la chaîne respiratoire (marquée par CTC) des bactéries *E. Coli.*

Finalement, une étude spécifique a été réalisée sur *E. coli* en vue d'approfondir la compréhension des mécanismes de dégradation des bactéries lors du traitement photocatalytique. Des marqueurs fluorescents, calcein-AM et 5-Cyano-2,3-ditolyl Tetrazolium Chloride (CTC), ont pour cela été utilisés comme indicateurs respectifs de l'activité enzymatique et de l'activité de la chaîne respiratoire des bactéries. Les résultats (Figure 6) montrent une diminution de ces activités, plus marquée sur les nanomatériaux PANaF que P25, confirmant ainsi l'efficacité antibactérienne optimisée des nanomatériaux PANaF. Ils montrent par ailleurs que des niveaux d'activités respiratoire et enzymatique normaux subsistent après 10 d'illumination, alors que la membrane bactérienne est déjà endommagée, et que ces activités ne sont affectées qu'après des temps d'illumination supérieurs (45 min), en accord avec les mécanismes de dégradation de bactérie proposés dans la littérature : la couche bi-lipidique et les protéines membranaire seraient atteintes dans un premier temps, avant que la membrane interne, siège de l'activité respiratoire notamment, et impliquée dans une partie de l'acitivité enzymatique, ne soit affectée.

En complément de ces travaux, les influences sur l'effet photo-bactéricide de la topographie de la surface de TiO_2 (tenant compte de l'analyse AFM), de la nature du milieu de culture dans lequel est appliqué le traitement photocatalytique et de la présence d'oxygène ont également été étudiées et discutées. La présence d'oxygène en particulier s'est révélée être un facteur essentiel de contrôle de l'efficacité photocatalytique antibactérienne dans un environnement liquide confiné

V. Conclusion générale

Dans ce travail, on a pu premièrement synthétisé des nanomatériaux photocatalytiques à base de TiO_2 par voie sol-gel modifiée en utilisant un liquide ionique ($BmimPF_6$) comme un structurant. Ces matériaux ont montré des propriétés physico-chimiques uniques avec des activés photocatalyses très intéressantes en dégradant MEK en phase gazeuse et aussi en éliminant les bactéries en phase liquide par rapport à TiO_2 P25. Ensuite en remplaçant $BmimPF_6$ par ces éléments constituants, on a pu révélé que c'est la présence de phosphore et fluor qui apporte une amélioration au niveau de l'activité photocatalytique au sein de ces matériaux. D'ailleurs, des études ont été réalisées pour comprendre les mécanismes de dégradation des bactéries lors du traitement photocatalytique. La couche bi-lipidique et les protéines membranaire seraient affectés dans un premier temps, avant que la membrane interne ne soit affectée. La présence d'oxygène s'est révélée être un facteur essentiel de contrôle de l'efficacité photocatalytique antibactérienne dans un environnement liquide confiné. En fin, un prototype préliminaire de revêtement photocatalytique a été élaboré, néanmoins, plusieurs propriétés et performances photocatalytiques restent encore à améliorer.

General introduction

Indoor air quality refers to the air quality within buildings and more globally confined spaces. It relates directly to the health and comfort of occupants, since men spend nowadays 70% to 90% of time in confined spaces like home, [1] public and private transports, work office.

Indoor air quality can be affected by gases, particulates, microbial contaminants and many others. Amongst the most common pollutants, the Volatile Organic Compounds (VOCs) are a major contribution to the Sick Building Syndrome caused by the poor indoor air quality. [2] Concentrations of many VOCs are consistently higher indoors than outdoors due to the lack of fresh air intake and ventilation, or the increasing use of organic based home products and materials (plastics, paints, lacquers…). Although some countries like France, Germany and Belgium have enacted regulations to limit VOC emissions from commercial products, [3] and industry has developed numerous voluntary ecolabels and rating systems, such as EMICODE, M1, Blue Angel and Indoor Air Comfort, no standards yet have been set for VOCs in non-industrial frame.

The microbial contamination is another source affecting the indoor air quality, and forms so-called bioaerosol. [4] Many bacteria of health significance are found in indoor air and on indoor surfaces. A large fraction of them are shed from humans, while other sources include organic dust, building materials or air inflow. Amongst the most important bacteria known to live in indoor air are *Mycobacterium tuberculosis*, *Staphylococcus aureus*, *Legionella* and etc. The findings of epidemiological research indicate that exposure to high concentrations of these bioaerosols frequently leads to allergies, asthma, pneumonia and many other health side-effects, including infections. [5] Some fungal spores and mites are also involved in the above mentioned Sick Building Syndrome.

To counteract the increasing indoor air pollution events, numerous techniques have emerged in recent years such as incoming air filter, activated carbon used as adsorbent, ionization, or ozone generation[6]. Among them, photocatalytic process has been suggested recently as a new remediation technology, for which titanium dioxide (TiO_2) nanoparticles are either deposited at the surface of a support or embedded in paint [7] or concrete. [8] Many studies

have shown the efficiency photocatalysis with TiO_2, as a chemical release free and green energy method, for removing the gas-phase pollutants such as VOCs, [9] nitrogen oxides [7] or H_2S, [10] and also bacteria. [11] Weschler *et al*. [12] demonstrated that the indoor surfaces may be more favorable than outdoor ones to surface photocatalysis, because of a much higher surface to volume ratio in indoor conditions. Photocatalytic coatings could thus be a promising approach for improving the indoor air quality, as it can be easily applied on relatively large indoor surfaces.

In general, a photocatalytic coating consists of a coating formula in which photocatalytic powder (TiO_2 for example) is incorporated as photoactive charge among other classical ingredients such as extenders, binders and stabilizers. Commercial photocatalytic coatings already exist at commercial scale, but its performance was sometimes reported adverse to customer satisfaction because of low efficiency and possible generation of harmful photocatalytic by-products due to photocatalytic degradation of organic coating ingredients. Also, incorporating photocatalysts in surfaces for the elimination of bacteria was less reported than demonstrating the anti-bacterial property of suspended TiO_2, [13] and consequently the mechanism of photocatalytic bactericidal activity occurring on surfaces.

This PhD thesis is part of the CLEANCOAT project funded by the CARNOT MICA (Materials Institute Carnot Alsace), whose aim was to elaborate active photocatalytic coatings. This project headed at ICPEES, was involving as well the Institut de Science des Matériaux de Mulhouse (IS2M, UMR 7361 CNRS/Université de Haute-Alsace, Dr. Lydie PLOUX), the CRITT Matériaux Alsace (Dr. Sara Mercado) and the CRITT Aerial (Dr. Marie-Hélène Desmonts). Four main tasks have to be performed: 1) search and comprehension of a new way to synthesize high performance TiO_2 photocatalysts; 2) photocatalytic evaluation of those new synthesized photocatalysts in the degradation of a model VOC as well as the elimination of bacteria; 3) study of correlation between the properties of TiO_2 materials and their photocatalytic activities; 4) elaboration of a functional photocatalytic coating formulation. This PhD thesis focused on the three first tasks. As a result, the present manuscript includes four main chapters:

The first chapter is the literature review, in which we will talk about the background context of the PhD topics, current challenges concerning air pollution and surface

contamination issues followed by an introduction of photocatalysis. At the end, depollution and anti-bacterial ability of TiO_2 materials will be reviewed.

The second chapter concerns the experimental methods and preparation of TiO_2 samples. Firstly, we will show the experimental protocol developed to synthesize new TiO_2 nanomaterials by a modified sol-gel route using an ionic liquid or combinations of the individual components of the ionic liquid as morphology properties modifier. Then, we will describe the characterization methods used in this work before presenting the characterizations results, and discussing the roles of diverse additives on changing the synthesis and final morphology properties of TiO_2 crystals.

The third chapter is the evaluation of photocatalytic performance of the TiO_2 samples. Firstly, the gas-phase photocatalytic activity of materials for degrading a common VOC, the Methyl Ethyl Ketone (MEK), under UVA irradiation was evluated and compared to commercial TiO_2 Degussa P25. The liquid-phase photocatalytic anti-bacterial activity tests (carried out at IS2M) against several bacterial strains including *E. coli, S. epidermidis*, and *P. fluoresences* under UVA irradiation was also performed and compared to that of P25. Finally from those tests results and the characterization of materials, a correlation between the high performance in the photocatalytic degradation of MEK and the photocatalytic bactericidal properties with the ionic liquid-modified TiO_2 properties were proposed. Results concerning the mechanism of photocatalytic attack on different biological targets in bacteria cells as well as the influence of environmental conditions on the bactericidal efficiency are also reported.

The last chapter displays the general conclusion and perspectives. We will review the important results of this PhD work, and propose possible further experiments or studies allowing enhanced photocatalytic activity for TiO_2 materials and better understanding of the photocatalytic reactions in depollution and decontamination.

I. Bibliography

I.1. Indoor air pollution issues

During the last two decades there has been increasing concern within the scientific community over the effects of indoor air quality on health. Changes in design and usages of new synthetic building materials have led to more comfortable buildings with improved energy efficiency. Meanwhile these improvements have also provided indoor environments in which contaminants are readily produced and may build up to much higher concentrations than those recorded outside. [14, 15] Indoor pollutants can emanate from a range of sources, including conventional combustion products from heating, cooking or smoke. Also from those new building materials, particular important substance known as volatile organic compounds (VOCs) are emitted from sources like paints, varnishes, solvents and cleaning products.

While attentions of indoor air pollution frequently concentrate on chemical pollutants, the health effects of inhaled biological agents can also be significant, as a large variety of biological materials are present in indoor environment. Their role in inducing illness through immune mechanisms, infectious processes, and a direct toxicity is considered. House dust in carpets, on sofas, and in air is a major source of biological allergens. The growth of molds is not only esthetically unpleasant, but can pose serious health problems, and some indoor environments provide ideal conditions for the maintenance of populations of harmful bacteria. A large number of bacterial species are found indoors, where they are associated with the presence of organic matter, such like wood, foodstuffs or wall coatings.

Investigations of time budgets amongst individuals found that they spent 70%-88% of their day inside buildings. [1] Increasing urbanization, technological development and specialized occupational activities are responsible for that people spend long time indoor. It is still relatively recent that indoor air quality has become an issue of great concern. More frequently appeared a phenomenon that has become known as sick building syndrome (SBS), attributed to poor indoor air quality. [16] In addition, the World Health Organization (WHO) recently reported that air pollution caused around seven million premature deaths in 2012, of which 4.3 million were related to indoor air pollution. [17] WHO has singled out indoor air quality as one of its concerns in public health in 1979, and in 2010 specific indoor air quality guidelines were published. [18] Other organizations in several countries have also adopted

guidelines for targeting in priority certain indoor air pollutants that represent a risk for human health. French Decree No. 2011-1727 establishes concentration values for formaldehyde and benzene. Despite many regulations of indoor air quality made in recent years, we know much less about the health risks from polluted indoor air than we do about those associated with outdoor contaminations. Thus it is clear that resolving the issues related to indoor air quality will be a considerable challenge in the future.

I.1.1. Common indoor VOCs

Organic compounds are divided into various categories which include volatile organic compounds (VOCs), semi-volatile organic compounds (SVOCs) and non-volatile organic compounds (NVOCs). VOCs are defined as having a boiling point that ranges between 50℃ and 260℃. They include a variety of chemicals emitted as gases from certain liquids or solids, whose composition makes it possible for them to evaporate under normal indoor atmospheric conditions of temperature and pressure. The fact that materials containing them exhibit the desirable characteristics of good insulation properties, fire resistance, low price, and ease of installation, means that their use in construction projects is widespread. Other VOC sources are often associated with domestic human activity like cooking [19], cleaning, painting and renovation. [20] Exposure to VOCs can result in both acute and chronic health effects. It is possible that asthmatics and other individuals with prior respiratory complaints may be particularly susceptible to low-dose VOC exposures. At high concentrations, many VOCs are potent narcotics, and can depress the central nervous system. [21] Exposures can also lead to irritation of the eyes and respiratory tract, and cause sensitization reactions involving the eyes, skin, and lungs. [22] Because of the similarity of these symptoms to Sick Building Syndrome (SBS), VOCs exposure has been frequently attributed as a cause.

Sources of common volatile organic compounds in indoor air

Sources	Examples of typical contaminants
Consumer and commercial products	Aliphatic hydrocarbons (*n*-decane, branched alkanes), aromatic hydrocarbons (toluene, xylenes), halogenated hydrocarbons (methylene chloride), alcohols, ketones (acetone, methyl ethyl ketone), aldehydes (formaldehyde), esters (alkyl ethoxylate), ethers (glycol ethers), terpenes (limonene, alpha-pinene).
Paints and associated supplies	Aliphatic hydrocarbons (*n*-hexane, *n*-heptane), aromatic hydrocarbons (toluene), halogenated hydrocarbons (methylene chloride, propylene dichloride), alcohols, ketones (methyl ethyl ketone), esters (ethyl acetate), ethers (methyl ether, ethyle ether, butyl ether).
Adhesives	Aliphatic hydrocarbons (hexane, heptane), aromatic hydrocarbons, halogenated hydrocarbons, alcohols, amines, ketones (acetone, methyl ethyl ketone), esters (vinyl acetate), ethers.
Furnishings and clothing	Aromatic hydrocarbons (styrene, brominated aromatics), halogenated hydrocarbons (vinyl chloride), aldehydes (formaldehyde), ethers, esters.
Building materials	Aliphatic hydrocarbons (*n*-decane, *n*-dodecane), aromatic hydrocarbons (toluene, styrene, ethylbenzene), halogenated hydrocarbons (vinyl-chloride), aldehydes (formaldehyde), ketones (acetone, butanone), ethers, esters (urethane, ethylacetate).
Combustion appliances	Aliphatic hydrocarbons (propane, butane, isobutane), aldehydes (acetaldehyde, acrolein).
Potable water	Halogenated hydrocarbons (1,1,1-trichloroethane, chloroform, trichloroethane).

Source: Maroni et al., 1995.

Table 1: Sources of common VOCs in indoor air [2]

More than 350 VOCs have been recorded at concentrations exceeding 1 ppb in indoor air. [23] The most common among them and their respective sources are listed in Table 1.

Formaldehyde is the most widespread aldehyde found in environment. Although it is a volatile compound, it's not detected by the gas chromatographic methods commonly applied to VOC analysis, and hence is often considered separately [21]. Other common VOCs include a large range of aliphatic hydrocarbons, aromatic hydrocarbons, alcohols, ketones or aldehydes, emitted from a large variety of building materials. Indoor environments in hospitals have their own specific contaminants, such as ethylene oxide, which is used for sterilization. [24] Offices where photocopiers, computers and other devices are used also have specific pollutants, such as ozone, PM10 (particulate matter with a mean aerodynamic diameter lower than 10 μm), acetone, ethylbenzene, xylene, and styrene. [25]

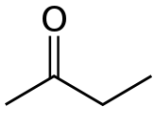

Fig 1: 2-Butanone, also known as methyl ethyl ketone (MEK)

The VOC we have chosen in this thesis as model is 2-Butanone, also known as methyl ethyl ketone (MEK). It is a typical VOC of indoor air pollutants [26, 27] with the formula

$CH_3C(O)CH_2CH_3$ (Fig 1). This colorless liquid ketone has a sharp, sweet odor reminiscent of butterscotch and acetone. It is also produced industrially on a large scale and used as a solvent or raw material for organic syntheses.

Butanone or MEK is an irritant, causing irritation to the eyes and nose of humans. Serious health effects in animals have been seen only at very high levels with a threshold limit value (TLV) in air of 0.6 mg L^{-1} (200 ppm). [28] There are no long-term studies with animals breathing or drinking MEK and no studies for carcinogenicity in animals breathing or drinking MEK. There is some evidence that methyl ethyl ketone can potentiate the toxicity of other solvents, [29] in contrast to the calculation of mixed solvent exposures by simple addition of exposures. Reviews have advised caution in using methyl ethyl ketone because of reports of neuropsychological effects. [30]

I.1.2. Main indoor air treatment technologies

Common strategies of controlling indoor air pollution include controlling pollution sources, increasing the air exchange rate and using air purifiers. When emission sources cannot be controlled or reduced for technical or financial reasons, air cleaning devices need to be used. [31] The technology behind such devices ranges from simple filters to hybrid treatment systems. Here are brief descriptions of some mainly used indoor air treatment technologies:

I.1.2.a. Mechanical and electronic filtration

Mechanical filtration is a simple and extensively used air purification technique for removing suspended particles from indoor air. Filters are essential components in all air conditioning systems, and can capture particles by interception, impact, or diffusion. This technique does not retain gases, thus mechanical filters are progressively saturated by particles; pressure loss is increased throughout time in service and, consequently, particle removal efficiency progressively decreases. This problem can be resolved by replacing the filter. The spent filters are new sources of contamination due to the accumulation of material that may promote the growth of harmful microorganisms. [32]

There are two types of electronic filters that involve particle removal. Electrostatic precipitators are medium-cost devices in which particles are ionized and then deflected by an electric field to be trapped on opposite polarity plates. Their maintenance includes the regular removal and cleaning of the plates. Conversely, ion generators or ionizers are high-cost devices without the need for replacement in which charged ions are dispersed into the air and attached to particles that become chemically charged and trapped in the filters. Nevertheless, those charged particles may adhere to nearby surfaces, such as walls, furniture and draperies, or become attracted to each other by their opposite charges, thereby forming a heavier particle that is deposited on the floor or on any other surface. [33] Although efficient in removing particles, electronic filters can generate hazardous charged particles. [34] They may also generate new pollutants such as ozone and other compounds derived from the ionization of VOCs.

I.1.2.b. Adsorption

Removal of pollutants by adsorption has been successfully applied for retaining contaminants on the surface of an adsorbent material, such as activated carbon, [35] zeolites, [36, 37] silica, [38] activated alumina, mineral clay, and some polymers. Contaminant treatment or destruction is not achieved with this technology, as the pollutant is simply transferred from one phase to another. Consequently, adsorbents should be regularly replaced in order to avoid the re-emission of the already adsorbed compounds. Another negative feature in the case of carbon-based absorbent is that airborne bacteria can deposit on the adsorbent surface and thrive because of the high biocompatibility of the carbon-based materials.

I.1.2.c. Ozonation

Ozone (O_3) is an oxidizing agent produced in generators using oxygen from the air. Dioxygen molecules (O_2) are exposed to a corona discharge or UV radiation to produce several hundred milligrams of ozone per hour. Contrary to the marketed description of ozone generators for their ability to eliminate odours and microbial agents, several studies have shown that an indoor ozone concentration in the range 50–100 ppbv (typical exposure limits) does not guarantee the efficient removal of many indoor VOC pollutants, and cannot compete with even moderate ventilation rates. [12, 39] Thus, several public agencies, such as the Federal department of Health in Canada, advise against using air cleaners that are designed to

intentionally generate ozone, because of concerns about possible health effects from exposure to higher levels of ozone. [40]

I.1.2.d. Photocatalytic oxidation

Photocatalysis promotes the degradation and mineralization of contaminants in the air by using a semiconductor and an irradiation source in the presence of oxygen. The semiconductor plays the role of heterogeneous catalyst, and is activated in the presence of radiations. Thus, oxidation occurs by positively charged holes as electron acceptors, generated from the excitation of an electron from valence band to conduction band, only when the energy provided is higher than the band-gap energy (usually UV radiation). Photocatalysis is a sustainable alternative to catalytic thermal oxidation, since the latter requires higher temperatures to oxidize VOCs, [41] while photocatalysis can occur at room temperature. [42] Compared to other techniques, it is affordable because it involves little maintenance and low power consumption. Photocatalytic oxidation using a semiconductor has been proven successful in degrading numerous VOCs. In addition to the mineralization of many organic compounds, photocatalysis has also a proven bactericidal effect. [13] Despite rapid spread of the use of photocatalysis in recent years, there are several challenges associated with the use of photocatalysts for indoor air treatment. Most investigations concentrate on contaminant degradation at ppmv levels, while ppbv concentrations have to be measured in indoor air. Other drawbacks include the deactivation or poisoning of the catalyst and the generation of harmful by-products. [43] Competitive adsorption in such a multi-pollutant application is a crucial challenge as well. The principle of heterogeneous photocatalysis and the most used semiconductors will be discussed later in chapter I.3.

I.1.2.e. Current commercialization of indoor air abatement technologies

As far as the consumer market is concerned, only devices based on adsorption, photocatalysis, ozonation and filtration are more or less widely commercialized today for indoor air abatement use, with filtration being the most popular one. Other technologies like cold plasma, biofiltration, botanical purification suffer from either low efficiency or high cost, which make them far from being commercialized. A qualitative comparison of additional features amongst conventional abatement technologies is listed in Table 2. Also the respective market percentages of those having high market sale values are presented in Fig 2.

Treatment	Waste generation	Energy consumption	Market sales	Pollutant concentration
Mechanical/Electronic-filtration	Spent filters and cleaning plates	Moderate	High	
Adsorption	Spent adsorbent	Moderate	High	Some ppm [44]
Ozonation	None	High	High	Some ppm [40]
Photocatalysis	Catalyst/lamps	Moderate	Moderate	Up to 1000 ppm [27]
Botanical purification	Organic waste	Low	Low	150 ppb [45]
Biofiltration	Biomass and packing material	Low	Nc[a]	300-400 ppm [46]
Cold plasma technology	None	High	Nc[a]	<1 g/m^3 HC [47]
Membrane separation	Clogged membrane/contaminated solution	High	Nc[a]	> 25 g/m^3 [48]

[a] Not widely commercialized

Table 2: Qualitative comparison of main features amongst common abatement technologies[43]

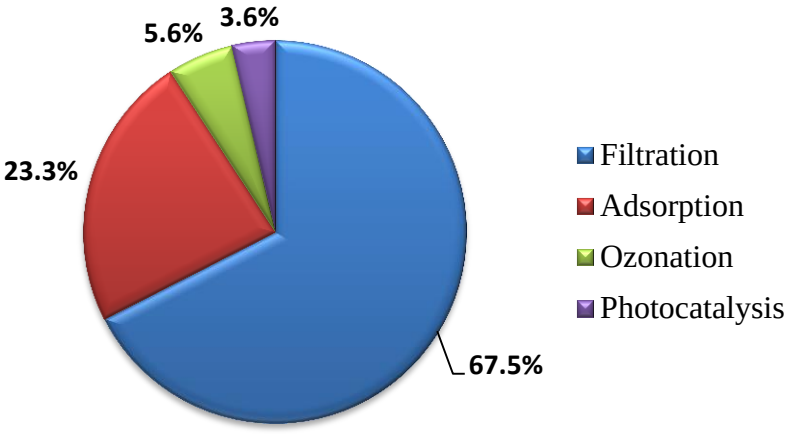

Fig 2: The market for devices based on adsorption, filtration, photocatalysis and ozonation for improving indoor air quality (2006) [43]

I.2. Indoor air and surface contamination by biological contaminants

Whilst the most frequent discussions about pollution focus on chemical sources, biological contaminants can also be responsible for a large variety of health issues and diseases through atopic mechanisms, infectious processes, or direct toxicity. Two major categories of biological contaminants are summarized by Jones *et al*. [2] which are biological allergens and microorganisms.

The main biological allergen found in indoor air is originated from the house dust mites. In temperate climates, ten species of mites can be found from the genera *Dermatophagoides*, *Euroglyphus*, *Malayoglyphus*, *Hirstia*, and *Sturnophagoides*. [4, 49] Most mite populations prefer constant temperatures of about 25 ^{o}C and a relative humidity between 70 and 80%, [50] which is readily provided by the indoor environment. Mites inhabit a range of soft furnishings, including sofas, fabrics, carpets, sheets, duvets, pillows, and mattresses. They can also be found on domestic cats, dogs, and associated with cockroaches. Droppings from mite are a primary source of indoor antigens. [51] Mite faces are encased in a coating of intestinal enzymes including a protein which is a strong allergen. High concentration of mite allergen in dust form appears to represent a significant factor for mite sensitization and to trigger an acute or severe asthma attack or respiratory disease in mite allergic individuals. [51]

Another important form of biological pollution in the indoor environment is constituted by microorganisms. A large number of species of fungi and bacteria are found indoors, and the exposure to them is associated with a number of well-defined disease and symptoms. [52] A list of diseases and disease syndromes associated with exposure to bacteria and fungi in indoor environment is given in Table 3. Exposure to poor indoor air quality could also result in virus-infested respiratory inflammation. [53]

Disease/Syndrome	Examples of causal organisms cited
Rhinitis (and other upper respiratory symptoms)	*Alternaria, Cladosporium, Epicoccum*
Asthma	Various aspergilli and penicillia, *Alternaria, Cladosporium, Mucor, Stachybotrys, Serpula* (dry rot)
Humidifier fever	Gram-negative bacteria and their lipopolysaccharide endotoxins, Actinomycetes and fungi
Extrinsic allergic alveolitis	*Cladosporium, Sporobolomyces, Aureobasidium, Acremonium, Rhodotorula, Trichosporon, Serpula, Penicillium, Bacillus*
Atopic dermatitis	*Alternaria, Aspergillus, Cladosporium*

Table 3: Diseases and disease syndromes associated with exposure to bacteria and fungi in indoor environment [2]

As generally known for bacteria, airborne bacterial microorganisms are preferentially found attached on indoor surfaces, [54] on which their growth is favored by relatively stable temperature and high humidity provided by indoor environment. When a pioneer population of sparse adherent microorganisms has grown by proliferation and has synthesized a matrix of biopolymer, then the so-called biofilm is formed. It can be described as a microbial derived sessile community characterized by cells that developed at an interface, embedded in a matrix of exo-polysaccharide which demonstrates an altered phenotype [55]. Biofilms are a biologically active matrix of cells and extra-cellular substances in association with a solid surface. [56] Depending on the involved bacteria species, the composition of extracellular polymeric substances (EPS) matrix can vary and it can reach up to 75-90 % in a biofilm. [57] The bacteria in biofilm, benefiting from the protection against hostile stress coming from high or low temperature, dehydration, detergents or biocides, can survive much longer and become more difficult to remove. [58] For bacterial cells, biofilm also provides protection against many stresses coming from the surroundings, such as high or low temperatures, dehydration, detergents, or biocides [58]. In addition, biofilm is very difficult to eradicate sub-populations of bacteria being usually surviving after any removal process. As a consequence of this bacteria survival strategy, adhesion of bacteria and formation of biofilm present health threat in many fields such as water distribution or treatment, [59] food production or storage, and most dramatically in biomedical field where bacterial adhesion on implants is often responsible for serious infections. [60] In the last decades, substantial scientific evidence has accumulated that contamination of environmental surfaces in hospital rooms plays an important role in the transmission of several key health care-associated pathogens, including methicillin-resistant *Staphylococcus aureus* (MRSA), vancomycin-resistant *Enterococcus* species (VRE), *Clostridium difficile, Acinetobacter* species. [61, 62] For these reasons and the emergence of restrictive legislation regarding the effects of cleaning agents on the environment and to the user health and safety, [63] there is a lot of interest in developing materials and methods which

can remove or actively prevent the formation of biofilms without release of potentially harmful chemical compounds..

I.2.1. Bacteria and biofilms

I.2.1.1. Bacteria

Bacteria are prokaryotic organisms i.e., simple unicellular organisms with no nuclear membrane, mitochondria, Golgi bodies, or endoplasmic reticulum, that reproduce by asexual division. [64] The cytoplasmic membrane has a lipid bilayer structure similar to the structure of eukaryotic membranes, but without steroids. It is responsible for many of the functions assigned to organelles in eukaryotes. These tasks include electron transport and energy production, which are achieved in eukaryotes' mitochondria. The cell wall encircling bacteria is itself complex and can take two basic forms: a Gram positive cell wall with a thick peptidoglycan layer and a Gram negative cell wall with a thin peptidoglycan layer and an overlying outer membrane. These two major classes of bacteria can be distinguished by the Gram stain method. [65] A general comparison between Gram negative and Gram positive bacteria is listed in Fig 3 and a detailed cell wall comparison is shown in Fig 4.

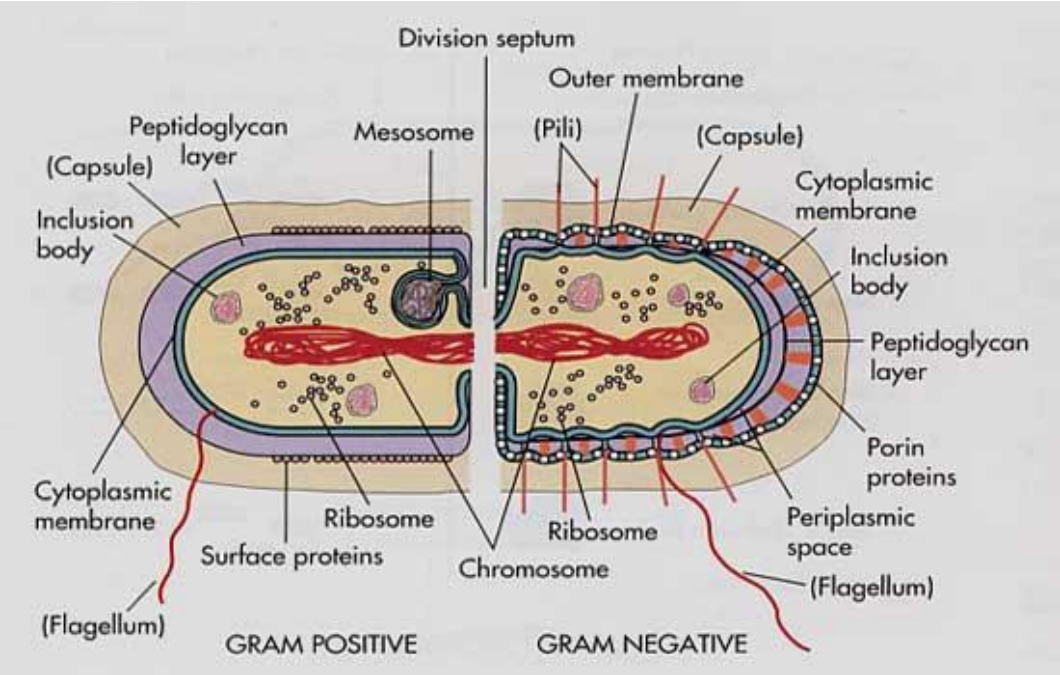

Fig 3: Gram positive and Gram negative bacteria. A Gram positive bacterium has a thick layer of peptidoglycan (left). A Gram negative bacterium has a thin peptidoglycan layer and an outer membrane (right) (digitalproteus.com).

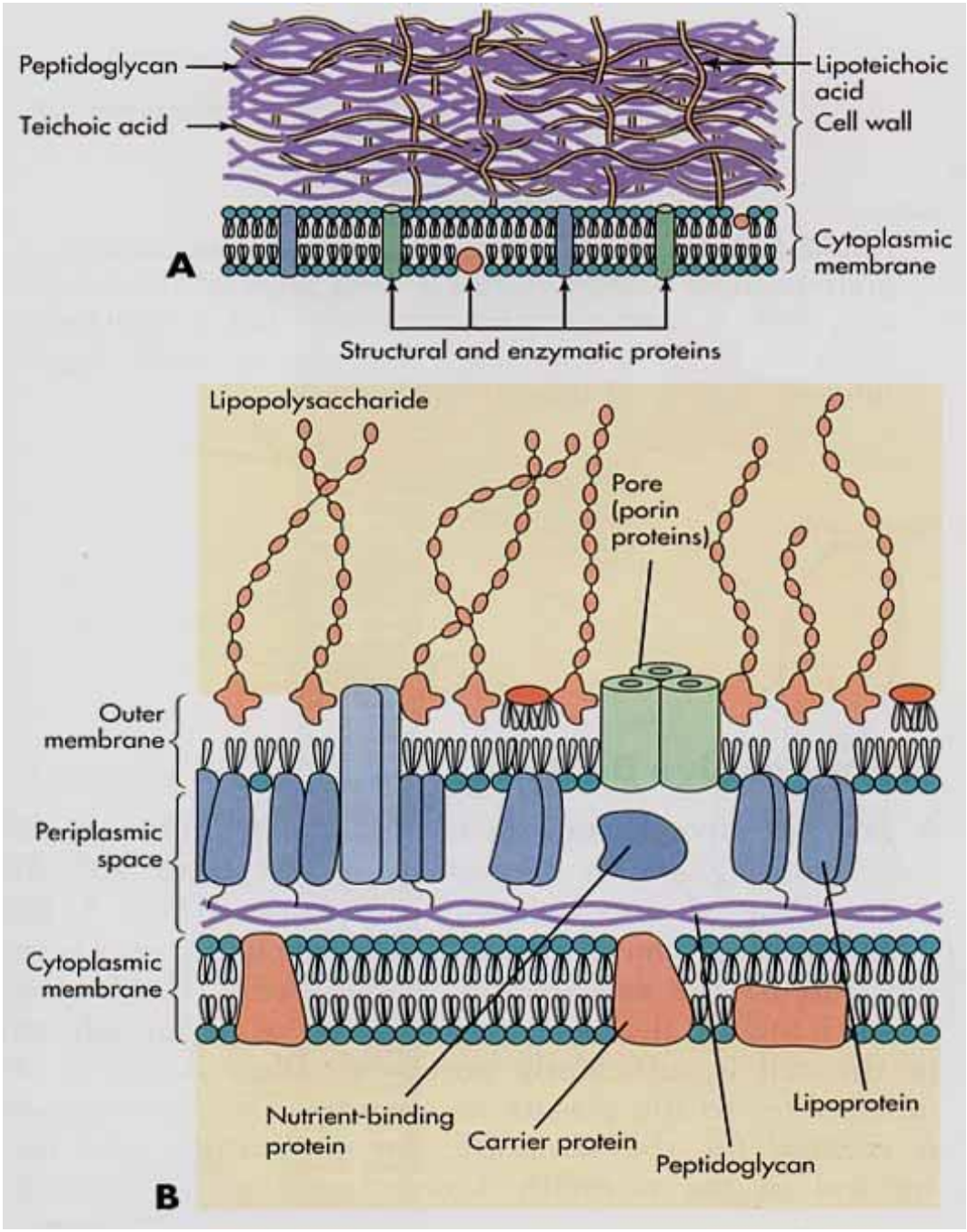

Fig 4: Comparison of the Gram positive and Gram negative bacterial cell walls. A, a Gram positive bacterium has a thick peptidoglycan layer that contains teichoic and lipoteichoic acids. B, a Gram negative bacterium has a thin peptidoglycan layer and an outer membrane that contains lipopolysaccharide, phospholipids, and proteins. The periplasmic space between the cytoplasmic and outer membranes contains transport, degradative, and cell wasll synthetic proteins. The outer membrane is joined to the cytoplasmic membrane at adhesion points and is attached to the peptidoglycan by lipoprotein links. (digitalproteus.com).

A Gram positive bacterium has a thick, multilayered cell wall mainly consisting of peptidoglycan surrounding the cytoplasmic membrane. The peptidoglycan layer is sufficiently porous to allow diffusion of metabolites to the cytoplasmic membrane. [66] Peptidoglycan is essential for the structure, for replication, and for survival of bacteria in the normally hostile conditions in which bacteria normally grow. Gram positive cell wall may also include other

components such as teichoic and lipoteichoic acids and complex polysaccharides. [67] These molecules are common surface antigens that distinguish bacterial serotypes and promote attachment to other bacteria as well as to specific receptors on mammalian cell surfaces. [68]

Bacterial genus (specific species used in the present work)	**Gram stain**	**Oxygen relationship**	**Catalase test**	**Oxidase test**	**Morphology (width/length)**
Enterobacteriaceae (*Escherichia coli*)	Negative	Facultatively anaerobic	Positive	Negative	 0.5/2.0 µm
Staphylococcus (*Staphylococcus epidermidis*)	Positive	Facultatively anaerobic	Positive	Negative	 0.8-1.0/0.8-1.0 µm
Pseudomonas (*Pseudomonas fluorescens*)	Negative	Aerobic	Positive	Positive	 0.5-0.6/1.5-2.0 µm
Listeria (*Listeria monocytogenes*)	Positive	Facultatively anaerobic	Positive	Negative	 0.4-0.5/0.5-2.0 µm

Table 4: Information about bacterial species frequently involved in surface contamination [69] and used in the present work.

Gram negative cell walls are more complex than Gram positive cell walls, both structurally and chemically. Structurally, Gram negative cell wall contains two layers external to the cytoplasmic membrane. First, immediately external to the cytoplasmic membrane is a thin peptidoglycan layer, which accounts for only 5% to 10% of the Gram negative cell wall by weight. There are no teichoic or lipoteichoic acids in Gram negative cell wall. External to the peptidoglycan layer is the outer membrane, which is composed of lipopolysaccharide, phospholipids, and proteins. The outer membrane maintains the bacterial structure and is a

permeability barrier to large harmful molecules and hydrophobic molecules. It also provides protection from adverse environmental conditions such as the digestive system of host.

Bacteria have numerous ways to ensure their survival in hostile environment, where respiration of oxygen can produce toxic hydrogen peroxide. Catalase is one type of enzyme that bacteria use to split peroxide into a water molecule and an oxygen atom; while the production of oxidase enzyme can generate reactive oxygen species that the bacteria use to defend and kill other microorganisms. Those defense mechanisms functionalize differently depending on the different bacteria strains, and should be discussed when studying bactericidal effect.

I.2.1.2. Bacterial adhesion and development of biofilms

Bacteria are known to exist in both planktonic and sessile forms of population. The former consists of free-living bacteria in bulk solution, and the later refers to bacteria attached on a surface or within the confines of a biofilm. [55] Biofilm results from the development of pioneer bacteria attached on the surface. Its growth is usually described as a 4-step process (Fig 5), [58] which includes:

1): Transport of the pioneer bacteria onto the surface

2): Adhesion of the pioneer bacteria to the surface

3): Proliferation of the pioneer bacteria and synthesis of the biofilm matrix by bacteria

4): Maturation of the biofilm and detachment events of parts of it

It is worthy knowing that the key step of the formation of a biofilm i.e., the initial adhesion of bacteria to the surface, is influenced by the surface physico-chemical properties of the bacterial cell and the substratum surface, such as surface roughness, surface charge, hydrophobicity and elemental surface composition. [70] Study performed by Mitik-Dineva *et al.* has shown that bacteria may be far more susceptible to nanoscale surface roughness than it was previously thought. [71] Also Gaboriaud *et al.* [72] has reported significant changes in bacterial adhesion according to pH and ionic strength of the medium. This behavior was attributed to modifications of mechanical and structural characteristics of the bacterial

envelope, rather than to sole contribution of electrostatic forces. Thus, surface parameters are heavily studied in biomedical or biomaterial field in the hope to modify bacterial adhesion or to affect early the biofilm formation.

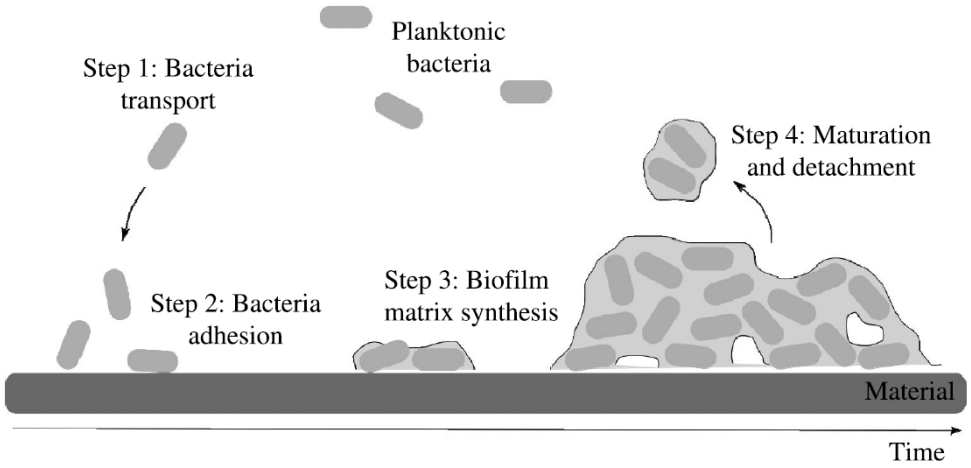

Fig 5 : Scheme of the biofilm development. The description is based on a common 4-step representation including bacteria transport onto the surface, bacteria adhesion, synthesis of the biofilm matrix, and maturation of the biofilm with related detachment of biofilm parts. [58]

I.2.2. Main disinfection methods on surfaces

To reduce the risk of bacterial contamination of materials and their environment, both environmental media (water or air) and surfaces need to be treated. Numerous technologies, both chemical (chlorination) and physical (UVC irradiation) have been applied for achieving this goal. Significant interest of the applications of nanomaterials in the environment field has also been raised. Generally, they are effective against certain range of bacteria for their ability to penetrate membrane and cause lysis of the cells. No disinfection by-products (DBPs) are expected to form during the disinfection process. However, this is not clear so far. The release of nanoparticles in the environment is a major drawback of those nanotechnologies. Due to the related environmental and health risks, these technologies are therefore mainly limited to experimental applications. A brief summary of available physico-chemical water phase disinfection technologies is shown in Table 5 (mechanical filtration is not included in this review).

Treatment	Target bacteria	Action mode	Advantages	Disadvantages
Chlorination [73]	Waterborne pathogens except *C.parvum* and *M.avium*	Free chlorine toxicity	Good potency and low coat	Disinfection by-product (DBP) Ineffective for certain species
UV irradiation [74]	Waterborne pathogens especially *Staphylococcus, E.coli*	UV-induced cell component decomposition	Simplicity Low cost No DBPs	Lack of global standard
Ozonation [75]	Wild range of bacteria in water especially *E.coli*	Strong oxidation	High efficiency	Formation of DBP carcinogen bromate ions in Br^- contained water
Ag nanoparticles [76]	Gram-negative bacteria	Release of toxic Ag^+ ions Penetration cause membrane or DNA damage	No DBPs	Release of Ag nanoparticles
Carbon nanotubes [77]	*E.coli*	Membrane damage by direct contact Possible oxidative stress	No DBPs	Complicate synthesis Release of carbon nanotubes which are also toxic to animal cells
TiO_2 nanoparticles [13, 78]	*E.coli*	Membrane damage, lipidic peroxidation by photocatalytic oxidation under UV irradiation	High efficiency No DBPs	Release of nanoparticles Difficult to recover

Table 5: Brief summary of available physico-chemical water phase disinfection technologies (mechanical filtration is excluded in this review).

Beside the treatment of media, anti-contamination treatments can be performed on surfaces as well, thanks to the rapid development of the interface science. Here we focus on introducing some surface decontamination technologies.

Methods for decreasing frequency and level of contamination of environmental surfaces in hospital rooms include routine and terminal disinfection with chemical germicides wiping (alcohols, aldehydes, anilides, bisphenols, halogen-releasing agents, quaternary ammonium compounds). [79] However, conventional methods of manual disinfection with wiping are not

effective enough in the long term, are difficult to be standardized, and are time-intensive and staff-intensive. In addition, health and safety problems are associated with the use of some aggressive chemicals. [80]

Therefore, "no-contact" methods of terminal room disinfection with ultraviolet (UV) light or aerosolized and/or vaporized hydrogen peroxide have been used. [81, 82] However, in addition to the very disputable efficiency of UV irradiation for surfaces located more than some centimeters from the lamp, major limitations are the requirement of removing any occupying person from the room, and the high costs associated to increased time of room turnover and to the acquisition of room decontamination units.

An alternative method for reducing frequency and level of surface contamination in hospital has been proposed in the last two decades: the self-preventing and the self-disinfecting surfaces. [83, 84] The general modes of action are microbial repelling or microbial killing, which should occur when bacteria are close to or in direct contact with the surface. In the following sections, we will present the main types of such surfaces.

I.2.2.1. Self-preventing surfaces

As already mentioned before, the adhesion of bacteria depends on a lot of physico-chemical properties of the material surfaces. Therefore, many works have been carried out in an effort to make bacterial repelling self-preventing surfaces by playing with the material interface properties.

Chemical functionalities can lead to a specific binding between a bacterium and a material surface through receptor/ligand-like interactions. [58] Some authors have altered the surface chemical functionalities for affecting bacterial adhesion in particular ways. As an example, Krsko *et al*. have used PEG hydrogel patterned surfaces to illustrate the cell-repulsive properties of PEG. [85] The well-known anti-adhesive properties of PEG are thought to be attributed to a stable interfacial water layer preventing direct contact between bacteria and surface. [86] Other anti-adhesive polymers have been used as well, such as poly(sulfobetaine methacrylate) (pSBMA), [87] poly(methylpropenoxyfluoroalkylsiloxane)s or poly(perfluoroacrylate)s. [83] Also, Veuillet *et al.* [88] have investigated plasma polymerization of dimethylaminoethyl methacrylate (DMAEMA) to obtain thin hydrogel films with a wide range of mechanical properties for reducing bacteria adhesion.

Surface topographic properties are other kinds of parameter, which can affect bacterial adhesion. A patent owned by Snyder *et al*. consists of a surface providing a plurality of

topographic features to reduce the available accessible area of the surface for adhesion by bacteria. [89] Washburn *et al.* have shown that the effect of nanotopography on cells is predominant for the smallest structures, suggesting that the size threshold for cell detection could be <10 nm. They have concluded that the effect of the surface topography is sensed by the cell as a disruption in the formation of focal adhesions at these size scales because of a reduced ability of integrin to cluster on the nanostructures. [90]

Certainly, more surface physico-chemical properties may be more efficiently exploited to prevent bacterial adhesion. Many works are therefore still needed to be done in this field.

I.2.2.2. Self-disinfecting surfaces impregnated with a heavy metal

It has been known since the antiquity that some heavy metals possess anti-infective activity. Among them are silver (Ag), cobalt (Co), copper (Cu), mercury (Hg), manganese (Mn) and lead (Pb). However, their efficiencies are very variable. Nowadays, the development of self-disinfecting surfaces impregnated, functionalized or coated with silver or copper is the most advanced. Silver ions have the highest level of antimicrobial activity of all the heavy metals. They are active through three main mechanisms: [76, 84]

1. Electrostatic interactions between positive Ag^+ ions and the cell membrane, resulting in its disruption,
2. The strong binding of Ag^+ ions with disulfide (S-S) and sulfhydral (-SH) groups that are present in proteins such as enzymes and proteins of the microbial cell wall, thus affecting many bacterial metabolic processes,
3. Interactions of Ag^+ ions with the DNA molecule, resulting in the disturbance of gene expression.

These different events finally lead to the cell death.

Silver can be incorporated in materials as nanoparticles for a role of Ag^+ reservoir, conferring antimicrobial activity to many consumer products *e.g.* toys, telephones, and infant pacifiers. Microorganisms contacting the coating or present in its surroundings accumulate silver until the toxicity threshold is exceeded. However, the development of surfaces with adequately active but harmless doses for human health is delicate. [91]

A number of commercial antimicrobial surface treatments also exist which rely on the microbicidal activity of the Ag^+ ion, these include AgION2 (AgION Technologies Inc.) [92] and

SilvaGard (AcryMed Inc.). [93] In all of these instances, the silver is impregnated on the products as nanoparticle or as a silver salt such as silver nitrate. The mode of action has been shown to correlate directly with the diffusion of Ag^+. In this last case, both safety and effectiveness of silver nanoparticles are controverted and have not been assessed for applications in the hospital environment yet.

I.2.2.3. Self-disinfecting surface impregnated with chemical germicide

Diverse surfaces and devices impregnated, functionalized or coated with a germicide such as antibiotics, triclosan and quaternary ammonium compounds are available. For example, triclosan impregnated cutting boards have been shown to lead to a decrease in the bacteria population of 0.5 to 1.0 $\log_{10}$ for *S.aureus* and *Serratia* species, and 1.5 to 1.7 $\log_{10}$ for *E.coli* and *Salmonella* species. [94] Another example is the application of a quaternary ammonium salt containing antimicrobial surfactant (Goldshild) on formica and stainless steel. It was demonstrated to kill 0.5 to 2.4 $\log_{10}$ MRSA and 0.6 to 0.9 $\log_{10}$ *P.aeruginosa* and *E.coli* within 30 minutes. [95] However, concern has been raised about the released chemical compound which is harmful for human health. [96] Moreover, the common use of such a bactericide might lead bacteria to develop resistance to the germicide, even with possible cross-resistance to clinically useful antibiotics. [84] Moreover, the difficulty to achieve the adequate revealing or releasing doses of germicide is emphasized by the risk to enhance the biofilm formation on the surface by the use of a sub-inhibitory concentration of the active compound. For example, sub-inhibitory concentrations of triclosan were demonstrated to promote the *Streptococcus mutans* biofilm formation and the adherence to oral epithelial cells, [97] and sub-inhibitory concentrations of aminoglycoside antibiotics have been shown by Hoffman *et al*. to induce biofilm formation for *P. aeruginosa* and *E.coli*. [98]

To counteract the drawbacks from synthetic chemical germicides, bio-inspired natural bactericidal substances have been produced and used recently for achieving surface disinfection. [99] Still, many studies have to be done in order to make progress of this new strategy.

I.2.2.4. Self-disinfecting surface by photocatalytic oxidation

Surface coated with specific semiconductors and stimulated by ultraviolet A (UVA) light (320–400 nm) can generate various reactive oxygen species (ROSs). Then, ROSs can oxidize organic material, even bacteria, up to complete mineralization, depending on the experimental

conditions. [100] During photocatalytic oxidation of *E. coli*, Jacoby *et al.* [101] measured released CO_2 and found 54% mineralization within 75 h of UVA illumination. While most research has been performed through bactericidal tests using a suspension of photocatalyst in water, some other approaches attempt to provide a self-disinfecting behavior to surfaces by adding a photocatalyst in tiles and glasses. [100-102] Bacterial inactivation over the entire area was then shown to be possible. The effectiveness of the method was demonstrated using bacteria relevant to the hygiene field such as *E. coli, Pseudomonas aeruginosa* (*P.aeruginosa*), *Staphylococcus aureus* (*S.aureus*) and *Enterococcus faecium* (*E.faecium*). For these bacteria, an efficiency reduction of more than 6 $\log_{10}$ of population in 60 min of UVA illumination was obtained on a glass substrate coated with commercial TiO_2 P25. [11]

In general, the purpose of most of the studies about photocatalytic self-disinfecting surfaces coated with photocatalytic TiO_2, was mainly focused on:

1. The feasibility trail of TiO_2 coated surface for disinfection usage. [11, 84, 103]
2. The study of the degradation mechanisms of adhesive bacteria on surface. [101, 104]

However for these studies, surface characterization is usually incomplete, and the lack of surface characterization information such as coated TiO_2 weight per surface area, coating thickness, size of particles or aggregates of particles and surface topography makes their photocatalytic results less comparable with other types of self-disinfection surfaces. As the above surface parameters are indeed factors potentially influencing the photocatalytic anti-bacteria efficiency due to their known effects in affecting the bacteria adhesion or the biofilm development, combined studies which include both aspects coming from the bacteria-surface adhesion and bacteria-photocatalyst interaction would be appreciated.

Although the use of TiO_2 photocatalyst as an antimicrobial component of construction material was proposed by Kuhn *et al.*, [11] yet to our knowledge, there has been no true TiO_2-incorporated self-disinfection construction materials or coating ever widely and commercially used in public locations due to numerous technical factors. In a study among very few in which Verdier *et al.* [105] have incorporated TiO_2 nanoparticles inside a polymer-based transparent varnish coat, the author have observed a reduced anti-bacterial effect of such a coating, and they have attributed this effect to a reduction of the contact between photogenerated ROSs and bacteria due to a blockage of the coating by the polymer. More issues for the incorporation of TiO_2 inside a coating will be later mentioned in section I.5.

Aside from surface characterizations, the intrinsic photocatalytic activity of TiO_2 incorporated in the coating is another important parameter capable of changing the anti-bacterial properties of the self-disinfection surface. Although the majority of studies about surface-immobilized TiO_2 were performed using commercial TiO_2 P25 as photocatalyst, some researches have used Cu/P25 or Cu/modified TiO_2 to enhance the overall bactericidal efficiency. [106, 107] Yet, the enhanced performance was simply speculated due to the difficulty to discriminate single bactericidal effect issued from TiO_2 and heavy metals. To our knowledge, very few works have been done to investigate the effect of (modified) TiO_2 physico-chemical properties such as particle size or shape on bactericidal efficiency in case of surface-immobilized TiO_2, and it will be a major task in this PhD work.

I.3. Heterogeneous photocatalysis

Catalytic processes may be considered in separate categories, depending on whether the catalyst is part of the same phase as the reactants and the products (homogeneous catalysis), or whether it forms a separate phase (heterogeneous catalysis). The basis of classic (thermal) heterogeneous catalysis implies different steps:

1. Transfer of the reactants to the surface
2. Adsorption at adjacent position on the surface
3. Reaction between adsorbed reactants requiring thermal activation. The reactions in adsorbed phase require less energy than those in non-adsorbed phase.
4. Desorption of products
5. Evacuation of the products to the medium.

Photocatalysis is also a heterogeneous catalysis process. However, it differs in step 3, where the activation step occurs *via* light activation instead of thermal activation, thus implying the use of a semiconductor material as photocatalyst. The activation step can then be detailed as: [108]

3.a. Absorption of photons

3.b. Creation of electron-hole pairs

3.c. Transfer of the photogenerated charges to the catalyst surface

3.d. Reaction of electrons or holes with the adsorbed species.

An important step of the photocatalytic reaction is the formation of electron-hole pairs, requiring energy to overcome the band gap between the valence band and the conduction band. Common energy sources are ultra-violet (UV) and in a lower extended visible lights, natural (sun) or artificial ones.

Main limitations are related to charge carrier life-time concerns and transfer of the charge carriers to the semi-conductor surface.

I.3.1. Principle of photo-oxidation

Photocatalysis oxidation promotes the degradation and mineralization of contaminants in the air, in water or on surface by using a semiconductor and an irradiation source in the presence of oxygen. The semiconductor plays the role of heterogeneous catalyst. When the light source energy provided is equal or larger than the band gap (E_g), an electron is promoted from the valence band (VB), into the conduction band (CB), creating a hole. Thus pairs of electron-hole are created in the photocatalyst particle. In the absence of suitable electron and hole scavengers, the stored energy is dissipated within a few nanoseconds by recombination in form of heat. If a suitable scavenger or surface defect state is available to trap the electron or hole, recombination is prevented and if those charges can migrate to the pollutant-catalyst interface and participate in the charge transfer with adsorbed species, then reaction happens. The holes issued from the VB are powerful oxidants (+1.0 to +3.5 V vs NHE depending on the semiconductor and pH), they can oxidize adsorbed water molecules into hydroxyl radicals (OH•) if the VB energy position is more positive than the redox potential of $•OH/H_2O$, while the CB electrons are good reductants (+0.5 to -1.5 V vs NHE), and if the CB band energy position is more negative than that of $O_2/O_2^-•$ redox potential, reduction of O_2 into superoxide radical anion ($O_2^-•$) can happen. Both OH• and $O_2^-•$ radical species are strong oxidizers and responsible for the degradation of various organic compounds. [109, 110] A schematic view of the photocatalytic reaction mechanism taking place with TiO_2 is presented in Fig 6. The kinetic and characteristic times for the various steps in the mechanism of photocatalysis are shown in Fig 7.

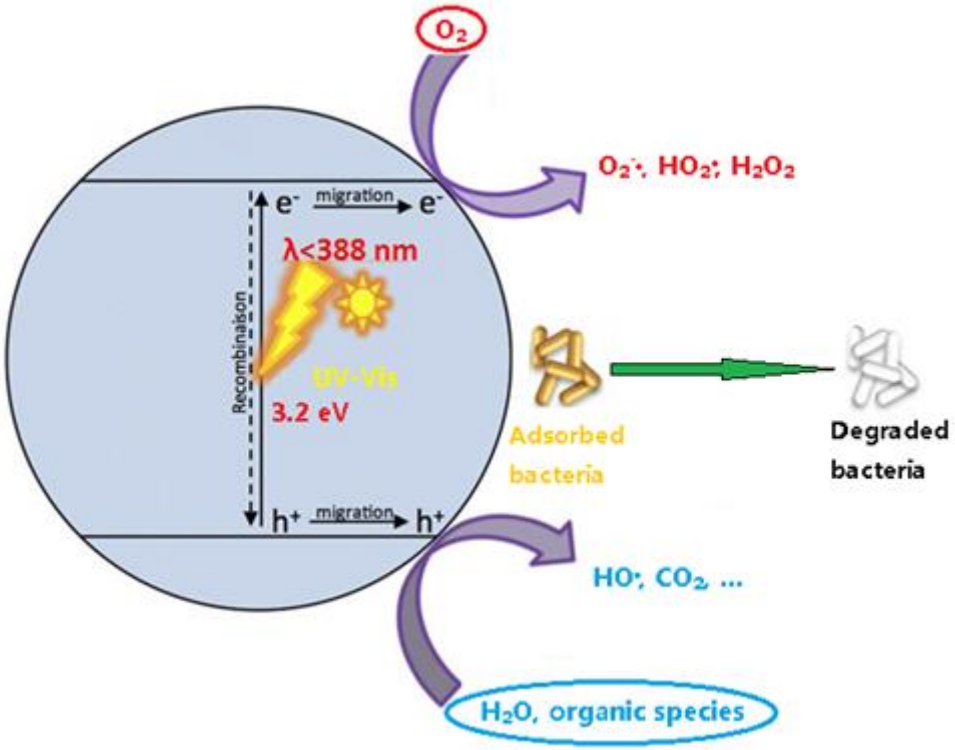

Fig 6: Schematic view of photocatalytic reactions occurring with activated TiO_2. [111]

Charge carrier generation

$$TiO_2 + h\nu \xrightarrow{(fs)} h_{vb}^{+} + e_{cb}^{-}$$

Charge carrier trapping

$$h_{vb}^{+} + Ti^{4+}OH \xrightarrow{\text{fast (10 ns)}} (Ti^{4+}OH\cdot)^{+}$$

$$e_{cb}^{-} + Ti^{4+}OH \xleftrightarrow{\text{shallow trap (100 ps)}} Ti^{3+}OH \text{ (Dynamic equilibrium)}$$

$$e_{cb}^{-} + Ti^{4+} \xrightarrow{\text{deep trap (10 ns)}} Ti^{3+} \text{ (Irreversible)}$$

Charge carrier recombination

$$h_{vb}^{+} + Ti^{3+}OH \xrightarrow{\text{fast (10 ns)}} Ti^{4+}OH$$

$$e_{cb}^{-} + (Ti^{4+}OH\cdot)^{+} \xrightarrow{\text{slow (100 ns)}} Ti^{4+}OH$$

Interfacial charge transfer

$$Red + (Ti^{4+}OH\cdot)^{+} \xrightarrow{\text{slow (100 ns)}} (Red\cdot)^{+} + Ti^{4+}OH$$

$$e_{tr}^{-} + Ox \xrightarrow{\text{very slow (ms)}} Ti^{4+}OH + (Ox\cdot)^{-}$$

Fig 7: Characteristic reaction durations for the various steps in the mechanism of photocatalysis for the case of TiO_2. [112]

Recombination is mediated primarily after Ti^{3+} formation in the first 10 ns. Valence-band holes are sequestered as long-lived $Ti^{4+}OH^{\bullet+}$ after 10 ns. And $Ti^{4+}OH$ is reformed by

recombination with conduction-band electrons or oxidation of the substrate on the time scale of 100 ns.

I.3.2. Main examples of semiconductors used in photocatalysis

Several simple oxide and sulfide semiconductors have band-gap energies sufficient for catalyzing a wide range of chemical reactions of environmental interest. They include TiO_2 (Eg = 3.2 eV), WO_3 (Eg = 2.8 eV), $SrTiO_3$ (Eg = 3.2 eV), Fe_2O_3 (Eg = 3.1 eV), ZnO (Eg = 3.2 eV), ZnS (Eg = 3.6 eV), among others. A simple overlook of the common used oxide and sulfide semiconductor photocatalysts and their band gap positions are shown in Fig 8.

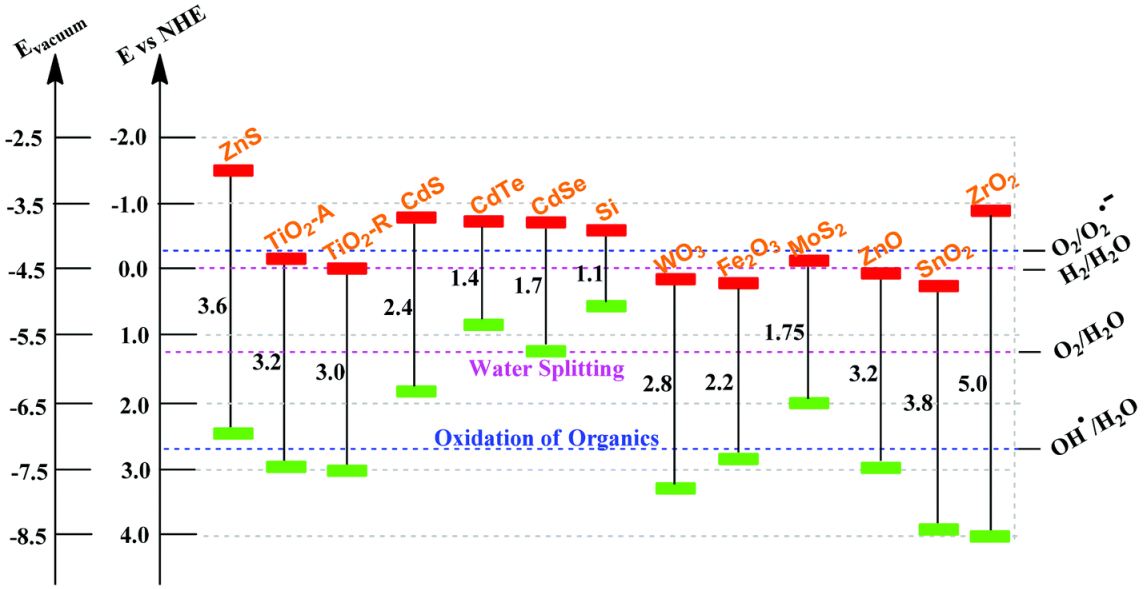

Fig 8: Common semiconductors and their band gap positions. [113] (At pH = 1-2)

However, among these semiconductors TiO_2 has proven to be one of the most photoactive [114] and the most suitable for widespread environmental applications. TiO_2 is biologically and chemically inert; it is stable with respect to photocorrosion and chemical corrosion, and is inexpensive for commercially available powders. The most remarkable advantage for TiO_2 to be a good semiconductor photocatalysts in terms of organic compound degradation is that the redox potential of the $\bullet OH/H_2O$ ($E° = +2.6$ eV) [110] couple lies within the bandgap domain of TiO_2, so that the main photogenerated oxidizing agent •OH can be able to oxidize the targeted organic species (MEK in our case), [115] and that the redox potential of the $O_2/O_2^{-}\bullet$ ($E° = - 0.3$ eV) couple lies within the TiO_2 bandgap as well. The metal sulfide semiconductors are unsuitable based on the stability requirements in that they readily undergo

photoanodic corrosion; [115] the iron oxide polymorphs (Fe_2O_3 and FeOOH) are not suitable semiconductors neither because of photocathodic corrosion, [116] even though they are inexpensive and have nominally high bandgap energies; ZnO appears to be a suitable alternative to TiO_2, however, ZnO in unstable as incongruous dissolution in water (pH<10) occurs to yield $Zn(OH)_2$ on particle surface leading to catalyst deactivation over illumination time. [117]

Except the application of illuminated semiconductors for the remediation of VOCs, other uses have been carried out for decontamination of halogenated alkanes [118] and alkenes [119], organic dyes, [120] and pesticides [121] as well as for photo-deposition of metals on semiconductor materials from solutions containing metal cations *via* photo-reduction [122, 123] (e.g., Pt^{4+}, Au^{3+}, Rh^{3+}, Cr^{5+}). In many cases, complete mineralization of organic compounds has been reported.

I.4. Titanium dioxide materials

I.4.1. Main characteristics and types of TiO_2 materials

Titanium dioxide, also known as titanium (IV) oxide or titania, is the naturally occurring oxide of titanium, chemical formula TiO_2. TiO_2 exists in many crystalline phases, including anatase, rutile, brookite, TiO_2-(B) and seven high-pressure phases. [124] These later phases do not occur in nature and they can only be synthesized by high pressure treatment methods. Anatase and rutile are the most studied and used phases in photocatalysis. In both structures, titanium atoms are at the center of an octahedron of O atoms. In rutile (tetragonal, space group $P4_2/mnm$), oxygen atoms build an hexagonal compact stacking, the TiO_6 octahedrals are linked sharing preferentially corners; while in anatase (tetragonal, space groupe $I4_1/amd$), the oxygen atoms form a cubic compact stacking and the TiO_6 octahedrals are linked sharing preferentially edges (Fig 9). The differences in crystalline structure are translated into differences in electronic structure between the two allotropic forms. The band gap of rutile is 2.8-3.0 eV, as that of anatase is 3.2 eV. [125] Anatase is a thermodynamically metastable phase; however it is stable for its nanoparticles size below 11nm. After annealing in the range of 630-1050℃ anatase becomes rutile with increased size. Rutile is the most stable phase for nanoparticles above 35nm. [126]

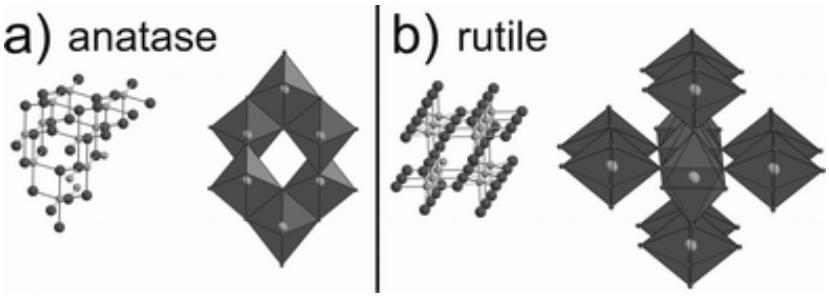

Fig 9: Crystalline structure of TiO_2 and the distorted octahedron (a) edge-sharing for anatase and octahedron (b) corner-sharing for rutile

Titanium dioxide has a wide range of applications already since the early twentieth century. It is used as a pigment in paints, coatings, sunscreens, ointments and toothpaste. The value derived from its whitening properties and opacifying ability (commonly referred to as hiding power), as a result of the high refractive index of TiO_2. Most of the TiO_2 pigments in industry are produced $FeTiO_3$ ilmenite ore by the so-called chloride or sulfate process. [127] The primary particles of the resulting rutile or anatase form TiO_2 pigments are typically between 200-600 nm in diameter. Within this range, the light scattering ability of TiO_2 is most effective, which in turn maximizes the level of gloss finish. TiO_2 has received a greater attention when its photocatalytic activity was mentioned as early as late 1960's [128] and more especially when Fujishima and Honda have studied the photoelectrochemical water-splitting on a TiO_2 photoanode in 1972. [129] This important activity demand optimal conditions and fine controls during the TiO_2 preparation process. The resulting highly photocatalytically active TiO_2 materials, often smaller in particle size and sometimes anisotropic, are called nanostructured TiO_2 or TiO_2 nanomaterials. TiO_2 nanocrystals have several advantages over their bulk counterparts in terms of potential applications because of their high specific surface area, thus high surface/volume ratio, increased chance for photogenerated charges to migrate towards the surface, and the efficient contribution in the separation of photo-generated holes and electrons, improving charge lifetime. [130, 131]

I.4.2. Photocatalytic properties of TiO_2 nanomaterials

As a photocatalytic nanomaterial, anatase TiO_2 is a semiconductor characterized by a band gap ranging from 3 to 3.2eV between the valence band and the conduction band. Basically, when TiO_2 is excited by photons of energy equal or higher than the value of its bandgap (generally by UV where the wavelength is shorter than 390nm), an electron jumps

from the valence band to the conduction band, creating a pair of hole/electron in valence band and conduction band respectively. [112]

As mentioned before, the E ϕ(•OH/H_2O) and E ϕ(O_2/O_2^-•) are situated within of the TiO_2 band gap, so that the photogenerated hydroxyl radical as a powerful oxidizing agent can oxidize many organic matters present at the surface of TiO_2 into harmless species (e.g. CO_2, H_2O, inorganic salts and etc). [132, 133] While the photogenerated superoxide anion radicals serve as electron traps thus increasing the lifetime of photogenerated charges, also they can react with molecular water adsorbed to generate hydroxyl radical. The above-mentioned reactions are described in the following equations:

$$h_{vb}^{+} + H_2O \rightarrow H^{+} + OH\cdot$$

$$h_{vb}^{+} + \text{pollutant} \rightarrow \text{pollutant}^{+}$$

$$OH\cdot + RH \rightarrow R\bullet + H_2O$$

$$e_{cb}^{-} + O_2 \rightarrow O_2^{-}\cdot$$

$$2O_2^{-}\cdot + 2H_2O \rightarrow 2OH^{-} + 2OH\cdot + O_2$$

Not all photogenerated charges can reach the surface of the semiconductor for taking part in the above redox reactions with pollutants and other adsorbed molecules. The photocatalytic performance of semiconductor is thus limited by the lifetime of the photogenerated charges, due to charge recombination phenomena.

$$h^{+} + e^{-} \rightarrow \text{emmited heat or radiation}$$

Spatial separation of photogenerated charges or surface trap can be used to reduce the recombination. The diffusion rate of photogenerated charges towards the surface influences directly the photocatalytic performance for degrading pollutants. The diffusion or the recombination rate of those charges depends on many structural factors of semiconductors such as the allotropic composition, [134] the crystallinity and the presence of defects, [135] the crystallite size, [136] and the morphology. [137]

As a result, the surface area, the surface chemical species, [138] the presence of bulk or surface defects, [139] the type and density of surface states [125] may affect the photocatalytic oxidation performances. Furthermore, the TiO_2 morphology (also in terms of various

surface/volume ratios) may impact the photocatalytic activity. [140] The chemical nature and molecular complexity of the adsorbed pollutant can affect photocatalytic activity as well.

I.4.2.1. Mechanism of photo-oxidation of MEK by TiO_2 in air

Photocatalytic oxidation by TiO_2 has been shown effective in removing many VOCs. [141] [142] Even if methyl ethyl ketone (MEK) is often considered as one of the model VOCs, yet few studies have analyzed the detailed reaction mechanism. Raillard *et al.* and Vincent *et al.* [143, 144] have investigated and reported the following mechanism for MEK oxidation after generation of the electron-hole pairs due to excitation by UV.

Firstly, the hydroxyl radicals are photogenerated at TiO_2 surface, this step is called initiation and it has been shown previously. Then H-abstraction happens when MEK reacts with hydroxyl radicals to generate alkyl radicals, this step consists in metathesis.

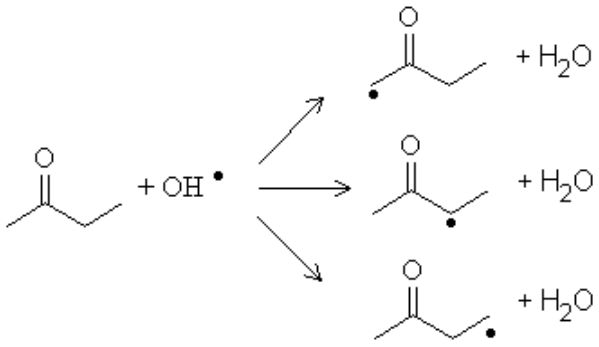

At room temperature, an alkyl radical readily decompose by β-scission to form another smaller alkyl radical and an organic molecule. Some of those organic molecules will tautomerize to become ethynol or 2-propynol while ethylene is a stable organic molecule for which no tautomerization is expected.

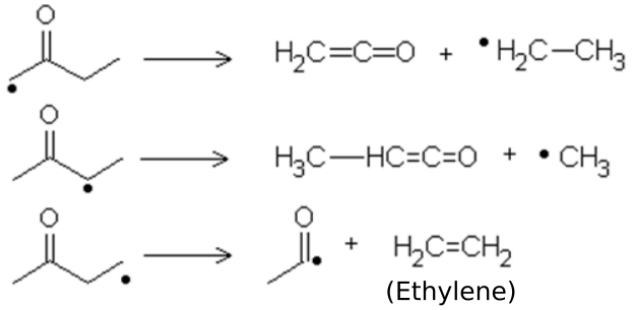

The smaller alkyl radicals immediately react with surface hydroxyl of TiO_2 to form ethane, methane or acetaldehyde as possible by-products.

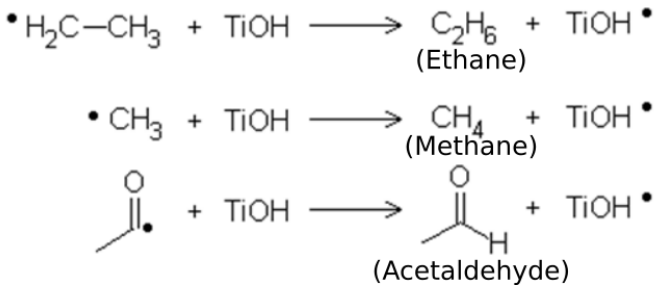

The radicals are also known to recombine themselves to form larger molecules through termination mechanism. Possible resulting products include MEK, ethanol, acetic acid, acetone or methanol.

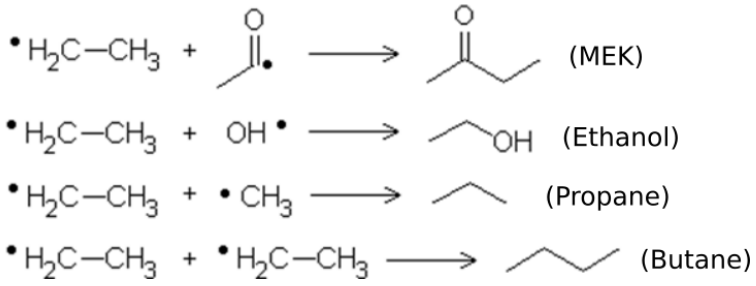

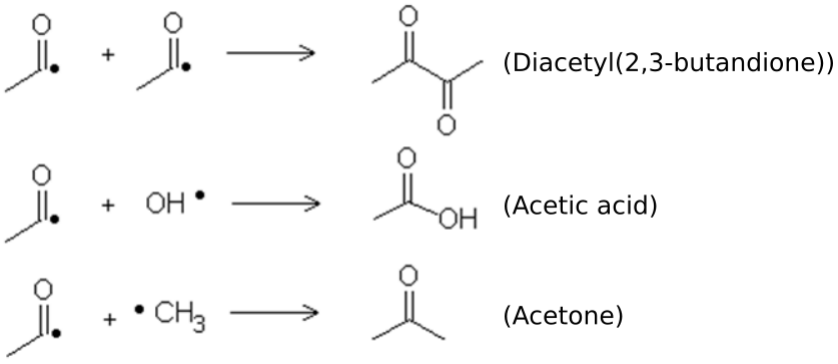

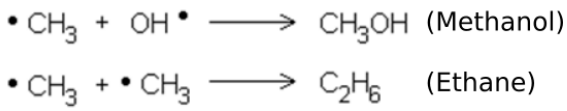

Despite all the possible by-products are shown in the above mechanism of MEK photocatalytic degradation, most of the studies have evidenced only the formation of acetaldehyde, acetone, acetic acid and methanol as detectable species. [27, 143]

I.4.2.2. Bactericidal photoxidation mechanism of TiO_2 in aqueous phase

As a parallel consequence of the photodegradation ability of TiO_2 to decompose organic chemicals, this semiconductor exhibits strong capability of killing a wide range of organisms including Gram-negative and Gram-positive bacteria. [103, 105, 145] The mode of action of photoactivated TiO_2 against bacteria has been studied with both Gram-positive and Gram-negative bacteria, and there is overwhelming evidence that the lethal action is due to membrane and cell wall damage induced by reactive oxygen species (ROSs). [146] Also, this is known that many parameters can affect the photocatalytic activity such as UV irradiation nature, time and power, contact quality between TiO_2 and bacteria, presence of ions in reaction media.

In this section, we will firstly consider the non-photocatalysis-related effects, including the direct UV irradiation effect, the pure toxicity of TiO_2 nanoparticles and the external influence by the presence of ions in the reaction media. Then, the photocatalysis-related effects of ROSs in photocatalytic anti-bacterial mechanism and its comparison for suspended TiO_2 nanoparticles or immobilized TiO_2 nanoparticles will be listed. Also the different cell components of bacteria already known as photodegradation targets will be discussed. Finally, we will address the self-repair and anti-oxygen stress mechanisms of bacteria potentially occurring against photocatalytic actions.

I.4.2.2.a. UV irradiation effects

For Ultraviolet irradiations, 3 ranges of wavelength intervals are usually distinguished: UVA (320-400 nm), UVB (280-320 nm) and UVC (100-280 nm). The shorter the wavelength, the higher energy the radiation carries. The UVC is known for causing multiple DNA damages *via* dimerization of pyrimidine and purine. [147] UV radiations of these low wavelengths are thus called genotoxic radiations. The UVB can cause lipid damage, low DNA damage and the loss of some metabolic activities. [148] The biological effects of UVA are usually attributed to the enhanced production of reactive oxygen species (ROS), which results in oxidative damage to lipids, proteins and DNA of cell, but in a much less severe manner. [148] UVA irradiation can be also capable of inducing pyrimidine dimers in bacterial DNA thus causing DNA damages. [149] Berney *et al*. have confirmed the production of reactive oxygen species under UVA light inside of cells of an *E.coli* strain by studying its gene expression. [150]

As a consequence, when a test of photocatalytic oxidation of bacteria by TiO_2 is performed, it is necessary to distinguish TiO_2 photo-induced bactericidal effect from UV-only-induced bactericidal effect by measuring effects with UVA in the absence TiO_2.

I.4.2.2.b. Effects of nanoparticles on bacteria

Impact of nanoparticles on bacteria has been intensively studied. Some studies have demonstrated that the contact between bacteria and Ag nanoparticles can lead to cell death. [76, 151] Sondi *et al*. have confirmed that the cause of death was not due to release of toxic Ag^+ ions from the Ag nanoparticles but resulted from the accumulation of small-size Ag nanoparticles inside the bacterial cell wall, which causes significant increase of cell membrane permeability. [151] Metal oxide nanoparticles have also been demonstrated of being capable to cause a loss of bacterial cell viability. [152, 153] Little is yet known about the mechanisms behind this effect, but some authors have proposed that it was related to the penetration of metal oxide nanoparticles through bacterial cell wall similar to what happens with other NPs, [154, 155] or to the redox activity of these nanoparticles. [156] Simon-Deckers *et al*. have studied the impact of size, composition and shape of metal oxide nanoparticles on toxicology properties, and they have observed that the small-size ZnO was especially cytotoxic while small-size TiO_2 was significantly less cytotoxic towards *E.coli*. [157] Aruoja *et al*. [158] have measured the toxicity of TiO_2 nanoparticles (EC50=5.83 mg Ti/l) compared to that of the very efficiency $ZnSO_4$ (EC50 ~0.04 mg Zn/l) using an algal growth inhibition test. Although very few applications of using TiO_2 nanoparticles for only its nanoparticle-induced cytotoxicity to eliminate bacteria have been reported, TEM analyses directly evidenced a limited damage to the membrane using TiO_2 nanoparticles, and some TiO_2 nanoparticles have been observed embedded inside the cell membrane (Fig 10).

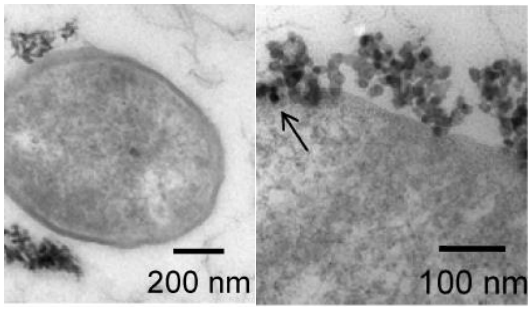

Fig 10 : Transmission electron microscopy observation of TiO_2 nanoparticle absorption inside a bacteria cell wall (*E.coli* MG1655), demonstrated by Simon-Deckers *et al*. [157]

I.4.2.2.c. Effect of inorganic ions on photocatalytic anti-bacterial activity in aqueous phase

Rincon *et al*. reported that inorganic ions may affect the photocatalytic activity. In particular, the addition of CO_3^{2-} and PO_4^{3-} in medium causes a meaningful decrease in the TiO_2 photocatalytic bactericidal effect for *E.coli*, while a weak influence of Cl^-, SO_4^{2-} and NO_3^- was noted. These ions are likely to retard the *E. coli* inactivation rates by competing for the oxidizing radicals or by blocking (adsorbed on TiO_2) the active sites of the TiO_2 catalyst. [159] The inorganic ions concentrations are therefore important parameters to be taken into account before carrying on any photocatalytic anti-bacterial performances in aqueous phase.

I.4.2.2.d. Roles of ROSs in the photocatalytic anti-bacterial mechanism

To date, ROSs like OH•, O_2^-•, HO_2•, H_2O_2 are known to be the principal cause for the photocatalytic degradation of bacteria in liquid phase. [160] Hydroxyl radicals were shown to be the major ROS involved in short range killing of many bacteria by numerous studies, [160-162] although OH• radicals are short-lived and would probably not diffuse further than 1 μm from the surface of the TiO_2 in aqueous medium. [162] H_2O_2 is known to be involved in a longer range bactericidal mechanism due to its longer diffusion distance benefiting from the absence of electric charges. [145] By using a 50 μm thick porous PTFE membrane between bacterial suspension and a TiO_2 coating on glass substrate, Kikuchi *et al*. have demonstrated that the observed bactericidal effect was induced by hydrogen peroxide (H_2O_2) rather than OH•, which cannot diffuse over a long distance in contrast to H_2O_2. [163] Few other studies have proposed possible bactericide actions by other ROSs like O_2^-•. In Fridovich's opinion, [164] O_2^-• radicals are readily formed by reduction of oxygen. Although O_2^-• radicals are weak ROSs, they can convert to their acid form HO_2•, which have much higher oxidative properties than the later. They can also form OH• in contact with H_2O_2 in liquid.

Finally, a complete photocatalytic bactericidal process is thought to result from a combination of the action of several ROSs at the same time. [145, 160]

I.4.2.2.e. Main bacterial cell components as targets by photocatalysis

Multiple bacterial cell components can be targeted by photocatalysis. A schematic resume of the above-mentioned targets of a bacteria cell which can be targeted by TiO_2 photocatalysis is shown in Fig 12 (e.g. Gram-negative and Gram-positive bacterial cell).

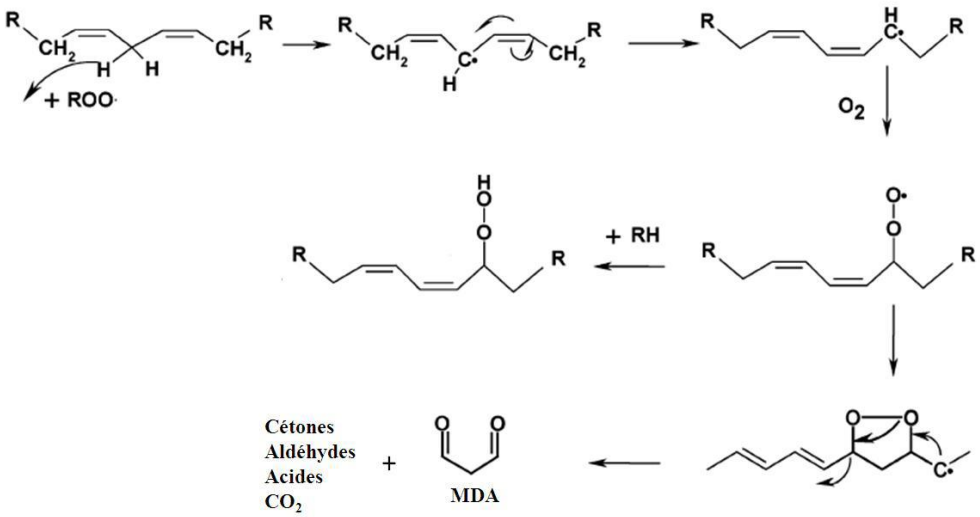

Fig 11: Lipidic peroxidation process and its by-product MDA. [111]

Bacterial cell membrane is the first target of TiO_2 photocatalysis. Sunada *et al.* [165] studied the killing of *E. coli* bacteria on thin films of TiO_2 and showed that the outer membrane was damaged at first. Cytoplasmic membrane was than completely degraded. Degradation of an important outer membrane constituent, the bi-layer of lipids, through lipid peroxidation by ROS (Fig 11), was demonstrated by the release of malondialdehyde (MDA) as a breakdown product. [13, 166] At the same time, there was a concurrent loss of the membrane-dependent respiratory activity [13], which is related to the fact that respiratory and electron transfer activity are mainly carried out in the cytoplasmic membrane of bacteria. Indirect evidence of the membrane damage has been also reported in studies showing the leakage of cellular components like K^+, RNA and protein. [167] At this point, the cell damage is irreversible. The photocatalytic bactericidal effects do not seem to create substantial degradation of peptidoglycan, as it was demonstrated on *E. coli*, [102] which suggested that, at least for Gram negative bacteria, cell disruption first impact the outer membrane, then the cytoplasmic membrane, while by-passing the peptidoglycan (PGN) layer. Kiwi *et al.* have confirmed that peptidoglycan layer is the most resistant cell wall component to photocatalysis. [104] Possibly, it is related to its relatively high permeability, pores being of similar average sizes in peptidoglycans from Gram-negative and Gram-positive species. Pores are also relatively homogeneous in size, with a mean radius of 2.06 nm in *E. coli* [66]. This pore size is large enough for allowing diffusion of ROSs and even of some big protein molecules. In Gram-negative bacteria for example, once the ROS species damage and pass through the outer membrane, they can penetrate the peptidoglycan layer and go on further to damage

directly the inner membrane part of bacteria without degrading the highly cross-linked peptidoglycan network. Thus, during photocatalytic bactericidal process, the cytoplasmic membrane is thought to be the real and final ROSs permeability barrier.

Aside from the membrane damage and the release of cell components in the extracellular medium, photogenerated ROSs were also shown to induce DNA damages. Different kinds of DNA damage were detected by Bock *et al.*, [168] such as single-strand breaks or photo-modified bases. Proteins are also possible targets by photocatalysis of TiO_2, [169] but only a few studies have really identified the degraded protein or evidenced the protein degradation mechanism. [170]

If the stress on the cell exceeds a certain threshold, the cell dies or becomes incapable of further division. Following the initial cell membrane damage and the cell death that require only few hours of UV illumination, photocatalysis has been shown to be capable of complete mineralization of bacteria after prolonged treatment. As an example, *E.coli* was shown to be completely degraded after a treatment of 75h. [101]

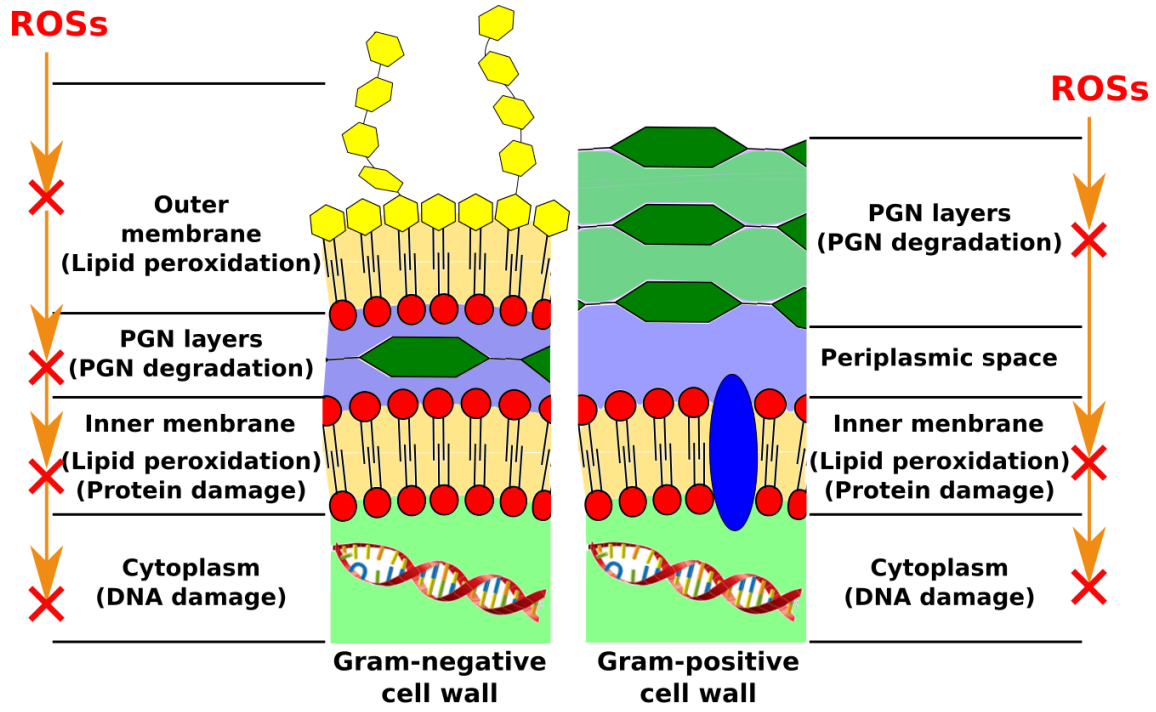

Fig 12: Susceptible targets of Gram-negative (left) and Gram-positive (right) bacterial cell to photocatalysis-produced ROS attacks. Degradation of lipid bi-layer and protein may affect membrane permeability firstly, but is reversible. If this is followed by increased damage to all cell wall layers, leakage of small molecules such as ions may happen. Damage at this stage may be irreversible, and this accompanies cell death. Furthermore, deeper membrane damage allows leakage of higher molecular weight components, which may be followed by protrusion of the cytoplasmic membrane into the surrounding media through degraded areas of the peptidoglycan and lysis of the cell. Degradation of the internal components of the cell such as DNA then occurs, followed by complete mineralization if the photocatalytic reaction time is long enough. [145]

I.4.2.2.f. Antibacterial photocatalytic effects of TiO_2 nanoparticles in suspension or immobilized on a surface

An intimate contact between bacteria and TiO_2 particles is thought to be a key factor in the photocatalytic process. Clearly, immobilized or suspended TiO_2 particles offers different kinds of contact with bacteria. Yet, no clear difference in relation to the contact differences has been well identified, results compared from different works being often controversial. Some studies [104, 171, 172] have shown that fixed TiO_2 can lead to a higher bacteria (*E.coli*) inactivation rate at the beginning of the photocatalytic process even though the total duration required to inactivate all bacteria was the same for both immobilized and suspended TiO_2. Their authors have attributed the cause of the initial faster inactivation rate for fixed TiO_2 to the concentrated photocatalytic effect on small areas with fixed TiO_2 while the same effect is uniformly distributed over the whole medium if TiO_2 particles are in suspension. On the other hand, Gumy *et al.* [173] found higher inactivation efficiency with suspended TiO_2 than with TiO_2 coated on a fibrous web. They proposed that particles dispersed in a liquid would provide more contact surface for the adsorption of bacteria, even if, besides, possible cell inactivation may have been due to direct nanoparticle-induced effects, as mentioned in section I.4.2.1.b. When TiO_2 particles are immobilized, also, the specific surface area of TiO_2 in contact with bacteria or the irradiated surface fraction may influence the photocatalytic efficiency. Nevertheless, surface parameters like topology and particle aggregations that are necessary to describe the surface morphology are usually missing in the available publications. Their impacts on the photocatalytic bactericidal mechanism of TiO_2 surfaces were therefore not elucidated so far.

I.4.2.2.g. Anti-oxygen-stress mechanisms of bacteria for counteracting photocatalysis

Many bacteria possess anti-oxygen-stress mechanisms that enable to counteract the action of photogenerated ROSs. The superoxide dismutase (SOD) is the main enzyme of the cell defense against oxygen stress, which is capable to transform $O_2^{-}\bullet$ to oxygen and hydrogen peroxide, as described by Bowler *et al.* [174] The corresponding equation is shown as follows:

$$2O_2{\cdot^-} + 2H^+ \xrightarrow{SOD} O_2 + H_2O_2$$

Catalase is another type of anti-oxygen-stress enzyme that exists in great quantities. It can catalyze the dismutation of hydrogen peroxide to water and oxygen as described in the following equation: [175]

$$H_2O_2 + H_2O_2 \xrightarrow{\text{Catalase}} O_2 + 2H_2O$$

In the specific case of oxidative damages caused by TiO_2, studies conducted with SOD mutants of *E.coli* have shown that the inactivation rate was inversely proportional to the SOD and catalase activities. [176] Gaetan *et al.* [177] have compared the photocatalytic bactericidal effect of a SOD- and catalase-deficit *E.coli* mutant strain with that of a normal *E.coli* strain, and they have reported that the mutant strain was much more sensitive to photocatalysis than the normal strain. Another study done by Rincon and Pulgarin revealed that the co-functional anti-oxygen-stress mechanism of both SOD and catalase in *E.coli* during the post-irradiation period of TiO_2 photocatalytic process are responsible for the bacterial repair if the time of post-irradiation is long enough. [178] While most of the above works have focused on the study of anti-ROS or repair mechanism of bacteria, few works have focused on the comparison of that mechanism between suspended TiO_2 and immobilized TiO_2.

I.4.3. Preparation of TiO_2 nanomaterials

In this section, the production of TiO_2 will be introduced in two ways, including the large scale industry approaches for which the technologies are relatively mature since years, and the more innovative small scale laboratory approaches focused on the synthesis of highly active photocatalytic-grade TiO_2. We will focus on the sol-gel method here especially.

I.4.3.1. Industrial approaches

Titanium dioxide is among the most important inorganic compounds used in modern industry. The titanium dioxide market generates relatively high profits, because there is a rising demand and a constant supply. [179] Only 5% of the total produced titanium ore is converted into metal titanium, whereas the main way of using titanium minerals (and in large majority the $FeTiO_3$ ilmenite ore) is to obtain finely dispersed TiO_2. The two main production methods are the sulfate process and the chloride process. [127]

In the sulfate process, ilmenite is used. It is treated with concentrated sulfuric acid (H_2SO_4) and the titanium oxygen sulfate ($TiOSO_4$) is selectively extracted and converted into titanium dioxide. [180] Water is removed at temperatures between 200–300 ℃. Seed crystals are

added to start the crystallization process. Depending on the final heating temperature (800−850 °C or 900−930 °C), either anatase or rutile is formed, respectively.

The chloride process is more economic and less environmentally harmful. [127] But it requires purer ore. Liquid $TiCl_4$ is distilled off and converted back into TiO_2 in a pure oxygen flame or in plasma at temperatures of 1200–1700 ℃. The majority of chlorine is recovered. Titanium dioxide is reduced with carbon and then oxidized again with recovered chlorine.

Except the large scale pigment-grade TiO_2 production, manufacturers also produce nanostructured titanium dioxide with good photocatalytic properties. Among generally commercialized photocatalytic TiO_2, P25 (Evonik) prepared *via* the chloride process is currently one of the de-facto commercial reference photocatalysts. [181] It is a fine white powder with a surface area of approximately 50 $m^2\ g^{-1}$ and a particle size of around 25 nm. The reason of its high photocatalytic performance level continues to be a matter of debate. Some researchers [182] have reported that a possible reason behind its high activity could be that the P25 contains a mixture of anatase and rutile in an approximately 4:1 proportion. The intimate contact of these two semiconductor phases forms a heterojunction structure. The photogenerated electron transfer from the conduction band of anatase to that of rutile (the position of that of anatase being 0.2 eV higher than that of rutile), yields to a beneficial spatial charge carrier separation phenomena which could limit charge recombination. [183]

I.4.3.2. Laboratory-scale approaches

In the framework of the rapid development of nanoscience and nanotechnology, the domain of nanostructured materials such as TiO_2 nanomaterials undergoes intense academic researches and development studies. To elaborate high performance nanoscale TiO_2, it is essential to control the particle size, shape, particle size distribution and crystalline phase of the material. A variety of TiO_2 nanostructures have thus been prepared, such as *e.g.* nanoparticles, nanotubes, nanorods, nanofibers, and nanoflowers, due to their desired characteristics, and these structures can be made through various preparation methods, both physical [184] and chemical, with the later including the sol–gel method, the hydrothermal method, the microwave method, and reverse micelle method amongst others. [185-192] Among these processes, the most used is the sol-gel method.

The sol-gel method has a relatively long history which started with the processing of oxide materials including glass and ceramics about 30 years ago. This simple, cost effective and low temperature synthesis method now has also been favored and largely applied in catalyst preparation due to its potential to fabricate catalysts with high purity, homogeneity, fine-scale and controllable morphology. [193, 194] The usual approach to prepare a sol-gel metal oxide solid is the hydrolysis and polycondensation of metal precursors followed by aging and drying under ambient atmosphere. The word "sol" refers to the dispersion of colloidal particles in a liquid, while "gel" is an interconnected rigid network with pores in the submicrometer range and polymeric chains whose average length is greater than a micrometer.

In the case of the syntheses of TiO_2 by sol-gel route, [195-198] titanium alkoxides (such as titanium isopropoxide, titanium n-butoxide), organic solvent, acid/base catalysts and water are introduced into the reaction system. The resulting TiO_2 gel as densely cross-linked 3D structure is formed during the hydrolysis and condensation process. Finally, the titanium oxide particles in different crystal phases can be obtained depending on the post-annealing temperature.

Numerous works have been done to study the reaction mechanism. [199, 200] Two main steps have been identified and shown as follows:

Hydrolysis

$$Ti(OR)_n + H_2O \rightarrow Ti(OH)(OR)_{n-1} + ROH$$
$$Ti(OH)(OR)_{n-1} + H_2O \rightarrow Ti(OH)(OR)_{n-2} + ROH$$

Water addition causes hydroxylation of alkoxides, which leads to the formation of M-OH bonds the (reaction continues until the formation of $Ti(OH)_n$).

Condensation

$$-Ti-OH + HO-Ti- \rightarrow -Ti-O-Ti- + H_2O$$
$$-Ti-OR + HO-Ti- \rightarrow -Ti-O-Ti- + ROH$$

Condensed species are formed by the formation of oxygen bridges *via* oxolation reactions with the release of water molecules, and *via* alcoxolation with the release of alcohol molecules.

Other reaction conditions such as molar ratio of reactants, pH, reaction temperature and the duration of the reaction can also alter the final morphology, structure and porosity of TiO_2.

[185, 201] For example, pH has been reported to strongly influence phase composition and particle size of sol-gel synthesized titanium dioxide nanoparticles. [202] In this work, anatase and brookite particle sizes and brookite content increase with increasing pH in the range of 0.5 to 3.

In addition of basic reagents, additives and shape controllers are widely added during the sol-gel synthesis to obtain specific morphology of TiO_2 nanoparticles. Eiden-Assman and coworkers have added alkali halide and nitrate salts to produce uniform spherical TiO_2 colloids. [203] Lee has used triethanolamine as a shape controller and $HClO_4$ or NaOH as pH controllers to synthesize uniform and high crystallinity TiO_2 in different morphologies. [204] Also many polymers and surfactants such as PEG, PVA, Brij 56, and CTAB [205-207] are reported to be used in sol-gel syntheses in order to increase specific surface area of the TiO_2 nanoparticles. Furthermore, modifications of TiO_2 by adding dopants during sol-gel syntheses have been performed as well. The addition of a carboxylic acid (acetic acid for instance), can chelate and reduce the reactivity of the metal precursor by its ability to form ligand with the later, and the resulting sol-gel synthesis can be thus performed in a more controlled manner.

I.4.4. Morphology modifications of TiO_2 nanomaterials

To date, the TiO_2 semiconductor has undoubtedly proven to be one of the excellent photocatalysts for the oxidative decomposition of many organic compounds and microorganisms. However, the bulk and surface physico-chemical properties of TiO_2 materials can still be tuned for enhancing/optimizing their response to the incident irradiation, and globally their efficiency as photocatalysts, whether UVA or visible light irradiation is used.

During the past decades, a variety of strategies have been employed to improve the photocatalytic efficiencies of photocatalysts under UVA, visible-light or solar light. Among them, we will report here on some selected approaches for controlling the morphology of TiO_2 materials.

Small changes of the synthesis parameters (e.g. duration, temperature, etc.) or the addition of additive compounds in small amounts in the synthesis of TiO_2 can result in

significant changes in the physico-chemical properties of TiO_2, and especially the morphology. [208, 209] In this section, we will discuss the changes of morphology of TiO_2 nanomaterials in two major aspects: size and shape.

I.4.4.1. Particle size modification

One basic example is that the use of a strong acid like HCl in sol-gel synthesis often gives larger size rutile nanoparticles,[205, 210] while the use of an organic acid like acetic acid gives smaller size anatase nanoparticles [206, 207]. Livage *et al.* [197] had demonstrated that the nucleophilic acetic acid can bind to the titanium precursor forming a ligand structure, lowering the reactivity of the precursor prior to the hydrolysis process. Thus the way of hydrolysis and condensation in the acetic acid-assisted sol-gel synthesis is totally changed compared to an acetic acid-free synthesis.

Besides of the different acids, many solvents, and templates or porogen agents such as amphiphilic polymers (PEG, [210] PVA etc...) or activated carbons, [211] are also added to the aqueous reaction media to alter the properties of the synthesized nanoparticles. Calcination of TiO_2 at high temperature could cause the collapse of the mesoporous framework and a loss of surface area due to a subsequent crystal growth during crystallization or phase transition. [212] Yu *et al.* was the first synthesizing phosphated mesoporous TiO_2 by directly incorporating phosphorus from phosphoric acid into the inorganic framework of mesoporous TiO_2. [213] In his study, he concluded that the high surface area resulted from the direct incorporation of phosphorous, which can stabilize the framework of mesoporous TiO_2 and thus inhibit the crystal growth during the calcination.

I.4.4.2. Crystal morphology engineering

The surface stability and reactivity of inorganic single crystals are reported to be dominated by their surface chemistry, whose effect on the stabilization of morphology is critical thermodynamically for the synthesis of crystals of photocatalyst with high reactivity. [214] Many studies show that nanoparticles with different morphologies expose different crystal facets and exhibit different surface physico-chemical properties. [215] Some have investigated the different photocatalytic properties of TiO_2 nanoparticles with tunable shapes and found that exposed {001} facets the enhanced photoelectric conversion of TiO_2 nanocrystals [216].

The photocatalytic activity of the photocatalyst clearly depends on the recombination rate of the electrons and holes. This implies that a low recombination rate will significantly enhance the photocatalytic properties of the photocatalyst. Recently, several studies have shown that the reduction and oxidation sites on the surface of the anatase TiO_2 single crystals are spatially separated because of the selective migration of excited electrons to the {101} crystal facets and positive holes to the {001} crystal facets. The {101} crystal facets serve as possible reservoirs for the photogenerated electrons. [140, 217] In fact, density functional theory (DFT) calculations have predicted that the conduction band potential of the anatase {101} surface is slightly lower than that of the anatase {001} surface. [218] Furthermore, the exposed {101} crystal facets yield a highly reactive surface for the reduction of O_2 molecules to superoxide radicals. [137] This directional flow of the photogenerated charge carriers towards these specific crystal facets improves the reaction efficiency and selectivity of the photocatalyst.

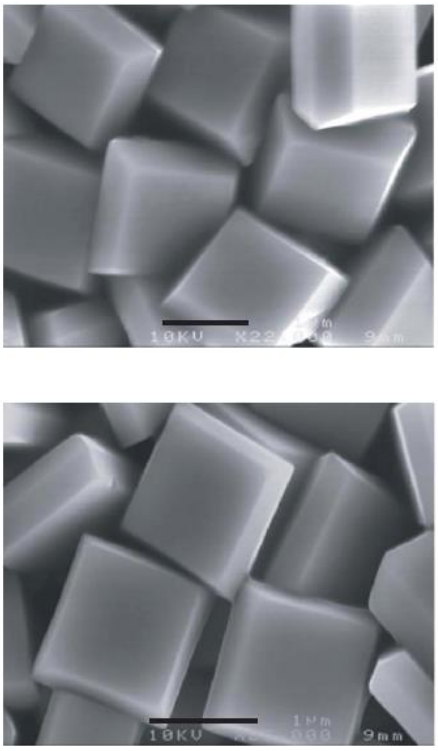

Fig 13: TiO_2 crystals with largely exposed {001} facet synthesized by Yang *et al.* using HF as capping agent [219]

Many efforts have been devoted to obtain nanostructured TiO_2 with a unitary size and morphology distribution. It is well-known that the essence of a shape-control is the tuning of

the growing rate in specific directions. A popular approach for controlling the shape is named the "surfactant-assisted method", in which, organic surfactants would selectively bind to specific crystal facets and control the growing rate of specific facets. However, it is reported being inefficient to largely favor the growth of {001} facets simply through the use of organic surfactants. [220]

Recently, a new method involving inorganic capping agent was used as a new strategy for the morphology control of TiO_2 nanocrystals. A capping agent is a special kind of additive (usually halogenate anions) which, like the above-mentioned surfactants, can favor the growth of certain crystal facets over other facets by binding to specific surfaces and lowering significantly the surface energy. The resulting crystal often has an anisotropic growth and has "unusual" large surface area coverage percentage of one specific facet. It was shown by Yang and *al* [219] that fluorine ions at high temperature can be preferentially adsorbed on the highly photoreactive {001} facet of anatase crystals, lowering its surface energy, and thus resulting in TiO_2 platelets with largely exposed {001} facet (Fig 13). The fluorine sources are mainly the hydrofluoric acid or fluorine-contained inorganic salts. They are often involved in hydrothermal syntheses of TiO_2 because the TiO_2 crystal growth is accelerated at high temperature and pressure conditions.

I.4.4.3. Ionic liquid assisted morphology modification

Room temperature ionic liquids (RTILs) have recently attracted a significant interest as a new kind of template agent. [221] Yoo *et al.* [222] investigated the use of 1-Butyl-3-methylimidazolium hexafluorophosphate ($BmimPF_6$) which resulted in smaller TiO_2 nanoparticles with a better crystallinity and a better thermal resistance.

RTILs are an exceptional type of chemical compounds which are composed nearly by only ions at room temperature. Their superior properties like a negligible vapor pressure and a high thermal stability are very much beneficial in many chemical industry areas. [221, 223, 224] But besides those well-known advantages as a solvent, they also possess the underrated nanostructure shaping ability due to their large size organic cation and a non-coordination anion combination configuration, so that they can be used as favorable additives for the synthesis of inorganic nanostructures. [224, 225]

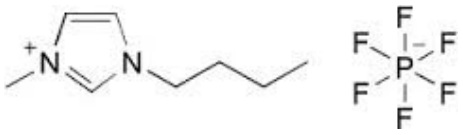

Fig 14: 1-Butyl-3-methylimidazolium hexafluorophosphate ($BmimPF_6$) molecular structure

Although thermally stable mesoporous anatase TiO_2 nanoparticles with high surface area and small size crystallites have been indeed obtained *via* the participation of RTILs like $BmimPF_6$, the large amount of RTIL (IL/Ti atomic ratio larger than 3) required in the process is a major economical drawback caused by relatively expensive test, when compared to the use of conventional template agents or surfactants. Choi and al. [226] were able to use 1/100 of the RTIL quantity used by Yoo *et al.*, but both the BET surface and the photocatalytic activity were strongly reduced compared to work of Yoo *et al.* To our knowledge, a detailed mechanism and the structuration role of the $BmimPF_6$ involved in sol-gel or solvothermal reactions were not described till now. Among scarce reports, Zhao *et al.* [227], have investigated the capping ability of $BmimBF_4$ for producing shape-controlled TiO_2 crystals, and they have shown that the fluorine and $Bmim^+$ ions released from the ionic liquid played a role of capping agent role to favor the {001} and {100} facets growth, respectively. But unfortunately the crystallized TiO_2 crystals were too large (crystal size diameter around 100-500 nm) to maintain a high surface area, and thus they cannot be used for environmental depollution approaches. Even if the capping mechanism of $BmimBF_4$ was well demonstrated, the $BmimPF_6$ ionic liquid differs from $BmimBF_4$ in many properties, [228] So that both role and mechanism in the TiO_2 synthesis and a detailed mechanism remains to be proposed.

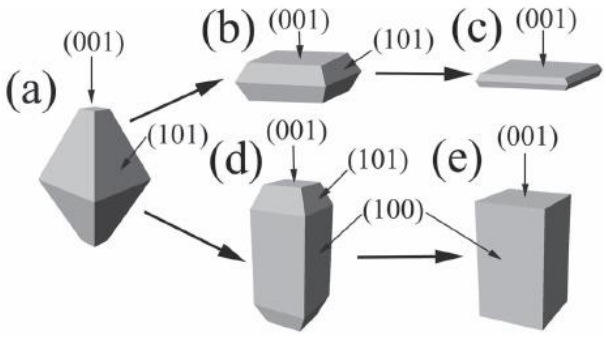

Fig 15: Different TiO_2 anatase crystal morphologies with different specific facet surface area coverage percentages obtained by applying different synthesis parameters or using different amounts of $BmimBF_4$, [227]
a) slightly truncated tetragonal bipyramid with dominant {101} facets (equilibrium crystal shape);
b) truncated tetragonal bipyramid with a large percentage of top {001} facets;
c) square sheet with dominant {001} facets;
d) elongated truncated tetragonal bipyramid with a large percentage of lateral {100} facets;
e) tetragonal cuboid enclosed by {100} and {001} facets

I.5. TiO_2 based photocatalytic coatings

TiO_2 powders have been incorporated as white pigment in different applications such as paints from ancient times because of the excellent light diffraction index and UV absorption ability. As early as 1929, before the works done in late 1960's which officially discovered photocatalytic activity of TiO_2, Keidel [229] stated that a titanium white pigment, under sunlight irradiation, was responsible for paint chalking because of the photodegradation of organic binders. In 1938, Goodeve *et al*. [230] reported that UV absorption produces active oxygen species on the TiO_2 surface that cause dyes to photobleach. Even knowing that TiO_2 has some ability to degrade polymer under UV or sunlight, people still search means to protect organic compounds in paint from photocatalytic TiO_2. So, almost all titanium dioxide used in plastics applications is subjected to a surface treatment. [231] The photocatalytic activity of the TiO_2-based pigment may be reduced by such a surface treatment with suitable inorganic compounds (oxyhydrates of aluminium and silicon, also oxides and oxyhydrates of zirconium, tin, zinc, cerium, and boron). The treatment works by placing a physical barrier between the pigment surface and the polymer matrix, blocking the active sites, thus minimizing reaction sites.

Long after Fujishima to the very present days, strategies of using TiO_2 nanomaterials in a paint formulation to photodegrade organic matters in the air rather than as a pigment, emerged from the development of nanotechnologies. Construction materials can be used to support photocatalytic TiO_2 nanoparticles and used as depolluting agents. [232] Paint coatings, among all construction materials, are especially attractive as support or host materials for photocatalytic TiO_2 since almost all surfaces in urban areas can be painted. In order to be commercially attractive, photocatalytic paints should exhibit a high photocatalytic activity while preventing its own degradation.

Paints can be divided into two major categories: solvent-based paints and water-based paints. As their name indicates, solvent-based paints sometimes referred to as "oil-based" or "alkyd" (glycerol and phthalic acid based binder) paints, contain a significantly higher level of organic solvents than water-based paints. These solvents are responsible for the strong odor noticeable (caused by VOCs) in buildings that have been freshly painted. They are also potentially hazardous for both human health and for the environment for which concerted efforts are being made to reduce or remove their presence in paints without negatively

impacting on the paint performances. Plus, oil paints content too much organic extenders and binders, so they are unsuitable to support photocatalytic TiO_2 nanoparticles due to self-photodegradation.

Fifty years ago, virtually all paints were solvent-based. Today, advances in paint technology means that modern, water-based paints, often referred to as acrylic emulsions, are increasingly replacing organic solvents across a broad range of paint applications and surface areas (and account for 80% of architectural paints). Legislation is in place to support this trend.

From a performance point of view, advances in the paint technology means that high quality water-based paints are in many respects equal to or superior to their solvent-based equivalents. High quality acrylic emulsions offer excellent durability, fast drying time, and the emission of fewer odors. Today, water-based paints dominate and account for roughly 80% of paints sold in the residential market. However, a non-negligible quantity of organic binders and surfactants still exist in water-based paints (around 10%).

Another new type of paints consists in using inorganic mineral particles (e.g. silicates, sulfates) as charges and extenders in the paint while keeping the organic binder quantity at a minimum quantity. Those paints are called mineral paints.

In none of the three cases above, the application of the photocatalytic paints is largely commercialized, because they suffer from the self-decomposition of organic paint constituents during prolonged exposure to the UV irradiation. There are already some reports showing that under UV light irradiation, the organic binder in the photocatalytic paints proceeds self-degradation and some stable toxic compounds such as acetaldehydes and ketones are produced, which are not going to further mineralization. [233] The resulting photocatalytic activity was often decreased compared to the samples without binders. [105] Thus, strategies for minimizing the paint photodegradation must be developed in this new emerging environmental application field.

II. Characterization methods and synthesis of TiO_2 nanomaterials

In this chapter, we will firstly describe the characterization methods used in this work in characterization techniques section. Then, in sample preparation and characterization section, different TiO_2 photocatalysts will be prepared *via* a sol-gel route in the presence of ionic liqud $BmimPF_6$ in HAc or in HCl medium. Roles of constituent elements of $BmimPF_6$ will be studied by adding $Bmim^+$, PF_6^- and PO_4^{3-} ions separately in TiO_2 synthesis in HCl medium as additive instead of $BmimPF_6$. Finally, search of alternative additive or additives of $BmimPF_6$ for synthesizing TiO_2 nanomaterials in HAc medium will be conducted, for obtaining materials with similar physico-chemical properties compared to the $BmimPF_6$-derived TiO_2 materials.

II.1. Characterization techniques

Several characterization techniques are used to evidence the main bulk and surface physico-chemical properties of materials. We report here on X-ray diffraction (XRD), surface area and porosity analysis, X-ray photoelectron spectroscopy (XPS) and Transmission electron microscopy (TEM).

II.1.1. X-ray diffraction (XRD)

X-ray powder diffraction (XRD) is a non-destructive analytical technique to identify crystal phase, phase composition and crystallite average size of crystallized materials. The principle of X-ray diffraction is based on constructive interference occurring when monochromatic X-rays are diffracted by a crystalline sample. The X-rays generated by a metallic anode are filtered to produce monochromatic radiation, collimated to concentrate, and directed toward the sample. The interaction of the incident rays with the sample then produces constructive interference when the diffracted rays satisfy Bragg's Law:

$$n\lambda = 2d_{hkl} \sin \theta.$$

Where n is a positive integer, λ is the wavelength of incident wave, θ is the scattering angle, and d_{hkl} is the interplanar distance for lattice (hkl) planes.

This law relates the wavelength of electromagnetic radiation to the diffraction angle and the lattice spacing in a crystalline sample. By scanning the sample through a range of 2θ angles, all possible diffraction directions of the lattice should be obtained due to the random orientation of the powdered material. The XRD diffractogram is obtained by relating counts of diffracted X-rays with 2θ angle. Identification of phases is achieved by comparing XRD diagrams to standard reference patterns.

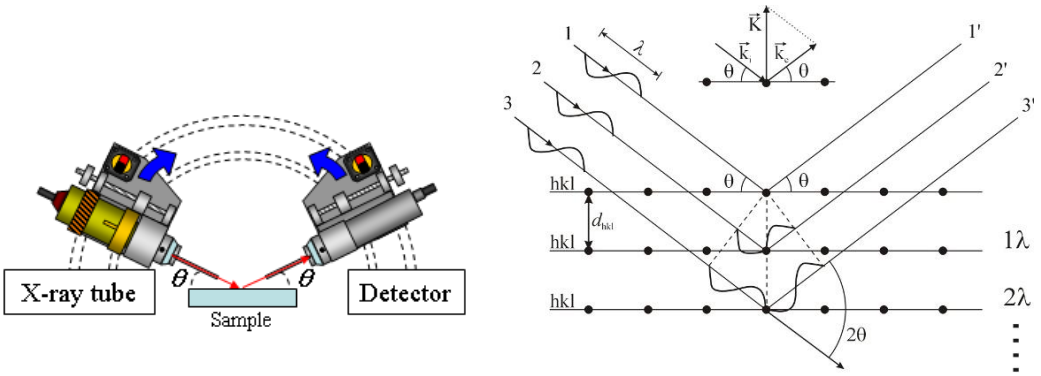

Fig 16: Working mechanism of a θ/θmode XRD instrument (left); Bragg's law and the constructive interference of the diffracted X-rays from crystal plans (right)

XRD characterization is performed on a Bruker D8 Advance diffractometer operating in the θ/θ mode, equipped with a copper anticathode producing X-rays with wavelength of $\lambda_{CuK\alpha l}$ = 1.5406Å. The database of patterns is from International Center for Diffraction Data's JCPDS files.

Considering the approximation of spherical (and thus isotropic) crystallites, the mean crystallite size is estimated *via* Scherrer formula:

$$FWHM = 0.9\ \lambda/t\ \cos(\theta_B)$$

where the FWHM (full width at half maximun) is applied to the most intense isolated peaks expressed in radians, λ is the wavelength of the X-rays, t is the thickness of the layer and θ_B the Bragg angle of the reflection. This formula can allow us to estimate the average diameters of coherently-diffracting domains size of crystallites (t).

II.1.2. Surface area measurement and porosity analysis

Specific surface area and porosity of materials are important properties in the field of heterogeneous catalysis. Total surface area is a crucial criterion for solid catalysts since it outlines the number of active sites and is thus often related to catalytic activity.

Gas sorption among other methods is routinely used in heterogeneous catalysis to characterize porous materials. Brunauer–Emmett–Teller (BET) theory can be used to derive the specific surface area of a solid material (usually in powder form) form the physical adsorption of gas molecules on a solid surface. In this model, the specific surface area is obtained by experimentally building the adsorption isotherm of an adsorbate gas at its boiling

temperature (in our case N_2 of 77.2K). The specific surface area in m^2/g is determined by calculating the amount of adsorbate gas corresponding to a mono-molecular layer on the surface as a function of the relative pressure, using the so-called BET equation:

$$\frac{\mathbf{1}}{\boldsymbol{V_a}(\frac{\boldsymbol{P_0}}{\boldsymbol{P}}-\mathbf{1})} = \frac{\mathbf{C}-\mathbf{1}}{\boldsymbol{V_m C}} \times \frac{\boldsymbol{P_0}}{\boldsymbol{P}} + \frac{\mathbf{1}}{\boldsymbol{V_m C}}$$

where

P = Partial vapor pressure of adsorbate gas in equilibrium with the surface at 77.2 K (b.p. of liquid nitrogen), in Pa

P_o = Saturated vapor pressure of adsorbate gas at 77.2 K, in Pa

V_a = Volume of gas adsorbed per gram of solid at standard temperature and pressure, in mL/g

V_m = Volume of a monolayer of gas adsorbed per gram of solid at STP on the sample surface, in mL/g

C = Dimensionless constant that is related to the enthalpy of adsorption of the adsorbate gas on the powder sample.

Then $1/V_a(\frac{Po}{P}-1)$ is plotted against $\frac{P}{P_0}$ and this plot should yield a straight line usually in the approximate relative pressure range 0.05 to 0.3. The slope, which is equal to $(C-1)/V_mC$, and the intercept, which is equal to $1/V_mC$, are derived from linear regression analysis. The specific surface area, S, in m^2/g, is derived from V_m by the equation given below:

$$S = \frac{\sigma V_m N_a}{V_M}$$

where

N_a = Avogadro constant (6.022×10^{23} mol^{-1})

σ = Effective cross-sectional area of one adsorbate molecule, 0.162 nm^2 for N_2

V_m = Volume of a monolayer of gas adsorbed per gram of solid at STP on the sample surface, in mL/g

V_M = Molar volume at STP, 22400 mL/mol

The specific surface area and porosity measurements are carried out by ASAP2010 Micromeritics Tristar 3000 analyzer using ultra-pure quality N_2 as adsorbent at 77 K. Before the N_2 adsorption, each sample has to be outgassed at 150 C° in a vacuum for 12 h in order to desorb the impurities or moisture from its surface.

Graphical information can be obtained from isotherm curve to reveal the type of porosity present in samples. Details can be found in work published by G. Leofanti *et al*. [234] Brunauer [235] has defined five different types (Fig 17 upper line). Type I isotherms are characteristic for microporous adsorbents, such as zeolites and carbons. Type II isotherms are characteristic for macroporous solid. Type IV isotherms are typical for mesoporous materials. Important features are the increase in volume adsorbed at higher P/P_0 caused by adsorption in mesopores. A distinct increase in adsorbate volume in the low P/P_0 region in type IV isotherms indicates the presence of micropores associated with mesopores. Type VI corresponds to the ultramicroporous materials.

The desorption is the opposite phenomena to that of adsorption, and is taking place during the analysis after the saturation of adsorbent. The evaporation of the adsorbate in mesopores usually occurs at a lower pressure than that of capillary condensation, resulting in a hysteresis pattern (differential pattern between both adsorption and desorption isotherms). Four types of hysteresis (H1 to H4) are listed according to the IUPAC classification (Fig 17 lower line). [236] The H1 and H2 hystereses are characteristic of solids with cylindrical porous channels or formed by aggregation or agglomeration of spherical particles. The difference between these two hystereses is the uniformity of the pores (uniform for H1 and non-uniform for H2). H3 and H4 hystereses are usually found on solids consisting in aggregates or agglomerates of particles forming slit-shaped pores (uniform for H3 and not uniform for H4). It is worth noting that the isotherms recorded experimentally scarcely correspond to a single IUPAC classification, and more usually consist in several contributions.

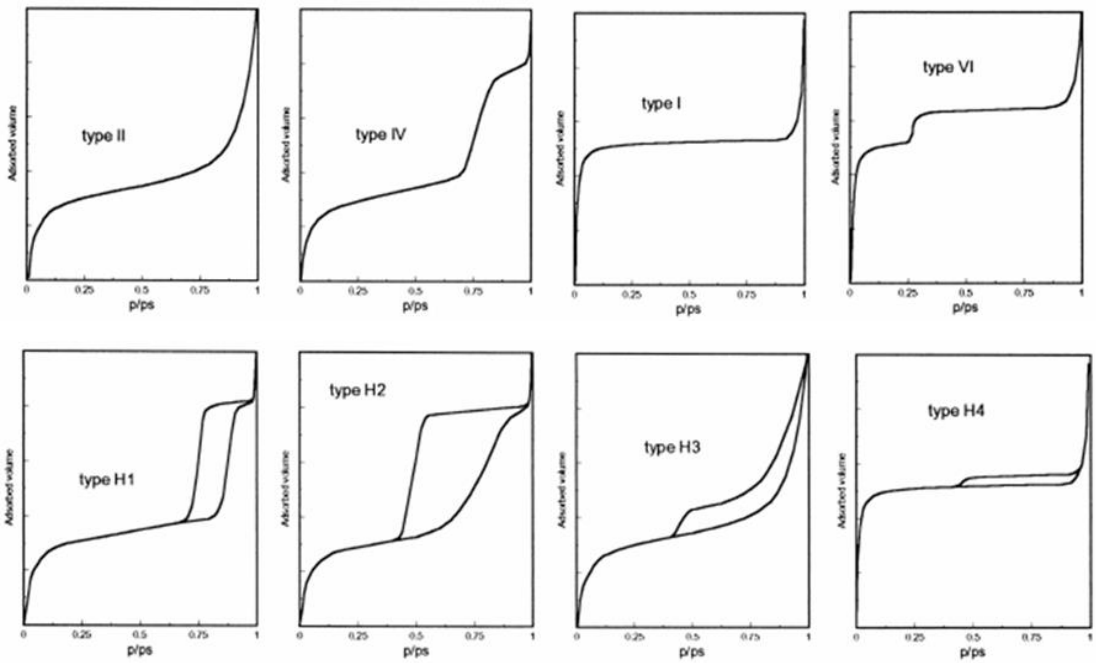

Fig 17: Types of adsorption isotherms defined by Brunauer [237] that are most observed (upper line), and the four types of hysteresis (lower line).

Pore size distribution information can also be obtained from the N_2 sorption isotherm at 77K. The Barrett-Joyner-Halenda (BJH) calculation method applied to N_2 desorption data uses the modified Kelvin equation to relate the amount of adsorbate removed from the pores of the material, as the relative pressure (P/P_0) is decreased during the isotherm desorption branch, to the size of the pores

II.1.3. X-Ray photoelectron spectroscopy (XPS)

The surface of a material is the point of interaction with its external environment. In the field of catalysis, surface modifications of materials are often performed to increase the specific surface area, to tune the surface composition or to modify their properties for enhancing catalytic activity of materials. Therefore, the analysis of the surface chemistry and of the surface composition is an important tool to evidence surface properties, and to understand the physical and chemical interactions that occur at the surface of solid, and/or at the interfaces within multimaterials. X-Ray photoelectron spectroscopy (XPS) is a non-destructive and semi-qualitative analysis method that can provide essential information such as elemental composition, empirical formula, chemical state and electronic state of the elements within the surface layer of materials.

The XPS principle is based on the measurement of the kinetic energy of photoelectrons emitted by the sample when irradiated by a soft (low energy) monochromatic X-ray beam under ultrahigh vacuum (ca. 10^{-9} tor). The X-ray photons excite the core electrons of the sample atoms with binding energy lower than the X-ray energy. The so-called photoelectrons emitted from the parent atom have kinetic energy corresponding to the difference between the incident energy (from the X-ray) and the binding energy, subtracted from the work function, dependent mainly on the spectrometer. Only the photoelectrons at the extreme outer surface (1-10 nm) can escape from the sample surface, so that XPS is a surface-sensitive analysis technique.

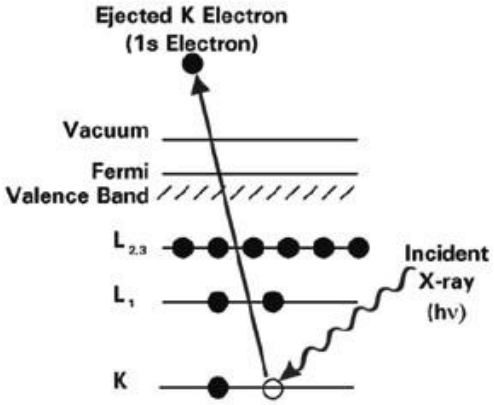

Fig 18: The photoemission process involved for XPS surface analysis. The discs represent electrons and the bars represent energy levels within the material being analyzed. Here is an example of a 1s electron.

The binding energy of a certain element is strongly dependent on its chemical environment and XPS provides information on the chemical binding between the element and its neighbour atoms. The influence of the atoms on its oxidation and electronic state results in measurable chemical shifts of orbital peaks, explained by electronegativity difference in the electrostatic model of atoms.

The XPS data can be viewed as an XPS spectrum, which consists of a series of peaks corresponding to the binding energies of the emitted and ejected photoelectrons. For non-conductive materials such as semi-conductors, positive charges can accumulate at the solid surface, thus reducing the kinetic energy of emitted photoelectrons. By consequence, the resulted binding energy will be overestimated. This so-called charge effect should be corrected by taking the sp_2 carbon 1s peak at 284.6 eV from contamination carbon as reference.

XPS is also a semi-quantitative analysis, since the intensity of the peak is proportional to the relative surface concentration of the atoms from which the photoelectrons are emitted. For a sample containing two elements A and B, the A/B surface atomic ratio is:

$$\frac{C_A}{C_B} = \frac{I_A}{I_B} \times \frac{\sigma_B}{\sigma_A} \times (\frac{E_{cB}}{E_{cA}})^{\frac{1}{2}} \times \frac{D_B}{D_A} \times \frac{n_B}{n_A}$$

Where

I = Surface of the peak

σ = Photoionization cross section as tabulated by Scofield [238] which refers to the probability of an electron to be emitted from its electronic state

E_C = kinetic energy

D = Transmission factor of the instrument dependent on E_C. D_B/D_A is 1 when E_{cA} is nearly equal to E_{cB}

n = Acquisition passage number

Even with all precautions, the overall accuracy of the semi-quantitative analysis of XPS is around 10% relative. XPS characterization is performed on a Thermo VG Scientific equipped with X-Ray source consisting in aluminium Kα radiation (hv = 1486.6 eV). After charge effect subtraction, the spectra were decomposed assuming contributions with Doniach-Sunjic shape [239] and a Shirley baseline subtraction. [240]

II.1.4. Transmission Electron Microscope (TEM)

The transmission electron microscope (TEM) is a microscopy technique using an electron beam as “light source”, generated and accelerated under ultrahigh vacuum in the column of the microscope. This microscopy operates in a bright field recording mode, meaning that the image is produced by the non-diffracted electron beam transmitted through a thin sample. Interaction between the electrons and the material leads to the recording of the image, possibly with nanometric resolution. The TEM technique provides information on size, morphology and structure of materials. Thicker regions of the sample or regions with a higher atomic number will appear dark, whilst regions with no sample in the beam path will appear bright.

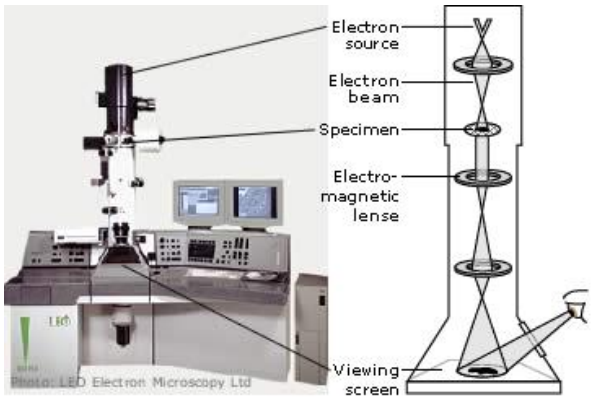

Fig 19: Schematic presentation of TEM's instrument

The TEM analysis is performed at IS2M (Institut de Science des Materiaux de Mulhouse) using a Philips CM200 as standard mode observation and a JEOL ARM200 as high resolution mode (HDTEM), equipped with thermo-ionic LaB_6 filament and cold Field Emission Gun FEG canon respectively, operating both at 200 kV acceleration voltage. The samples are firstly grinded and sonicated in ethanol solution, before a drop of the solution is deposited onto a copper grid covered by holey carbon membrane for observation.

Fig 20: TEM JOEL ARM200 (left) and Philips CM200 (right) at IS2M

II.2. Preparation and characterization of samples

II.2.1. $BmimPF_6$ assisted sol-gel synthesis of TiO_2 using HAc as acid catalyst

II.2.1.1. Sample preparation

In this work, TiO_2 nanomaterials have been synthesized by a room temperature ionic liquid-assisted sol-gel route. We have used titanium (IV) isopropoxide ($Ti(O^iPr)_4$ 97% from ALDRICH) as titanium precursor, propan-2-ol (AnalaR Normapur, >99.5%, VWR Chemicals CHEMICALS) as organic solvent and a solution of diluted acetic acid (ACS reagent >99.8%, Sigma-Aldrich) in distilled water as acidic catalyst. 1-butyl-3-methylimidazolium hexafluorophosphate ($BmimPF_6$, >99%, Carl ROTH) has been used as the ionic liquid additive.

For a typical synthesis protocol, 5 g of $Ti(O^iPr)_4$ was mixed in 10 g of propan-2-ol, before 0.09 g, 0.49 g or 2.02 g of $BmimPF_6$ ionic liquid was added corresponding to a $BmimPF_6$/Ti molar ratio of 0.03, 0.1 and 0.4 respectively. After stirring for 30 min, a $BmimPF_6$/alcohol two-phase mixture was formed since $BmimPF_6$ is not miscible with neither $Ti(O^iPr)_4$ nor propan-2-ol. Then 6.2 g of 2.2 mol/L acetic acid solution was further added dropwise. A white milky precipitate was formed immediately upon hydrolysis process and the solution was kept under stirring for 1 h, before being further sealed by parafilm and aged at room temperature for 18 h, 72 h and 6 days without any stirring. After filtering the powder from the rest of the solvent, the solid was dried for 2 h at 100 ^oC, than the light yellow powder obtained was washed through 100ml acetonitrile for one night and further with 2 x 50ml distillated water for 10 min, before being dried again for 2 h at 100 ^oC. The white powder so-obtained was finally annealed in air at 550 ^oC for 2 h with a heating rate of 5 ^oC/min, and a white powder was obtained after calcination.

Reagents	Role in the synthesis	Molar ratio to Ti
Titanium (IV) isopropoxide (TTIP)	Ti precursor	-
Propan-2-ol	Organic solvent	9.6
Distilled H_2O	Hydrolysis	20
Acetic acid (HAc)	Acidic catalyst	1
$BmimPF_6$	Ionic liquid additive	0.03, 0.1, or 0.4

Table 6: Reagents used in the room temperature ionic liquid-assisted sol-gel route for synthesizing TiO_2 nanomaterials

For comparison, reference TiO_2 was also synthesized by following the same protocol in absence of any $BmimPF_6$ ionic liquid. A detailed list of TiO_2 nanomaterials as well as the synthesis parameters and the respective reagents quantity used are shown below in Table 6 and Table 7, and in Fig 21. Aeroxide® TiO_2 P25 from Evonik is used as commercial powder reference.

The fixed parameters are the molar ratios of Propan-2-ol, distilled water and acetic acid to Ti at 9.6, 20 and 1, respectively. Also the temperature of calcination is fixed at 550℃. **The variable parameters are the molar ratio of $BmimPF_6$ to Ti (from 0 to 0.4) and the aging time (from 18 h to 6 days).**

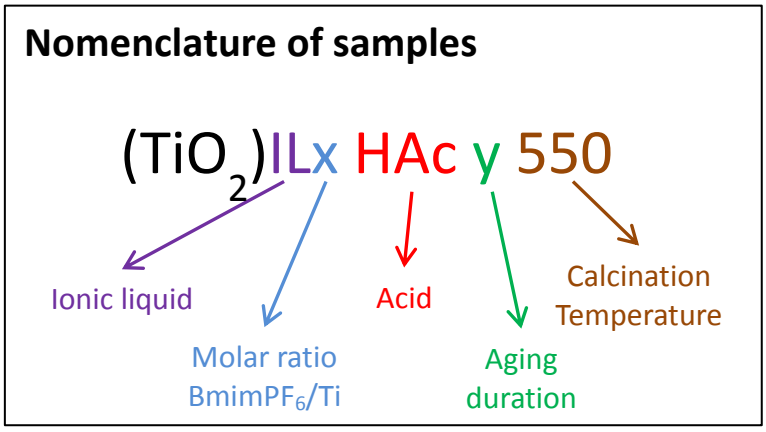

Fig 21: Nomenclature of TiO_2 samples synthesized by $BmimPF_6$ ionic liquid assisted sol-gel route. For the samples before calcination, no calcination temperature is added.

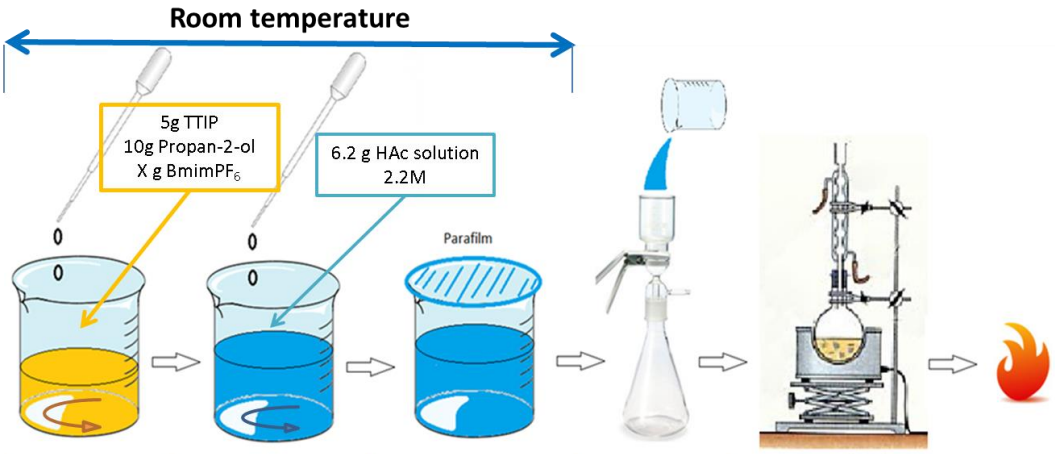

	1	2	3	4	5	6
Steps	Preparation of precursor solution	Hydrolysis	Aging	Solid filtering and drying	Solid washing and drying	Calcination at 550 °C
Duration	30 min	1h	18 h – 6 days	-	-	2h

Fig 22: Schematic view of protocol of the $BmimPF_6$ ionic liquid assisted sol-gel TiO_2 synthesis

Sample name	*$BmimPF_6$/Ti molar ratio*	*Aging duration*	*BET surface area/T-plot surface area (m^2/g)*		*Mean crystallite size (nm)*		*BET-derived calculated particle size (nm)*	
			Dried samples	*Calcined samples*	*Dried samples*	*Calcined samples*	*Dried samples*	*Calcined samples*
P25	-	-	-	55	-	22[a]		
IL0 HAc 6d	0	6 days	286/312	50/44	6	19	5	31
IL0.03 HAc 18h	0.03	18 h	294/283	110/107		10		14
IL0.03 HAc 72h	0.03	72 h	238/208	104/107		10		15
IL0.03 HAc 6d	0.03	6 days	251/250	97/100	8	11	6	16
IL0.1 HAc 18h	0.1	18 h		101/96		10		15
IL0.1 HAc 72h	0.1	72 h	242/298	113/136		10		14
IL0.1 HAc 6d	0.1	6 days		109/127	8	10		14
IL0.4 HAc 18h	0.4	18 h	273/268	118/214		7		13
IL0.4 HAc 72h	0.4	72 h	266/264	114/231		8		14
IL0.4 HAc 6d	0.4	6 days	237/232	96/190	7	12	7	16

Table 7: BET Specific surface areas, mean crystallite sizes and BET-derived calculated particle size of TiO_2 materials as a function of the $BmimPF_6$/Ti molar ratio (0.03, 0.1, and 0.4), and of the aging duration (18h, 72h and 6 days). The heat treatment temperature of all samples – except the commercial TiO_2 P25 reference – was 550 ^oC.

[a] corresponding to the anatase phase

II.2.1.2. XRD characterizations

The XRD patterns of the different TiO_2 samples are shown in Fig 23 and Fig 24. Their main bulk physico-chemical properties such as the mean crystallite sizes derived from XRD measurements and the specific surface areas are reported in Table 7. XRD patterns show only anatase phase as crystalline phase, with or without addition of BmimPF6, and whether the samples were calcined at 550 ^{o}C or dried at 100 ^{o}C. No rutile phase of TiO_2 was observed. In Fig 23 A, the XRD patterns of the non-calcined sample after 6 days of aging synthesized without $BmimPF_6$ already shows the presence of partially crystallized anatase TiO_2 phase with a small mean crystallite size of 6 nm. However, whatever the $BmimPF_6$/Ti molar ratio, the presence of $BmimPF_6$ somehow favored the crystallization of TiO_2 during the aging step, while the mean crystallite size was not significantly increased, from 6 nm for the BmimPF6-free sample to 7-8 nm when TiO_2 is synthesized in the presence of $BmimPF_6$.

After heat treatment at 550 ^{o}C, the crystallinity of the TiO_2 sample synthesized in the absence of $BmimPF_6$ strongly increased for achieving that of the TiO_2 P25 reference (except the absence of rutile phase), together with a large increase of the mean crystallite size to 19 nm, close to that of 22 nm shown by the anatase phase in TiO_2 P25.

By contrast, and similarly for all $BmimPF_6$/Ti molar ratios, the heat treatment at 550 ^{o}C of samples synthesized in the presence of $BmimPF_6$ and aged for 6 days resulted only in a moderate increase in the mean TiO_2 crystallite size, from 7-8 nm to 10-12 nm, *i.e.* much smaller than in the absence of $BmimPF_6$. The presence of $BmimPF_6$ somehow provided to the materials thermal resistance by hindering the crystal growth during heat treatment. The limitation of the crystal size growth during the $BmimPF_6$ ionic liquid template-based sol-gel synthesis of TiO_2 was already reported, even if no explanation was proposed. [222, 226]

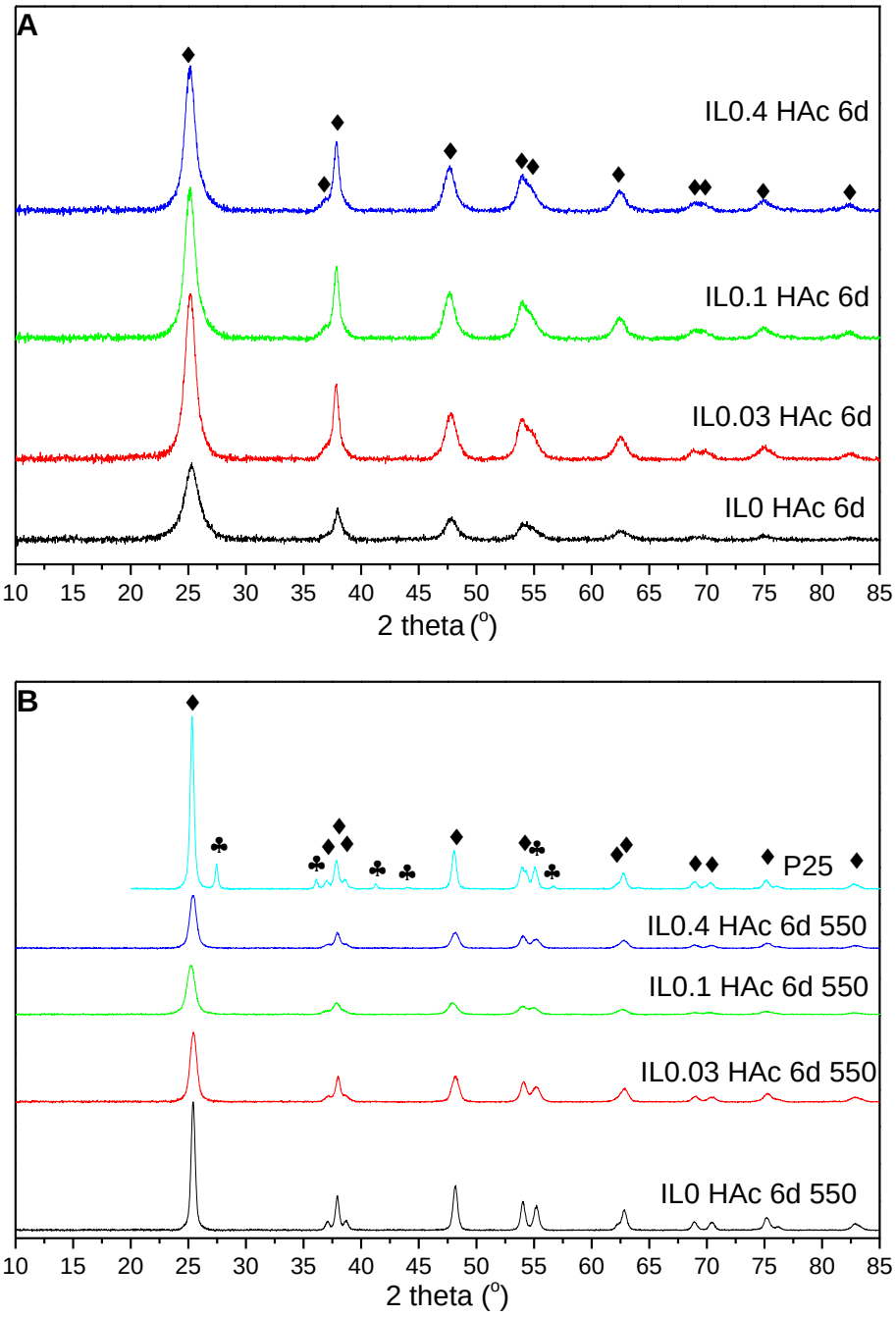

Fig 23: XRD patterns of TiO_2 samples synthesized with a $BmimPF_6$/Ti molar ratio ranging from 0 to 0.4 (down to up) and an aging duration of 6 days (A) after the drying step before calcination and (B) after calcination at 550 ℃. Black diamonds are anatase peaks, black clubs are rutile peaks. (**Influence of the $BmimPF_6$/Ti molar ratio**)

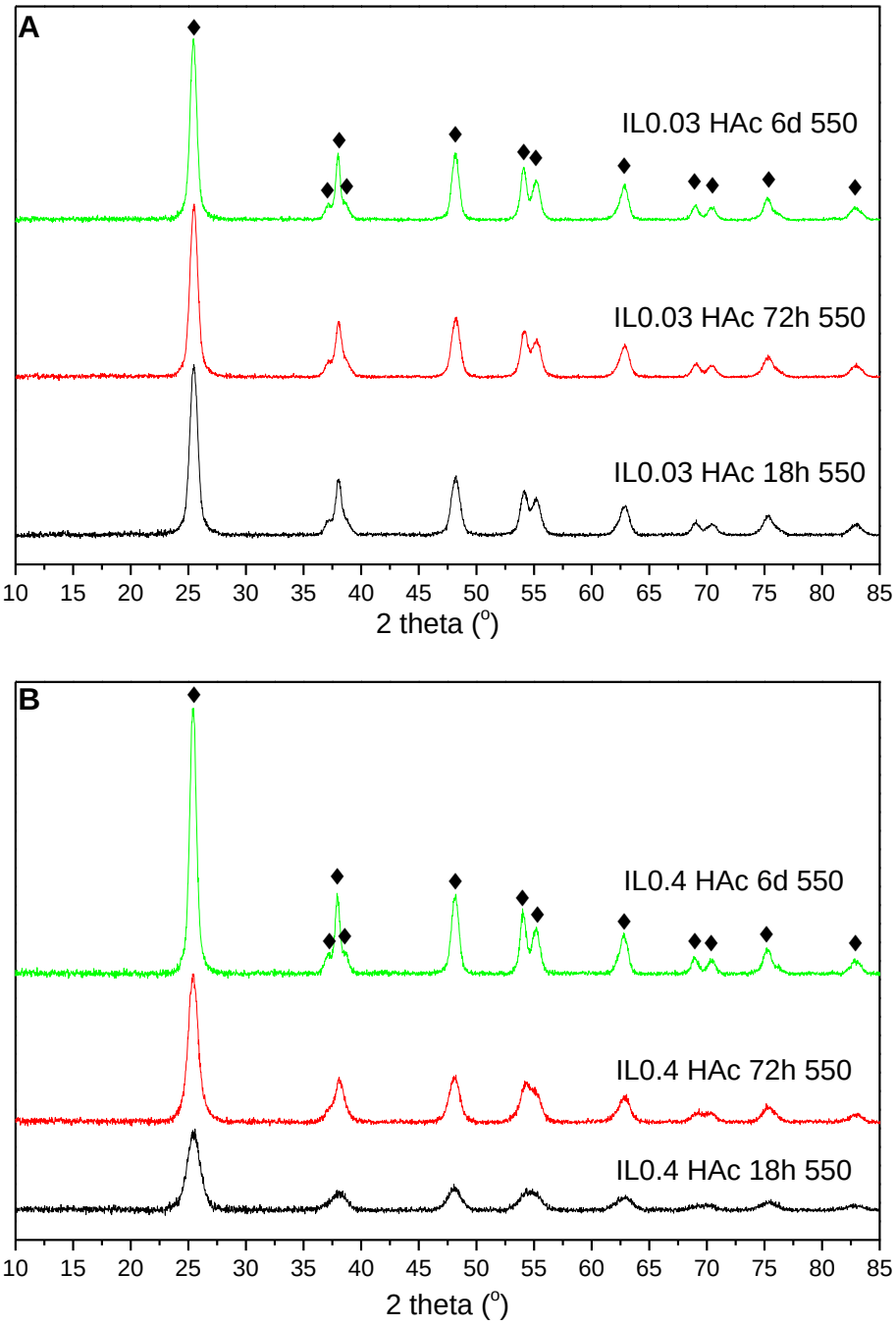

Fig 24: XRD patterns of TiO_2 samples synthesized with a $BmimPF_6$/Ti molar ratio of (A) 0.03, (B) 0.4, for aging durations of 18 h, 72 h and 6 days from down to up. All samples were annealed at 550 ℃. Black diamonds are anatase peaks. (**Influence of the aging duration**)

It was also worth noting that increasing the aging duration did not result after calcination at 550 °C in a significant increase in the mean crystallite size of TiO_2 - estimated at about 10 nm -, except for the highest $BmimPF_6$/Ti molar ratio of 0.4, for which the mean crystallite size increased from 7 nm to 12 nm when the aging duration was extended from 18h to 6 days, together with a gain in crystallinity of the anatase phase (Table 7).

II.2.1.3. Specific surface area and porosity studies

Specific surface areas of TiO_2 samples are reported in Table 7. The dried TiO_2 materials displayed a very high and non-microporous specific surface area within the 237-294 m^2/g range, resulting from a small mean crystallite size. Compared to the reference commercial TiO_2 P25 sample, TiO_2 synthesized in the presence of $BmimPF_6$ displayed after calcination much higher BET specific surface areas along with much smaller crystallite particle size (discussed above). Both parameters are usually reversely linked one to each other, because a higher specific surface area generally resulted from a small particle size, in the case of non-porous materials. [138] After calcination, the specific area of TiO_2 synthesized in the absence of $BmimPF_6$ drastically decreased down to 50 m^2/g, close to that of the TiO_2 P25 reference, as a result from similar mean crystallite sizes. By contrast, when synthesized in the presence of $BmimPF_6$, TiO_2 calcined at 550 ^oC was able to maintain a high specific surface area around 107 ± 7 m^2/g, depending on both the aging duration and the $BmimPF_6$/Ti molar ratio, despite the high temperature of calcination used. **Here, the presence of $BmimPF_6$ seems to be the key factor for controlling the crystallite size and thus the specific areas.**

Calculated particle size of TiO_2 samples derived from BET results are also reported in Table 7. The results show a good general variation tendency between IL-free and IL-TiO_2 samples, but with slightly larger values compared to mean crystallite sizes derived from XRD characterizations, probably due to the non-spherical form of the crystallites along/or with the existence of grain boundary.

Fig 25 shows the influence of the $BmimPF_6$/Ti molar ratio, the aging duration and the calcination step on the N_2 sorption isotherms and the pore size distribution of the TiO_2 materials. Whatever the TiO_2 sample, mainly type-IV isotherms were observed, and the hysteresis observed was a fingerprint of the presence of mesopores within the materials, resulting from the anticipated capillary condensation in mesopores after multi-molecular multilayer adsorption. [235] This differs from the isotherm obtained on the non-porous TiO_2 P25. The comparison between both BET and t-plot specific surface areas of TiO_2 samples (Table 7) confirmed that the TiO_2 samples are not microporous. For dried TiO_2 materials, in the absence of $BmimPF_6$ during the sol-gel synthesis, the isotherm exhibited a H_3-type hysteresis, characteristic of materials with no well-defined mesoporosity, consisting of aggregates or agglomerates of particles forming slit shaped pores with non-uniform size and/or shape. By

contrast, when $BmimPF_6$ was used, H_2-type of hysteresis was observed, corresponding to interconnected mesopores, with non-uniform size or shape.

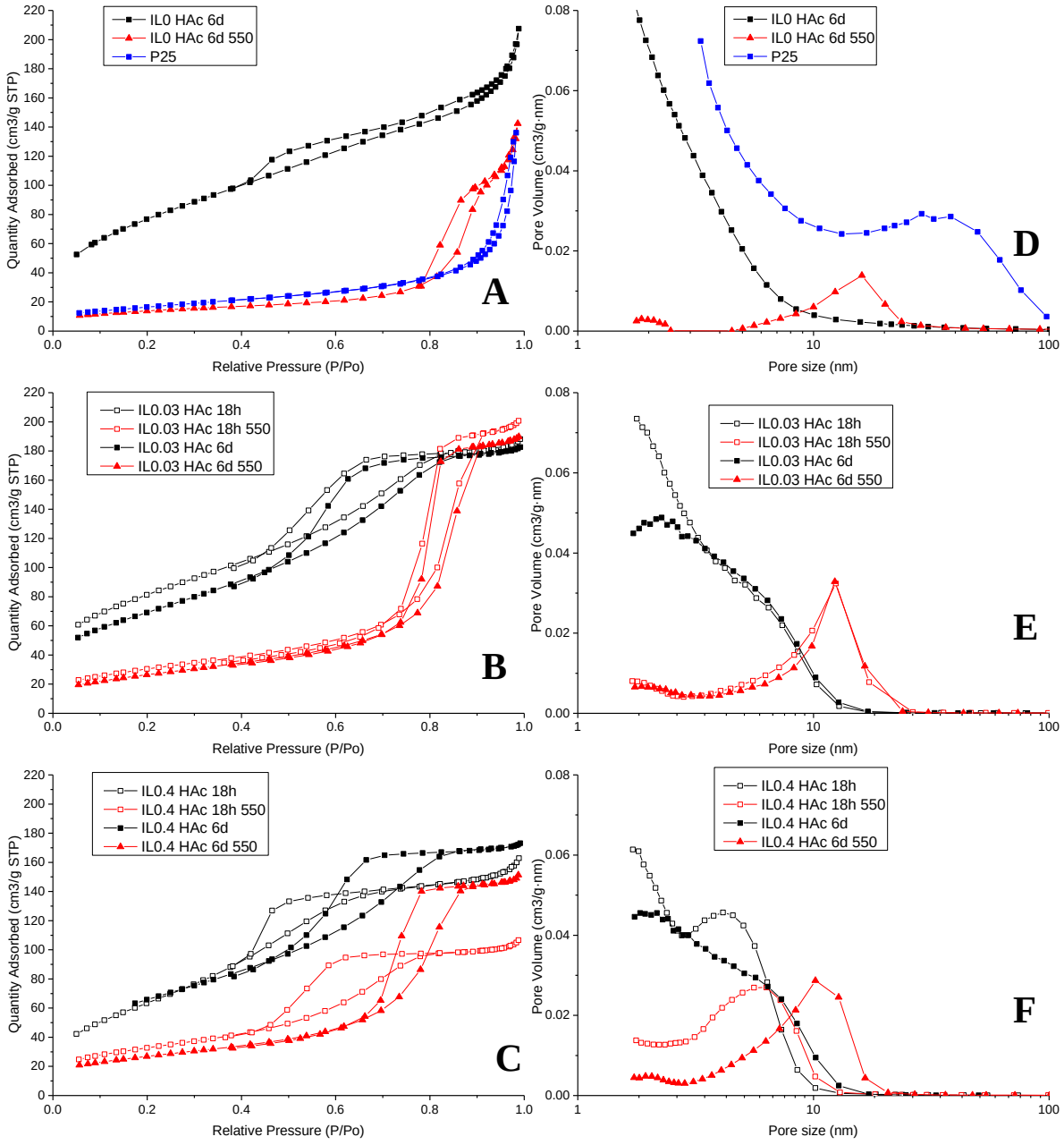

Fig 25: N_2 adsorption/desorption isotherms and pore size distribution of dried and calcined TiO_2 materials synthesized with aging durations ranging from 18 h to 6 days, (A, D) without $BmimPF_6$, (B, E) with a $BmimPF_6$/Ti ratio of 0.03, and (C, F) with a $BmimPF_6$/Ti ratio of 0.4. Influence of the aging duration is reported. Aeroxide TiO_2 P25 is shown as reference in (A, D).

The influence of the aging duration on the kind of mesopores was not significant at the lowest $BmimPF_6$/Ti molar ratio, while this parameter was impacting towards slightly larger size mesopores at the highest $BmimPF_6$/Ti molar ratio.

In the absence of $BmimPF_6$, the calcination treatment at 550 ^oC resulted in the appearance of a H_1-type contribution within the isotherm hysteresis, corresponding to the formation of more uniform and larger mesopores with a monomodal distribution centered on about 15 nm. In the presence of $BmimPF_6$, the H_2-type hysteresis was mainly turned into a H_1-type hysteresis, with a monomodal pore size distribution centered on about 10 nm whatever the $BmimPF_6$/Ti molar ratio. However, this change during the calcination step was delayed when the highest $BmimPF_6$/Ti molar ratio was used, 6 days of aging duration being necessary instead of already 18 h at the lowest $BmimPF_6$/Ti molar ratio. The monomodal mean pore size was shifted from 5 nm to 10 nm with increasing aging duration from 18 h to 6 days.

Fig 26 details the influence of the $BmimPF_6$/Ti ratio during the aging period, on the adsorption/desorption isotherm patterns. No influence was observed as a function of the aging duration for a low $BmimPF_6$/Ti ratio of 0.03, whereas a longer aging duration of 6 days was necessary for achieving a similar sorption pattern after calcination at 550 ^oC, in agreement with the evolution of pore size distributions of both TiO_2 materials. This confirmed the important role played by $BmimPF_6$ ionic liquid during the synthesis and aging.

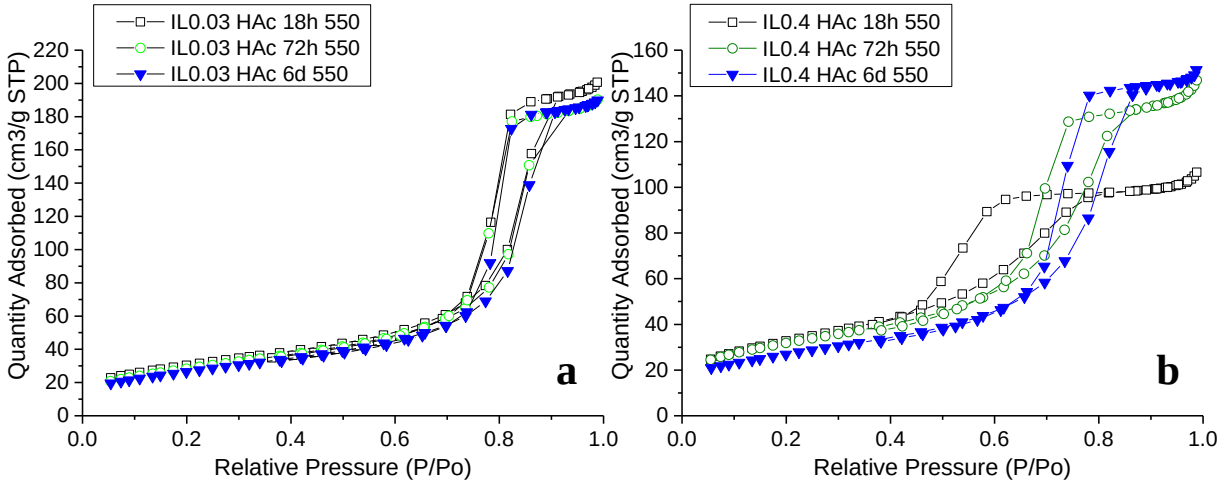

Fig 26: N_2 sorption isotherm plots as a function of the aging time. The TiO_2 samples were synthesized by using a $BmimPF_6$/Ti ratio of 0.03 (a) and 0.4 (b) and were annealed at 550^oC.

Combined with XRD and specific surface area results, both evolution of isotherm plot shapes and pore size distributions evidenced that the usage of $BmimPF_6$ provides to TiO_2 more thermal resistance against high temperature, preventing successfully a brutal TiO_2 crystal growth during heat treatment. The detailed self-crystallization mechanism influenced by $BmimPF_6$, and the role of $BmimPF_6$ in the limitation of the TiO_2 crystal size growth and the resistance to heat treatment will be described in further chapters.

II.2.1.4. TEM characterization

Fig 27 shows TEM images of TiO_2 samples synthesized with a $BmimPF_6$/Ti ratio of 0.03 and 0.4, as well as of TiO_2 sample synthesized in the absence of ionic liquid, in both cases with an aging duration of 6 days and calcination at 550 ^oC, and TiO_2 P25.

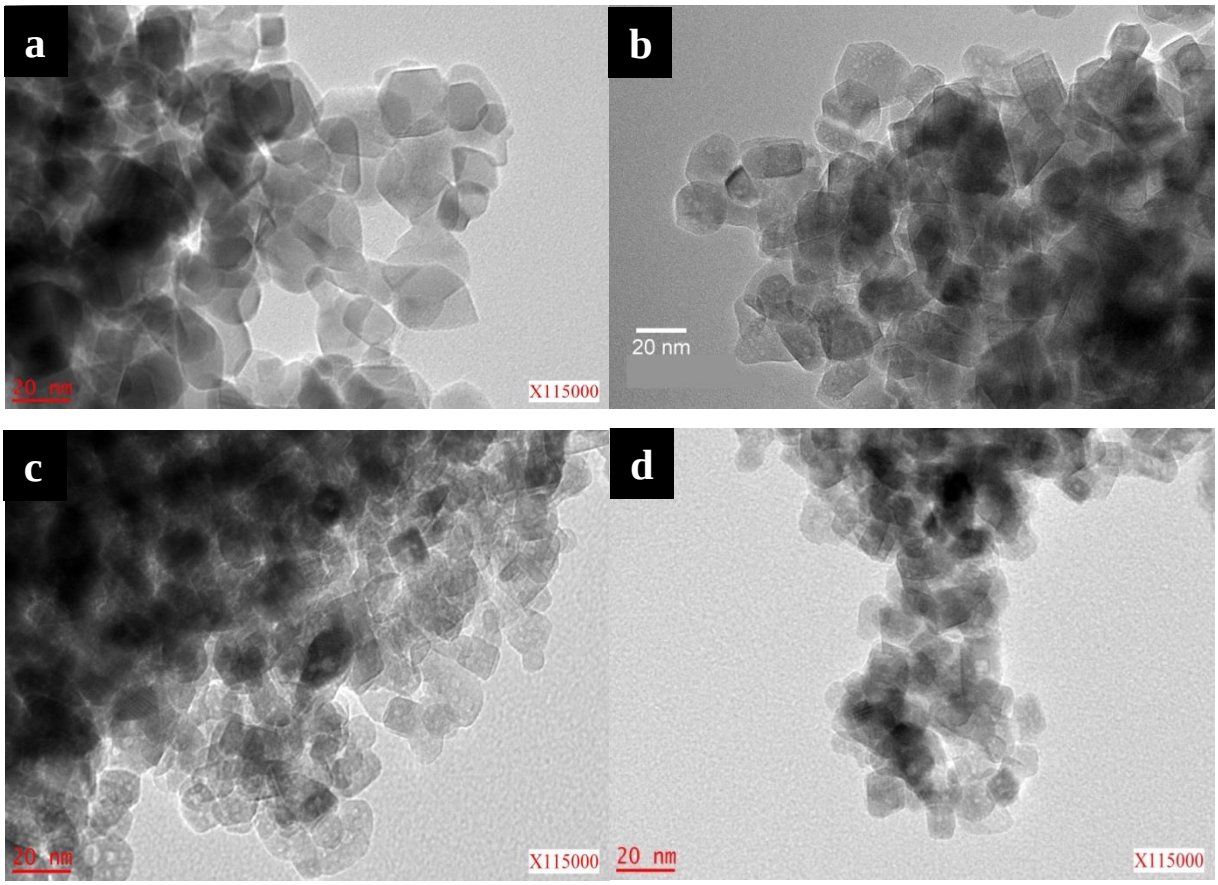

Fig 27: TEM images of TiO_2 P25 (a) and TiO_2 samples aged for 6 days and annealed at 550^0C. The $BmimPF_6$/Ti ratio was 0 (b), 0.03 (c), 0.4 (d).

TiO_2 P25 shows average particle size of about 20-25 nm. The mean crystal size of the $BmimPF_6$-free sample is around 20 nm as well, with a moderately homogeneous distribution (e.g. particles larger than 35nm being observed). By contrast, both TiO_2 samples prepared with $BmimPF_6$ (Fig 27 B, C) present a smaller average crystal size (14 nm and 12 nm for a $BmimPF_6$/Ti ratio of 0.03 and 0.4, respectively) with a more homogeneous distribution (no particle smaller than 11 nm or larger than 25 nm being observed) than TiO_2 prepared without $BmimPF_6$ (Fig 27 A), in agreement with the above XRD calculation. The crystal size distribution heterogeneity of the $BmimPF_6$-free sample could result from a fast crystal growth during calcination step.

In addition to the obtention of a small crystallite size, the use of $BmimPF_6$ also led to a unique shape evolution with the aging time. Taking as example, the IL 0.03 series, from 18h to 6 days of aging (Fig 28), the shape turned from the round-like shape to more square-like and faceted shape. The change in shape with the aging time was not accompanied with an increase in the mean crystallite size, which stayed constant at 13 nm, whatever the aging time, in agreement with XRD. This shape change could be due to the better crystallinity achieved after a longer aging step (confirmed in Fig 24 A), or due to the capping ability of fluoride ions either from simple fluoride salts [219, 241] or from fluorine-containing ionic liquid during the synthesis. [227] In Zhao and co-workers' work, the use of fluorine-containing additives (fluoride salts or BF_4-based ionic liquid) caused a shape change for TiO_2 crystals. They concluded that the increased square-like facet was {001} plan of anatase. The increase of area for that facet was caused by preferential adsorption of fluoride ions on {001} facet during the synthesis which lowers the surface energy thus favors the growth of this facet during crystallization over other facets, and especially over the thermodynamically stable {101} facet when fluorine-free condition is applied. Since the only source of fluoride ions in ours synthesis is the hexafluorophosphate anion of $BmimPF_6$, we will study and discuss in the further chapters the role of $BmimPF_6$ during the synthesis, involved in the aging duration-dependent crystal growth.

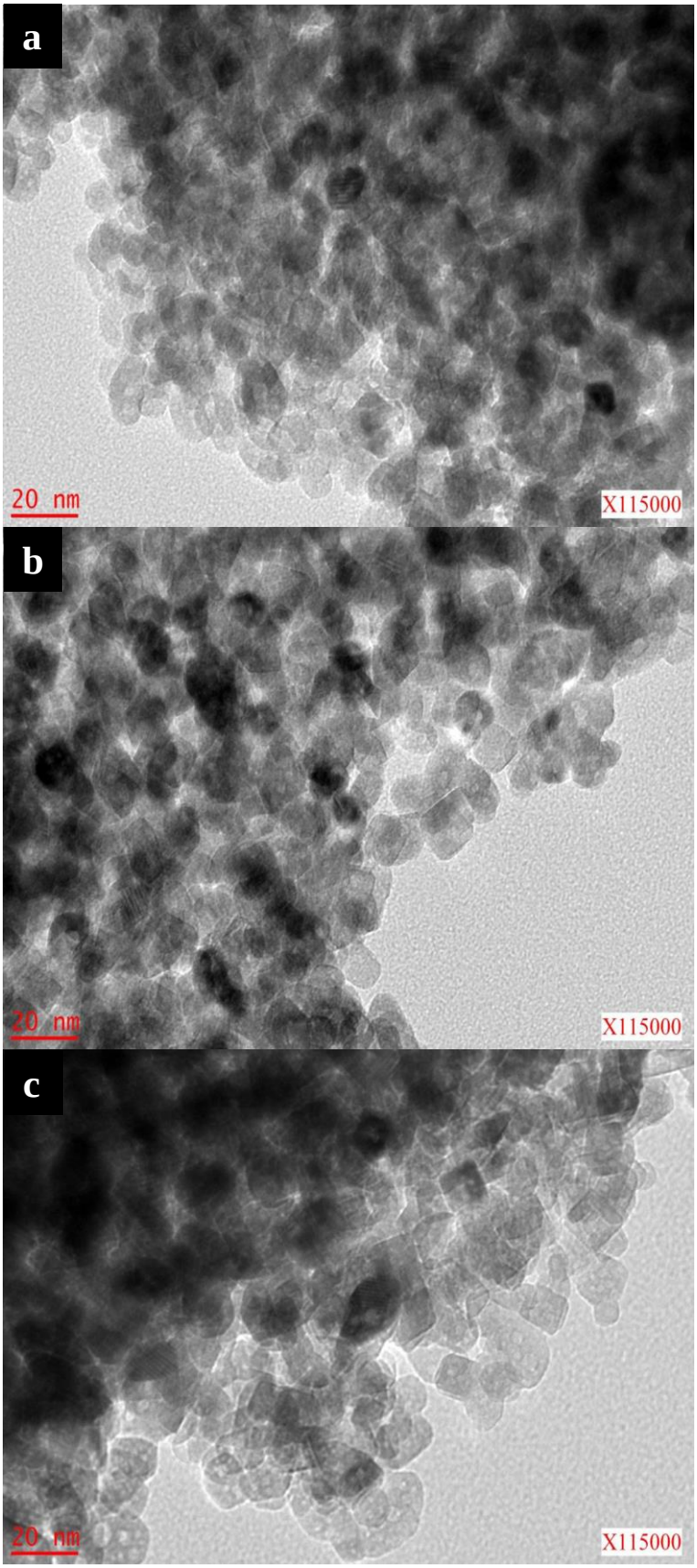

Fig 28: TEM images of TiO_2 samples synthesized with a $BmimPF_6$/Ti ratio of 0.03 and annealed at 550^0C. The aging duration was (a) 18h, (b) 72h, (c) 6 days.

II.2.1.5. XPS analysis

Fig 29 shows the high-resolution XPS spectra of Ti_{2p}, O_{1s} and P_{2p} recorded on dried TiO_2 samples with different $BmimPF_6$/Ti ratios of 0 (a), 0.03 (b) and 0.4 (c) used in the sol-gel synthesis. Table 8 shows binding energies for the different contributions assigned.

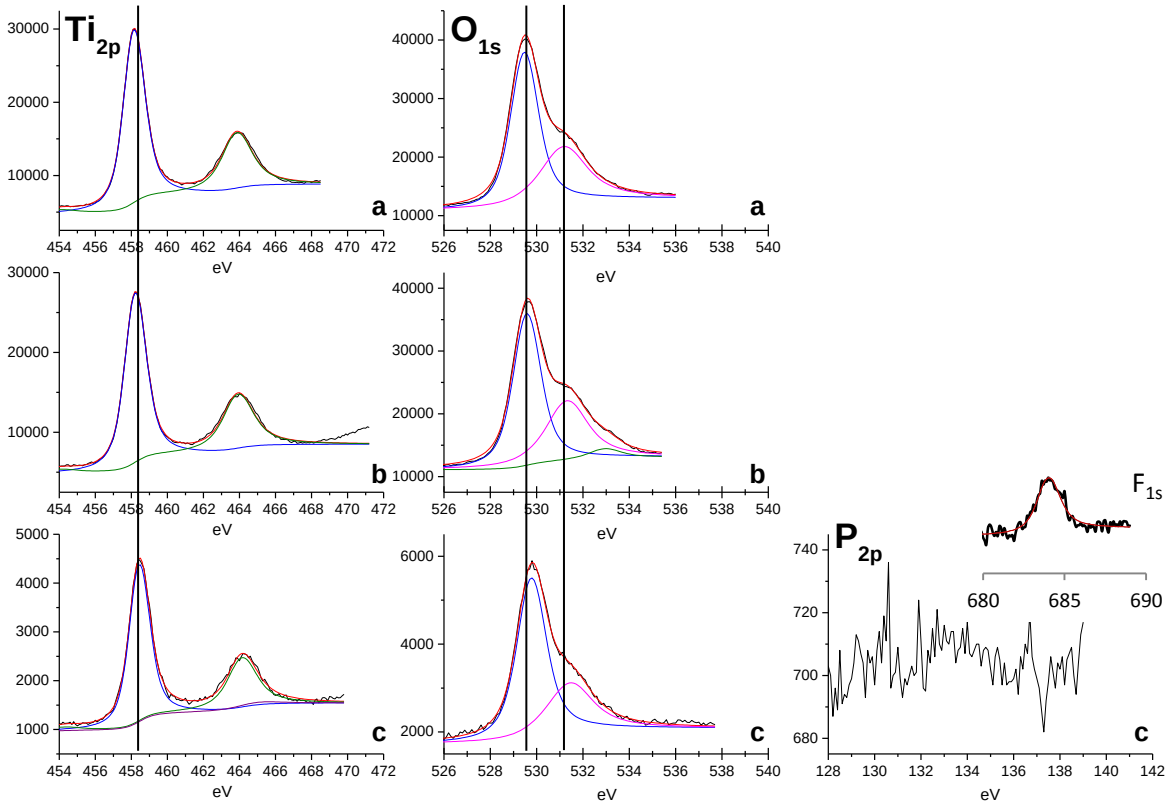

Fig 29: Ti_{2p}, O_{1s} and P_{2p} XPS patterns of **dried TiO_2 samples** with different $BmimPF_6$/Ti ratio in the sol-gel synthesis: 0 (a), 0.03 (b) and 0.4 (c). The acid used was HAc and the aging duration was fixed at 6 days.

Sample name	***Orbitals***		***Contributions***	***Binding energy (eV)***	
IL0 HAc 6d	$Ti_{2p\ 3/2}$	$Ti_{2p\ 1/2}$	Ti-O-Ti	458.0	463.7
	O_{1s}		O-Ti	529.2	
			O-H	531.2	
IL0.03 HAc 6d	$Ti_{2p\ 3/2}$	$Ti_{2p\ 1/2}$	Ti-O-Ti	458.3	464.0
	O_{1s}		O-Ti	529.4	
			O-H	531.1	
			H_2O abs	532.7	
IL0.4 HAc 6d	$Ti_{2p\ 3/2}$	$Ti_{2p\ 1/2}$	Ti-O-Ti	458.5	464.2
	O_{1s}		O-Ti	529.5	
			O-H	531.2	

Table 8: XPS binding energies for the Ti_{2p} and O_{1s} orbitals and the different contributions assigned for **dried TiO_2 samples** with different $BmimPF_6$/Ti ratios from 0 to 0.4 used in the sol-gel synthesis. The acid used was HAc and the aging duration was fixed at 6 days.

The Ti_{2p} region patterns show the typical $Ti_{2p}3/2$-$Ti_{2p}1/2$ doublets, with a spin-orbit coupling constant of 5.7 eV, with $Ti_{2p}3/2$ peaks at 458.0 eV (a), 458.3 eV (b) and 458.5 eV (c) and at 463.7 eV (a), 464.0 eV (b), 464.2 eV (c) for $Ti_{2p}1/2$ orbitals, respectively. They can be assigned to Ti^{4+} (Ti-O) in an octahedral coordination with oxygen in typical TiO_2 crystalline structure. For IL-based TiO_2 samples, no higher energy contribution was observed. This differs from Yu *et al.* who attributed a higher energy peak (at 459.7 eV with Δ = + 0.8 eV) to Ti^{4+} in a tetrahedral environment, as a result of the presence of phosphorus in TiO_2 samples. [242, 213]

The O_{1s} region patterns show a typical spectra with TiO_2 lattice O^{2-} in O-Ti bond at 529.2 eV (a), 529.4 eV (b) and 529.5 eV (c), and oxygen from O-H bond in surface hydroxyl group at 531.2 eV (a), 531.1 eV (b) and 531.2 eV (c). A very small contribution assigned to adsorbed water was observed at 532.7 eV on the IL0.03 HAc 6d sample, at the accuracy limit of the analyses.

The P_{2p} spectra did not evidence the presence of any phosphorus contributions even for a high $BmimPF_6$/Ti molar ratio of 0.4 (c).

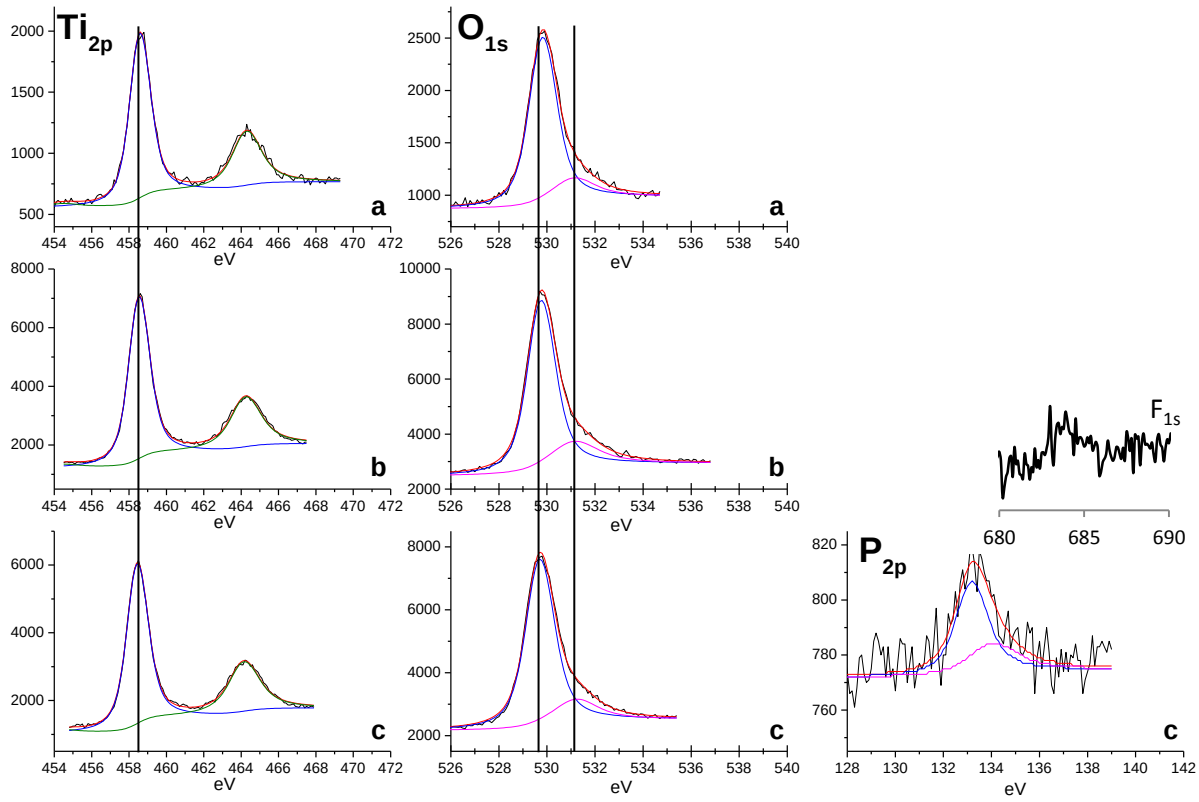

Fig 30: Ti_{2p}, O_{1s} and P_{2p} XPS patterns of **calcined TiO_2 samples** with different $BmimPF_6$/Ti ratio in the sol-gel synthesis: 0 (a), 0.03 (b) and 0.4 (c). The acid used was HAc and the aging duration was fixed at 6 days. All samples were annealed at 550^0C.

Sample name	*Orbitals*		*Contributions*	*Binding energy (eV)*	
IL0 HAc 6d 550	$Ti_{2p\ 3/2}$	$Ti_{2p\ 1/2}$	Ti-O-Ti	458.7	464.3
	O_{1s}		O-Ti	529.6	
			O-H	530.9	
IL0.03 HAc 6d 550	$Ti_{2p\ 3/2}$	$Ti_{2p\ 1/2}$	Ti-O-Ti	458.6	464.3
	O_{1s}		O-Ti	529.5	
			O-H	530.9	
IL0.4 HAc 6d 550	$Ti_{2p\ 3/2}$	$Ti_{2p\ 1/2}$	Ti-O-Ti	458.5	464.2
	O_{1s}		O-Ti	529.5	
			O-H	531.0	
	$P_{2p\ 3/2}$	$P_{2p\ 1/2}$	P-O-P	132.9	133.8

Table 9: XPS binding energies for the Ti_{2p}, O_{1s} and P_{2p} orbitals and the different contributions assigned for **calcined TiO_2 samples** with different $BmimPF_6$/Ti ratios from 0 to 0.4 used in the sol-gel synthesis. The acid used was HAc and the aging duration was fixed at 6 days.

Fig 30 shows the XPS spectra of Ti_{2p}, O_{1s} and P_{2p} orbitals regions recorded on the same samples after washing and calcination at 550 ^{o}C (IL0 HAc 6d 550, IL0.03 HAc 6d 550 and IL0.4 HAc 6d 550). The binding energies of the different contributions are shown in Table 9.

On calcined samples, the Ti_{2p} spectra also evidenced a single contribution for the doublet at 458.7 and 464.3 eV (a), 458.6 and 464.3 eV (b), 458.5 and 464.2 eV (c), whether $BmimPF_6$ was used or not in the sol-gel synthesis. Ti^{4+}-O centers in octahedral environment could be observed, with no evidence after calcination of a higher energy contribution that could be attributed to Ti-O-P bonds.

Similarly, the O_{1s} spectra shows the usual contribution for O-Ti from lattice TiO_2 and O-H surface groups at 529.6 and 530.9 eV (a), 529.5 and 530.9 eV (b), 529.5 and 531.0 eV (c), respectively, whether $BmimPF_6$ was used or not. Compared to uncalcined samples, the OH content was strongly reduced after calcination, in agreement with the decrease in surface area and the enhancement of crystallinity.

No phosphorus contribution was observed on the P_{2p} spectra for a $BmimPF_6$/Ti ratio of 0.03. By contrast, the P_{2p} spectra of IL0.4 HAc 6d 550 sample evidenced unambiguously the presence of phosphorous, with a $P_{2p}3/2$-$P_{2p}1/2$ doublet at 132.9 and 133.8 eV (with a spin-orbit coupling constant of 0.87 eV), characteristic of phosphorus in a pentavalent oxidation state (P^{5+}), and usually attributed to phosphate groups. [243-245] The P/Ti surface atomic ratio was calculated as 0.06.

So, except the presence of P^{5+} in a phosphate oxidation state (environment) at the surface of IL0.4 HAc 6d 550 sample, no significant difference was observed between uncalcined and calcined TiO_2 samples. We could hypothesize that before calcination, the phosphates species

were finely and widely dispersed within the TiO_2 bulk (matrix), so that its content at the surface remained very low, even at an IL/Ti ratio of 0.4. The calcination could cause partial migration of phosphates towards the surface and resulted in increase of P_{2p} peak's intensity. However, the presence of phosphorous was not observed on the Ti_{2p} spectra, like for the uncalcined samples. Indeed, we could expect the appearance of a Ti-O-P bond contribution at higher binding energy to correlate with the P_{2p} spectra. This resulted probably from the low content of phosphorous in the TiO_2 samples. This could also explain why no O-P contribution could be observed on the O_{1s} spectra.

One can note that trace of residual fluorine has been detected for the IL0.4 HAc 6d sample, with F_{1s} orbital peak at 683.3 eV. This residual content diminished strongly after calcination (Fig 29 and Fig 30 c F_{1s}), with a F/Ti surface atomic ratio decreasing from 0.18 to detection limit level. This may consist of fluorine adsorbed on material surface rather than fluorine incorporated in TiO_2 host as substituent of O^{2-}, for which the F-Ti-O attribution at 688.3 eV was never observed whatever the TiO_2 samples. [246] Calcination at 550 ^oC was thought enough to desorb fluorine from surface of TiO_2. No trace of fluorine was detected for TiO_2 samples synthesized with a lower $BmimPF_6$/Ti ratio of 0.03 even before calcination.

II.2.1.6. Conclusions

We have synthesized TiO_2 materials *via* a $BmimPF_6$ ionic liquid assisted sol-gel route in HAc. The main physico-chemical characterizations performed evidenced that the use of $BmimPF_6$ provided valuable features to the TiO_2 materials compared to $BmimPF_6$-free samples and commercial P25, promising for photocatalytic applications.

The use of $BmimPF_6$ in HAc allowed a faster crystallization of anatase during aging step and inhibited the growth of crystallites, for maintaining a high specific surface area and small size anatase crystallites after calcination.

After calcination, we evidenced the presence of phosphorus at the surface of TiO_2 sample (IL/Ti ratio of 0.4), as P^{5+} species (phosphate centers), originated from $BmimPF_6$. So, **we hypothesize that the chemical species originated from $BmimPF_6$ during the $BmimPF_6$ assisted TiO_2 sol-gel synthesis, are playing a crucial role.** Additional experiments have been conducted in the next sub-chapters for demonstrating more of the role of $BmimPF_6$.

II.2.2. $BmimPF_6$ assisted sol-gel synthesis of TiO_2 using HCl as acid catalyst

We have suspected the role played by phosphorus in $BmimPF_6$ during the synthesis of TiO_2 nanomaterials. Therefore, we have carried out new routes of synthesis for getting more information on the role of phosphorous.

Firstly we have changed the acid catalyst used in synthesis from acetic acid (HAc) to hydrochloric acid (HCl). We believe that the coordination ability of HAc [195] to hydrolyzed titanium precursor limits the interaction between Ti and other species such as phosphate, so that the formation of Ti-O-P bonds could be hardly observed. By contrast, HCl is not believed to coordinate to Ti centers, and could allow titanium atoms to liberate their coordination sites for other elements, so that the presence of phosphate bound to Ti could be more easily evidenced.

II.2.2.1. Sample preparation

All reagents were similar to those used in the synthesis with acetic acid (HAc), except the replacement of acetic acid by HCl (ACS reagent, 37%, Sigma-Aldrich). Neither the molar ratios between reagents nor the main experimental protocol were changed. The substitution of HAc by HCl was performed for TiO_2 synthesized with $BmimPF_6$/Ti ratio of 0.03 and 0.4, aging duration of 6 days and a calcination temperature of 550 ^oC. Fig 32 and Table 9 summarized the nomenclature of TiO_2 samples.

Reagents	Role in the synthesis	Molar ratio to Ti
Titanium (IV) isopropoxide (TTIP)	Ti precursor	-
Propan-2-ol	Organic solvent	9.6
Distilled H_2O	Hydrolysis	20
Hydrochloric acid (HAc)	Acidic catalyst	1
$BmimPF_6$	Ionic liquid additive	0.03, or 0.4

Table 10: Reagents used in the room temperature ionic liquid-assisted sol-gel route for synthesizing TiO_2 nanomaterials using HCl as acid catalyst.

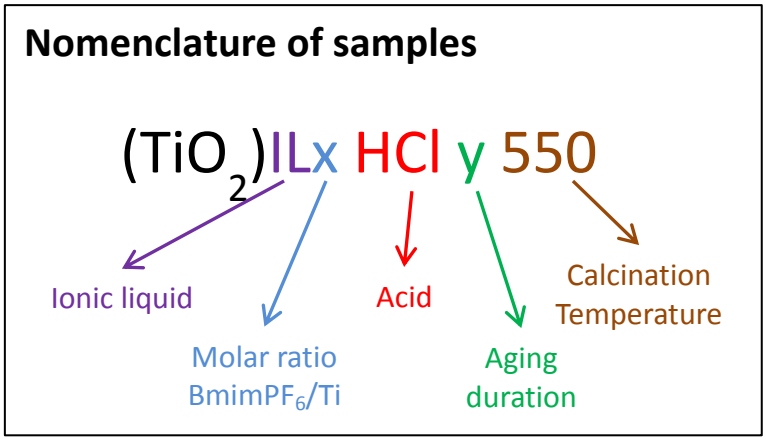

Fig 31: Nomenclature ofl TiO_2 samples synthesized by $BmimPF_6$ ionic liquid assisted sol-gel route using HCl as acid catalyst (compared to the previous synthesis, "HAc" is changed to "HCl"). For the samples before calcination, no calcination temperature is added.

Sample name	*$BmimPF_6$/Ti molar ratio*	*Aging duration*
IL0 HCl 6d 550	0	6 days
IL0.03 HCl 6d 550	0.03	6 days
IL0.4 HCl 6d 550	0.4	6 days

Fig 32: Synthetic view of names and synthesis parameters of the TiO_2 samples synthesized by $BmimPF_6$ ionic liquid assisted sol-gel route using HCl as acid catalyst instead of HAc.

Although the synthesis protocol was not changed when shifting from HAc to HCl, the visual aspect of the course of the reaction was different. In $BmimPF_6$ assisted sol-gel synthesis using HAc, a white precipitate was formed immediately after water was added into TTIP/isopropanol mixture, and after 6 days of aging, the mass of the solid precipitate after drying at 100 ^oC corresponded to a good yield of synthesis to TiO_2 (more than 90%). By contrast, in $BmimPF_6$ assisted sol-gel synthesis using HCl, the precipitation was not visible directly after the addition of water, but after several hours of aging (eg. overnight). After 6 days of aging, a thin layer of sedimentation of a white precipitate was formed at the bottom of the synthesis beaker, below a volume of clear supernatant. The sedimentation part was weighed after being filtered and dried at 100 ^oC and the mass of obtained solid corresponded only to less than 25 % of the theoretical TiO_2 weight. So we hypothesized that the majority of Ti remained in the clear supernatant. And eventually the majority part of solid was indeed obtained by drying the supernatant at 100 ^oC. This behavior was observed for all TiO_2 samples in the case of a $BmimPF_6$ assisted sol-gel synthesis using HCl as acid catalyst.

II.2.2.2. XRD characterizations

The phase separation in $BmimPF_6$ assisted sol-gel synthesis using HCl as acid catalyst could cause different nature of materials formed in each phase. Thus XRD characterization has been performed on both sedimentation part and supernatant part, of dry TiO_2 samples and TiO_2 samples calcined at 550 ^oC in the case of IL0 HCl 6d (Fig 33), as well as with IL/Ti ratio of 0.03 and 0.4 (Fig 34, Fig 35).

The sedimentation part of solid showed only rutile phase before calcination and nearly all rutile phase after calcination at 550 ^oC. We are not sure about the origin of this slight portion of anatase in the calcined sample, since rutile is not expected to transform into anatase during thermal treatment of 550 ^oC [247]. It could result from the crystallization into anatase TiO_2 of amorphous oxide or hydroxide. So basically we can say that only rutile was found in the sedimentation part of the IL0 HCl 6d sample before and after calcination. By contrast, the solid dried from the clear supernatant part showed much different crystallographic evolution. Pure anatase as crystalline phase was obtained from drying the clear supernatant at 100 ^oC, and a typical anatase to rutile phase transition was observed after calcination at 550 ^oC resulting in an anatase/rutile mixed phase TiO_2 (with rutile as main phase).

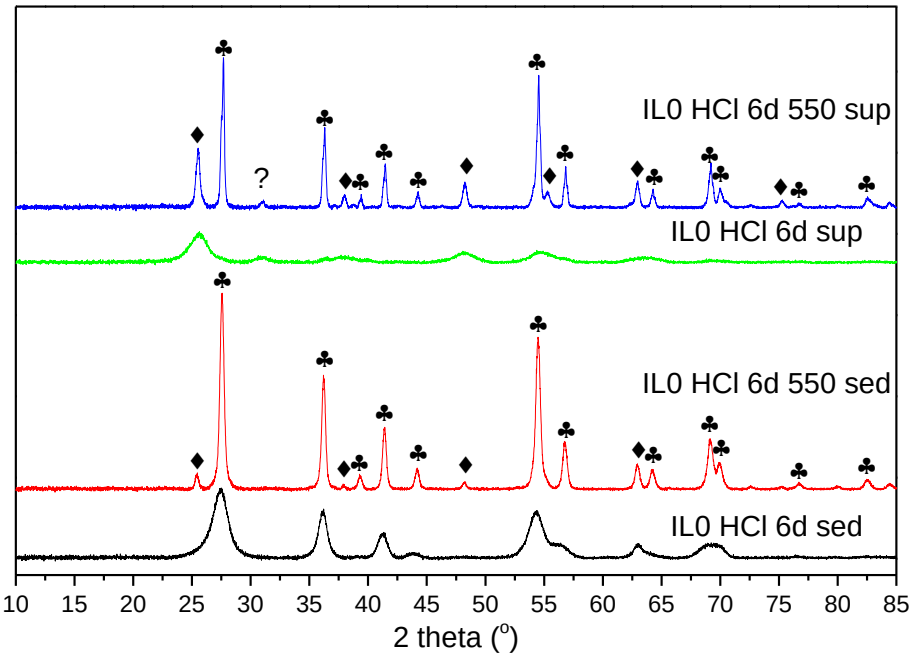

Fig 33: XRD patterns of TiO_2 IL0 HCl 6d samples. Sedimentation part of IL0 HCl 6d sample before calcination (black) and after calcination at 550 ^oC (red). Supernatant part of IL0 HCl 6d sample before calcination (green) and the one after calcination at 550 ^oC (blue). Black diamonds are anatase peaks, black clubs are rutile peaks.

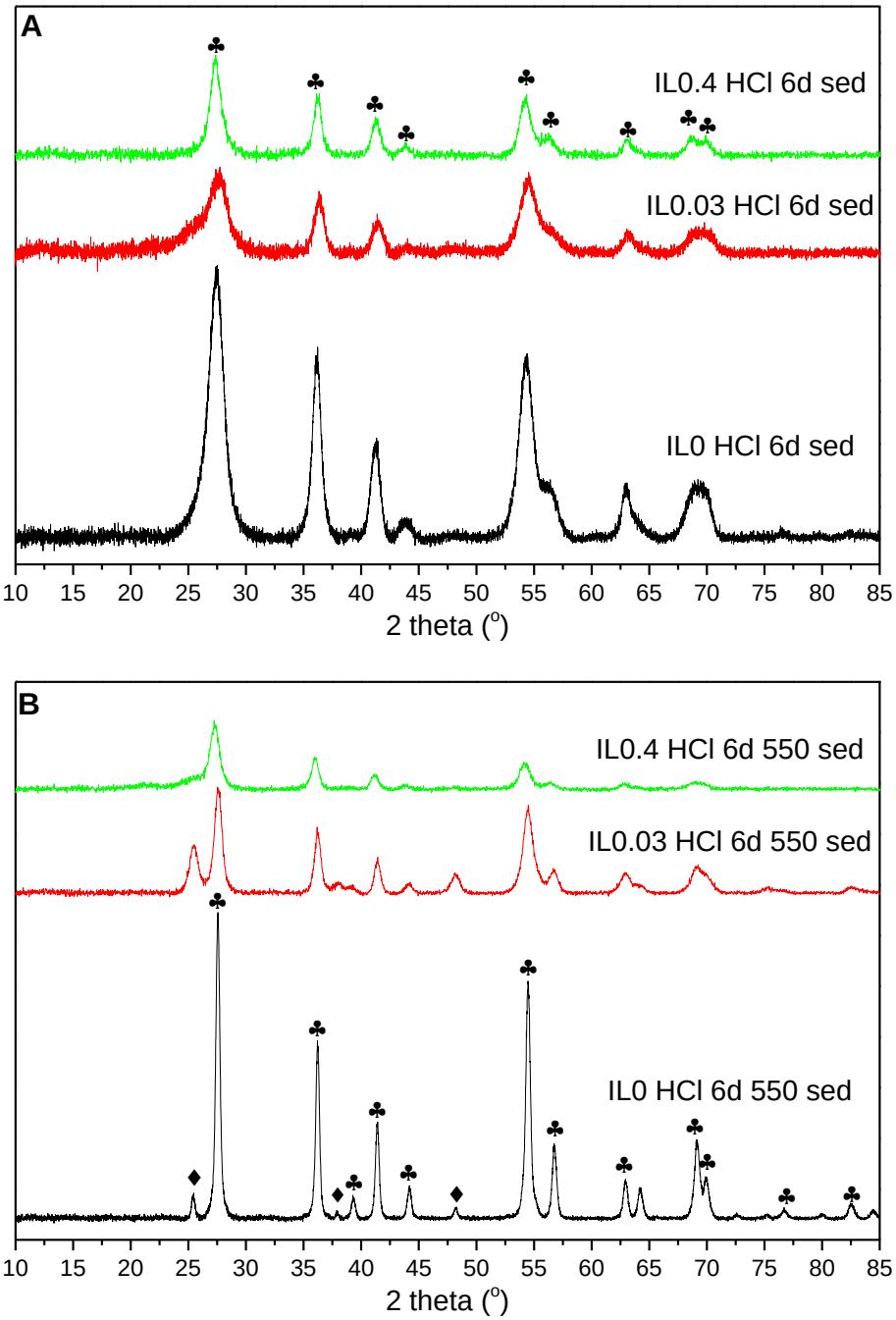

Fig 34: XRD patterns obtained from the sedimentation part of IL0 HCl 6d (black), IL0.03 HCl 6d (red), and IL0.4 HCl 6d (green) TiO_2 samples, before calcination (A) and after calcination at 550 °C (B). Black diamonds are anatase peaks, black clubs are rutile peaks.

Fig 34 (sedimentation part) and Fig 35 (supernatant part) show the influence of the use of $BmimPF_6$ ionic liquid on the XRD patterns of TiO_2 synthesized with HCl. The sedimentation part of all samples showed pure rutile phase before calcination (Fig 34 A), except some anatase contamination, and sharper rutile peaks were observed after calcination (Fig 34 B). In sedimentation part of the sample, the presence of $BmimPF_6$ did not favor the formation of anatase before or after calcination, although it did limit particle size growth of

rutile and provided to the rutile crystals thermal-resistance against high temperature calcination. Indeed the increase in the $BmimPF_6$/Ti ratio allowed to strongly reduce the rutile crystallite growth during the calcination. Calcination did not change the mean rutile crystallite size for IL0.4 sample (at 8 nm), while it moderately increased from 5 nm to 11 nm for IL0.03 sample, compared to a strong increase from 5 nm to 21 nm in the absence of $BmimPF_6$ (Table 11).

Sample name	***Anatase/Rutile ratio***	***Anatase mean crystallite size (nm)***	***Rutile mean crystallite size (nm)***
IL0 HCl 6d sed	0/100	-	5
IL0.03 HCl 6d sed *	0/100 *	- *	5 *
IL0.4 HCl 6d sed	0/100	-	8
IL0 HCl 6d 550 sed	7/93	23	21
IL0.03 HCl 6d 550 sed	35/65	10	11
IL0.4 HCl 6d 550 sed *	0/100 *	- *	8 *

Table 11: Anatase/rutile ratio and their respective mean crystallite sizes from the sedimentation part of IL0 HCl 6d, IL0.03 HCl 6d, and IL0.4 HCl 6d TiO_2 samples, before and after calcination at 550 ℃.
* The presence of anatase TiO_2 can be detected, but not quantified, so that the calculations on rutile TiO_2 are only approximate.

By contrast, the XRD patterns of Fig 35 for the solid obtained by drying the clear supernatant part (except IL0.4 HCl 6d sup) show the influence of $BmimPF_6$ on the nature and the mean size of TiO_2 crystallites. Especially in Fig 35 B, no more rutile has been obtained and anatase is the only crystallized phase obtained after calcination at 550 ^oC when $BmimPF_6$/HCl is used, and the increase of the anatase mean crystallite size during calcination was inhibited (Table 12). Furthermore, this effect was more pronounced in $BmimPF_6$/HCl assisted TiO_2 synthesis than in $BmimPF_6$/HAc assisted TiO_2 synthesis. The peak at about $2\theta = 32^o$ for the supernatant part of IL0 HCl 6d sample correspond to neither anatase nor to rutile phase, thus was unidentified.

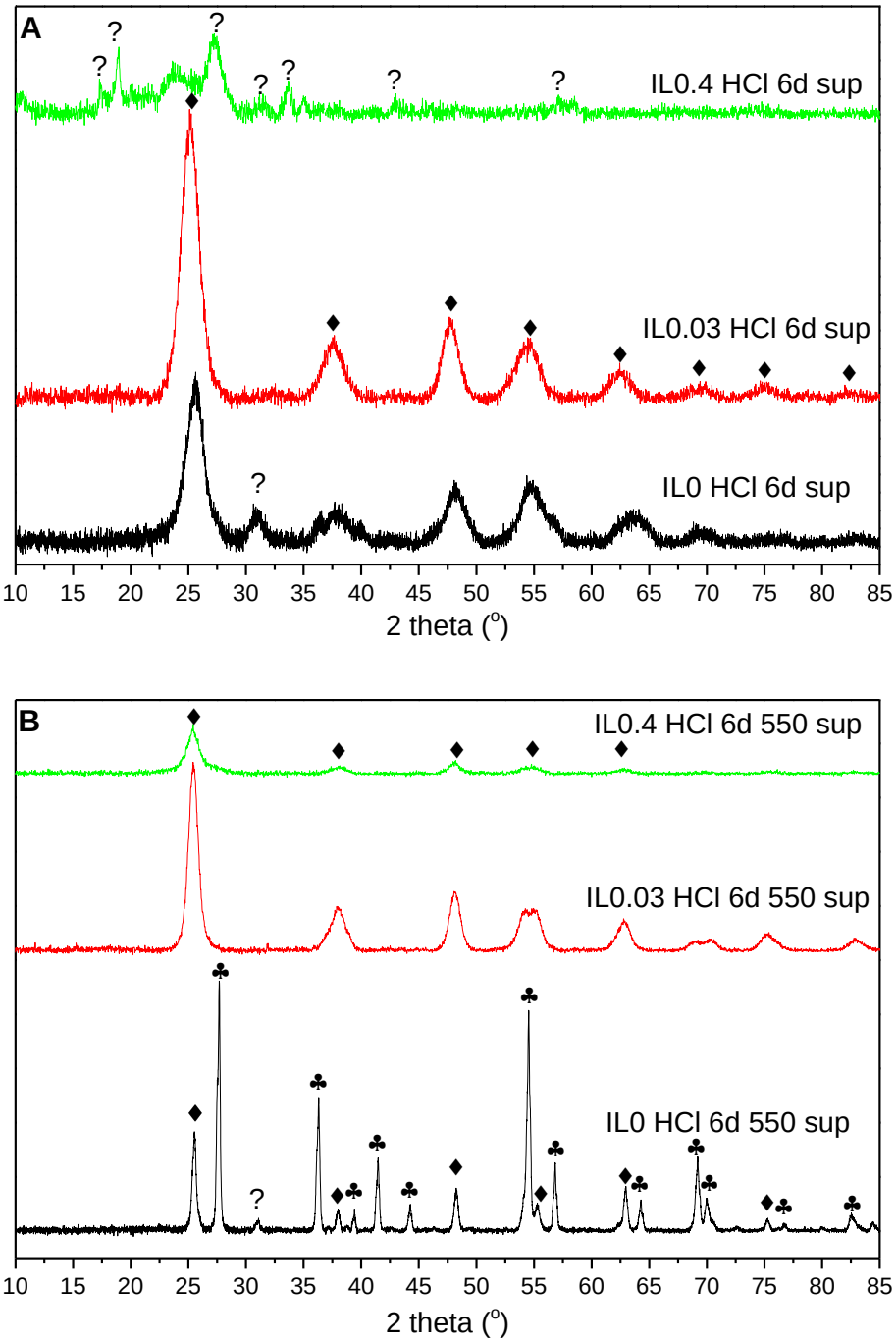

Fig 35: XRD patterns obtained from drying the clear supernatant part of IL0 HCl 6d (black), IL0.03 HCl 6d (red), and IL0.4 HCl 6d (green) samples before calcination (A), and after calcination at 550 °C (B).Black diamonds are anatase peaks, black clubs are rutile peaks. The rest of the peaks have not been identified yet.

Further, the presence of phosphorus in TiO_2 samples synthesized with $BmimPF_6$ in HCl has been finally evidenced by annealing the IL0.4 HCl 6d TiO_2 sample at 800 °C, considering only the clear supernatant part of the sample.

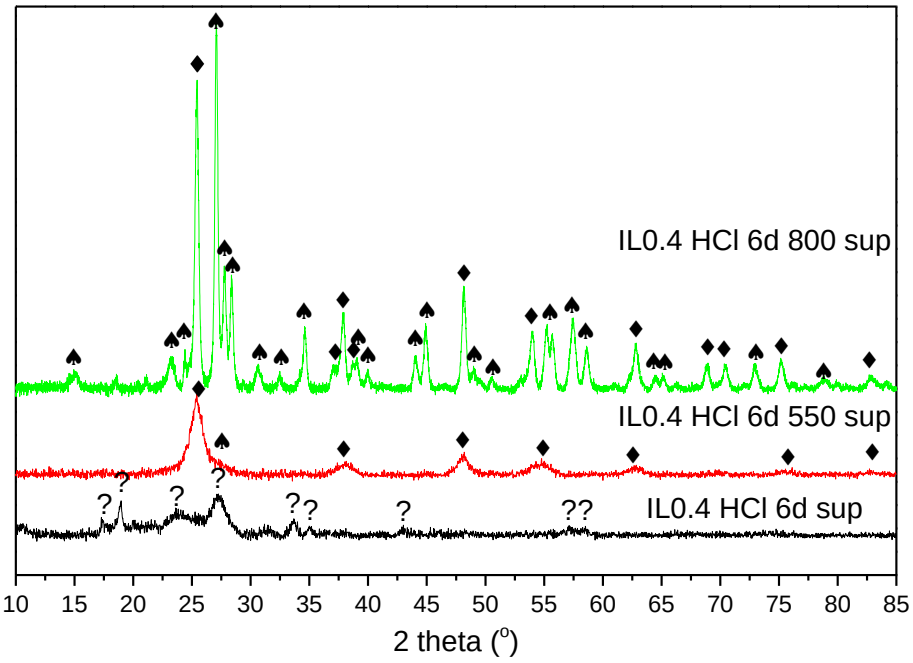

Fig 36: XRD patterns obtained from drying the clear supernatant part of IL0.4 HCl 6d before calcination (black), and after calcination at 550 °C (red) and 800 °C (green). Black diamonds are anatase peak, black spades are $Ti_5O_4(PO_4)_4$ peaks, the rest of peaks has not been identified.

In addition to anatase TiO_2, XRD pattern in Fig 36 (green) shows the appearance of a new crystalline phase, identified as $Ti_5O_4(PO_4)_4$ (Pentatitanium-tetroxide-tetrakis(phosphate), JCPDS 039-0207). This new titanium phosphate phase was probably already present in the sample after calcination at 550 °C, but probably as amorphous phase due to a high crystallization temperature reported to be higher than 650 °C, [248] or as very small-size crystallites. We could hypothesize that the main characteristic peak of this phase at $2\theta = 27.1°$ could be already distinguished at 550 °C (Fig 36 red). In addition, a large quantity of phosphorus (synthesis with $BmimPF_6/Ti = 0.4$) was necessary for evidencing this phosphate phase, even for the HCl assisted synthesis, since the IL0.03 HCl 6d TiO_2 sample did not shown new crystallized phases other than anatase TiO_2 even after annealing at 800 °C (not shown here).

Sample name	*Anatase/Rutile ratio*	*Anatase mean crystallite size (nm)*	*Rutile mean crystallite size (nm)*
IL0 HCl 6d sup	100/0	5	-
IL0.03 HCl 6d sup	100/0	5	-
IL0.4 HCl 6d sup	-	-	-
IL0 HCl 6d 550 sup	38/62	20	26
IL0.03 HCl 6d 550 sup	100/0	8	-
IL0.4 HCl 6d 550 sup	100/0	7	-

Table 12: Anatase/rutile ratio and their respective mean crystallite sizes from drying the clear supernatant part of IL0 HCl 6d, IL0.03 HCl 6d, and IL0.4 HCl 6d TiO_2 samples, before and after calcination at 550 ^oC.

XRD provided us the first evidence of the presence of phosphorus in the bulk of TiO_2 materials synthesized by $BmimPF_6$ assisted sol-gel route in the presence of HCl.

II.2.2.3. TEM characterization

TEM images were taken from the TiO_2 materials after annealing at 550 ^oC, issued from clear supernatant part of IL0.03 HCl 6d sample (Fig 37 a), and of IL0.4 HCl 6d sample (Fig 37 b), as well as from the TiO_2 material after annealing at 550 ^oC, obtained from the sedimentation part of the IL0.03 HCl 6d sample (Fig 37 c), and of IL0.4 HCl 6d 550 sample (Fig 37 d).

The sedimentation parts of TiO_2 samples after calcination present an anisotropic morphology, with large characteristic length of about 50 nm compared to the square faceted crystals for $BmimPF_6$/anatase TiO_2 samples synthesized in HAc, with average size around 10 nm. Although it seems interesting that the mechanism involved in the formation and crystallization of these crystals could be related to the presence of $BmimPF_6$, it will not be discussed in this work, because we are not studying special crystallization process of rutile (main phase observed).

The solid dried from the clear supernatant part of the anatase TiO_2 samples after calcination display isotropic and small nanoparticles with a mean particle size of about 8-9 nm for IL0.03 HCl and IL 0.4 HCl samples. The small particle sizes correspond to that calculated by XRD analysis, evidencing the effect of $BmimPF_6$ on the size of crystals, with **an increased resistance towards growth/sintering during calcination**. This confirms the

similarities between both $BmimPF_6$-assisted syntheses in presence of HCl and HAc, and between the resulting TiO_2 materials.

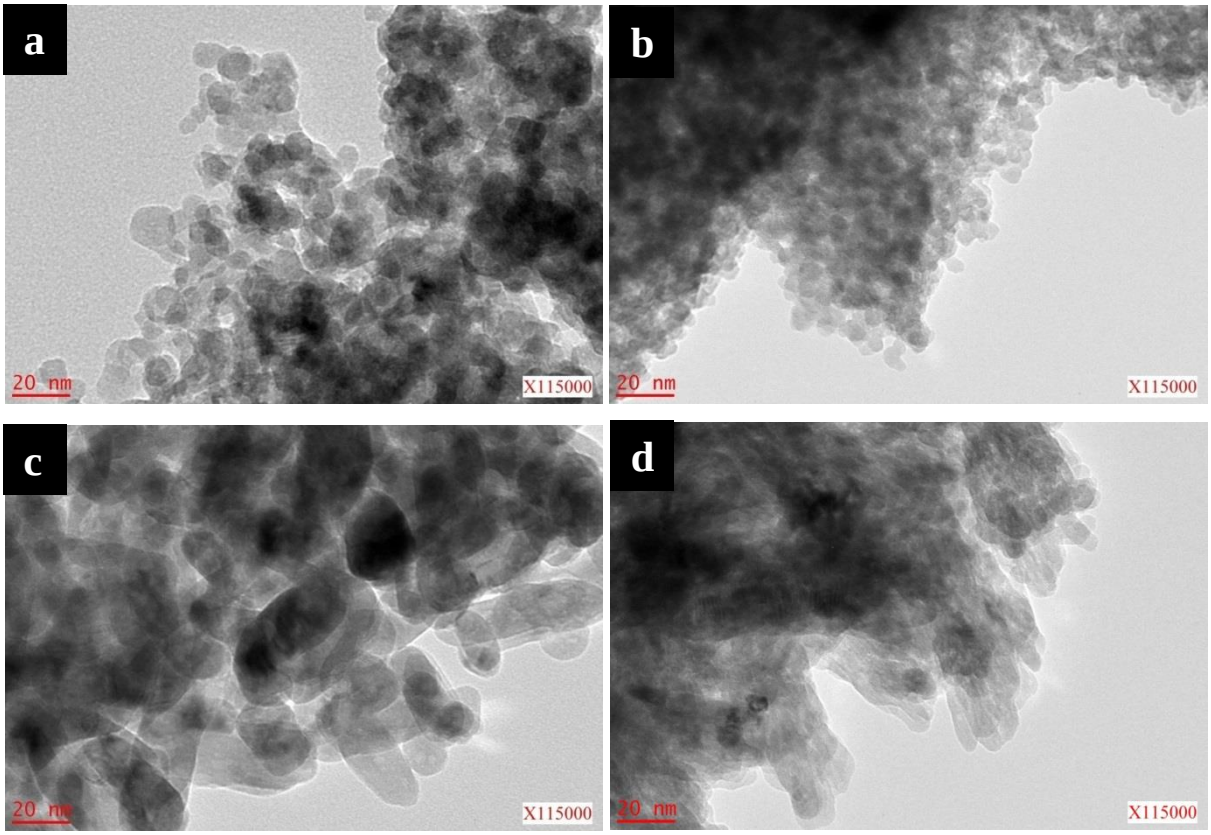

Fig 37: TEM images of TiO_2 materials annealed at 550℃ from clear supernatant part of IL0.03 HCl 6d sample (a), and of IL0.4 HCl 6d sample (b). Also the TiO_2 materials annealed at 550℃ from sedimentation part of the IL0.03 HCl 6d sample (c), and of IL0.4 HCl 6d sample (d).

We know now the crystallographic and morphological differences between the TiO_2 material from clear supernatant part and the sedimentation part of the TiO_2 sample when HCl is used. We have observed that both the sedimentation part and the solid dried from the clear supernatant part were influenced by the use of $BmimPF_6$ in different ways. For the TiO_2 materials from the clear supernatant part in HCl synthesis, the characteristic behavior/properties such as the preferential formation of anatase or the isotropic small-size crystal shape with size growth inhibition during calcination match that of TiO_2 samples synthesized with $BmimPF_6$ when HAc is used. Furthermore, the TiO_2 materials from the clear supernatant part of sample composed the majority (more than 75% of yield) of the total amount of TiO_2. As a consequence, further characterization of TiO_2 materials synthesized with $BmimPF_6$ in HCl will only involve the clear supernatant part, and no more the sedimentation part in the further sections.

II.2.2.4. XPS analysis

In addition to XRD and TEM analyses, XPS characterization has been performed on the solid dried from clear supernatant part of the $BmimPF_6/TiO_2$ samples synthesized with HCl to get more information on the presence of phosphorous inside the samples synthesized with $BmimPF_6$, and its electronic influence on the surface states of the TiO_2 materials.

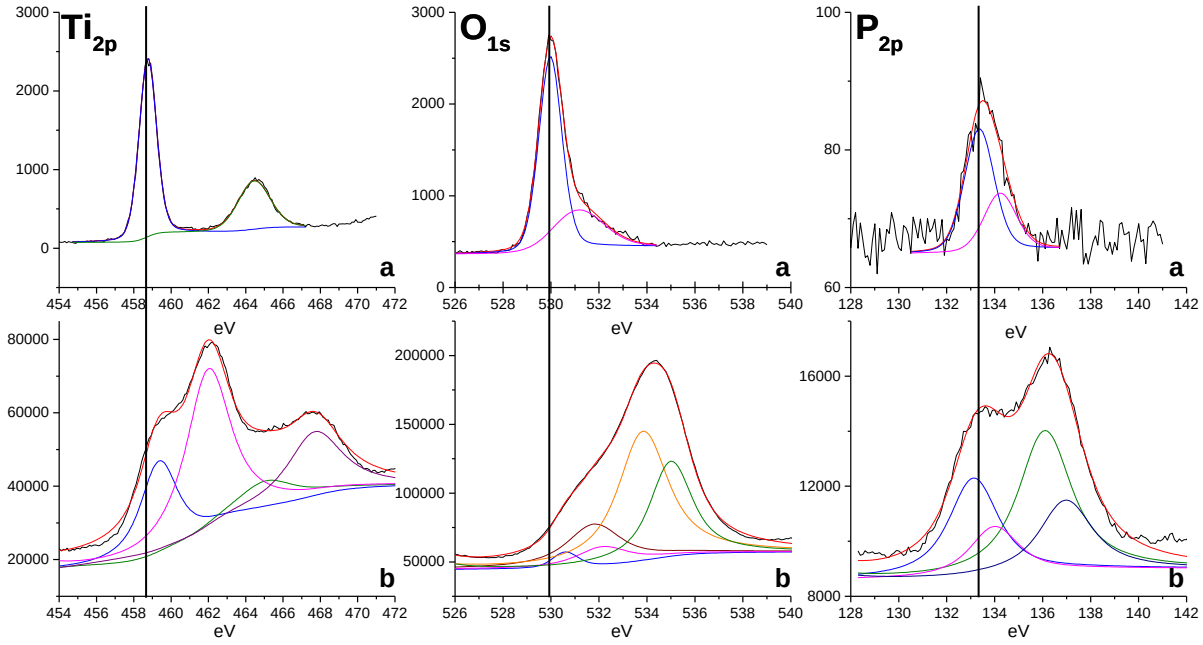

Fig 38: Ti_{2p}, O_{1s} and P_{2p} (from left to right) XPS patterns of two dried $BmimPF_6$/HCl assisted TiO_2 samples with different $BmimPF_6$/Ti ratios used in the sol-gel synthesis. The ratio is 0.03 (a) and 0.4 (b).

Sample name	***Orbitals***		***Contributions***	***Binding energy (eV)***	
IL0.03 HCl 6d	$Ti_{2p\ 3/2}$	$Ti_{2p\ 1/2}$	Ti-O-Ti	458.8	464.5
	O_{1s}		O-Ti	530.0	
			O-H	531.2	
	$P_{2p\ 3/2}$	$P_{2p\ 1/2}$	P-O-P	133.4	134.2
IL0.4 HCl 6d	$Ti_{2p\ 3/2}$	$Ti_{2p\ 1/2}$	Ti-O-Ti	459.4	465.1
	$Ti_{2p\ 3/2}$	$Ti_{2p\ 1/2}$	Ti-O-P	462.0	467.8
	O_{1s}		O-Ti	530.4	
			O-P	531.6	
			O=P	531.9	
			P-O-H	533.6	
			H_2O ads	534.8	
	$P_{2p\ 3/2}$	$P_{2p\ 1/2}$	P-O-P	133.1	134.0
	$P_{2p\ 3/2}$	$P_{2p\ 1/2}$	$(P-O)_n$	136.1	137.0

Table 13: XPS binding energies for the Ti_{2p}, O_{1s} and P_{2p} orbitals and the different contributions assigned for dried TiO_2 samples before calcination with different $BmimPF_6$/Ti ratios from 0.03 to 0.4 used in the sol-gel synthesis. The acid used was HCl and the aging duration was fixed at 6 days.

Fig 38 shows the XPS spectra of Ti_{2p}, O_{1s} and P_{2p} regions recorded on IL0.03 HCL 6d and IL0.4 HCl 6d TiO_2 materials. XPS patterns recorded on $BmimPF_6$-free TiO_2 sample synthesized in HCl is not reported, since they are similar to that shown for ionic liquid-free TiO_2 synthesized with HAc in the previous section. From Fig 38, the IL0.03 HCl 6d TiO_2 sample displays usual patterns of Ti_{2p} and O_{1s} spectra, except that phosphorus with classical peak doublet can be observed in the P_{2p} spectra. At 133.4 eV, the phosphorus exists in a P^{5+} oxidation state assigned to phosphate form which is similar to that recorded for IL0.4 HAc 6d TiO_2 sample ($BmimPF_6$/Ti ratio of 0.4), but with a higher P/Ti surface atomic ratio of 0.1 (already at a low $BmimPF_6$/Ti ratio of 0.03), than the P/Ti surface atomic ratio of 0.06 observed for IL0.4 HAc 6d TiO_2 with $BmimPF_6$/Ti ratio of 0.4. The use of HCl at the place of HAc may favor the contact between titanium ions and phosphate ions in solution during the synthesis, since HAc has been reported to form ligand with metal alkoxides to decrease its reactivity in sol-gel reaction. [195]

When a $BmimPF_6$ ratio of 0.4 is used, the Ti_{2p}, O_{1s} and P_{2p} XPS spectra are strongly more complex. On Ti_{2p} spectrum, the typical octahedral Ti^{4+}-O peak in TiO_2 anatase phase was shifted from 458.8 and 464.5 eV ($Ti_{2p}3/2$ and $Ti_{2p}1/2$) to 459.4 and 465.1 eV ($Ti_{2p}3/2$ and $Ti_{2p}1/2$) as the phosphorous quantity increased from $BmimPF_6$/Ti ratio of 0.03 to 0.4. Also, the full width at half maximum (FWHM) increased strongly from 1.09 to 1.88 eV. These two variations correlated with the work of Korosi *et al.* [213] and that of Han *et al.*, [249] in which they observed both a shift of the Ti^{4+}-O peak towards higher binding energy and a broadened FWHM with increased P concentration for their P-incorporated TiO_2 material synthesized in the presence of H_3PO_4 *via* sol-gel method. We hypothesize that the origin of this shift and this broadening of peak is due to the existence of another Ti^{4+}-O peak at higher binding energy, that we may assign to Ti^{4+}-O in another chemical state influenced by the presence of P. As in none of the work we found studying the XPS spectra of their P-incorporated TiO_2 materials, the authors have decomposed this peak, thus comparison of our results with others would unavailable, as a result we will leave this peak unfitted as other studies did.

In addition, a second peak doublet could be evidenced at 462.0 and 467.8 eV aside with Ti^{4+}-O double peaks. Yu *et al.* attributed a second additional peak to Ti^{4+} in a tetrahedral environment, indicating possible Ti-O-P bonds in titanium phosphate phase. [213] Here we differ from the work of Yu with a major high binding energy Ti-O-P peak being more energy shifted compared to the initial Ti^{4+}-O peak (2.7 eV higher *vs* 0.9 eV), and the additional peak intensity is much greater than that of the Ti^{4+}-O peak. Because of the large difference in

binding energy, we might assign this new contribution to a different Ti-O-P chemical environment where the electron density around Ti atoms is even more strongly polarized towards electron withdrawal phosphates. It may be caused by the higher P concentration involved in our study, since a P/Ti ratio of only 0.1 was used in Yu's work.

Here we hypothesize that two types of P chemical environment exist in the IL0.4 HCl 6d sample. The first consists of dispersed phosphate in TiO_2 environment, which has resulted in higher binding energy shift and broadening of initial Ti^{4+}-O peak in Ti_{2p} spectra. The second consists of a distinguishable titanium phosphate phase from TiO_2, which results from assemblage of large quantity of polymerized phosphate chain with Ti centers. This results in an additional contribution of Ti^{4+} in a tetrahedral environment at a much higher binding energy compared to initial Ti^{4+}-O peak, since the chemical environment of titanium centers in this phase might be strongly modified compared to those in TiO_2. The appearance of this phase might be possible only when high P quantity is involved in the synthesis of TiO_2.

The calculated P/Ti surface atomic ratio was about 0.1 for a $BmimPF_6$/Ti ratio of 0.03 and 0.7 for a $BmimPF_6$/Ti ratio of 0.4, which indicate large coverage of phosphorus. The P_{2p} spectra showed also additional doublet contribution at 136.1 and 137.0 eV (Fig 38 P_{2p} b) beside the contribution corresponding to phosphorus in a pentavalent-oxidation state (P^{5+}), in the P-O bond of usual phosphate group at 133.1 and 134.0 eV. This additional P contribution was rarely described in the literature of P-TiO_2 before, Zhao *et al.* [250] have noticed a new $P_{2p}3/2$ contribution at 134.5 eV for phosphate-treated TiO_2, and have assigned this peak to phosphate species bonded by bidentate form (bi-phosphate). Beside studies on P-TiO_2, works of Gasik [251] and Lyakishev *et al.* [252] have assigned new P_{2p} contributions at even higher binding energy (135.8 eV) to phosphorus within island, ring-shaped and chain-like orthophosphates or diorthophosphate motives (complex polyphosphate like $[P_3O_9]^{3-}$, $[P_2O_7]^{4-}$ and $[P_3O_{10}]^{5-}$) connected to central transition metal atoms, in their cases with manganese. And they have noticed that the relatively high binding energy of the P-metal peak was resulted from the strong transfer of electron density from the phosphorus atom in complex phosphate form, to the 3*d* transition metal central atom.

On the O_{1s} spectra of IL0.4 HCl 6d TiO_2, a broader and more complex O_{1s} peak envelope was observed, with a significant increase of the oxygen amount and a strong high energy shift of the envelope maximum. This may be caused by the increased oxygen quantity brought by the titanium phosphate compound, which correlates with many studies mentioned previously in which H_3PO_4 was used during their sol-gel synthesis of TiO_2. [213, 250, 253] The calculated

O/Ti surface atomic ratio in IL0.4 HCl 6d TiO_2 was more than two times higher than that in TiO_2 synthesized in the absence of $BmimPF_6$ (about 3.4 to 2.0 without considering the contribution from adsorbed H_2O). The O_{1s} spectra showed an obvious asymmetry for the IL0.4 HCl 6d TiO_2 sample (Fig 38 O_{1s} b). The position of O-Ti peak has shifted from 530.0 to 530.4 eV with the increase of the P/Ti ratio from 0.03 to 0.4. Massive new broadened O_{1s} attributions appeared and may result from the influence of P on electron density in TiO_2. [249, 253] The envelop could be decomposed into five contribution peaks, assigned to oxygen participating in O-Ti^{4+} at 530.4 eV, O-P in phosphate at 531.6 eV [213, 249, 253], O=P in phosphate at 531.9 eV, [254] P-O-H in phosphate at 533.6 eV as demonstrated by Lebugle *et al.* [255] and adsorbed H_2O at 534.8 eV. The result of the decomposition is displayed in Table 13. The major contributions correspond to oxygen in phosphates and in adsorbed H_2O in contact with phosphate, O-Ti^{4+} and –OH are now minor contributions at the surface of the sample (even not fitted here for –OH groups since O-Ti^{4+} peak is already very small). Also, the calculated P/Ti surface atomic ratio reaches to 0.8. We can thus assume that TiO_2 is mainly covered by a phosphate phase. This correlates with the energy shift observed for H_2O_{ads}. That corresponds mainly to H_2O adsorbed on phosphates rather than on TiO_2. Although no direct comparison between water adsorption on titanium phosphate and on TiO_2 has been found, it is known that titanium phosphate phase has a similar strong affinity to H_2O comparable to Al-rich aluminosilicates, which adsorb more easily water than pure mesoporous silica, as Bhaumik and Inagaki [256] have observed an type IV high level H_2O vapor adsorption isotherm on their titanium phosphate material, which differs with that of silica.

The large shift is resulted from a strongly modified chemical environment of titanium centers, attributed to the strong electron-withdrawal character of phosphate groups. This pronounced influence could be correlated to the high chemical affinity between titanium centers and phosphate anions. It is known that hydroxyapatite (a form of calcium phosphate phase) can be easily formed on titanium oxide surface in calcium- and phosphate-containing solution without calcination thanks to the strong adsorption ability of calcium and phosphate ions on Ti to generate nucleation sites. [257] In our case, XRD analysis evidenced the formation of complex titanium phosphate phase for a calcination at 650 ^oC when a high P/Ti ratio is used. We hypothesize that the slightly higher binding energy shift and broadening of Ti^{4+}-O peak in Ti_{2p} spectra, and the appearance of a new high energy phosphate-related contribution

in majority in Ti_{2p}, O_{1s} and P_{2p} spectra, resulted from the surface chemical state change induced by the presence of phosphorus in large amount during the TiO_2 synthesis.

Traces of adsorbed fluorine were observed in both TiO_2 samples. But since no F-Ti-O was noticed, the F_{1s} XPS spectra will not be detailed here.

II.2.2.5. Conclusion

The replacement of HAc by HCl allowed to evidence and characterize more clearly the influence of $BmimPF_6$ on the sol-gel synthesis of TiO_2.

XRD and XPS characterization evidenced the presence of phosphorus in TiO_2 samples synthesized in the presence of $BmimPF_6$, even for a low IL/Ti ratio. Even more, we hypothesized the existence for a high IL/Ti ratio of 0.4 a possible titanium phosphate phase in addition to TiO_2. We reported that the presence of phosphorus strongly modified the surface electron environment of titanium centers.

In the next sections, we will study the roles brought in $BmimPF_6$ assisted synthesis by each element in $BmimPF_6$ ($Bmim^+$, F^- and PO_4^{3-}).

II.2.3. Synthesis of TiO_2 using HCl as acid catalyst and BmimCl, HPF_6 and phosphoric acid as replacement of $BmimPF_6$

Investigation on the role of phosphorus in $BmimPF_6$ ionic liquid in sol-gel synthesis of TiO_2 has been performed by replacing the $BmimPF_6$ ionic liquid by single chemical compound providing partially constituent elements of $BmimPF_6$ each.

Protons and chloride anions [258] in moderate concentration or lower are thought to act as simple counter ions in sol-gel synthesis of TiO_2. So the use of BmimCl was to provide to the reaction mixture $Bmim^+$ cations with neither phosphorus nor fluorine, the use of HPF_6 was to provide PF_6 anions with no $Bmim^+$ cations, and that of H_3PO_4 to provide phosphate anions with no $Bmim^+$ cations and fluorides.

II.2.3.1. Sample preparation

Additives for the substitution of $BmimPF_6$ are reported in Table 14. Two additive/Ti molar ratios were used (0.03 and 0.4), the aging duration was fixed at 6 days, the samples were calcined at 550 °C, and neither the other synthesis parameters nor the synthesis protocol were changed.

Replacement additives for $BmimPF_6$	Abbreviation
BmimCl (1-butyl-3-methylimidazolium chloride)	BC
HPF_6 (Hexafluorophosphoric acid)	PF
H_3PO_4 (Phosphoric acid)	PA

Table 14: Replacement additives for $BmimPF_6$ used to study the role of phosphorus in the $BmimPF_6$ assisted sol-gel synthesis of TiO_2

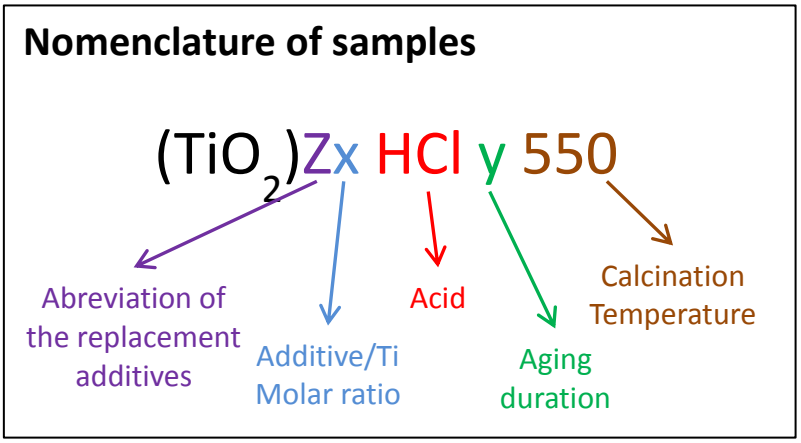

Fig 39: Nomenclature of TiO_2 samples synthesized with the replacement additives for $BmimPF_6$ assisted sol-gel route using HCl as acid catalyst. For the samples before calcination, no calcination temperature is added.

Sample name	*Additive/Ti molar ratio*	*Aging duration*
BC0.03 HCl 6d 550	0.03	6 days
BC0.4 HCl 6d 550	0.4	6 days
PF0.03 HCl 6d 550	0.03	6 days
PF0.4 HCl 6d 550	0.4	6 days
PA0.03 HCl 6d 550	0.03	6 days
PA0.4 HCl 6d 550	0.4	6 days

Table 15: Synthetic view of names and synthesis parameters of the samples synthesized with replacement additives for $BmimPF_6$ assisted sol-gel route using HCl as acid catalyst.

II.2.3.2. XRD characterizations

From visual observation during the BC and PF assisted TiO_2 sol-gel synthesis in HCl medium, we have noted similar phenomena that in the $BmimPF_6$/HCl assisted TiO_2 sol-gel synthesis. Two types of solids were obtained after 6 days of aging, by filtering the sedimentation part of the reaction medium, and by drying the clear supernatant part of the reaction medium. XRD has been run to see the crystallographic information of those samples and the results are shown in the following figures.

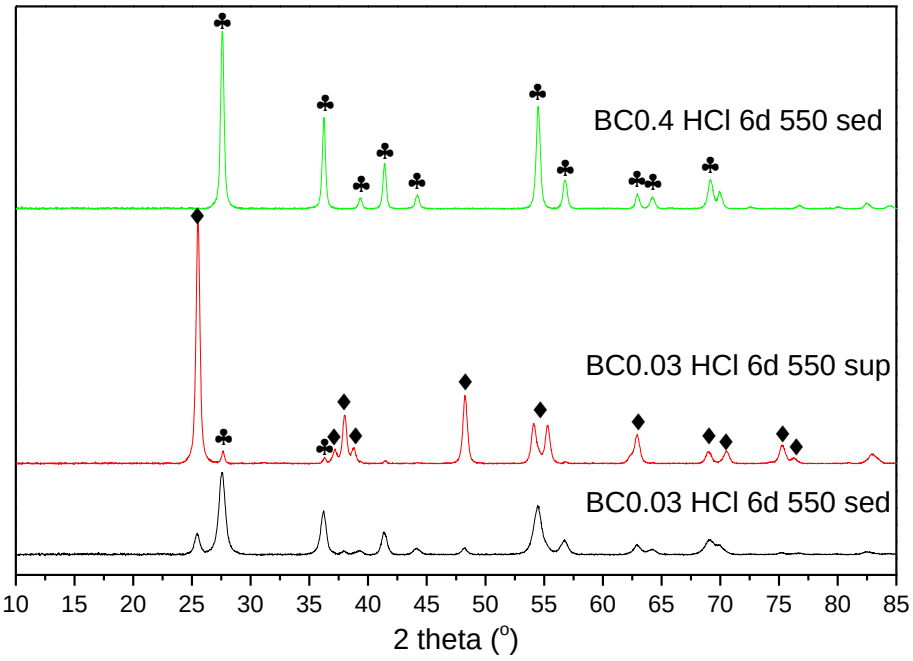

Fig 40: XRD patterns of the solid filtrated from sedimentation part of BC/HCl TiO_2 samples annealed at 550 °C, the BC/Ti ratio is 0.03 (black) and 0.4 (green). Also the XRD pattern of the solid dried from the clear supernatant part of BC/HCl TiO_2 sample is shown as red one, the BC/Ti ratio is 0.03. Black diamonds are anatase peaks, black clubs are rutile peaks.

XRD characterization of the samples **prepared with $Bmim^+$** did not evidence any resistance to crystal growth after calcination in terms of size evolution, in contrary to the samples prepared in HCl with $BmimPF_6$ with the same $Bmim^+$/Ti ratio. From Fig 40 and in Table 16, the mean crystallite size of the BC0.03 HCl 6d 550 sedimentation and supernatant part are 16 nm and 20 nm, respectively (Fig 40 black and red), strongly larger compared to that of the TiO_2 sample synthesized with the same amount of $BmimPF_6$ (Fig 34 B red and Fig 35 B red), at 10 nm and 8 nm, respectively. In addition, BmimCl did not stop completely rutile formation for the solid dried from the supernatant part of BC0.03 HCl 6d 550 sample

(Fig 40 red and Table 16). By contrast, samples prepared with $BmimPF_6$ with the same $Bmim^+$/Ti ratio aged for 6 days and annealed at 550 °C (IL0.03 HCl 6d 550 in Fig 35 B red) did not show any rutile phase.

We could not succeed in obtaining pure solid dried from the clear supernatant part of the BC0.4 HCl 6d 550, probably due to the important quantity of BmimCl that could neither be washed off during washing step nor be completely degraded during calcination. The TiO_2 particles after calcination were encapsulated in yellow rubber-like rigid paste, and were unable to be analyzed.

Sample name	*Anatase/Rutile ratio*	*Anatase mean crystallite size (nm)*	*Rutile mean crystallite size (nm)*
BC0.03 HCl 6d 550 sed	17/83	16	13
BC0.03 HCl 6d 550 sup	96/4	20	28
BC0.4 HCl 6d 550 sed	0/100	-	24

Table 16: Anatase/rutile ratio and their respective mean crystallite sizes for the sedimentation part of BC/HCl TiO_2 samples annealed at 550 °C (BC/Ti ratio of 0.03 and 0.4), and from the clear supernatant part of BC/HCl TiO_2 sample annealed at 550 °C (BC/Ti ratio of 0.03).

Using PF in HCl has provided TiO_2 samples with much more similar characteristics to TiO_2 prepared with $BmimPF_6$, including thermo-resistance and anatase-favored phase stability that can be derived from XRD analysis (Fig 41). Sedimentation part and clear supernatant part of the reaction medium were observed. When the PF/Ti ratio is 0.03, the sample was characterized as small-size anatase crystals with a mean crystallite size of 8 nm (Table 17) as sole crystallized phase for the solid dried from clear supernatant part of sample (Fig 41 red). Also, the sedimentation part of the sample (Fig 41 black) had a higher anatase to rutile ratio of 66/34 than when $BmimPF_6$ is used in HCl with the same $BmimPF_6$/Ti ratio of 0.03 (Table 11, anatase/rutile ratio of 0/100). When the PF/Ti ratio was increased to 0.4, the sedimentation part of the sample consisted in sole anatase phase with a mean crystallite size of 11 nm as crystallized phase (Fig 41 green), and some unique crystal phases were formed for the solid dried from clear supernatant part of reaction medium (Fig 41 blue). We could not identify all the detailed phase composition for this sample, but we could note that this material matches at least with one hydrate titanium hydrogen phosphate compound ($Ti(HPO_4)_2.H_2O$, JCPDS 089-7024) [244] and another titanium phosphate phases (Ti_4P_6O23, JCPDS 039-0004) as well. One can note that the phosphate phase observed here as well as the other(s) different phase(s) differ from the $Ti_5O_4(PO_4)_4$ titanium phosphate phase observed in IL0.4 HCl 6d

sample after annealing at 800 °C (See Fig 36). The mechanism for the formation of this phase is not clear, though it could have something to do with the high concentration of PF in HCl used during the synthesis.

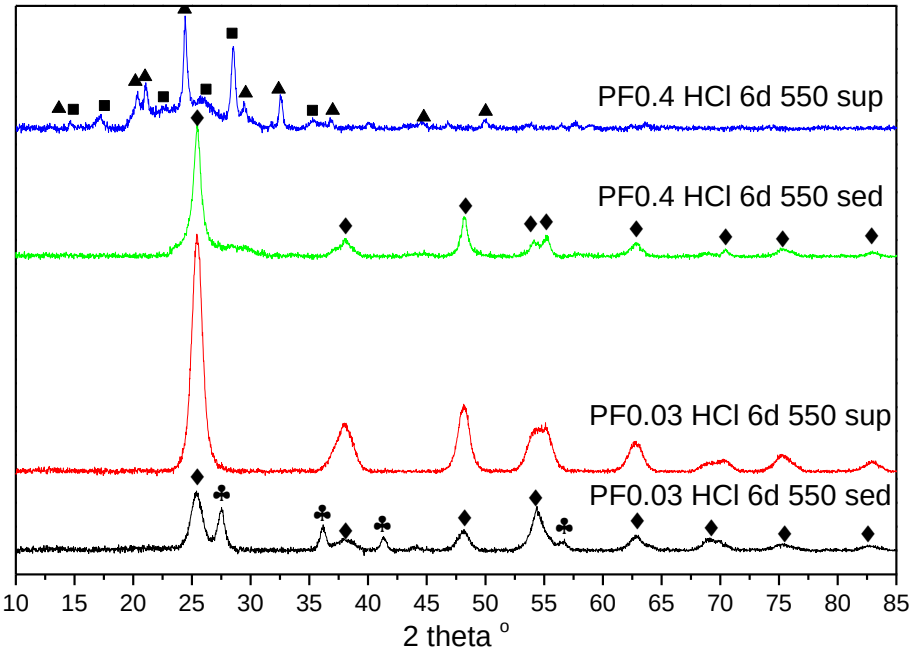

Fig 41: XRD patterns of the solid filtrated from sedimentation part of PF/HCl TiO_2 samples annealed at 550 °C, the PF/Ti ratio is 0.03 (black) and 0.4 (green). Also the XRD patterns of the solid dried from the clear supernatant part of PF/HCl TiO_2 samples annealed at 550 °C are shown, the PF/Ti ratio is 0.03 (red) and 0.4 (blue). Black diamonds are anatase peaks, black clubs are rutile peaks, black triangles are $Ti_4P_6O_{23}$ peaks and black squares are $Ti(PO_4)(H_2PO_4)$ peaks.

Sample name	*Anatase/Rutile ratio*	*Anatase mean crystallite size (nm)*	*Rutile mean crystallite size (nm)*
PF0.03 HCl 6d 550 sed	66/34	8	13
PF0.03 HCl 6d 550 sup	100/0	8	-
PF0.4 HCl 6d 550 sed	100/0	11	-
PF0.4 HCl 6d 550 sup	-	-	-

Table 17: Anatase/rutile ratio and their respective mean crystallite sizes for the sedimentation part of BC/HCl TiO_2 samples annealed at 550 °C (BC/Ti ratio of 0.03 and 0.4), and from the clear supernatant part of BC/HCl TiO_2 samples annealed at 550 °C (BC/Ti ratio of 0.03 and 0.4).

Using PA instead of $BmimPF_6$ has given a different visual aspect during the synthesis. In this case, no separate solid formation was observed like reported for the IL, BC or PF-assisted synthesis in HCl. Instead of the slow precipitation from a clear sol during the aging step, a white precipitate was formed immediately after aqueous solution containing phosphoric acid was added into Ti precursor solution. The final mass of the dried

precipitation recovered after 6 days of aging corresponded to more than 90% of yield. We believed this fast-formed precipitate was formed due to interaction between hydrolyzed titanium precursors and phosphate anions, resulting in the formation of stable titanium phosphate compound. The presence of a titanium phosphate phase can be evidenced in the XRD patterns of PA/HCl TiO_2 samples (Fig 42). At a PA/Ti ratio of 0.03, only anatase was observed as crystallized phase, and the crystallite size was relatively small around 9 nm, showing resistance to thermal treatment in terms of size against calcination and anatase stability, as already observed when $BmimPF_6$ is used (Fig 35 B red). At a PA/Ti ratio of 0.4, the crystallization was strongly inhibited, and a new phase was observed alongside with anatase but its crystallinity was too low for a precise identification or all major characteristic peaks. In order to make this phase more crystallized, a calcination at 650 ^{o}C was performed, and the $Ti_5O_4(PO_4)_4$ phase was successfully identified, similarly to the phase observed for the $BmimPF_6$/HCl TiO_2 sample after calcination at 800 ^{o}C (Fig 36).

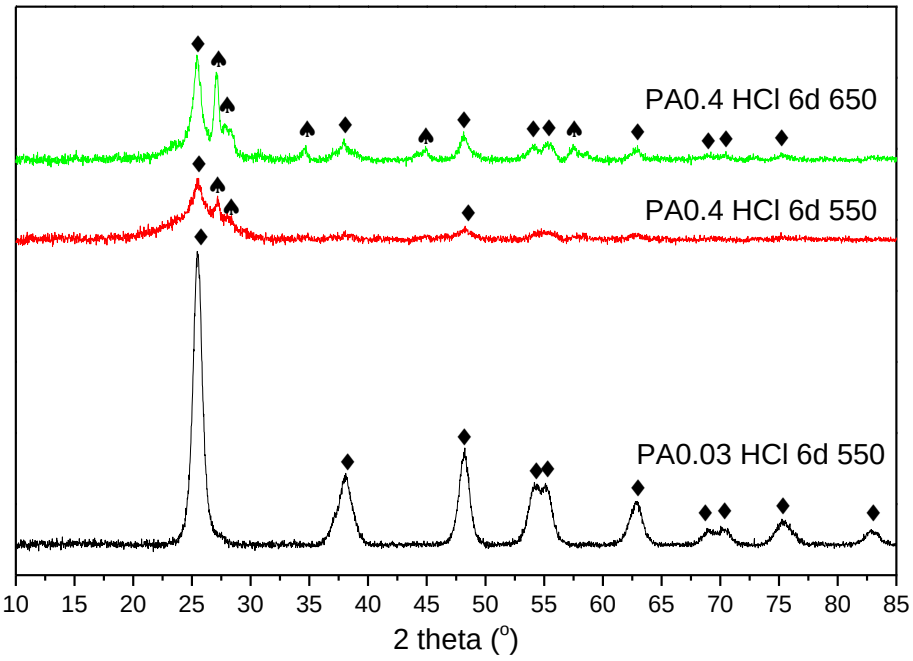

Fig 42: XRD patterns of the PA/HCl TiO_2 samples annealed at 550 ^{o}C, the PA/Ti ratio is 0.03 (black) and 0.4 (red). Also the XRD pattern of the PA/HCl TiO_2 sample annealed at 650 ^{o}C is shown (green), the PA/Ti ratio is 0.4. Black diamonds are anatase peaks, black spades are $Ti_5O_4(PO_4)_4$ peaks.

Sample name	*Anatase/Rutile ratio*	*Anatase mean crystallite size (nm)*	*Rutile mean crystallite size (nm)*
PA0.03 HCl 6d 550	100/0	9	-
PA0.4 HCl 6d 550	-	10	-
PA0.4 HCl 6d 650	-	12	-

Table 18: Anatase/rutile ratio and their respective mean crystallite sizes for the PA/HCl TiO_2 samples annealed at 550 ^oC (PA/Ti ratio of 0.03 and 0.4), and for the PA/HCl TiO_2 samples, annealed at 650 ^oC (PA/Ti ratio of 0.4).

Among the TiO_2 materials synthesized in HCl with the assistance of BC, PF and PA, **the XRD results have shown us that only the phosphorus containing additives (PF and PA) have provided to TiO_2 a resistance to thermal treatment in terms of crystallite size growth inhibition and anatase phase stabilization.** Even more, a similar $Ti_5O_4(PO_4)_4$ titanium phosphate phase was observed in both PA/HCl- and $BmimPF_6$/HCl- TiO_2 samples. In the next section, XPS will be conducted to further compare surface composition of TiO_2 synthesized in HCl with BC, PF or PA with that of TiO_2 prepared with $BmimPF_6$, and to study possible surface interactions between phosphorus and titanium species. For the same reason that in the previous section, only the dried supernatant part of samples (for BC/HCl and PF/HCl TiO_2 samples) will be analyzed.

II.2.3.3. XPS analysis

To further evidence that the additional peak contribution of Ti_{2p}, O_{1s} and P_{2p} XPS patterns of $BmimPF_6$-TiO_2 samples resulted only from the titanium phosphate formation but not from the interaction of titanium with other species, and to evidence the influence of the replacement additives on the surface species nature, XPS analysis has been carried out on BC, PF and PA/HCl – TiO_2 samples aged for 6 days. Two additive/Ti ratios were used, at 0.03 and 0.4, and only the solid dried from the clear supernatant part of reaction medium was analyzed if possible (because of anatase formation).

Fig 44 shows the Ti_{2p}, O_{1s} and P_{2p} XPS spectra recorded on PA and PF/HCl-TiO_2 samples with a P/Ti ratio of 0.03 and 0.4. The BC0.4 HCl 6d sample contained too much organic residues to be handled, whereas the spectra recorded on the BC0.03 HCl 6d sample showed no difference compared to those of pure TiO_2 sample (not reported). Thus we have no information about the reaction mechanism involving $Bmim^+$ and titanium, but more important,

the presence of $Bmim^+$ could not be considered as impacting on the surface nature of TiO_2 sample.

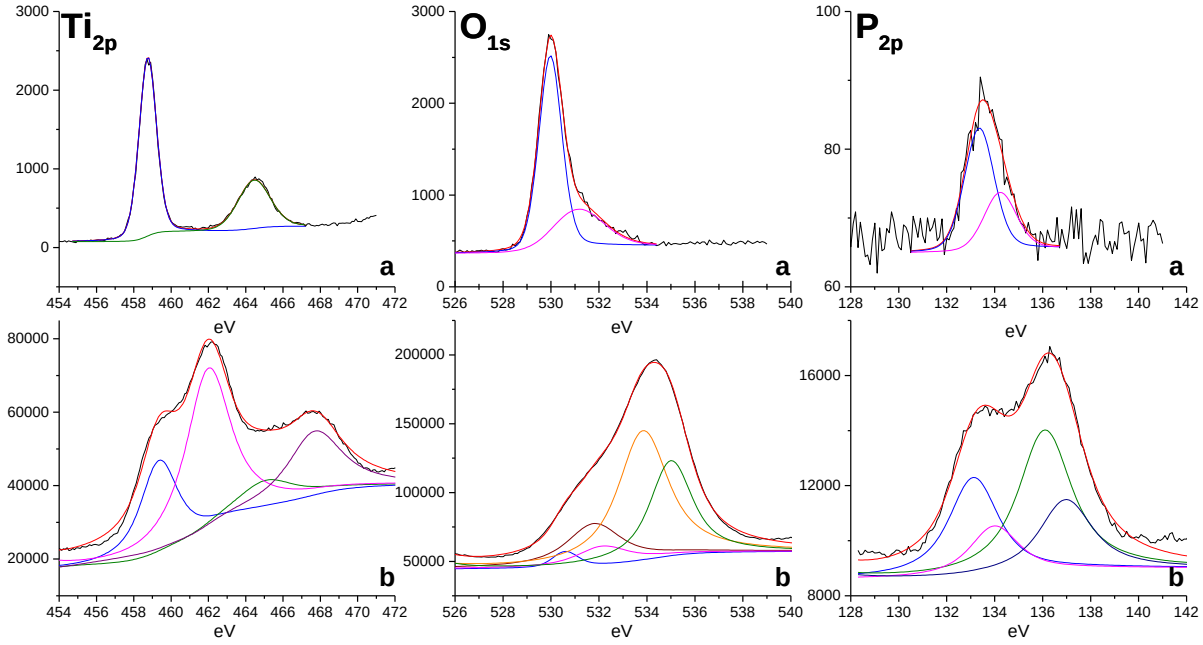

Fig 43: Ti_{2p}, O_{1s} and P_{2p} XPS patterns of IL0.03 HCl 6d (a) and IL0.4 HCl 6d (b) dried TiO_2 samples, same as presented in Fig 38. This figure serves as reference to compare with Fig 44.

First, it is worth noting that the XPS spectra recorded on PA and PF/HCl-TiO_2 displayed similar patterns that those recorded on $BmimPF_6$/HCl-TiO_2 samples, for both additive/Ti ratios of 0.03 and 0.4.

Indeed, for both PA0.03 HCl 6d and PF0.03 HCl 6d sample, the XPS spectra for Ti_{2p}, O_{1s} and P_{2p} orbitals, were fully similar to those shown by $BmimPF_6$-derived TiO_2, with Ti_{2p} and O_{1s} orbital spectra similar to those of IL-free TiO_2, and P_{2p} spectra evidencing the doublet of P^{5+} in phosphates at 133.2/134.1 eV and at 133.5/134.3 eV, respectively. Also, for PA0.4 HCl 6d and PF0.4 HCl 6d samples, similar patterns were obtained that on $BmimPF_6$ 0.4 HCl 6d TiO_2 sample, with the evidence of two $Ti_{2p}3/2$-$Ti_{2p}1/2$ doublets and two $P_{2p}3/2$-$P_{2p}1/2$ doublets, as well as the appearance of new contributions broadening strongly the O_{1s} envelope. The calculated P/Ti surface atomic ratio was also about 0.1 for PA or PF/Ti ratio of 0.03 and 0.8 for PA/Ti ratio of 0.4 and 0.7 for PF/Ti ratio of 0.4. This indicates that the surface chemical environment of TiO_2 was influenced similarly by the presence of $BmimPF_6$, phosphoric acid or hexafluorophosphoric acid during the synthesis in HCl medium.

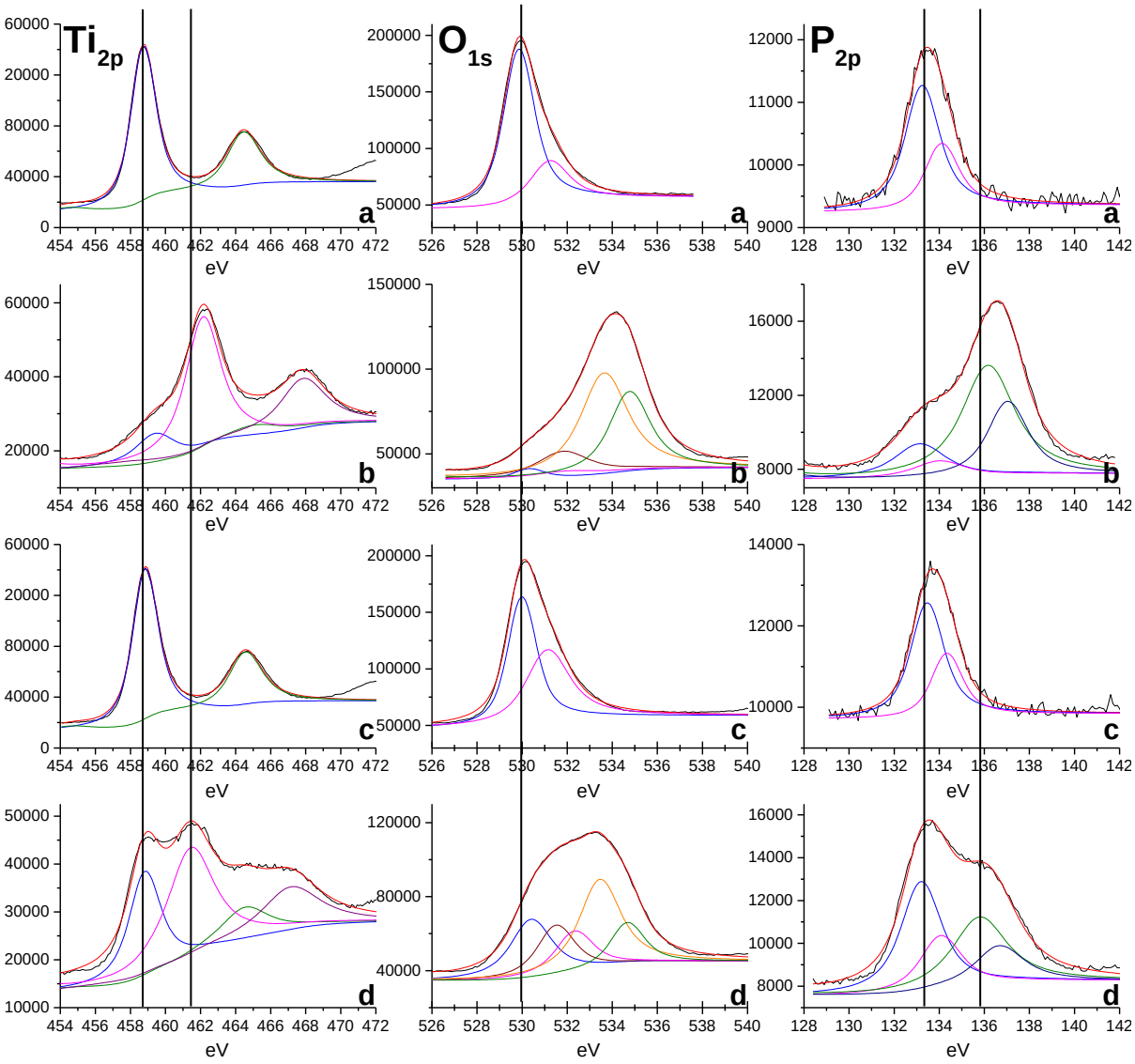

Fig 44: Ti_{2p}, O_{2s} and P_{2p} XPS patterns of PA and PF/HCl assisted dried TiO_2 samples with different phosphor/Ti ratios used in the sol-gel synthesis.
The upper two series are phosphoric acid-assisted dried TiO_2 samples with phosphor/Ti ratio of 0.03 (a) and 0.4 (b).
The lower two series are hexafluorophosphoric acid-assisted dried TiO_2 samples with phosphor/Ti ratio of 0.03 (c) and 0.4 (d).

Actually, even if the P/Ti surface atomic ratio is similar for IL/PF/or PA/HCl-TiO_2, the PA-derived TiO_2 sample had a much more dominant Ti-O-P, P-O-H and $(P-O)_n$ contribution in Ti_{2p}, O_{1s} and P_{2p} spectra than the two others. This could result from the direct implication of phosphate from PA in TiO_2 rather than from the slow release of phosphate and fluoride anions by hydrolyzed $BmimPF_6$ in the sol-gel synthesis medium.

Sample name	*Orbitals*		*Contributions*	*Binding energy (eV)*	
PA0.03 HCl 6d	$Ti_{2p\ 3/2}$	$Ti_{2p\ 1/2}$	Ti-O-Ti	458.7	464.5
	O_{1s}		O-Ti	529.6	
			O-H	531.0	
	$P_{2p\ 3/2}$	$P_{2p\ 1/2}$	P-O-P	133.2	134.1
PA0.4 HCl 6d	$Ti_{2p\ 3/2}$	$Ti_{2p\ 1/2}$	Ti-O-Ti	459.5	465.2
	$Ti_{2p\ 3/2}$	$Ti_{2p\ 1/2}$	Ti-O-P	462.2	467.9
	O_{1s}		O-Ti	530.1	
			O-P	531.6	
			O=P	531.8	
			P-O-H	533.4	
			H_2O ads	534.5	
	$P_{2p\ 3/2}$	$P_{2p\ 1/2}$	P-O-P	133.2	134.1
	$P_{2p\ 3/2}$	$P_{2p\ 1/2}$	$(P-O)_n$	135.9	137.0
PF0.03 HCl 6d	$Ti_{2p\ 3/2}$	$Ti_{2p\ 1/2}$	Ti-O-Ti	458.9	464.6
	O_{1s}		O-Ti	529.8	
			O-H	530.9	
	$P_{2p\ 3/2}$	$P_{2p\ 1/2}$	P-O-P	133.5	134.3
PF0.4 HCl 6d	$Ti_{2p\ 3/2}$	$Ti_{2p\ 1/2}$	Ti-O-Ti	458.8	464.7
	$Ti_{2p\ 3/2}$	$Ti_{2p\ 1/2}$	Ti-O-P	461.5	467.3
	O_{1s}		O-Ti	530.2	
			O-P	531.3	
			O=P	532.1	
			P-O-H	533.2	
			H_2O abs	534.4	
	$P_{2p\ 3/2}$	$P_{2p\ 1/2}$	P-O-P	133.2	134.1
	$P_{2p\ 3/2}$	$P_{2p\ 1/2}$	$(P-O)_n$	135.8	136.7

Table 19: XPS Peak binding energies for Ti_{2p}, O_{1s} and P_{2p} orbitals and the different elements for PA and PF/HCl assisted dried TiO_2 samples with different phosphor/Ti ratios used in the sol-gel synthesis. The acid used was HCl and the aging duration was fixed at 6 days.

Traces of adsorbed fluorine were observed in all TiO_2 samples prepared with F-containing additive. But since no F-Ti-O was noticed, the F_{1s} XPS spectra will not be detailed here.

II.2.3.4. Conclusion

The replacement of IL by BC, PF and PA in sol-gel synthesis of TiO_2 in HCl medium allowed to precisely identify and to confirm the role of phosphorus during synthesis.

XRD and XPS characterizations evidenced the presence of phosphorus in TiO_2 samples synthesized in the presence of P-containing additive, just like that synthesized in the presence of IL, even for a low P/Ti ratio. Furthermore, the existence of the possible titanium phosphate

phase we have hypothesized previously in addition to TiO_2 was confirmed for a high P/Ti ratio of 0.4 where PF or PA was used. Similar strong modification of the surface electron environment of titanium centers by the presence of phosphorus has been observed in above two cases. The use of PA seemed to cause the most dominant Ti-O-P, P-O-H and $(P-O)_n$ contributions in Ti_{2p}, O_{1s} and P_{2p} spectra among TiO_2 samples synthesized in the presence of other additives. The reason was hypothesized as the direct interaction between phosphate anions and titanium centers compared to other cases in which phosphate anions have to be firstly released from hydrolysis of PF_6 anions.

Combining with observations from the last section, **we hypothesize that the thermal resistance in terms of crystal size growth and anatase phase stability of TiO_2 samples prepared with $BmimPF_6$ resulted from the formation of titanium phosphate phase within TiO_2 samples.** Phosphate could be originated from decomposition of PF_6 anion of the ionic liquid.

II.2.4. Replacement of $BmimPF_6$ for ionic liquid-free sol-gel synthesis of TiO_2 using HAc as acid catalyst

HCl was used instead of HAc in the sol-gel synthesis of TiO_2 in the two previous sections. The objective was to study the presence and influence of phosphorus element in $BmimPF_6$-derived TiO_2 samples. Since we know now that the titanium phosphate formation within TiO_2 is a key parameter to bring numerous advantages to the synthesized TiO_2 nanomaterial, we will now search for the proper replacement of $BmimPF_6$ by low-cost additives to synthesize photocatalytically active TiO_2 reusing more chemical-friendly HAc as acid. The aim of this section is:

1: to propose the replacement of expensive $BmimPF_6$ by much cheaper molecules providing to the TiO_2 photocatalyst the same advantages than the ionic liquid.

2: to perform the synthesis in easy-to-process and less harmful operating conditions if applied for large scale production. Indeed, the use of HCl requires expensive anti-corrosion protective coating in reactor as well as costly and non-environmentally friendly neutralization system. Also the 2 phase-formation needs extra filtration steps which increase also the production cost.

We hypothesized that three components could have played important role in $BmimPF_6$ assisted TiO_2 synthesis: $Bmim^+$, phosphate anion, and fluoride anion. In this section, we will use combination of two out of three of those elements as additives in the TiO_2 sol-gel synthesis, and HAc as acid catalyst to synthesize TiO_2 nanomaterials with similar properties and advantages than when $BmimPF_6$ is used. Three chemical compounds were selected, with each of them providing one constituent element of $BmimPF_6$. We have carried out three sets of combinations of those chemical compounds, removing one constituent element of $BmimPF_6$ in each synthesis: $Bmim^+$, NaF and H_3PO_4 (Table 20). The aim is to get idea about which element or elements are necessary for replacing $BmimPF_6$, and also to study the role of fluoride in the synthesis.

II.2.4.1. Sample preparation

The molar ratio of both additives used in the same synthesis was equally attributed and fixed at 0.03 for all syntheses in this section. Two aging durations were applied to each set of additive combination: 18 h and 6 days. The calcination temperature was fixed at 550℃ for all samples. The other parameters as well as the synthesis protocol were not changed, thus identical to those used in $BmimPF_6$/HAc assisted TiO_2 sol-gel synthesis. A list of samples is reported in Table 21.

Combination of additives as replacement of $BmimPF_6$	Abbreviation
BmimCl (1-butyl-3-methylimidazolium chloride) + NaF (sodium fluoride)	BCNaF
BmimCl (1-butyl-3-methylimidazolium chloride) + H_3PO_4 (phosphoric acid)	BCPA
H_3PO_4 (Phosphoric acid) + NaF (sodium fluoride)	PANaF

Table 20: Combinations of replacement additives for $BmimPF_6$ used in sol-gel synthesis of TiO_2.

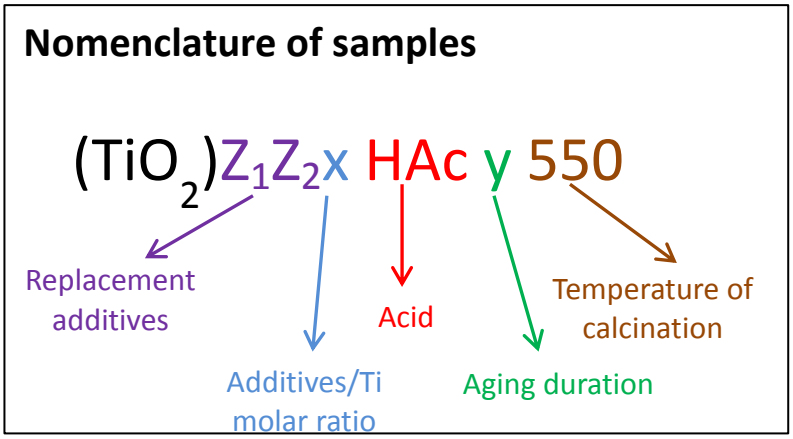

Fig 45: Nomenclature of TiO_2 samples synthesized with $BmimPF_6$ ionic liquid replacement additives in the assisted sol-gel route using HAc as acid catalyst. For the samples before calcination, no calcination temperature is added.

Sample name	*Additive/Ti molar ratio*	*Aging duration*
BCNaF0.03 HAc 18h 550	0.03	18 h
BCNaF0.03 HAc 6d 550	0.03	6 days
BCPA0.03 HAc 18h 550	0.03	18 h
BCPA0.03 HAc 6d 550	0.03	6 days
PANaF0.03 HAc 18h 550	0.03	18 h
PANaF0.03 HAc 6d 550	0.03	6 days

Table 21: Synthetic view of names and parameters for samples synthesized by combination of replacement additives for $BmimPF_6$, in the assisted sol-gel route using HAc as acid catalyst. The two replacement additives in one set of combination for each synthesis shared same molar ratio to Ti.

II.2.4.2. XRD and surface specific area characterizations

The XRD patterns of the different TiO_2 samples are reported in Fig 46. Firstly, whatever the replacement additive combination and the aging duration, only anatase is observed as crystallized phase in dried and calcined materials. From the comparison between XRD patterns recorded on TiO_2 samples before and after calcination (Fig 46 A with Fig 46 B), only samples prepared with phosphorus-containing additives except BCPA0.03 HAc 18h sample (BCPA and PANaF – TiO_2 samples, Fig 46 red, cyan and pink) presented an inhibition effect of the crystallite size growth during calcination. They maintained after calcination a relatively small mean crystallite size, around 10 nm *vs* 7 nm for dried samples, associated to a high specific surface area within the 90-130 m^2/g range (Table 22). By contrast, both BCNaF-TiO_2 samples had a strong mean crystallite size increase after calcination, whatever the aging

duration, from 5 and 8 nm before calcination to 24 and 19 nm after calcination (Fig 46 B green and blue). This was correlated to a media specific surface area of 31 and 46 m^2/g respectively.

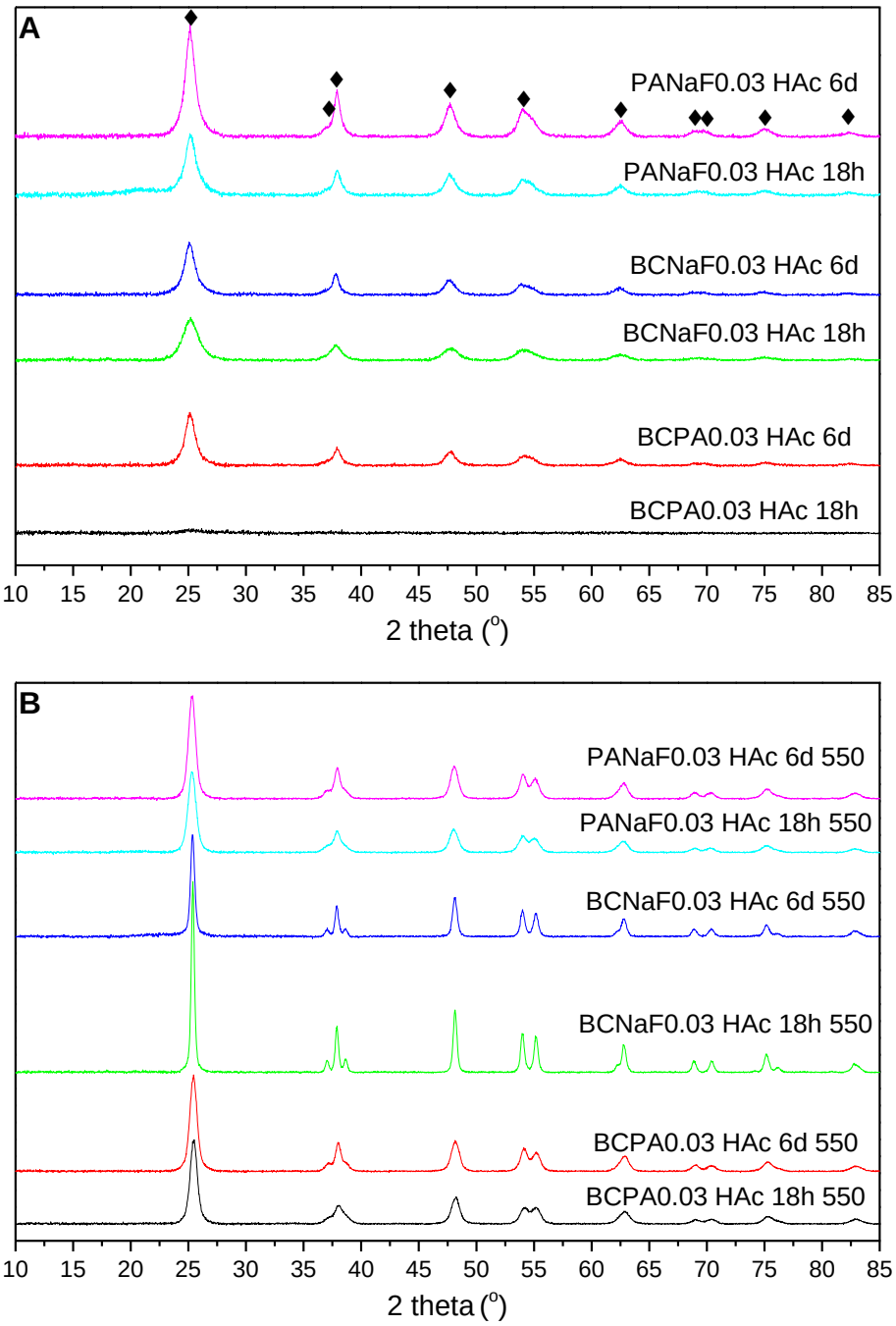

Fig 46: (A) XRD patterns of TiO_2 samples synthesized by combination of replacement additives for $BmimPF_6$ in the assisted sol-gel route using HAc as acid catalyst after drying: BCPA0.03 HAc 18h (black); BCPA0.03 HAc 6d (red); BCNaF0.03 HAc 18h (green); BCNaF0.03 HAc 6d (blue); PANaF0.03 HAc 18h (cyan); PANaF0.03 HAc 6d (pink). (B) XRD patterns of the above samples after calcination at 550 °C. Black diamonds are anatase phase.

TiO_2 samples with phosphorus-containing additives resulted in a better crystallization during the aging step (Fig 46 A black, red, cyan and pink), although longer aging duration led to a better crystallinity whatever the samples (Fig 46 A, samples aged for 18h *vs* 6 days).

Samples	***BET surface area (m^2/g)***	***Mean crystallite size (nm) (Mean crystallite size before annealing)***
BCNaF0.03 HAc 18h 550	31	24 (5)
BCNaF0.03 HAc 6d 550	46	19 (8)
BCPA0.03 HAc 18h 550	91	11 (-)
BCPA0.03 HAc 6d 550	109	10 (8)
PANaF0.03 HAc 18h 550	108	10 (8)
PANaF0.03 HAc 6d 550	131	11 (8)

Table 22: Specific surface areas and mean crystallite sizes of TiO_2 samples synthesized by combination of replacement additives for $BmimPF_6$, in the assisted sol-gel route using HAc as acid catalyst. The two replacement additives in one set of combination for each synthesis shared same molar ratio to Ti.

Interestingly, the use of phosphorus-containing additives resulted in TiO_2 samples with similar characteristics/advantages to those brought by $BmimPF_6$ in terms of specific surface area and resistance to crystallite growth. Although evidence of phosphorus in TiO_2 samples prepared with PF and PA in HCl has been shown, the presence of phosphorus in TiO_2 samples synthesized in HAc has been investigated by using a similar manner that has been used in the previous section, i.e. through the calcination of large-dose phosphorus assisted sample at higher temperature.

Therefore, further syntheses with PANaF have been performed by increasing both the PA/Ti molar ratio from 0.03 to 0.4 and the calcination temperature to 800 ^oC to crystallize the titanium phosphate phase.

From Fig 47, when PA/Ti ratio was 0.03, the XRD patterns of the sample annealed at 550 ^oC and 800 ^oC did not reveal crystallized phases other than anatase (Fig 47 black, red). By contrast, when PA/Ti was increased to 0.4, the crystallization was strongly inhibited, and the sample annealed at 550 ^oC showed a very weak crystallinity (Fig 47 green).

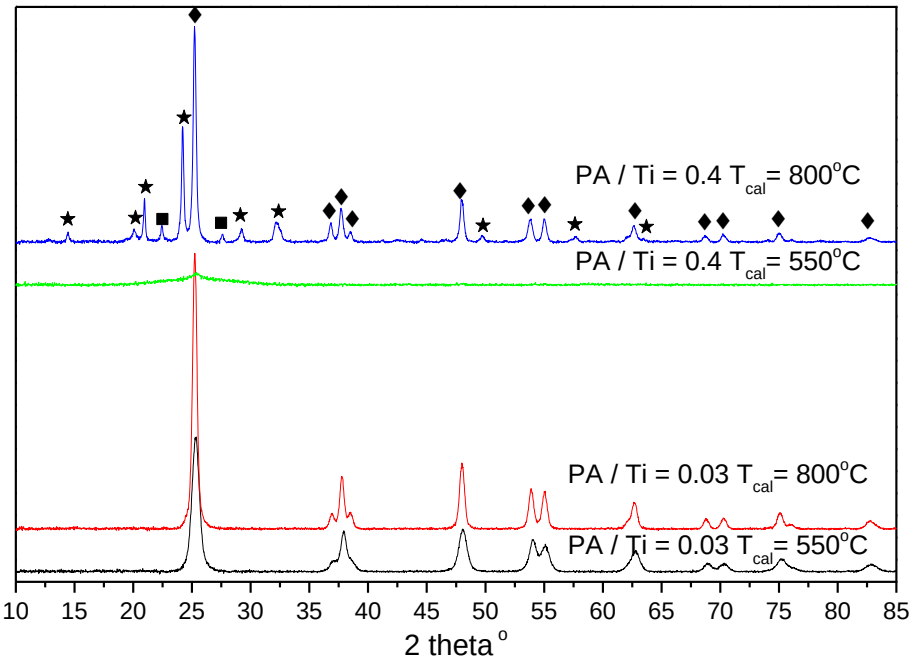

Fig 47: XRD patterns of samples synthesized by using phosphoric acid (PA) and sodium fluoride (NaF) as additives and acetic acid (HAc) as acid catalyst. The NaF/Ti ratio was fixed at 0.03, while the PA/Ti ratio and the calcination temperature were varied as followed: PA/Ti = 0.03, 550 °C (black); PA/Ti = 0.03, 800 °C (red); PA/Ti = 0.4, 550 °C (green); PA/Ti = 0.4, 800 °C (blue). Black diamonds are anatase phase, black stars are $Ti_4P_6O_{23}$ phase, and black squares are TiP_2O_7 phase.

The XRD patterns of the sample annealed at 800 °C evidenced sharp anatase peaks alongside with additional sharp peaks corresponding to both $Ti_4P_6O_{23}$ (JCPDS 039-0004) and TiP_2O_7 (JCPDS 038-1468) phases (Fig 47 blue). These two titanium phosphate phases differ from the $Ti_5O_4(PO_4)_4$ phosphate phase observed after annealing at 650 °C of the TiO_2 samples synthesized in HCl medium with PA (Fig 42). Although different formation mechanisms of titanium phosphate was probably involved in this case, the presence of phosphorus within the TiO_2 sample was confirmed. Similarly to $BmimPF_6$/HAc-TiO_2 samples, at lower phosphorus additive content, traces of phosphorus may not be detected in TiO_2 by XRD. However, the resistance of TiO_2 against crystallite growth during calcination for samples with low P/Ti molar ratio of 0.03 may hypothesize the presence of phosphorus in TiO_2 samples for BCPA and PANaF – derived samples even at a low P/Ti molar ratio.

II.2.4.3. XPS analysis

XPS analysis has been performed on both phosphorus-containing BCPA-, and PANaF-derived TiO_2 samples (Fig 49). TiO_2 sample prepared with BCNaF are not reported here.

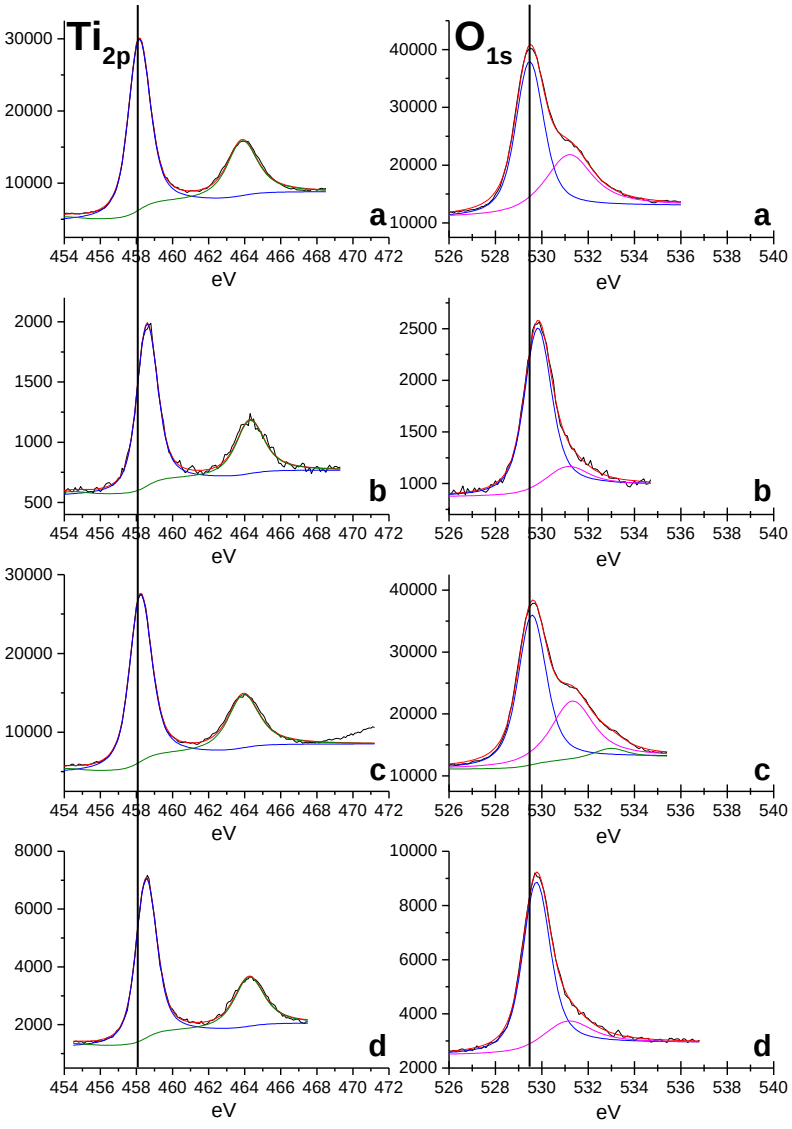

Fig 48: Ti_{2p}, O_{1s} XPS patterns of IL0 HAc 6d (a), IL0 HAc 6d 550 (b), IL0.03 HAc 6d (c) and IL0.03 HAc 6d 550 (d). This figure is reference to be compared with Fig 49.

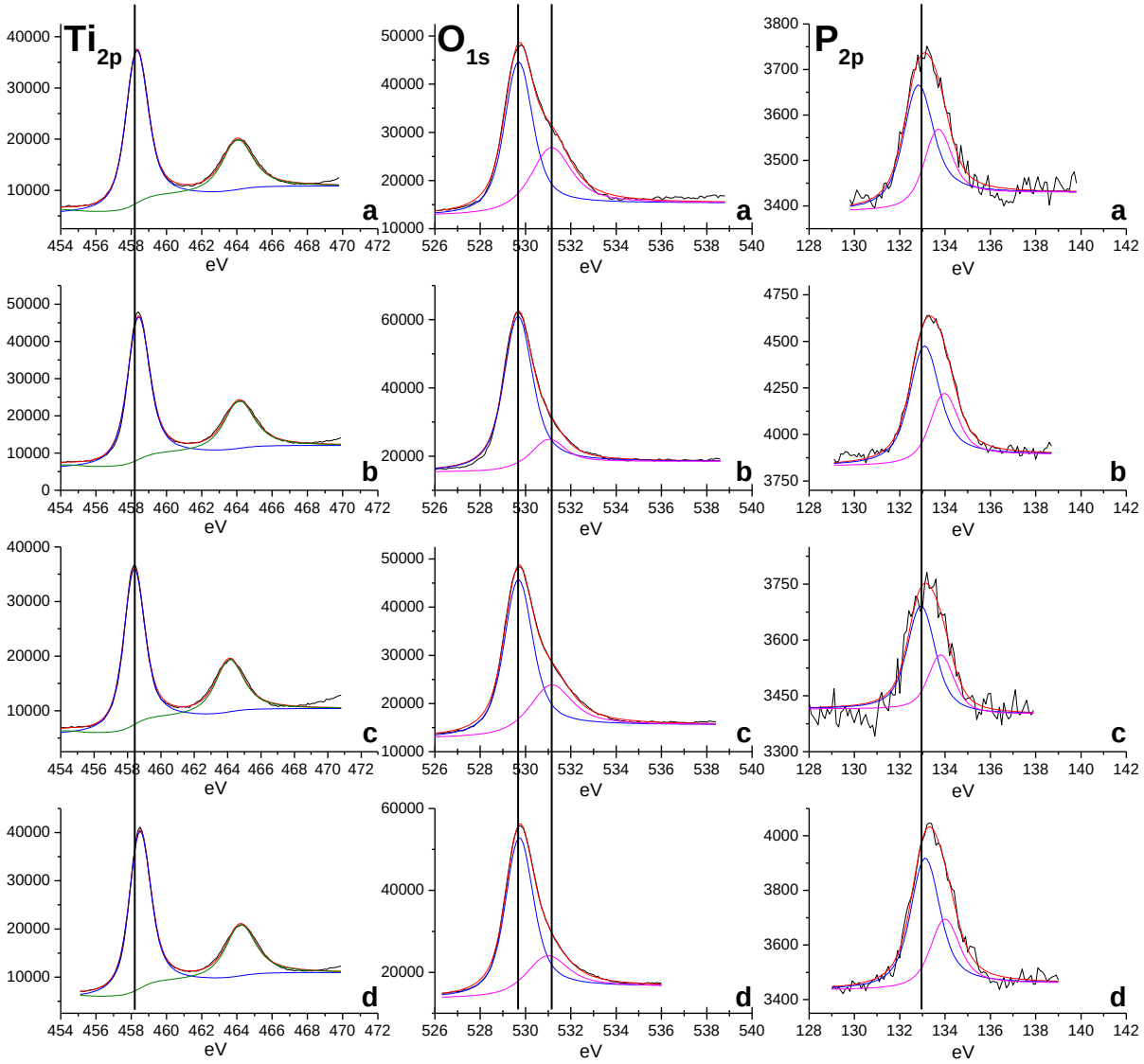

Fig 49: Ti_{2p}, O_{1s}, P_{2p} XPS patterns of BCPA0.03 HAc 6d (a), BCPA0.03 HAc 6d 550 (b), PANaF0.03 HAc 6d (c) and PANaF 0.03 HAc 6d 550 (d).

In general, both BCPA- and PANaF- series samples (dried or calcined) did not show any strong differences for Ti_{2p}, and O_{1s} orbitals compared to those recorded on TiO_2 synthesized with $BmimPF_6$ in HAc or in HCl. Indeed, Ti_{2p} orbital patterns display the characteristic doublet at the binding energies of Ti-O-Ti centers (Table 23), identical to that recorded on additive-free TiO_2 samples synthesized in HAc or in HCl. The O_{1s} spectra display usual patterns for TiO_2 samples with O-Ti and O-H contributions.

However, in BCPA- and PANaF-derived TiO_2 samples, the presence of phosphorus has been evidenced (Fig 50 P_{2p}), with the characteristic doublet of $P_{2p}3/2$-$P_{2p}1/2$ orbitals corresponding to P-O bond in non-polymerized phosphate, at 132.9/133.8 eV (BCPA no-

calcined), at 133.2/134.1 eV (BCPA calcined), at 132.9/133.8 eV (PANaF no-calcined) and at 133.3/134.2 eV (PANaF calcined). Again, this is similar to that of IL-TiO_2 samples synthesized in HCl but different to IL-TiO_2 samples synthesized in HAc medium, even though the P/Ti ratios were all at 0.03 (Fig 48). It indicates probably that the use of PA in HAc medium might release more phosphate anions than IL does during synthesis if containing the same amount of P, because IL needs to be hydrolyzed first before releasing phosphate anions. And the similar P_{2p} spectra between TiO_2 samples synthesized in HCl in the presence of PA or IL at a P/Ti ratio of 0.03 might result from a more rapid hydrolyze of IL in more acidic HCl medium, so that the actual released phosphate quantity matches that provided from PA directly.

Also, one can note that the P/Ti surface atomic ratios increased after calcination for both TiO_2 samples, the P/Ti ratio increased from 0.05 to 0.1 and from 0.06 to 0.09 for the BCPA-derived and PANaF-derived TiO_2 sample, respectively. The increase in P/Ti ratio after calcination could result from phosphate migration from bulk to surface, like it was proposed in the case of IL-assisted synthesis of TiO_2.

Sample name	***Orbitals***		***Contributions***	***Binding energy (eV)***	
BCPA0.03 HAc 6d	$Ti_{2p\ 3/2}$	$Ti_{2p\ 1/2}$	Ti-O-Ti	458.3	464.1
	O_{1s}		O-Ti	529.5	
			O-H	530.9	
	$P_{2p\ 3/2}$	$P_{2p\ 1/2}$	P-O-P	132.9	133.8
BCPA0.03 HAc 6d 550	$Ti_{2p\ 3/2}$	$Ti_{2p\ 1/2}$	Ti-O-Ti	458.4	464.2
	O_{1s}		O-Ti	529.4	
			O-H	530.8	
	$P_{2p\ 3/2}$	$P_{2p\ 1/2}$	P-O-P	133.2	134.1
PANaF0.03 HAc 6d	$Ti_{2p\ 3/2}$	$Ti_{2p\ 1/2}$	Ti-O-Ti	458.4	464.1
	O_{1s}		O-Ti	530.1	
			O-H	531.1	
	$P_{2p\ 3/2}$	$P_{2p\ 1/2}$	P-O-P	132.9	133.8
PANaF0.03 HAc 6d 550	$Ti_{2p\ 3/2}$	$Ti_{2p\ 1/2}$	Ti-O-Ti	458.5	464.2
	O_{1s}		O-Ti	529.5	
			O-H	531.0	
	$P_{2p\ 3/2}$	$P_{2p\ 1/2}$	P-O-P	133.3	134.2

Table 23: XPS binding energies for Ti_{2p}, O_{1s} and P_{2p} orbitals and the different contributions assigned for BCPA0.03 HAc 6d, BCPA0.03 HAc 6d 550, PANaF0.03 HAc 6d and PANaF 0.03 HAc 6d 550.

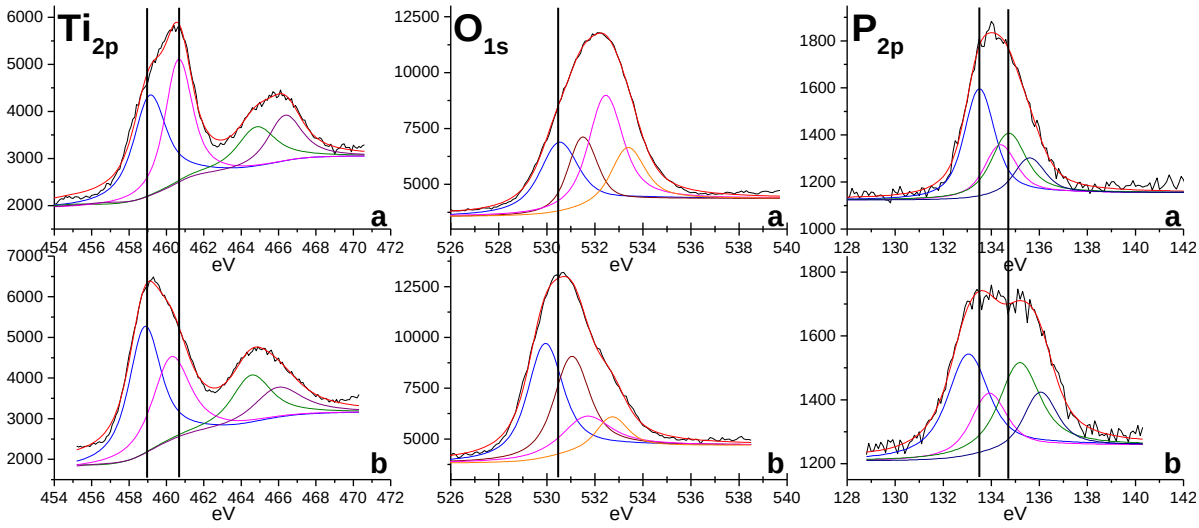

Fig 50: Ti_{2p}, O_{1s} and P_{2p} XPS patterns of PANaF-derived TiO_2 sample synthesized in HAc with a PA/Ti ratio equal to 0.4, the other synthesis parameters were not changed compared to PANaF0.03 HAc 6d. (a) dried sample; (b) sample after calcination at 550°C.

Sample name	***Orbitals***		***Contributions***	***Binding energy (eV)***	
PA/Ti = 0.4 HAc 6d	$Ti_{2p\ 3/2}$	$Ti_{2p\ 1/2}$	Ti-O-Ti	459.2	464.9
	$Ti_{2p\ 3/2}$	$Ti_{2p\ 1/2}$	Ti-O-P	460.7	466.4
	O_{1s}		O-Ti	530.3	
			O-P	531.2	
			O=P	532.2	
			P-O-H	533.1	
	$P_{2p\ 3/2}$	$P_{2p\ 1/2}$	P-O-P	133.5	134.4
	$P_{2p\ 3/2}$	$P_{2p\ 1/2}$	$(P\text{-}O)_n$	134.7	135.6
PA/Ti = 0.4 HAc 6d 550	$Ti_{2p\ 3/2}$	$Ti_{2p\ 1/2}$	Ti-O-Ti	458.9	464.6
	$Ti_{2p\ 3/2}$	$Ti_{2p\ 1/2}$	Ti-O-P	460.3	466.1
	O_{1s}		O-Ti	529.7	
			O-P	530.8	
			O=P	531.4	
			P-O-H	532.5	
	$P_{2p\ 3/2}$	$P_{2p\ 1/2}$	P-O-P	133.1	133.9
	$P_{2p\ 3/2}$	$P_{2p\ 1/2}$	$(P\text{-}O)_n$	135.2	136.1

Table 24: XPS Peak binding energies for Ti_{2p}, O_{1s} and P_{2p} orbital contributions for PANaF-derived TiO_2 dried and calcined samples synthesized in HAc with a PA/Ti ratio of 0.4. Other parameters were not changed compared to PANaF0.03 HAc 6d.

When increasing the PA/Ti ratio to 0.4 (instead of 0.03), the XPS patterns and the assigned contributions for TiO_2 before and after calcination are shown in Fig 50 and Table 24. The XPS spectra are globally similar to those recorded on IL-derived TiO_2 samples synthesized in HCl medium, and the presence of a new phosphate phase has been evidenced again by the appearance of new contributions in Ti_{2p}, O_{1s} and P_{2p} patterns. Also, the strongly

increase in the O_{1s} peak area with change of envelope profile is due to extra oxygen brought by phosphate as the O/Ti calculated surface atomic ratio is 4.5 and 4.8 (H_2O_{ads} was not attributed in this case) before and after calcination. However, two main differences could be noted:

1: The energy shift of new contributions in Ti_{2p} and P_{2p} was weaker than that of IL-derived TiO_2 samples synthesized in HCl medium. (*e.g.* about 1.5 eV *vs* 2.7 eV for Ti_{2p}).

2: The spectra are similar to those recorded on TiO_2 synthesized in the HCl rather than in HAc.

A possible explanation for those differences could be the different kinds of polyphosphate formation in TiO_2 samples prepared in HAc compared to those prepared in HCl medium, and/or with PANaF compared to IL. This is in agreement with XRD analysis showing a different kind of titanium phosphate phase after calcination at 800 ^oC in TiO_2 prepared with HAc when PA/Ti ratio is 0.4. We think that the HCl favors the direct interaction of phosphate to initially condensed Ti-O-Ti network, and thus favors the formation of phosphate in large polyphosphate state cluster instead of phosphate in dispersed state in case of sample synthesized in HAc. With this less favored interaction between phosphates and Ti-O-Ti network, we hypothesize that the electron chemical state around Ti centers is less influenced by phosphates. So the energy of new contributions in Ti_{2p} and P_{2p} was manifested by a weaker shift than that of IL-derived TiO_2 samples synthesized in HCl medium. In the meantime, we hypothesize that the actual phosphate amount released from phosphorus-contained additives in different scenarios decreases in the following order: PA/IL in HCl > PA in HAc > IL in HAc. So that, in our case for PANaF-derived TiO_2 samples (in case of P/Ti ratio of 0.4) synthesized in HAc, large amount of phosphate anions were directly provided and their interaction with Ti-O-Ti network was still much more favored than that for IL-derived TiO_2 samples. While for IL-derived TiO_2 samples synthesized in HAc, despite the P/Ti ratio was increased from 0.03 to 0.4, except the slight appearance of P^{5+} peak in P_{2p} spectra, still no new additional peaks were observed in Ti_{2p}, O_{1s} and P_{2p} spectra. But we could state that, even if phosphates were in dispersed state and could not be read out by XPS as new contribution, contrarily to that of the cluster polyphosphates, the electron chemical state of Ti center is still influenced by the presence of phosphates in IL-derived TiO_2 samples synthesized in HAc. Dispersed titanium phosphate phase exists in IL-derived TiO_2 samples synthesized in HAc but cannot be seen, because just it is so dispersed and not being crystalized yet, which has already been observed by means of XRD results.

Traces of fluorine were barely detectable after calcination at 550 ^{o}C for all above mentioned samples. A fluorine-free final product is thus obtained.

II.2.4.4. TEM characterization

TEM has been performed to study which additive compound among BC, PA and NaF can change the morphology of the TiO_2 sample like it has been observed when $BmimPF_6$ is used. Here in Fig 51, role of phosphorus in limiting the crystal size during calcination was visualized by comparing TiO_2 materials prepared with PANaF (phosphorus-containing) with well-calibrated mean crystallite size around 12-15 nm to TiO_2 materials prepared with BCNaF (phosphorus-free additive), with a larger mean crystallite size around 22-25 nm. Both mean sizes match with the XRD results previously presented.

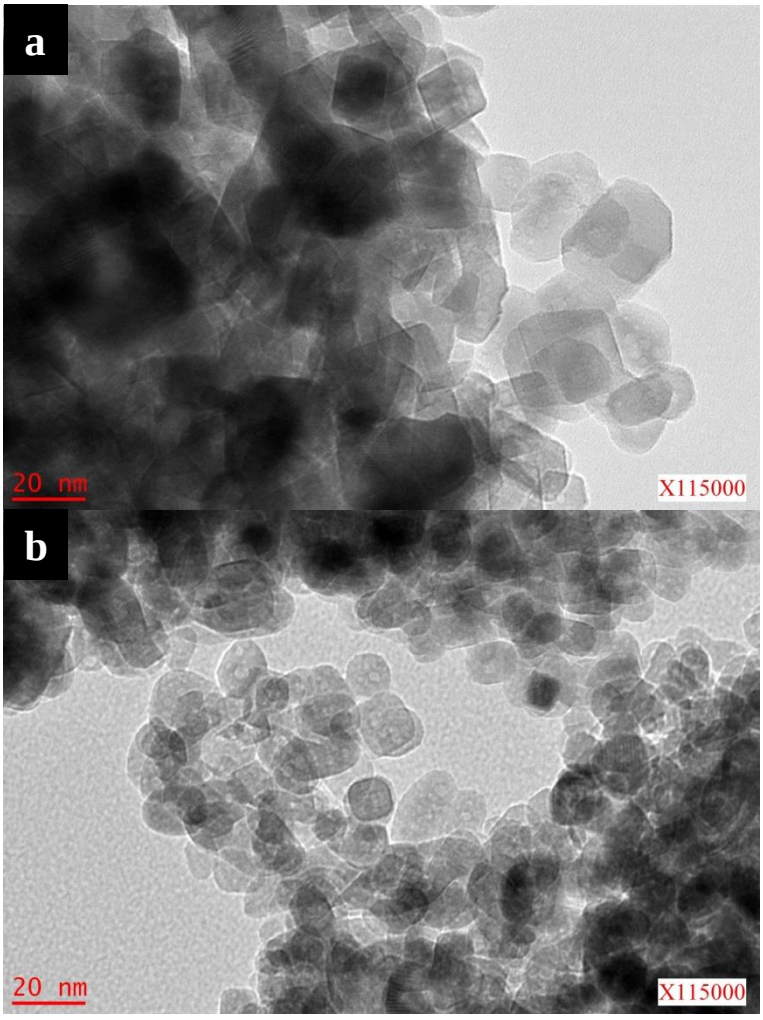

Fig 51: TEM images of BCNaF0.03 HAc 6d 550 (a) and PANaF0.03 HAc 6d 550 (b).

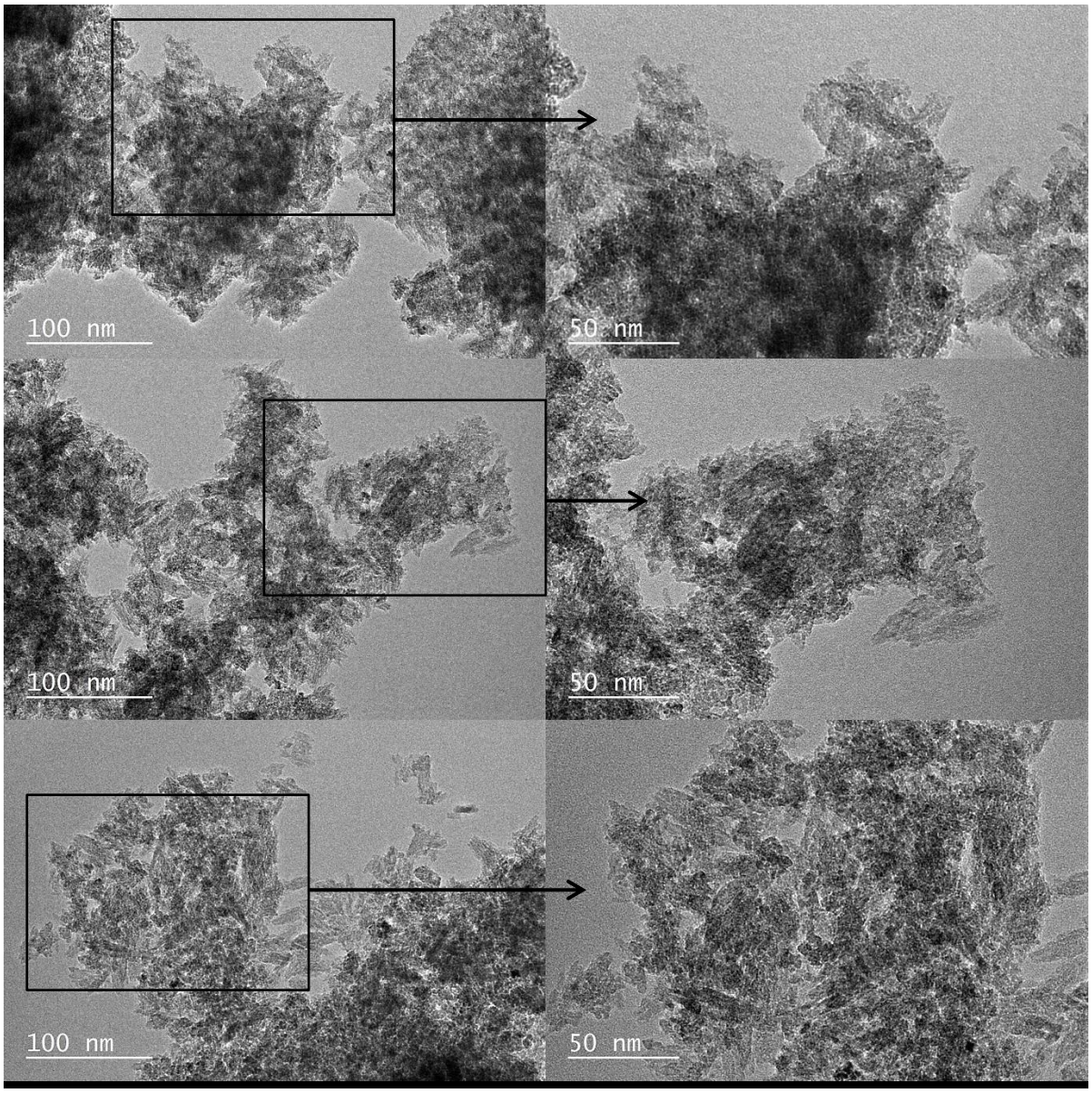

Fig 52: TEM images of PANaF0.03 HAc 6d sample at different magnifications, this sample was aged for 6 days and dried.

TEM images of PANaF0.03 HAc 6d sample are shown in Fig 52. Firstly, 6 days of aging indeed have created crystallized TiO_2 nanoparticles which can be observed with a good magnification. Secondly, this PANaF0.03 HAc 6d sample has shown unique morphology of the crystals formed during aging step before calcination. Instead of being like round shape in the case of classic synthesized TiO_2 nanocrystals, those PANaF/HAc assisted samples have anisotropic spindle-like morphology. We believe it is related to the capping ability of fluoride anions present in the reaction medium, even if it did not show the mostly reported bi-pyramid crystal shaping effect. The capping ability of fluoride ions is not limited only to form large and flat exposed {001} facet on TiO_2 crystals. It was reported that the etching chemistry of

fluoride on TiO_2 depends on a lot of parameters such as concentration of capping agent, time and temperature of the reaction during aging and etc. In one particular case, Yu *et al.* [259] have shown that extra fluorine-contained $BmimBF_4$ quantity can result in spindle-like TiO_2 crystals, while a lower quantity can result in typical bi-pyramid shape. Thus we may have reason to believe that the fluoride ions from $BmimPF_6$ indeed have played capping agent role on TiO_2 samples, but in a non-conventional way.

II.2.4.5. Conclusion

In this section, we have succeeded in synthesizing TiO_2 materials using replacement additives of $BmimPF_6$ (BCPA, BCNaF and PANaF) and HAc as acid catalyst. TiO_2 materials with similar specific surface area and mean crystal size with that of IL-derived TiO_2 samples were obtained by using P-contained additives (BCPA and PANaF). XPS analyses have evidenced the presence of phosphorus in P^{5+} state in those samples. If P/Ti ratio was increased to 0.4 for PANaF-derived TiO_2 sample, we have observed that the surface electron environment of titanium centers was again strongly modified. Also, crystallized titanium phosphate phase has been detected by XRD. We hypothesize that the similar property advantages of P-derived TiO_2 sample to that of $BmimPF_6$-derived samples were resulted by the influence of titanium phosphate phase in TiO_2 nanocrystals, even if when P/Ti is low. A possible phosphate migration phenomenon has been observed during calcination process as well.

At the same time, fluoride was believed to be responsible for the strange anisotropic morphology of aged F-derived TiO_2 nanocrystals. We have succeed in eliminating fluorine trace in all calcined samples by heating TiO_2 at 550℃.

Not much information allows us to determine the roles of $Bmim^+$ in $Bmim^+$-derived TiO_2 samples.

II.2.5. Chapter conclusion

Firstly, $BmimPF_6$-derived TiO_2 samples using HAc as acid catalyst have shown numerous physical-chemical advantages compared to $BmimPF_6$-free TiO_2 sample and commercial TiO_2 P25:

- Smaller crystal size
- Higher specific surface area
- Faster crystallization during aging step
- Thermal-resistance against calcination

By switching HAc to HCl, and by using BmimCl, HPF_6 and H_3PO_4 as replacement additive of $BmimPF_6$, we have identified the role of phosphorus in $BmimPF_6$-derived TiO_2 synthesis using BET, XRD, XPS and TEM as characterization methods. Briefly, all above physico-chemical property advantages are related to the formation of titanium phosphate species in TiO_2 nanocrystals during syntheses, even P/Ti ratio was low.

Finally, replacement of $BmimPF_6$ ionic liquid by cheaper additives (H_3PO_4 and NaF) was achieved in an easy sol-gel synthesis using less-strong acidic HAc as catalyst. The resulted product behaviors the same physical-chemical advantages of that for $BmimPF_6$-derived TiO_2 samples synthesized in HAc medium. Fluoride was hypothesized to induce anisotropic growth of TiO_2 nanocrystals during the aging step, observed in TEM images.

III. Photocatalytic behavior and performances of TiO_2 nanomaterials

In this chapter, we will firstly perform tests of photocatalytic degradation of MEK to evaluate the photocatalytic activity and behavior of the synthesized TiO_2 nanomaterials in comparison with TiO_2 P25. Investigation on the role of phosphorus and chlorine elements on the modification of the properties of TiO_2 synthesized in the presence of P/F containing additives will be performed. Also, correlation between the physico-chemical properties of TiO_2 powdery photocatalyst and of the TiO_2 powder coating and their corresponding photocatalytic activity and behavior will be discussed. A mechanism of the elaboration of TiO_2 nanomaterials describing the role of the different compounds from the synthesis media will be proposed. Then, the most efficient TiO_2 nanomaterial and the P25 reference will be chosen for studying the behavior in terms of photocatalytic bactericidal activity against various Gram-negative and Gram-positive bacteria strains. Influence of parameters such as the TiO_2 coating surface topography, The TiO_2 material nature, the illumination time, the presence of inorganic components, the concentration of dissolved oxygen in the reaction media and the different bacterial strains on the photocatalytic bactericidal effect of TiO_2 samples will be studied.

III.1. Gas-phase photocatalytic degradation of MEK

In this section, the photocatalytic performance and behavior of different TiO_2 samples are assessed by their ability to degrade and mineralize MEK under UVA irradiation in a single-pass continuous gas flow reactor. First, both photocatalytic reactor and set-up are described, followed by the test protocols and the reaction conditions, and further the analytical system and the way to derive usable representative data from experiments.

III.1.1. Experimental protocols

III.1.1.1. Set-up of gas-phase photocatalytic tests

We have used a continuous gas flow test set-up which is shown in Fig 53.

In general, it consists of 3 parts which are:

1. Generation of inlet polluted air flow
2. Photocatalytic reactor
3. On-line analysis of outlet gas

Two synthetic air flows were bubbled at ambient temperature and atmospheric pressure through two temperature-controlled saturators containing MEK (Sigma–Aldrich, 99%) and distilled water, respectively, and mixed with an additional synthetic air flow to set both MEK concentration and relative humidity (RH), as well as the total air flow rate. 100% of RH was defined as the saturated vapor pressure of water at 25◦C and atmospheric pressure, which corresponds to about 24 Torr, i.e. about 3% relatively to the total atmospheric pressure.

The photocatalytic reactor is derived from that detailed in the ISO 22197 standard series. [260] It consists in a metallic aluminum chamber (inner dimension: 260 mm length x 50 mm width x 40 mm height) closed with a quartz window, and inside which is located an aluminum support on which the pollutant flow passes. A photocatalyst-coated glass plate (100 mm length, 50 mm width and 3 mm thickness) was located in an especially-hollowed cavity in the center of this support, so that the distance between the photocatalyst powder surface and the quartz window was 5 mm (Fig 54). The UV-A illumination was provided by a 8W UV-A

blacklight lamp (Sylvania Blacklight Blue F8W/BLB T5), with a spectral peak centered on 365 nm (Fig 55) and located at the top of the reactor, parallel to the photocatalyst sample. So an irradiance of 3.0 $mW.cm^{-2}$ (30 $W.m^{-2}$) was received by the photocatalyst coating, as recorded using a wideband spectroradiometer (RPS900-W ILT). Since the 1.5 cm distance between the UV-A lamp and the photocatalyst surface is relatively small, the center-to-edge deviation of the received irradiance could be neglected. The photocatalytic reactor was located inside a thermostated chamber maintained at a test temperature of 25 ℃ according to the ISO standard. Indeed, the heat issued from the irradiation of the lamp cannot be neglected due to the short distance between the lamp and the sample surface.

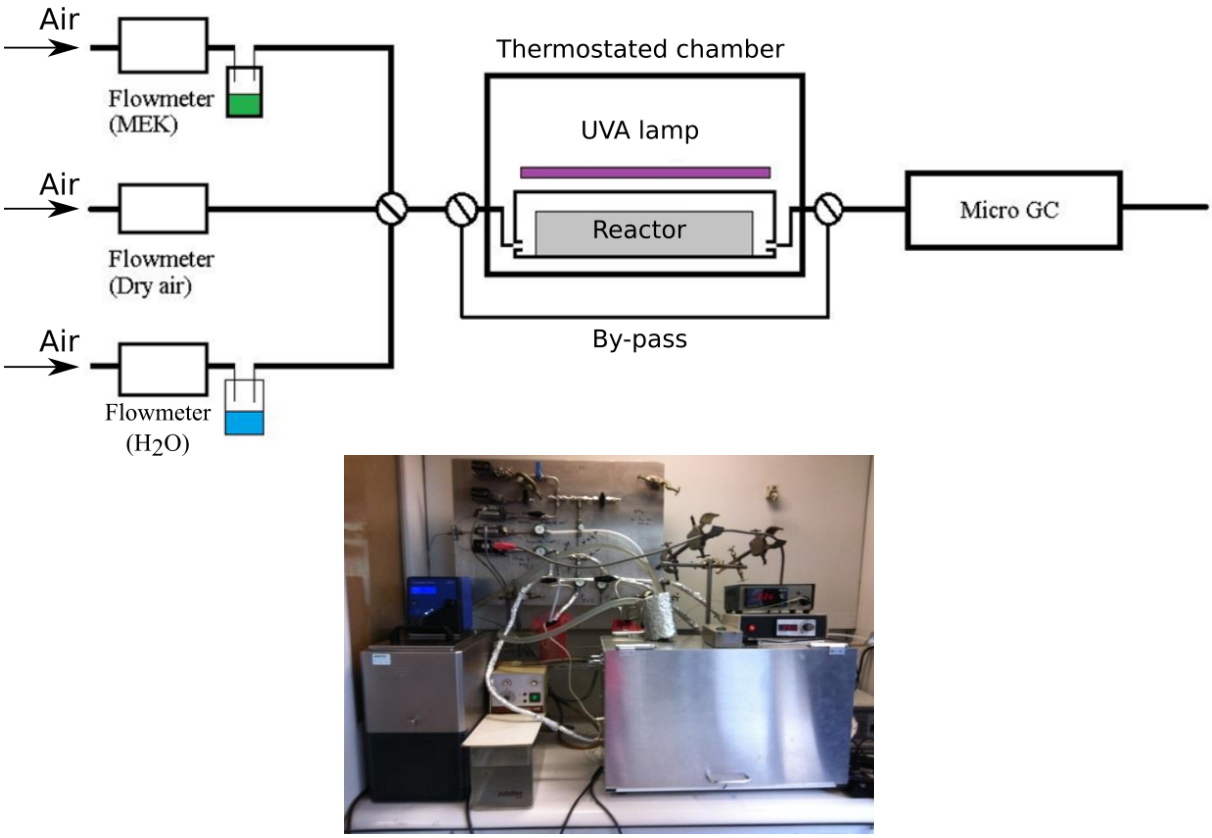

Fig 53 : Gas phase photocatalytic test set-up (photocatalytic degradation of MEK).

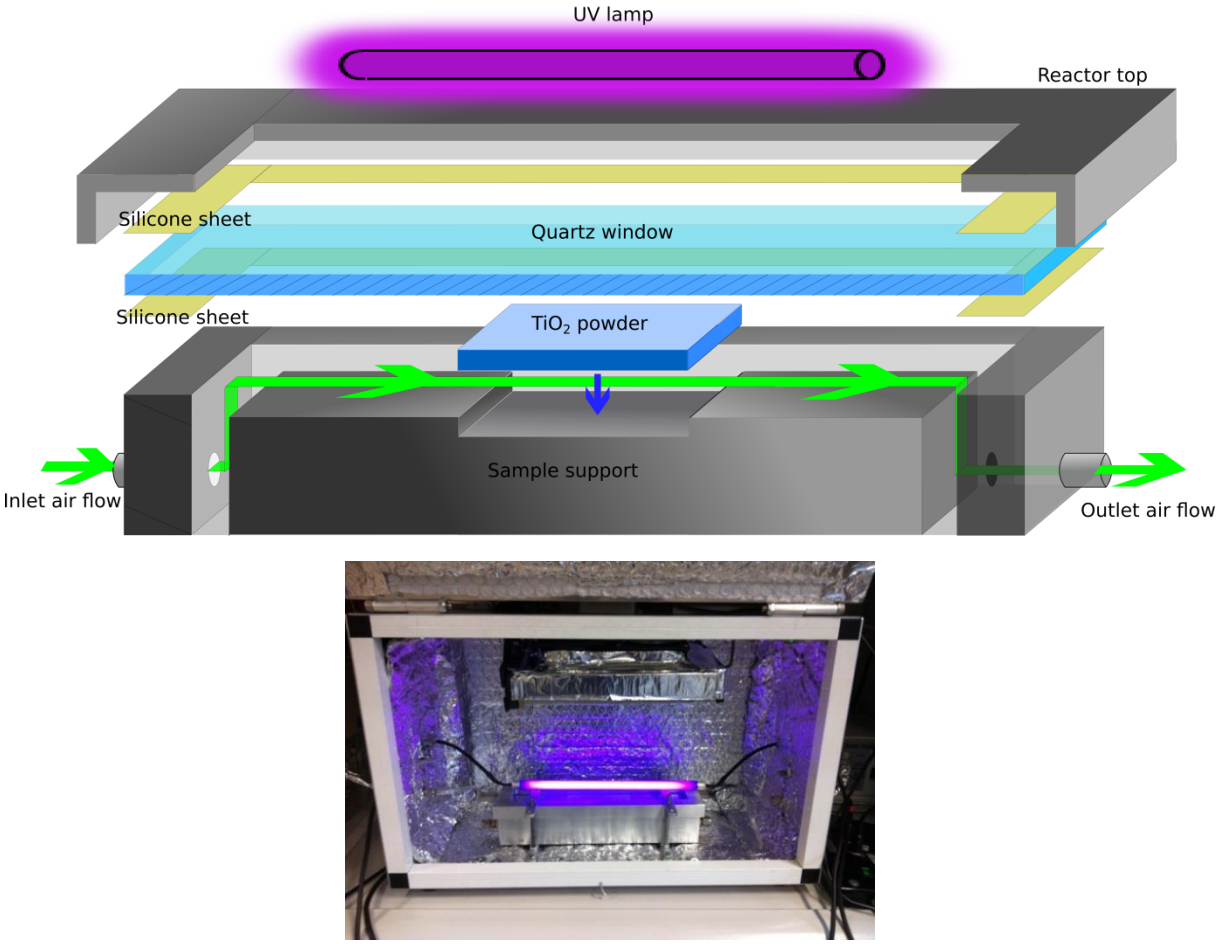

Fig 54: Reactor and thermostated chamber for the gas phase photocatalytic test

For preparing the samples, 50 mg of TiO_2 powder was evenly coated on a glass plate (100 mm length, 50 mm width and 3 mm thickness for fitting to the cavity on support) by dropping drop-wisely onto the glass plate and simultaneously evaporating TiO_2 ethanoic suspensions to dryness. Prior to that, the suspension was sonicated for 30 min and stirred overnight. Finally, the TiO_2-coated glass plates were dried at 100 ℃ for overnight. 50 mg of TiO_2 powder corresponded to a surface density of 1 mg/cm^2, previously determined as the optimized surface density for TiO_2 P25 and TiO_2 UV100 Hombikat powders in such operating conditions. [27]

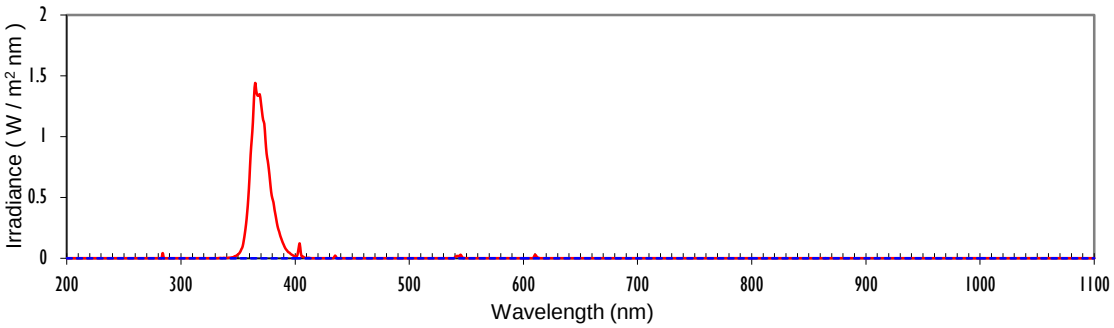

Fig 55 : Irradiance spectra of the UVA lamp used in this work.

By controlling each of the three air flow ways, the gas-phase photocatalytic degradation test were performed at an inlet MEK concentration of 100 ppmv, 50% of RH and a total air flow rate of 227 ml/min, corresponding to a velocity of 1.33 cm/s and a residence time of 7.5 s in the reactor (Table 25).

Fixed parameters	***Values***
MEK concentration	100 ppmv
RH %	50 %
Total flow rate	227 ml/min
Residence time	7.5 s
Air flow velocity	1.33 cm/s
Test temperature	25 ℃
UVA irradiance received at the sample surface	3.0 $mW.cm^{-2}$
TiO_2 surface density	50 mg/50 cm^2 (1 mg/cm^2)

Table 25 : Fixed test parameters for evaluating the photocatalytic activity of TiO_2 samples.

The photocatalytic performances were obtained by *on-line* quantifying both inlet and outlet flows using a 4-column R3000A gas micro-chromatography (SRA instruments), equipped with thermal conductivity micro-detectors (TCDs), allowing quantification of MEK, water, CO_2 and acetaldehyde. Carrier gas is Helium. The settings of each column are shown in Table 26.

Column name	*Stationary phase*	*Column temperature (°C)*	*Column pressure (psi)*	*Molecule detected/Retention time (s)*
MS5A [a]	Zeolite 5A molecular sieve	-	-	-
PoraPlot Q	Divinylbenzene Ethylene glycol	50	25	CO_2/38.3
Stabiliwax	Polyethylene glycol	105	25	MEK/32.2 H_2O/59.7
OV 1	Dimethylpolysiloxane	100	25	Acetaldehyde/106.0

[a] Not used in this work

Table 26 : Settings of columns for the gas micro-chromatography.

III.1.1.2. Calculations for evaluating the photocatalytic activity

The inlet polluted air flow rate was first stabilized on the "by-pass" zone located outside of the reactor. The photocatalysts were then exposed to the inlet polluted air flow with no illumination by switching the flow from the by-pass to the reactor. When dark adsorption equilibrium was reached, the UV-A illumination was switched on, and the illumination was carried on for about 3h before being switched off. A typical concentration profile recorded with time on TiO_2 P25 is shown in Fig 56.

The photocatalytic activity was expressed in terms of **MEK conversion (C_{MEK})**, which represents in percent the amount of degraded MEK over that of inlet MEK;

$$C_{MEK}(\%) = \frac{([MEK_{dark}] - [MEK_{UV}])}{[MEK_{dark}]} * 100$$

of **selectivity to acetaldehyde** as main reaction intermediate byproduct (S_{Ac}), **and to CO_2** as final oxidation product (S_{CO_2}), which represents in percentage the amount of carbon atoms converted into acetaldehyde and CO_2 over that of converted carbon atoms, respectively;

$$S_{Ac}(\%) = \frac{[Ac_{out}]}{([MEK_{dark}] - [MEK_{UV}]) * 2} * 100$$

$$S_{CO_2}(\%) = \frac{[CO_{2\ out}]}{([MEK_{dark}] - [MEK_{UV}]) * 4} * 100$$

as well as of **CO_2 mineralization yield** ($\mathbf{Y_{CO_2}}$), which represents in percentage the amount of carbon atoms converted into CO_2 over that of all available carbon atoms contained in the initial amount of inlet MEK;

$$Y_{CO_2}(\%) = \frac{[CO_{2\ out}]}{[MEK_{dark}] * 4} * 100$$

So, Y_{CO_2} represents the overall ability of the TiO_2 material to mineralize MEK into CO_2.

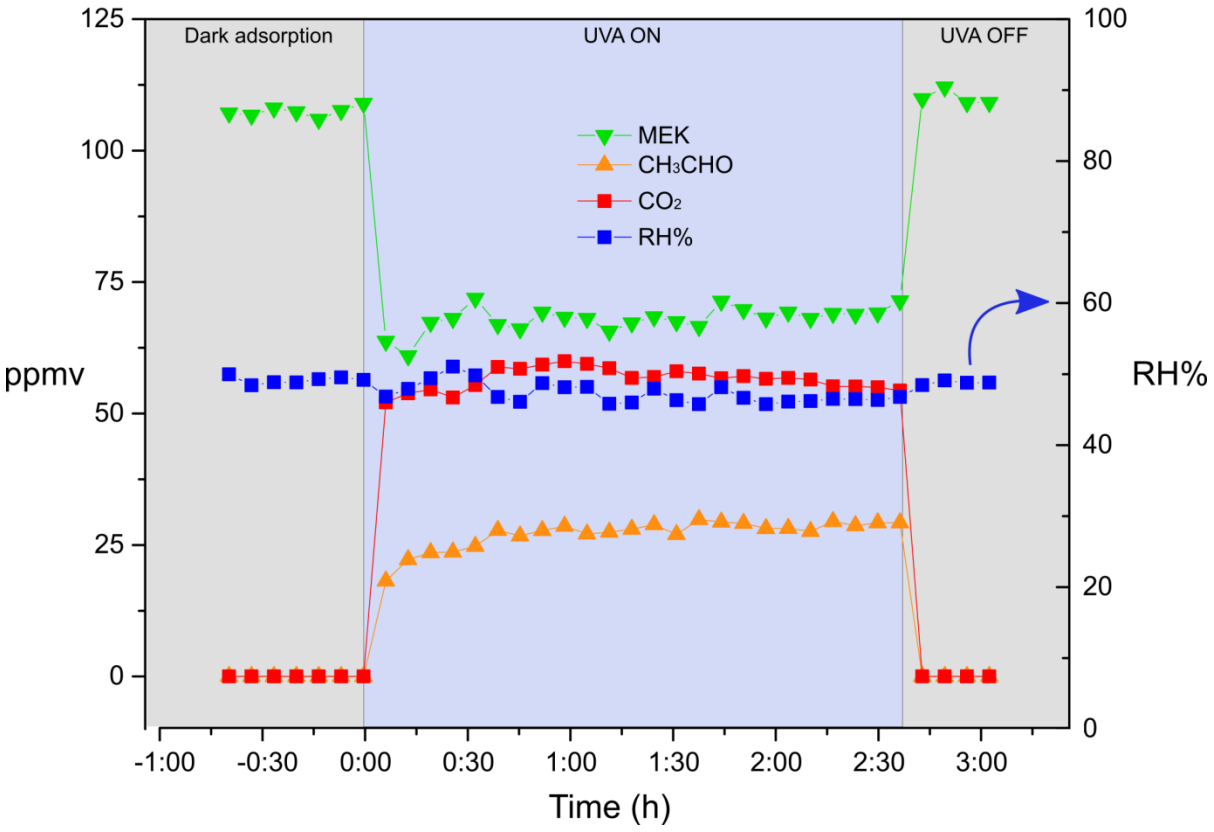

Fig 56 : Concentration profiles of MEK, acetaldehyde and CO_2 and RH as a function of time recorded for the gas phase photocatalytic test on TiO_2 P25

$[MEK_{dark}]$ is the average MEK concentration in ppmv of the last five measurement points of the dark adsorption equilibrium after illumination is switched off, $[MEK_{UV}]$ is the average MEK concentration in ppmv of the last five measurement points during the illumination period, $[CO_{2\ out}]$ is the average CO_2 concentration in ppmv of the last five

measurement points of the illumination period, and lastly $[Ac_{out}]$ is the average acetaldehyde concentration in ppmv of the last five measurement points of the illumination period. Average values were thus calculated each time over a time-period of 30 min. Each TiO_2 sample has been tested twice, so that the final photocatalytic results reported are the average of the two results.

III.1.2. Results of the gas-phase photocatalytic degradation of MEK

III.1.2.1. TiO_2 synthesized in HAc in the presence of $BmimPF_6$

The results of the gas-phase photocatalytic degradation of MEK for calcined TiO2 samples synthesized in HAc with different BmimPF6/Ti ratios (from 0 to 0.03) and with different aging durations (18h and 6 days) are presented in Fig 57 and Table 27. Performances achieved with the TiO2 P25 and the control sol-gel TiO2 synthesized in the absence of BmimPF6 are also reported as reference.

The TiO2 P25, as reference, shows a MEK conversion of 37 % with selectivities to CO2 and CH3CHO of 36 % and 34 % respectively, resulting in a CO2 mineralization yield of 13 %. It demonstrates a slightly higher activity than the ionic liquid-free sample that shows a MEK conversion of 32 %, and a resulting CO2 mineralization yield of 10 %. Considering that both materials have similar main characteristics in terms of specific surface area, crystallite size and crystallinity, the presence of anatase-rutile phase mixture in the P25 reference could be put forward for explaining the slight superiority of the P25 photocatalyst. 261 However, we know that the literature can be controversial when explaining the activity of the commercial P25 reference.

Generally, the TiO2 samples synthesized in the presence of BmimPF6 show higher activity in terms of MEK conversion and CO2 mineralization yield compared to TiO2 P25 and ionic liquid-free TiO2. Except for the “IL0.03 HAc 6d 550” sample that exhibits a higher selectivity, the CO2 selectivity is globally similar or lower to that obtained on TiO2 P25 reference (and ionic liquid-free sample), so that the overall higher performance in terms of CO2 mineralization yield shown by TiO2 synthesized with ionic liquid resulted mainly from the much greater improvement of MEK conversion. Indeed, for all IL TiO2 materials, MEK

conversions within the range 43-70 % were achieved, corresponding to CO2 mineralization yields within the range 14-25 %.

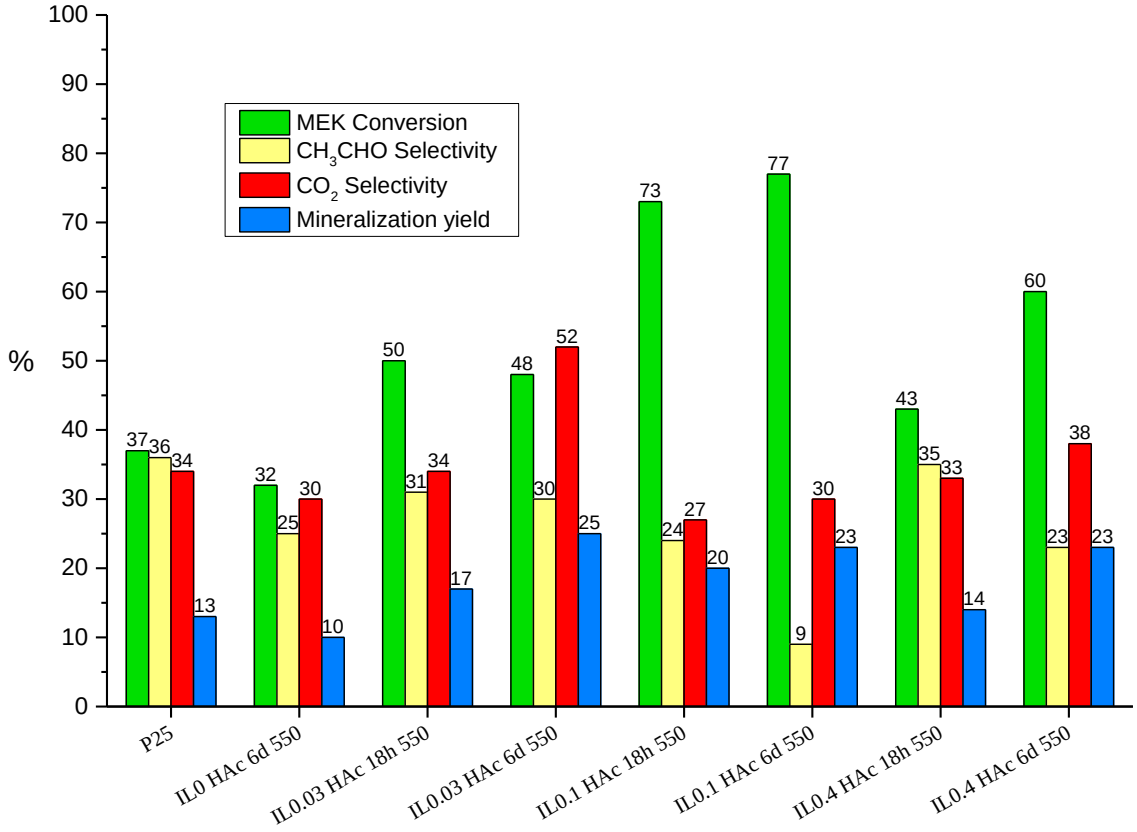

Fig 57 : Results of the gas-phase photocatalytic degradation of MEK for calcined TiO_2 samples synthesized in HAc with different $BmimPF_6$/Ti ratios, expressed in terms of MEK conversion, acetaldehyde selectivity, CO_2 selectivity and CO_2 mineralization yield in percents. P25 is the commercial reference to be compared with.

Note that whatever the above samples, the carbon balance was not closed by MEK, CO_2 and CH_3CHO. It means that other possible byproducts were formed along with CO_2 and CH_3CHO, but not detectable in our tests due to their small quantity or to the sensitivity of the μGC. Possible byproducts have been listed in chapter I.4.2.1 in the case of the photocatalytic degradation of MEK.

In a first approximation, except the "IL0.4 HAc 18d 550" sample, one can note that the higher specific surface area of TiO_2 synthesized with IL (and the inversely smaller mean crystallite size) is beneficial to the performance achieved. The higher MEK conversion could benefit from the higher specific surface area, as a good correlation between those two is reported in Table 27.

Sample name	*$BmimPF_6$/Ti molar ratio*	*Aging duration*	*BET surface area (m^2/g)*	*MEK conversion %*	*CO_2 selectivity %*	*CO_2 mineralization yield %*
P25	-	-	55	37	34	13
IL0 HAc 6d 550	0	6 days	50	32	30	10
IL0.03 HAc 18h 550	0.03	18 h	110	50	34	17
IL0.03 HAc 6d 550	0.03	6 days	97	48	52	25
IL0.1 HAc 18h 550	0.1	18 h	101	73	27	20
IL0.1 HAc 6d 550	0.1	6 days	109	77	30	23
IL0.4 HAc 18d 550	0.4	18 h	118	43	33	14
IL0.4 HAc 6d 550	0.4	6 days	96	60	38	23

Table 27 : Correlation between specific surface area and MEK conversion for all samples reported in Fig 57.

Another observation is that the photocatalytic activity of some ionic liquid assisted TiO_2 samples shows an aging duration-dependency. We compared the photocatalytic activity, especially the CO_2 selectivity and the CO_2 mineralization yield, of the IL0.03 and IL0.1 series samples aged for 18h (CO_2 selectivity of 34% and 27%; CO_2 mineralization yield of 17% and 20%) to that aged for 6 days (CO_2 selectivity of 52% and 30%; CO_2 mineralization yield of 25% and 23%) respectively: an increase of both photocatalytic activity indications has been evidenced along with the increase of the aging duration (Fig 57). We assume that this is not simply related to the change of specific surface area, because the different samples displayed approximatively a similar specific surface area and a similar mean crystallite size (Table 27). By contrast, we assume that this is rather related to the morphology change of TiO_2 crystals during the aging step which has been evidenced previously by TEM analysis. Crystal morphology has been reported to influence the proportion and the composition of different TiO_2 crystal facets resulting in different photocatalytic activities. [140, 262]

No correlation is observed between the amount of $BmimPF_6$ used during synthesis and the photocatalytic activity of the synthesized TiO_2 samples. It may imply different action modes of $BmimPF_6$ used in the sol-gel reaction medium in different concentrations, as this will be discussed in section III.1.3. Also, a detailed discussion of the correlation between the TiO_2 crystal morphology and its photocatalytic activity (especially in terms of CO_2 selectivity) will be presented.

Seen from the concentration profiles of MEK, acetaldehyde and CO_2 for all above samples (shown here is for the P25 sample in Fig 56 and the IL0.4 HAc 6d 550 sample in Fig 58), MEK conversion with production of CO_2 and acetaldehyde takes place immediately after

UVA is switched on. Blank test performed using a bare glass support has shown no activity (not shown here). Also no deactivation phenomenon has been recorded and all concentrations are fairly stable for 3h of UVA illumination. A longer test for 3 days of UVA illumination has been carried out on the "IL0.4 HAc 6d 550" sample, and no deactivation was observed neither. We think that the adsorbed intermediates (acetaldehyde, etc.), if any, do not affect the activity of the photocatalyst. Deactivation, also referred by others as fouling or poisoning of the catalyst would result in a gradual decrease in activity because all active sites are occupied. [138] Because no deactivation was observed, no post-test characterizations have been done on the photocatalysts in this part of the work to study the adsorbed species on the surface after the photocatalytic reaction.

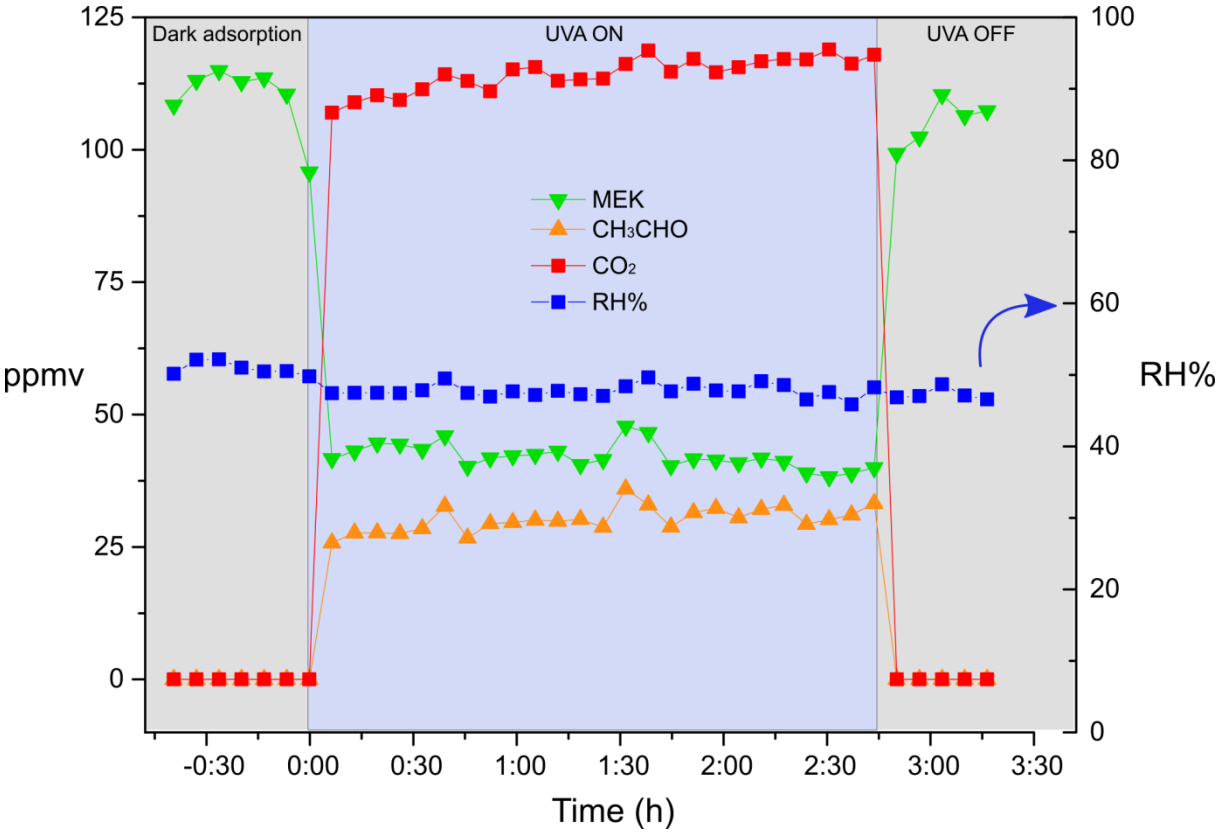

Fig 58 : Concentration profiles of MEK, acetaldehyde and CO_2 and RH as a function of time recorded for the gas phase photocatalytic test on IL0.4 HAc 6d 550

Photocatalytic tests on non-calcined samples have also been performed. No activity has been noticed whatever the samples regardless of the $BmimPF_6$ amount. One possible cause could be related to their relatively low crystallinity observed by XRD characterization, and the amorphous parts of the catalysts could act as charge recombination centers. TiO_2 samples synthesized in the presence of $BmimPF_6$ showed increased crystallinity before calcination, for

some of them with a crystallinity before calcination close to that after calcination, yet, no activity has been noticed for them neither. The possible cause will be discussed later in section III.1.3.

III.1.2.2. TiO_2 synthesized in HCl in the presence of $BmimPF_6$ and each constituent element of $BmimPF_6$

Results of the gas-phase photocatalytic degradation of MEK for calcined TiO_2 samples synthesized in the presence of $BmimPF_6$, BmimCl (BC), phosphoric acid (PA) and hexafluorophosphoric (PF) acid in HCl, are presented in Fig 59. The molar ratio of the additives to Ti is fixed at 0.03 and the aging duration is fixed at 6 days. The photocatalytic activity of TiO_2 P25 is also presented as reference.

To remind, the samples used in the section were elaborated in order to evidence the role of each constituent element of $BmimPF_6$ during the ionic liquid assisted TiO_2 sol-gel synthesis. HCl was chosen for an easy observation of the effects brought by phosphorus. As shown earlier, - except in the case we used PA as additive -, a phase separation phenomena was evidenced visually during the aging step for all other additives if HCl was used instead of HAc as acid catalyst, resulting in two kinds of solid obtained. The solid obtained from the sedimentation part of the reaction medium was excluded from testing, because it showed a reduced interest in terms of amount synthesized. In consequence, only the solid dried from the supernatant part of the reaction medium has been tested in this section.

The results indicate that the photocatalytic activity of TiO_2 P25 is the highest in terms of CO_2 selectivity and CO_2 mineralization compared to TiO_2 samples synthesized in HCl in the presence of additives, although it does not display the highest MEK conversion. All four tested samples have shown similar or lower photocatalytic activity compared to that of P25 in terms of yield. The three samples synthesized in the presence of phosphorus “IL0.03 HCl 6d 550 sup, PA0.03 HCl 6d 550 and PF0.03 HCl 6d 550 sup” have displayed a low photocatalytic activity. The “IL0.03 HCl 6d 550 sup” with similar crystallinity and mean crystal size compared to its HAc analogue (IL0.03 HAc 6d 550), showed even a nearly three times lower photocatalytic activity than that of its HAc analogue in terms of yield to CO_2. A similar observation was obtained for “PA0.03 HCl 6d 550” and “PF0.03 HCl 60 550 sup” samples. For the later, the CO_2 and acetaldehyde concentrations were lower than the µGC

detection limit. By contrast, the phosphorus-free "BC0.03 HCl 6d 550 sup" sample exhibited a photocatalytic activity similar to that of P25. This sample had a mean crystallite size of 20 nm close to that of P25, and displayed an anatase-rutile phase mixture (with 4% of rutile).

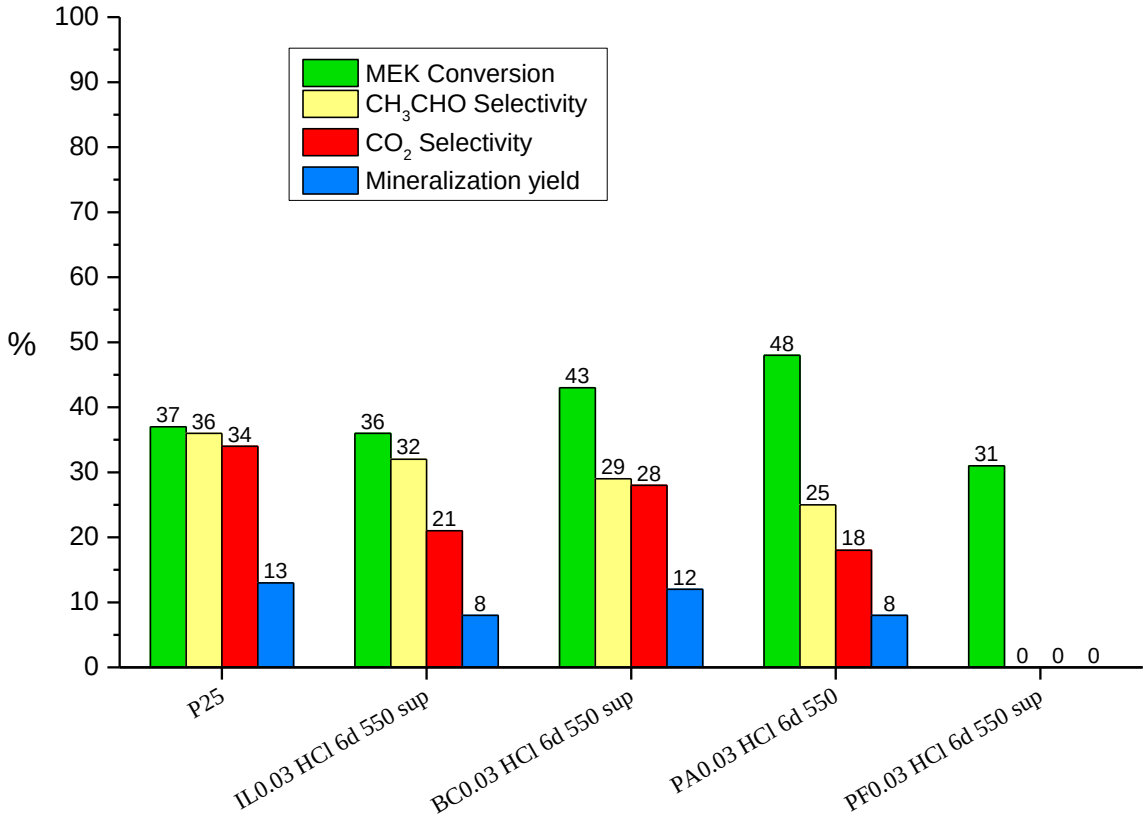

Fig 59 : Results of gas-phase photocatalytic degradation of MEK for calcined TiO_2 samples synthesized in the presence of $BmimPF_6$, BmimCl, phosphoric acid and hexafluorophosphoric acid in HCl, expressed in terms of MEK conversion, acetaldehyde selectivity, CO_2 selectivity and CO_2 mineralization yield in percentage. The molar ratio of additives to Ti is fixed at 0.03 and the aging duration is fixed at 6 days. For the syntheses with phase separation during the aging step in HCl medium, only the solid dried from the supernatant part was considered. P25 is the commercial reference to be compared with.

We have also tested the samples for which the additive to Ti molar ratio was increased to 0.4. All three phosphorus-involved samples have shown no photocatalytic activities (not shown here). Unfortunately, no activity results have been obtained for the "BC0.4 HCl 6d 550 sup" sample in order to compare with, because the excessive residue of BmimCl remaining in sample made the sample too sticky to be manipulated.

It seems that the use of phosphorus in HCl environment might have caused increasing detrimental effect on photocatalysts along with increasing phosphorus quantity. In comparison, Fan *et al.* [263] have incorporated P inside TiO_2 materials by adding a H_3PO_4

aqueous solution of different concentrations into a $TiCl_4$ precursor solution. They observed that the sample with an optimum P quantity containing 1mol% of phosphorus has shown the best photocatalytic activity, while a higher P content resulted in a decrease in the photocatalytic activity, due to the formation of titanium phosphate phase serving as charge recombination centers according to the authors. Also in comparison, Korosi *et al.* [253] have synthesized P-incorporated TiO_2 materials by adding H_3PO_4 into a hydrolyzed $Ti(OPr^i)_4$ precursor solution and they have attributed the low photocatalytic activity observed for the high P-content sample to the lower availability of anatase sites at the material surface. Both above-conclusions might explain the lower photocatalytic performance of TiO_2 materials synthesized in HCl in our case, yet a detailed explanation of this low photocatalytic activity and of the roles of HCl and phosphorus on the photocatalytic activity of TiO_2-based materials will be more developed in the III.1.3 section.

No deactivation phenomena have been observed throughout 3h of UVA illumination for all tests done in the section.

III.1.2.3. Ionic liquid-free TiO_2 synthesized in HAc in the presence of $BmimPF_6$ substitutes

In this section, the tested samples were synthesized using one combination of two $BmimPF_6$ replacement elements out of three. That includes phosphoric acid (PA) for providing the phosphorus element, sodium fluoride (NaF) for providing the fluorine element and BmimCl (BC) which provides The $Bmim^+$ ions. The objective was to search equivalent but much cheaper additives to $BmimPF_6$ for obtaining TiO_2 with equal photocatalytic performances.

Results of the gas-phase photocatalytic degradation of MEK for calcined TiO_2 samples synthesized in the presence of two additives among BmimCl (BC), phosphoric acid (PA) and sodium fluoride (NaF) in HAc, expressed in terms of MEK conversion, acetaldehyde selectivity, CO_2 selectivity and CO_2 mineralization yield in percentage are shown in Fig 60. The molar ratio of additives to Ti is fixed at 0.03 and the aging duration is fixed at 6 days. P25 is the commercial reference to be compared with.

The "BCPA0.03 HAc 6d 550" and "PANaF0.03 HAc 6d 550" samples exhibit high MEK conversion of 52% and 53% respectively, compared to that of P25 at 37%. Both samples displayed a higher specific surface area and a smaller crystal size than the P25 sample. The phosphorus-free "BCNaF0.03 HAc 6d 550" sample had a lowest MEK conversion, and displayed a lower specific surface area compared to phosphorus-based samples. A correlation between the MEK conversion performance and the specific surface area of concerned TiO_2 samples is listed in Table 28.

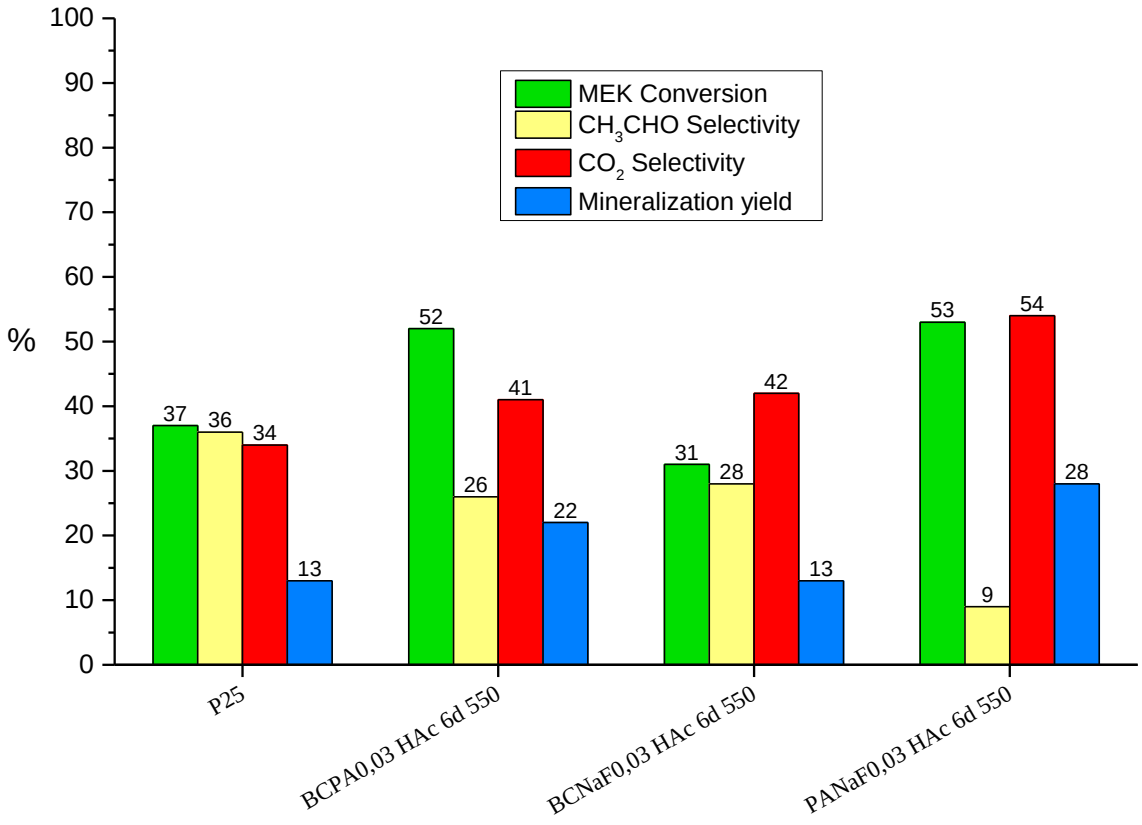

Fig 60 : Results of the gas-phase photocatalytic degradation of MEK for calcined TiO_2 samples synthesized in the presence of two additives among BmimCl (BC), phosphoric acid (PA) and sodium fluoride (NaF) in HAc, expressed in terms of MEK conversion, acetaldehyde selectivity, CO_2 selectivity and CO_2 mineralization yield in percentage. The molar ratio of additives to Ti is fixed at 0.03 and the aging duration is fixed at 6 days. P25 is the commercial reference to be compared with.

We did not evidence much of the role of $Bmim^+$ on the TiO_2 morphology in chapter II. Here, as well, the results obtained did not allow us to evidence a possible direct role of $Bmim^+$ on the photocatalytic activity of TiO_2. The "BCNaF0.03 HAc 6d 550" sample has shown a lower photocatalytic activity compared to P25, except for CO_2 selectivity, which is surprisingly high (42%) for a TiO_2 material that possesses a moderate specific surface area

and a large mean crystal size. If not by the presence of $Bmim^+$, this enhanced CO_2 selectivity might be caused by the fluorine element when NaF is used as an additive. Furthermore, besides of a high MEK conversion, the "PANaF0.03 HAc 6d 550" sample has the highest CO_2 selectivity (54%) and the lowest acetaldehyde selectivity (9%) as well, showing an excellent mineralization efficiency (28%) which is more than two times higher than that of TiO_2 P25 (12%). If the high photocatalytic activity of the "BCPA0.03 HAc 6d 550" sample compared to that of the "BCNaF0.03 6d 550" sample is due to the phosphorus-induced higher specific surface area effect, then the higher photocatalytic activity of the "PANaF0.03 HAc 6d 550" sample *vs.* that of the "BCPA0.03 HAc 6d 550" sample might **result from the presence of the fluorine element** in the synthesis medium when NaF is used as additive. A proposition of the role of the fluorine element in fluorine-assisted sol-gel synthesis of TiO_2 and of the effect of the fluorine element on the activity of TiO_2 will be detailed in the next III.1.3 section.

Sample name	***$BmimPF_6$/ Ti molar ratio***	***Aging duration***	***BET surface area (m^2/g)***	***MEK conversion %***	***CO_2 selectivity %***	***CO_2 mineralization yield %***
P25	-	-	55	37	34	13
BCPA0.03 HAc 6d 550	0.03	6 days	109	52	41	22
BCNaF0.03 HAc 6d 550	0.03	6 days	46	31	42	13
PANaF0.03HAc 6d 550	0.03	6 days	131	53	54	28

Table 28 : Correlation between specific surface area and MEK conversion for all samples reported in Fig 60.

It is worth noticing that the photocatalytic activity performances of the "PANaF0.03 HAc 6d 550" sample are not only the highest ones among TiO_2 samples synthesized with the use of $BmimPF_6$ replacement additives, but also are slightly superior to the performance achieved over the most active ionic liquid-assisted TiO_2 sample (IL0.03HAc 6d 550). This indicates that only the combination of phosphorus and fluorine elements can result in a comparable or even higher photocatalytic activity than that obtained on samples synthesized in the presence of $BmimPF_6$. It also proves that the high photocatalytic activity of samples synthesized in the presence of $BmimPF_6$ might result from the presence of phosphorus and fluorine elements in $BmimPF_6$. The high photocatalytic performance of the "PANaF0.03 HAc 6d 550" sample has demonstrated a feasible and facile approach of replacing expensive ionic liquid for targeting large scale TiO_2 nanomaterial production process.

However, it is noteworthy that a "PANaF" sample has been specifically synthesized with only one modification consisting in the increase of the P to Ti ratio from 0.03 to 0.4 (no changes in other parameters including the non-changed F to Ti ratio). No photocatalytic activity in MEK oxidation was observed (not shown here). Considering the weak crystallinity of this sample shown in Fig 47 green, we can hypothesize that the use of too much phosphorus might result in the formation of too much amorphous TiO_2 phase as well as in a titanium-phosphate-based phase acting as charge recombination centers or blocking the access to active TiO_2 phase.

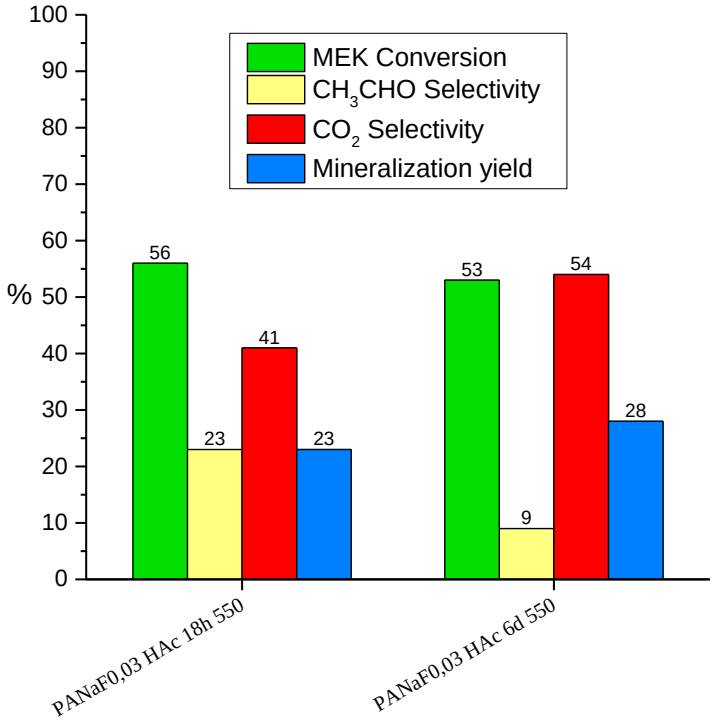

Fig 61 : Results of the gas-phase photocatalytic degradation of MEK for the "PANaF0.03 HAc 18h 550" and the "PANaF0.03 HAc 6d 550" samples, expressed in terms of MEK conversion, acetaldehyde selectivity, CO_2 selectivity and CO_2 mineralization yield in percentage. The molar ratio of additives to Ti is fixed at 0.03, the only variable parameter is the aging duration (18h and 6 days).

Remember that the "IL0.03" and "IL0.1" series TiO_2 samples have shown an aging duration-dependence for both CO_2 selectivity and CO_2 mineralization yield. Here, a similar behavior has been evidenced for the "PANaF0.03" series TiO_2 samples (18h *vs* 6 days of aging duration). A longer aging duration of 6 days has resulted in a CO_2 selectivity of 54% and a CO_2 mineralization yield of 28%, whereas by contrast the shorter aging duration of 18h has resulted in a CO_2 selectivity of 41% and CO_2 mineralization yield of 23% (Fig 61). For

now we just have identified that phosphorus and fluorine elements could be responsible for the interesting TiO_2 morphology properties and the enhanced photocatalytic activity, and we believe that the action of those two elements on the TiO_2 crystal morphology mainly occurred during the aging step of the synthesis. In section III.1.3, we will discuss on the detailed action mode of phosphorus and fluorine elements during the $BmimPF_6$ or PANaF assisted TiO_2 sol-gel synthesis, especially during the aging step.

No deactivation phenomena were observed over samples tested in this section, therefore no post-test characterizations have been performed.

Photocatalytic tests have also been performed on the non-calcined analogues of the above-mentioned samples. No activity has been noticed for the samples regardless the additive amount used. Again, one possible cause could be related to their relatively low crystallinity observed by XRD characterizations. The amorphous part of the catalysts served as charge recombination centers. TiO_2 samples synthesized in the presence of phosphorus showed an increased crystallinity before calcination, in some cases close to that of the calcined samples; yet, no activity has been noticed for them either. This will be discussed later along with the explanation of the synthesis mechanism and the combined roles of phosphorus and fluorine during the $BmimPF_6$ assisted sol-gel synthesis of TiO_2.

III.1.3. Phosphorus- and fluorine- induced modification of TiO_2 properties and correlation with photocatalytic activity

Phosphorus and fluorine are evidenced to be the two elements in $BmimPF_6$ involved in the sol-gel synthesis of TiO_2 nanomaterials when HAc was used as acid catalyst. Derived from the previously reported characterizations and photocatalytic activity tests of TiO_2 materials, we have noticed three major impacts of the presence of phosphorus and fluorine from additives or from $BmimPF_6$ that influenced the physico-chemical properties of TiO_2 and affected the photocatalytic behavior.

1. The photocatalytic activity of TiO_2 samples synthesized in the presence of phosphorus and fluorine from additives or from $BmimPF_6$ showed an **aging-duration dependency**.

2. The photocatalytic activity (especially the CO_2 selectivity) of TiO_2 samples synthesized in the presence of phosphorus and fluorine from additives or from $BmimPF_6$ was influenced by a **fluorine-induced crystal shape modification** effect dependency.
3. The photocatalytic activity (especially the MEK conversion) of TiO_2 samples synthesized in the presence of phosphorus and fluorine from additives or from $BmimPF_6$ showed a dependency with a **phosphorus-induced size effect**.

In this section, we will investigate the influence of phosphorus and fluorine from additives or from $BmimPF_6$ on the properties and the photocatalytic activity of TiO_2, by discussing the three above-specified relationships consecutively. In each discussion, action mode and reaction mechanism of the related element on the formation of TiO_2 nanocrystals during the synthesis, and their impact on the TiO_2 photocatalytic activity, will be studied. Although efficient TiO_2 nanomaterials were synthesized using HAc as acid catalyst, the influence of HCl on TiO_2 properties and the resulting activity will be briefly discussed at the end as well.

III.1.3.1. Room-temperature aging effect

It was showed by the BET and XRD analyses that we had an aging duration-dependent crystal size evolution in TiO_2 sol-gel synthesis at room-temperature. Generally this evolution was manifested by a decrease in the BET specific surface area, an increase in the XRD peak intensity and the mean crystallite size, when the aging duration was increased. We assumed that the crystallinity and crystal size variation resulted from a room temperature self-crystallization process of TiO_2 in solution during the aging step.

Conventionally, most of the crystallization processes of TiO_2 material from amorphous to anatase were achieved and studied in high-pressure and high-temperature hydrothermal conditions, although studies have reported possible low-temperature sol-gel approaches for synthesizing anatase crystals by aging the sol. For example, Seo *et al.* [264] have synthesized anatase or mixed-phase anatase/rutile TiO_2 nanocrystalline powders by aging NaOH-treated powders in boiling water or HCl solution at 60 ℃. However, the temperature applied in that work was still above room-temperature, and they have not mentioned if whether the TiO_2 powders were photocatalytically active or not. Qi *et al.* [265] were able to synthesis anatase

nanocrystals by sol-gel reaction in an aqueous acetic acid medium followed by aging the sol at "true" room-temperature for 24h. They claimed to get a better anatase crystallinity compared to the previous similar works, and they have reported an anatase TiO_2-coated cotton fabric with significant photocatalytic activity for degrading Neolan Blue 2G, red wine and coffee stains under UV irradiation. However, unfortunately, no comparison with commercial TiO_2 photocatalysts was reported. Although they have used similar reagents (TTIP, acetic acid) and similar room-temperature aging duration, the visual observation during their reaction differs from the present work. In detail, they have aged the milky reaction medium for a week and were able to obtain a transparent sol after aging, from which the anatase TiO_2 powder was extracted by adding sodium carbonate aqueous solution until precipitation occurred.

By contrast, in the present work, in a typical case such as the synthesis of the "IL0 HAc 6d" sample, for which no ionic liquid was used, no transparent sol has been obtained; sedimentation of the white solid occurred throughout the whole aging period, resulting after 6 days of aging in the evidence of a thick layer of a white solid at the bottom of the beaker. No further precipitation operation was required to obtain TiO_2 powders, as the solid powders were simply filtered from the solution. Similar observations were confirmed for all TiO_2 syntheses performed in the present work in which a aging step has been applied. As example, the sedimentation occurring for "PANaF0.03 HAc 6d" can be visualized in Fig 62.

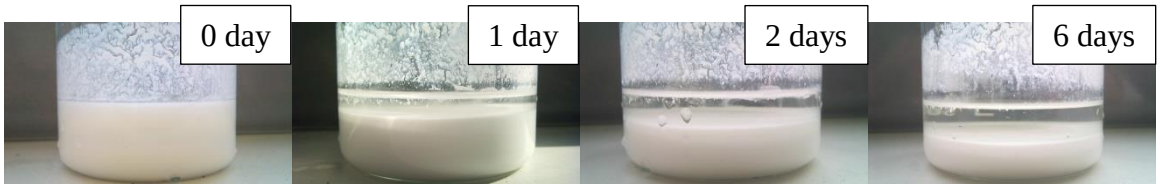

Fig 62 : Sedimentation evolution with aging duration for the "PANaF0.03 HAc 6d" sample.

In none of the above works about synthesizing anatase TiO_2 crystals by aging the sol at room temperature, the authors have explained the crystallization mechanism. However, many propositions of crystallization mechanism for many inorganic oxides in different solution conditions have been putted forward by researchers from the inorganic crystal engineering field. [266, 267] In one recent review about crystal growth of inorganic functional materials, [268] Zhang *et al.* stated that the classical growth of crystals occurs through atom-by-atom or monomer-by-monomer addition to an inorganic or organic template, or through the dissolution of unstable phases (small particles or metastable polymorphs) and re-precipitation

of the more stable phase. This implies, in the case of TiO_2, that amorphous TiO_2 formed upon hydrolysis of the Ti precursor would go re-dissolution and re-crystallization to achieve amorphous to anatase phase transition, which has been evidenced in the work done by Ayral *et al*. [206, 207]

It is known that in the sol-gel process, TiO_2 is usually formed through hydrolysis and polycondensation of titanium alkoxides, $Ti(OR)_n$ to form oxopolymers, which are then transformed into an oxide network *via* dehydration and dealcoholation mechanisms. [269] In our particular sol-gel synthesis, we hypothesize a mechanism underlying in the aging duration-dependent TiO_2 crystal growth as follows: as water with a relatively high H_2O/Ti molar ratio of 9.5 was added into the TTIP/isopropanol solution, TTIP was hydrolyzed immediately, before the formed $Ti(OR)_{n-x}(OH)_x$ started quickly to condense for forming the initial Ti-O-Ti network, observed as a white precipitate (polymerization form of $Ti(OR)_{n-x}(OH)_x$). It is also known that for a particular solvent, there is a certain solubility for a solute, and any excess solute will result in the precipitation and the formation of small nanocrystals serving as nucleation seeds; crystallization subsequently happens from those seeds. Normally, with the coordination ability and the specific adsorption of HAc on TiO_2, [196, 270] monodispersed and small amorphous TiO_2 nanoparticles would be able to be stabilized and these very small size nanoparticles could serve as heterogeneous nucleation sites for the further crystallization. However, we hypothesize that only *via* HAc, those nucleation seeds are not enough protected from being re-dissolved in acidic environment, thus they are more likely involved in a re-dissolution/re-crystallization equilibrium. This hypothesis is supported by the relatively low crystallinity of anatase TiO_2 crystals aged for 6 days (confirmed by the XRD spectra of "IL0 HAc 6d" sample in Fig 23 A) compared to the expected crystallinity of TiO_2 in the case of a non-limited continuous crystal growth process. The crystallinity of this sample is similar to that of the sample reported by Qi *et al*., [265] who claimed to have prepared one of the more crystallized anatase TiO_2 samples ever synthesized at room-temperature. In addition, our reaction medium contains continuously white TiO_2 solute (as it can be visualized), which makes the solution supersaturated along the course of the aging period, so that the crystallization process should not be limited by a possible lack of solute during the aging step. Compared to studies reporting on similar TiO_2 sol-gel syntheses using HAc and water, [264, 265] for which lower crystallinity TiO_2 materials were synthesized, we might propose that no better crystallized anatase TiO_2 nanocrystals might be obtained thanks to only HAc and an

appropriate aging duration at room temperature. This results probably from the non-stability of nucleation seeds which prevents the formation of better crystallized crystals in a limited time.

A schematized explanation that we hypothesized to illustrate the room temperature crystallization mechanism of TiO_2 during the aging step in the aqueous acetic acid medium is presented in Fig 63. Note that this schema does not represent directly the atoms and their arrangement, but is rather conceptual and represents small size tridimensional Ti-O-Ti chains for the titanium oxide network in different polymerization degrees and in different orders of arrangement:

a. Initial condensation to form polymerized Ti-O-Ti chains;
b. Those chains could go re-dissolution to form smaller size segments of chains in acidic condition;
c. Seeds of nucleation could be formed by ordered arrangement of those small segments;
d. If those seeds are stabilized, crystallization can occur from the seeds by re-arranging the rest of small chains in a ordered manner to minimize energy.

In most of the cases for TiO_2 synthesized *via* a traditional sol-gel route, highly porous amorphous TiO_2 materials were obtained when no calcination was applied, and final calcination was then required for transforming amorphous TiO_2 into crystalline phases like anatase or rutile. Generally the temperature-induced phase transformation comes along with a brutal crystal size increase and a sharply diminished porosity if a high temperature is used (550 ^oC being considered as relatively high for forming anatase). We hypothesize that, as a longer aging duration usually leads to more crystallized materials already before calcination, it might be expected that the longer-aged samples would benefit from a lower crystal size increase during the calcination step, since the already crystallized materials do not grow the way that the amorphous materials do. This was one of the reasons why the longer-aged samples possess superior resistance against heat treatment than the shorter-aged samples. Relatively small but well crystallized TiO_2 nanocrystals might result from samples aged for a longer duration. This size advantage can have a very important influence on the photocatalytic activity of the sample, as small crystals provide a higher specific surface area and a better crystallinity provides less crystal defects which are often considered as acting as charge recombination centers.

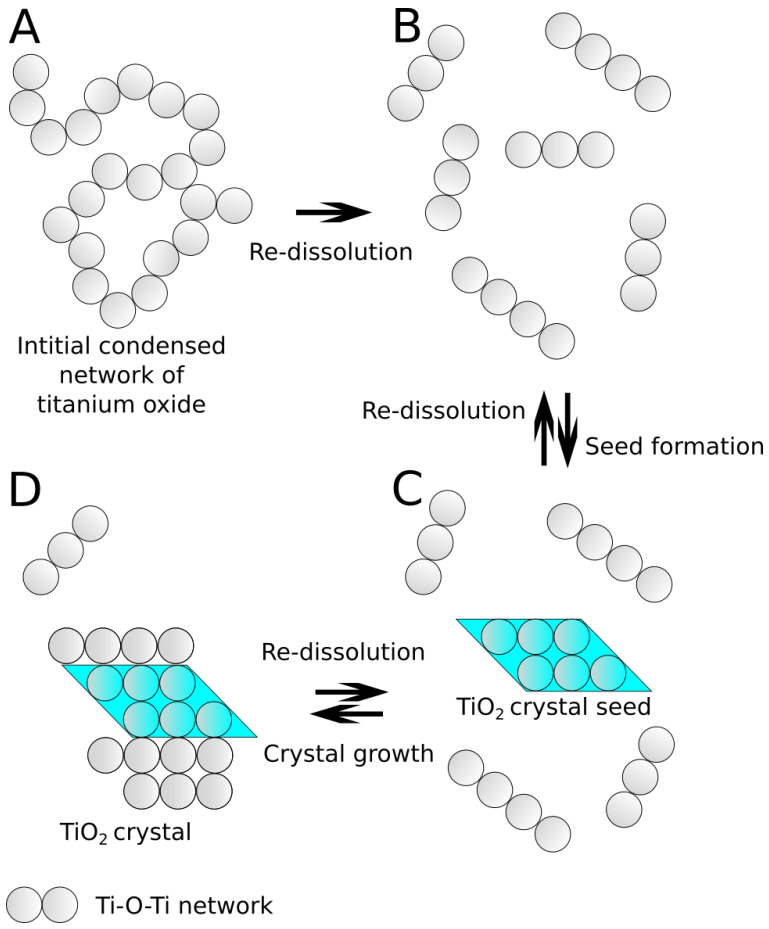

Fig 63 : Schematic illustration of the room temperature crystallization mechanism of TiO_2 without IL and additives during the aging step in acetic acid aqueous medium. Note that this schema does not represent the atoms and their arrangement, but is rather conceptual and represents small size tridimensional Ti-O-Ti chains for the titanium oxide network in different polymerization degrees and in different orders of arrangement.

It was worth noting that the use of $BmimPF_6$ or of phosphorous-containing additive (phosphoric acid) led already before calcination to a better crystallinity and also to a more homogeneous crystal size distribution compared to the "IL0 HAc 6d" sample, as if it could boost the crystallization rate. We would like to point out that the superior crystallization rate of the IL-derived samples was obtained with a $BmimPF_6$ to Ti molar ratio of 0.03, because the mean size of the crystals, at about 8 nm for the dried sample, did not increase further beyond 10-11 nm during calcination. This sample displayed the smallest crystal size increase during calcination. It is very noteworthy that the same behavior was observed for the "PANaF0.03 HAc 6d" sample, as phosphorus played an identical role mentioned previously. Maybe those advantages have contributed to their highest photocatalytic activities. We have already identified that the phosphorus element was the element responsible for the better crystallized anatase TiO_2 nanocrystals before calcination, as well as for the reduced crystal size with narrow distribution of TiO_2 after calcination. Thus we might propose that the phosphorus

might have taken actions on size modifications of TiO_2 nanocrystals during the aging step, and this will be discussed in further section III.1.3.3.

Fluorine was suspected to cause TiO_2 crystal shape, *i.e.* morphology change, at the origin of an enhanced CO_2 selectivity. The corresponding action mode is hypothesized to occur during the aging step also, and this will be discussed in further section III.1.3.2.

The high efficiency TiO_2 samples were all synthesized using HAc as acid catalyst. However, interesting properties have been observed when HCl was used instead of HAc. We think that in HCl, the aging mechanism was totally different compared to the case with aging in HAc. This was responsible for the much lowered photocatalytic activity obtained even when IL or the same additives were used. Both the action mode of the different additives to the TiO_2 synthesis in HCl medium and the influence of the acid catalyst used on the photocatalytic activity of TiO_2 samples, are not topics to be discussed in this chapter, because the use of HCl shows less interest in the large scale production of efficient photocatalytic TiO_2 nanomaterials; also we did not perform enough specific study to evidence/establish a correlation between the HCl-induced properties of TiO_2 and the resulted photocatalytic activity.

III.1.3.2. Effect of fluorine on TiO_2 properties and photocatalytic activity

The TEM images of the IL-derived TiO_2 samples after heat treatment not only confirmed their smaller crystallite sizes calculated from XRD patterns, but also showed a unique shape evolution with the increasing aging duration. The example of the "IL0.03 HAc" series sample, aged from 18h to 6 days, has been shown in Fig 28, in which the shape turned from the irregular round-like shape to more square-like shape, with sharper and more visible crystals. We related this shape evolution to the capping ability of fluoride ions provided by the ionic liquid to the reaction medium during the synthesis. [216, 219, 241, 246, 262, 271-273]

The thermodynamically unstable {001} facet usually represents a minority facet for anatase TiO_2 crystals, but it has been shown that the {001} facet is much more reactive than the thermodynamically stable {101} facet, exposed as the majority facet of anatase TiO_2. [274]

The fluoride ions in acidic media are known to be adsorbed more easily compared to hydroxyl ions or other ions on the highly reactive {001} facet of the TiO_2 crystals. [219] This facet-selective adsorption of fluoride ions could lower the surface energy of the {001} facet, which was attributed to the lower bonding energy of F-F (158.8 kJ/mol) in the case of a fluorinated surface against that of H-H (436.0 kJ/mol) and O-O (498.4 kJ/mol) in the case of a fluoride-free surface. [219, 246] So the crystals were likely to grow along the lower energy, more stable fluoride-covered {001} facet instead of along the thermodynamically more stable fluoride-free {101} facet, to form a thin truncated bipyramid crystal shape (Fig 13, page 45). This could explain the clear observation on the TEM images of the largely exposed square {001} facet, thanks to their thin square-like plate shape. [262]

Unfortunately, we could not perform HRTEM analysis on dried TiO_2 samples synthesized in the presence of $BmimPF_6$ in HAc medium because of the PhD schedule concern. However, we performed HRTEM analysis on dried TiO_2 samples synthesized in the presence of phosphoric acid/sodium fluoride ("PANaF") in HAc medium, and we have noticed the small size rod-like shape of the nanocrystals (showed in Fig 52) instead of the typical defect-free and isolated "truncated bipyramid"-shaped nanosheets obtained in related papers. [219, 241] We were unable to record higher magnification TEM images further to evidence the crystal lattice fringe other than the visible one following {101} direction (d = 0.35 nm). Still, we suppose that the shape of the crystals might reflect the capping and tuning effect of fluorine on the TiO_2 crystal growth despite the shape of our nanocrystals is much different to that reported in many of papers using fluorine for the engineering of TiO_2 crystals. In most of those papers, the authors used hydrofluoric acid (HF) to control the anisotropic growth of TiO_2 crystals in hydrothermal condition. However, the shape and morphology of the resulted crystals are reported to be sensible to parameters such as the fluoride concentration, the hydrothermal temperature, the reaction duration, and the pH value of the solution. [216, 227, 275] For example, Zhang *et al*. [275] have obtained rod-like anatase crystals instead of bipyramid sheet-like crystals in HF solution at 180 ^oC at relative higher pH values. As a consequence, at room-temperature and atmospheric pressure, it might be expected that the action mode of fluoride on the control of TiO_2 crystal growth and the resulting crystal shape or morphology are much different than in hydrothermal conditions.

To our knowledge, crystal shape control on TiO_2 anatase crystal by using fluoride-derived capping agent in mild conditions (room-temperature and atmospheric-pressure sol-gel synthesis) has never been reported, so great difficulty might be expected when comparing our TiO_2 crystal morphology to that demonstrated in many papers. We were unable to obtain clear HRTEM images on the $BmimPF_6$-free "IL0 HAc 6d" dried sample which could result from the relatively low crystallinity of the sample. Therefore it is unfortunate to not be able to compare the crystal morphology with and without the presence of fluorine.

In the cases where calcined TiO_2 nanocrystals were obtained with the participation of fluorine-containing additives ($BmimPF_6$ and NaF), we did not observe the typical perfect "truncated bipyramid" shape nanosheets neither (Fig 27 and Fig 51). Still, fluorine-induced formation of {001} facets were evidenced in HRTEM images of calcined TiO_2 samples synthesized with the $BmimPF_6$ or with the combination of phosphoric acid/sodium fluoride (IL0.03 HAc 6d 550 and PANaF0.03 HAc 6d 550 respectively). The lattice fringe details in each of those two samples are presented in Fig 64. Relatively large {001} and {200} lattice fringe coverage compared to that of {101} indicates at least that the growth of {101} facets was indeed inhibited. Calcination-induced crystal morphology evolution will be discussed in detail in the section III.1.3.3 as it might be influenced by the presence of the phosphorus element.

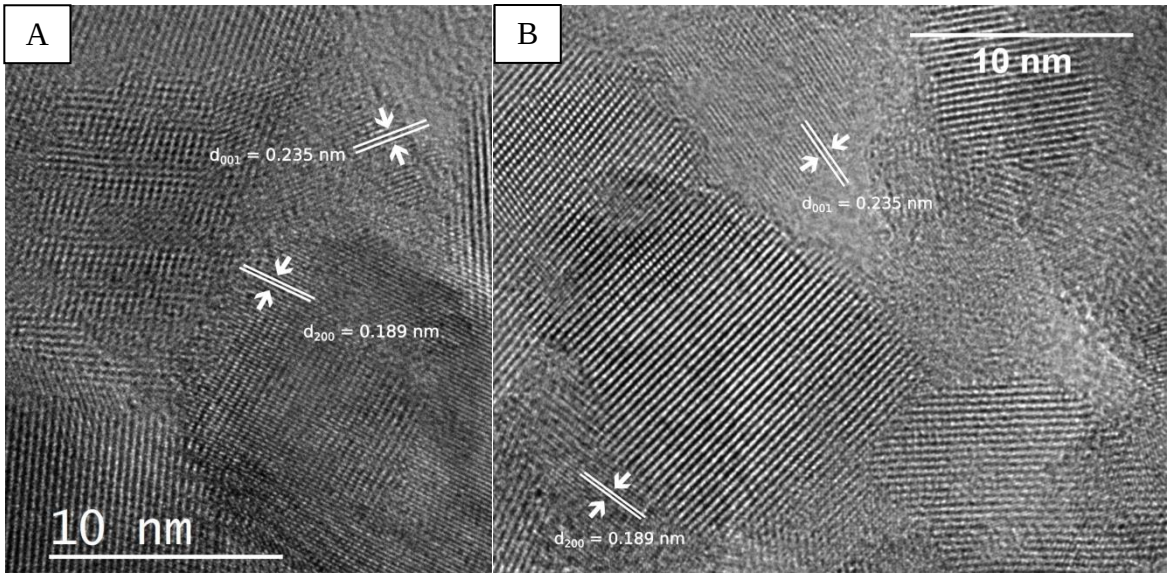

Fig 64 : HRTEM images and lattice fring details of «IL0.03 HAc 6d 550 »(A) and «PANaF0.03 HAc 6d 550 » (B) samples.

We think that the fluoride ions are involved in the aging step along with the aging-induced crystallization process. In the case of $BmimPF_6$, the only fluoride source must be the PF_6 ions of the ionic liquid. In early studies devoted to $BmimPF_6$, it has been reported that the hydrolysis of $BmimPF_6$ into phosphate anions and HF can take place in acidic solution. [228, 276] In our case, traces of F have been observed by XPS in $BmimPF_6$-derived samples before heat treatment, which was a clue that the PF_6 ion could be hydrolyzed in our acidic reaction medium (pH around 4). However, the kinetic of this hydrolysis in our case was unknown.

The $BmimPF_6$ hydrolysis equilibrium can be proposed as follows:

$$PF_6^- \overset{H^+,\ H_2O}{\longleftrightarrow} PO_4^{3-} + 6F^-$$

In the case of the PANaF-derived samples, the action of fluoride during the aging step is proposed to be more direct than in the case of the IL-derived samples, since fluoride ions released by NaF are available in solution from the beginning of aging. Indeed, this would differ from the synthesis with $BmimPF_6$ ionic liquid (being described as a very stable chemical compound), so that we can assume that the hydrolysis of $BmimPF_6$ could be considered as a rate-limiting step in the release process of fluoride ions. We did not observe fluorine traces *via* XPS for the "PANaF0.03 HAc" series probably because of a too low fluorine amount. Heat treatment at 550 ^oC was necessary to remove fluorine traces in terms of safety concern of the product.

The largely exposed {001} facets of anatase TiO_2 crystals are hypothesized to increase the gas-phase photocatalytic activity in the degradation of MEK according to two general aspects.

First, recombination of photogenerated electrons and holes was reported to be inhibited by spatial separation of redox sites, as photogenerated electrons and holes selectively migrate to specific exposed crystal faces (anisotropic electron flow). [277] Tachikawa *et al.* [140] have used a single-molecule, single-particle fluorescence approach to show that the oxidation reaction mainly occurs on the {001} facets, while the reduction reaction mainly occurs on the {101} facets. In fact, the preferential photogenerated electron flow towards {101} has been predicted by density functional theory (DFT) calculations with the conduction band potential of anatase (101) being slightly lower than that of anatase (001). [218] This prediction is in agreement with

the observation that the exposed (101) facet being a highly reactive surface for the reduction of molecular O_2 (good electron acceptor) to superoxide radical anions and for the selective deposition of platinum. [278] However, a too large ratio between exposed {001} to {101} area could decrease the photocatalytic activity due to unbalanced oxidation-reduction site number. [279] We assumed that in our case: (i) the degradation of MEK is mainly done by sequential oxidation reactions taking place on the highly oxidant 5-coordinated Ti sites on anatase TiO_2 {001} facets where hole-related oxidizing radicals such as OH• could be mainly generated with the presence of water; while (ii) {101} facets generate mainly electrons which would be picked up by oxygen to form moderate oxidant superoxide radical anions, thus ensuring good electron evacuation.

So in consequence, anatase TiO_2 crystals with enlarged but not over-exposed {001} facets are expected to reduce the charge recombination and thus to enhance the overall photocatalytic oxidation of MEK in our work. Here shown in the Fig 65 is the schematic representation of an anatase TiO_2 single crystal with largely exposed {001} facets, and the resulting spatial charge separation effect.

Secondly, the highly reactive {001} facet can favor adsorption for certain VOC molecules. [280] Although we did not find studies on preferential adsorption of MEK on different anatase crystal facets, we did however find reports showing favored dissociative adsorption of methanol [217] and formaldehyde [281, 282] on the {001} facet by using density functional theory (DFT) calculations, thanks to the presence of 5-coordinated Ti and 2-cordinated O atoms.

These molecules were not detected as intermediate products from the photocatalytic degradation of MEK in our tests, but formaldehyde exhibits chemical similarities with acetaldehyde (the confirmed intermediate product). Thus we hypothesize that a higher percentage of exposed {001} facet would result in a higher acetaldehyde adsorption rate, and therefore a higher probability for performing a full mineralization of MEK into CO_2. This may explained the increase in the CO_2 selectivity coincident with the increase in the aging duration, for the $BmimPF_6$ or fluorine derived sample series ("BCNaF" and "PANaF" sample series), as a longer aging contributed to a larger {001} facet percentage.

Note that the increased $BmimPF_6$ quantity used did not further increase the CO_2 selectivity for the IL-derived TiO_2 sample synthesized in HAc: it was possible that the lowest

$BmimPF_6$ quantity (in this work a molar ratio of 0.03) could already release enough fluoride ions to saturate the adsorption sites on the {001} facets of TiO_2 crystals, thus making no difference in terms of photocatalytic activity regardless the quantity of $BmimPF_6$ used.

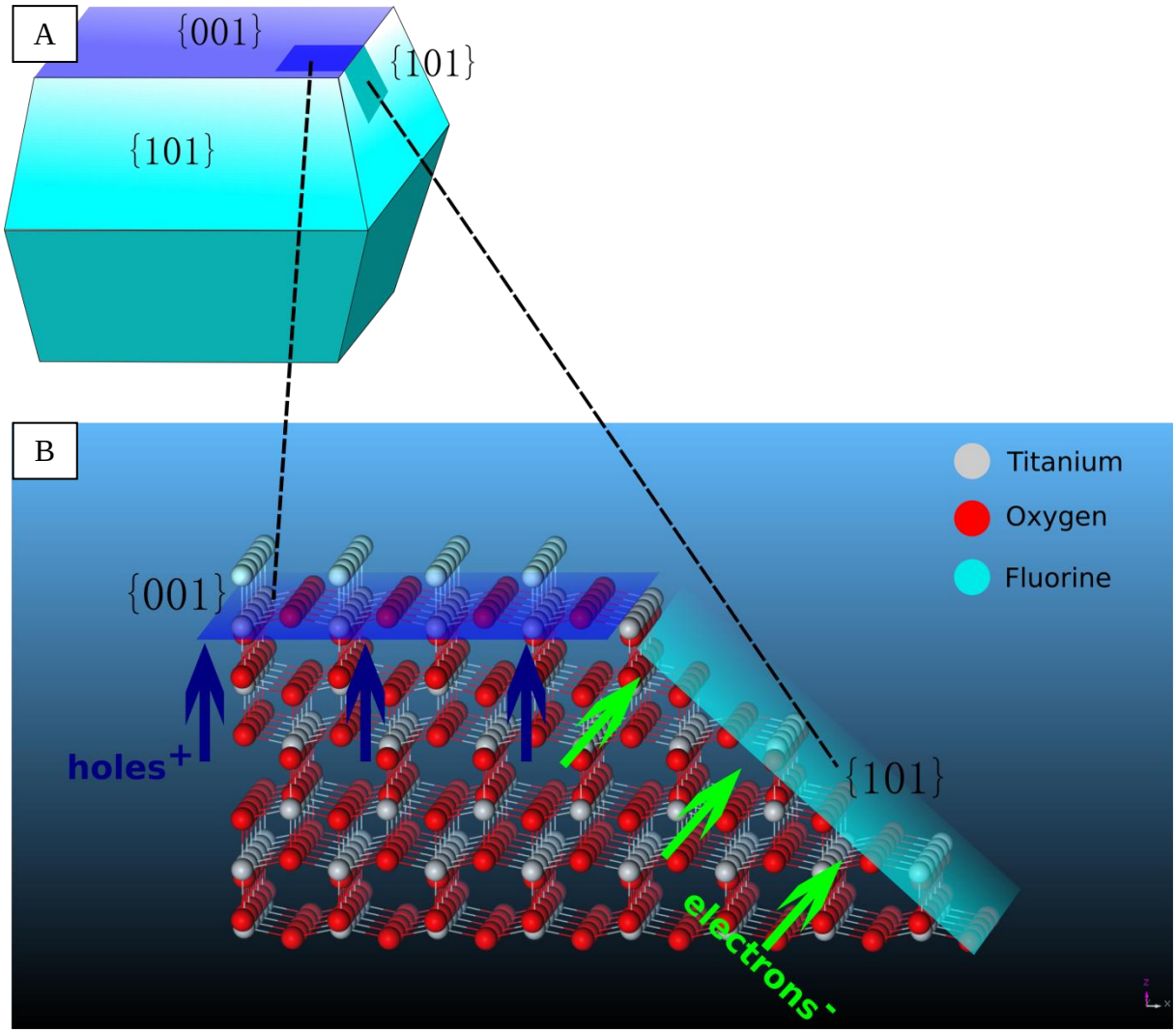

Fig 65 : Schematic representation of an anatase TiO_2 single crystal with largely exposed {001} facets (A), and a scaled-up illustration of the resulted idea spatial electron-hole charge separation effect near an intersection of {001} and {101} facets, the {001} facet is covered by fluoride anions after fluorination (B).

In conclusion, the fluoride ions released from $BmimPF_6$ or NaF played a role as TiO_2 anatase crystal shape capping agent during the aging step by increasing the most reactive facet surface percentage. CO_2 selectivity was able to be increased with. Although the fluoride ions can alter the shape of the TiO_2 crystals, yet, they are not known to have ability to decrease the size of the anatase TiO_2 crystals. In the next section, the roles of the last, but probably the most important element, phosphorus, on TiO_2 during the aging step will be highlighted.

III.1.3.3. Effect of phosphorus on TiO_2 properties and photocatalytic activity

Thermal resistance of P-involved TiO_2 materials

From our XRD, BET and TEM characterization results for the calcined P-involved TiO_2 samples synthesized in HAc medium (TiO_2 samples of the "$BmimPF_6$", "BCPA" and "PANaF" series), it seemed that the presence of the phosphorus element, even at a relatively low level (P/Ti = 0.03), is responsible for a smaller crystal size (around 10 nm) and a larger specific surface area (around 100 m^2/g) compared to the P-free samples ("IL0 HAc" series). We hypothesized that this results in the enhancement of the MEK conversion rate of the TiO_2 samples. This has been scarcely reported. We have proposed a phosphorous-induced thermal-resistance in terms of crystal size growth inhibition during the calcination, for TiO_2 samples synthesized with $BmimPF_6$ or any phosphorus-containing additives. According to us, this is the most important feature brought by phosphorus, since without phosphorus, calcined TiO_2 samples do not show any high specific surface area and any high MEK conversion rate. A larger specific surface area can increase the number of adsorbed molecules and of reactive sites at the surface of an heterogeneous catalyst, allowing to enhance the conversion.

Step of the phosphate action during the synthesis of P-involved TiO_2 samples

Comparing the phosphorus-involved "IL0.03 HAc" and "PANaF0.03 HAc" sample series after aging and the phosphorus-free "IL0 HAc" sample, the presence of phosphorus has resulted in a faster and better crystallization of TiO_2 crystals during the aging step. However, both specific surface area and crystallinity of the calcined IL-/PANaF-derived TiO_2 samples are similar, no matter the aging duration. So, in terms of photocatalytic activity for the calcined phosphorus-involved TiO_2 samples, the aging duration did not seem to influence the MEK conversion rate, between calcined samples aged for 18h and 6 days (Fig 57 comparison between "IL0.03 HAc 18h 550" and "IL0.03 HAc 6d 550"; Fig 61 comparison between "PANaF0.03 HAc 18h 550" and "PANaF0.03 HAc 6d 550"). A greater CO_2 selectivity - thus a greater overall photocatalytic performance - was however previously noticed and discussed as a result of the effect of the presence of fluoride during the aging step. Therefore we can say that the positive effect brought by phosphorus on the enhanced overall photocatalytic activity of the IL- and PANaF-derived samples were simply determined by the initial presence of phosphorus and not by the action of phosphorus during the aging step. Thus in terms of action

timing of phosphorus in the phosphorus-involved TiO_2 syntheses, we think that the positive effect of the use of phosphorus would be already provided at the beginning of the aging.

XRD analysis of high level phosphorous-involved samples for which the P/Ti molar ratio was increased to 0.4 has revealed crystalline phases other than TiO_2, and consisting in titanium poly-phosphate phases ($Ti_5O_4(PO_4)_4$ for TiO_2 synthesized with high $BmimPF_6$/Ti ratio in HCl medium, and in $Ti_4P_6O_{23}/TiP_2O_7$ phases for TiO_2 synthesized with high PA/Ti ratio in HAc medium). XPS analysis confirmed the formation of poly-phosphate phase at the surface of the above samples. The strong modification of the surface chemical environment of the high-amount-P-involved TiO_2 samples suggested a strong Ti-PO_4 interaction, and with a high affinity between Ti and P centers. For the P-TiO_2 sample with a low P/Ti ratio, we hypothesize that the Ti-PO_4 interaction takes place but with more dispersed phosphate centers. The origin of the phosphate anions in the reaction medium in the case of the "BCPA" and "PANaF" series samples is directly the phosphoric acid, while for IL-derived TiO_2 samples, phosphate anions were proposed to be released through the hydrolysis of $BmimPF_6$ along with the release of the fluoride anions. Also, we remember in an early test where phosphoric acid was the sole additive causing a white precipitate formation immediately after addition, when different additives (BmimCl, HPF_6, H_3PO_4 or $BmimPF_6$) were added to the transparent sol resulting from TiO_2 sol-gel synthesis in HCl. This precipitate was believed to result from a direct chelation of Ti by phosphate anions. Furthermore, if $BmimPF_6$ or HPF_6 was added instead of H_3PO_4, no transparency change of the sol was noticed initially; however, heating the solution at 80^0C resulted in the appearance of a white precipitate. It is believed that this later phenomena was caused by the heat which has accelerated the hydrolysis of the PF_6 ions, and the phosphate ions upon release reacted immediately with the hydrolyzed titanium hydroxyls to cause the Ti-PO_4 precipitation. The above observation indicates that the Ti-PO_4 precipitation was formed immediately upon contact of just-released phosphate with the titanium precursor, prior to the formation of a Ti-O-Ti network by condensation of the hydrolyzed titanium precursor in strongly acidic sol-gel synthesis medium. We think that the same behavior (with Ti-PO_4 interaction prior to Ti-O-Ti condensation) occurs during all the P-involved TiO_2 syntheses, no matter the amount of P or the type of acid used.

P-action mode during aging in the case of IL in HAc and of PA in HAc media

If we suppose that the action of phosphorus in the phosphorus-involved TiO_2 syntheses is taking place before the aging step, then we believe that the chelation of titanium by

phosphates marks the beginning of the action of phosphorus. Here, let us discuss about the detailed action mode of the phosphorus element in both cases, where $BmimPF_6$ was used in HAc medium, or where H_3PO_4 was used as one of the additives in HAc medium.

Using $BmimPF_6$ in HAc medium

The reaction begins with the hydrolysis of the Ti precursor and that of $BmimPF_6$ at the same time when the water was added into the solvent. This makes that the $(Ti(OR)_{n-x}(OH)_x)$ hydrolyzed titanium precursor species, partially released phosphate and fluoride ions in the reaction medium from the start (co-existence of ions). The fluoride ions usually do not have the chelating ability to bind to more than one titanium atom, while Ti-PO_4 chelation takes place first. Titanium phosphate bond is thought to be very stable, and such a material was shown to resist to high temperature treatment. [256] In our case, Ti-PO_4 formation was evidenced after calcination at 550 ^oC. So we think that it is less probable for such a material to undergo re-dissolution in an acidic medium like it could happen to condensed Ti-O-Ti network described early in the section III.1.3.1. As a result, the aforementioned re-dissolution/re-crystallization equilibrium for the condensed Ti-O-P-O-Ti network (thanks to Ti-PO_4 interaction) is strongly shifted towards re-crystallization through the aid of phosphorus. In another way to say, if the condensed Ti-O-P-O-Ti polymers serve as nucleation centers for further crystal growth, the suppression of re-dissolution direction favors the stability of the future nucleation sites. We believe that in the early stage of the aging step, a large number of Ti and phosphate centers reacted, since the phosphate ions and the newly formed Ti-O-P-O-Ti centers were very well dispersed thanks to the coordination ability and specific adsorption of HAc. Thus by the combined effect of HAc and phosphorus, a large number of Ti-O-P-O-Ti clusters were generated in the beginning of the $BmimPF_6$ assisted sol-gel synthesis, and those future nucleation centers were preserved in large number, because the stability of the Ti-PO_4 bonds prevents from their dissolution. Note that the mean crystal size of P-involved TiO_2 samples (*e.g.* PANaF-derived TiO_2 synthesized in HAc medium) did not significantly grow during the aging step, with a mean size after 18h of aging already of about 7-8 nm, which is close to the final size after calcination of about 11 nm. This suggests that the initial crystallization of Ti-O-P-O-Ti already occurred after 18h (even if partially), and the room-temperature crystallization process continued with aging time with the progressive re-arrangement and crystallization of Ti-O-Ti chains. As a result, the crystallinity of crystals further increased during aging. If provided that the raw Ti material quantity was similar at the beginning of the crystallization whatever the synthesis condition, a larger number of

phosphorus-induced stable Ti-O-P-O-Ti nucleation centers results in a smaller final crystallized crystal size compared to the synthesis with no phosphorus-contained additives. Combined with the fact that the amount of amorphous materials remaining after aging is very low, they are the main reasons why the $BmimPF_6$ or phosphoric acid assisted TiO_2 samples possessed a smaller mean crystal size and a larger BET specific surface area, thus allowing to achieve a higher MEK conversion rate than on phosphorus-free TiO_2 samples. As normally without any ionic liquid or phosphorus-containing additives, there could be only relatively less stable Ti-O-Ti polymerized clusters whose numbers was possibly decreasing throughout the aging-timeline.

Using H_3PO_4 as one of the additives in HAc media

The action mode and the influence of phosphorous on the TiO_2 crystal growth is believed to be similar to the case where $BmimPF_6$ was used. Except that this time, the whole amount of phosphate ions was already available at the beginning of the crystallization process. This is thought to be an advantage, since even a faster formation and an earlier stabilization of the Ti-O-P-O-Ti nucleation centers is expected, which might lead to a better final crystallization for TiO_2 nanocrystals.

Location of phosphates in the TiO_2 crystals

Because of the presence of titanium phosphate species in the bulk of TiO_2, the dried TiO_2 material could be actually seen as nanocomposite of anatase TiO_2 with the titanium phosphate. Concerning the location of the phosphates, XPS studies estimated that the P/Ti surface molar ratio for "PANaF0.03 HAc 6d" was 0.06, although theoretical P/Ti molar ratio was supposed to be 0.03. The higher effective P/Ti molar ratio means that the concentration of phosphates at the surface is higher than that in the bulk of TiO_2 crystals. Then, XPS analysis has been performed on the calcined sample and evidenced that the P/Ti surface molar ratio increased to 0.09. This increase can result from a migration of the phosphates from the bulk to the surface, and/or from a growth/sintering of titanium phosphates at the surface. Elghniji *et al.* [283] have observed that, at a high temperature (above 550 ^oC), phosphorus inside the bulk of TiO_2 starts to migrate to the surface. In our case for "PANaF" series at a P/Ti molar ratio of 0.03, the XRD analysis did not evidence any titanium phosphate phase, even at a calcination of 800 ^oC (Fig 47 red). The reason could be that the titanium phosphates remained not crystallized enough or formed too small domains for being detected by XRD. For the IL-derived samples, regardless of the $BmimPF_6$/Ti molar ratio, only slight traces of phosphorus were detected in

calcined or non-calcined samples (XPS analysis). This could be due to the even smaller quantity of phosphate ions partially released by $BmimPF_6$ used in synthesis, compared to the case where the same PA/Ti ratio was used.

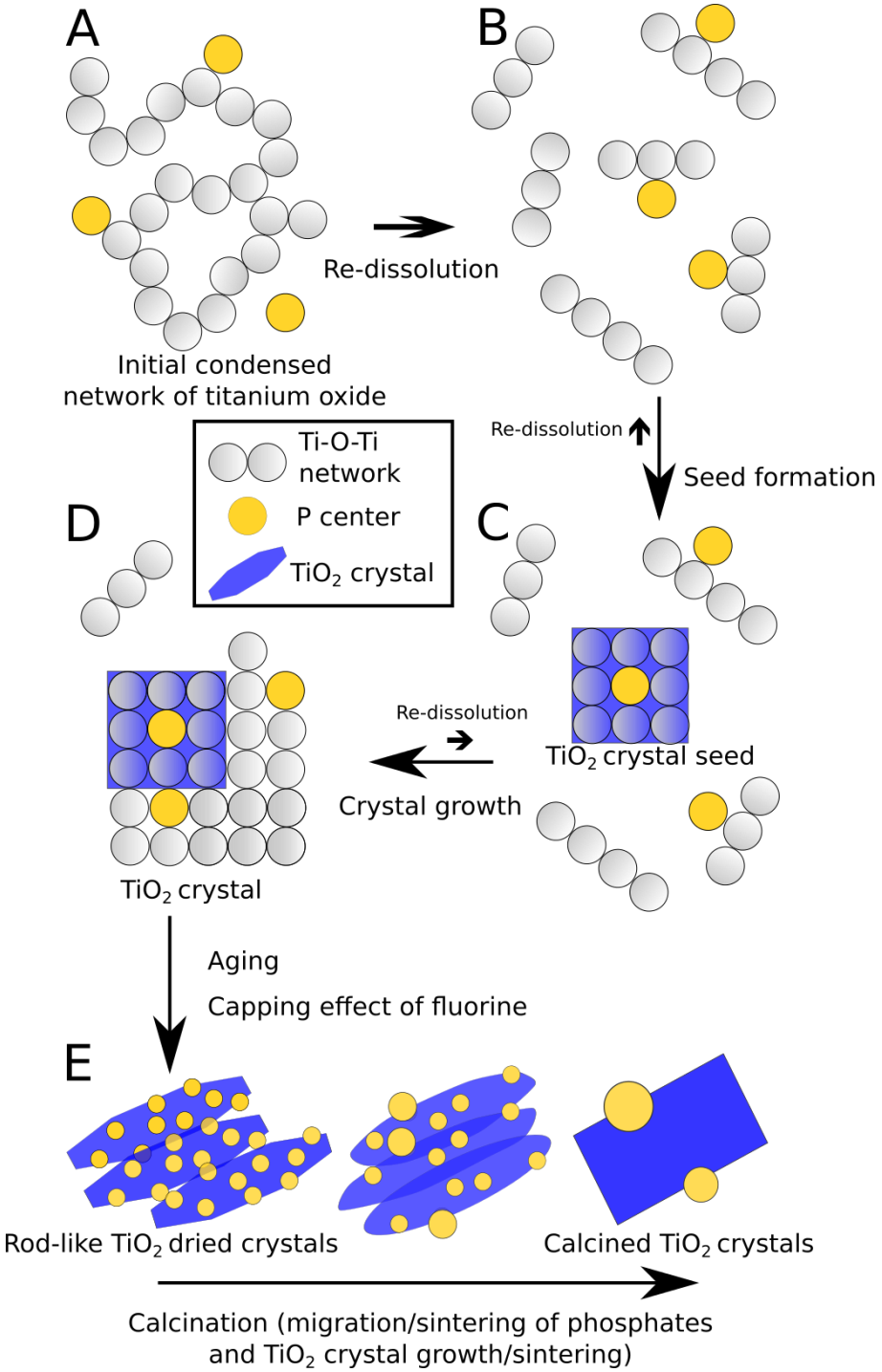

Fig 66 : Complete proposed explanation of the action mode of phosphorous on TiO_2 synthesized in HAc medium during aging step and calcination process.

P-induced charge separation effect

No significant difference in terms of anatase crystallinity, crystallite size and surface area was observed between the dried and the calcined samples for P-involved TiO_2 materials. So, this could not be putted forward for explaining the absence of MEK conversion for the dried samples compared to the sample calcined at 550 ^oC. We prefer to highlight the role of phosphate species, and to put forward the phosphate-related change occurring during the calcination, as discussed above. Before calcination, we proposed that the phosphates are well dispersed in the TiO_2 materials, more concentrated at the surface of TiO_2 crystals than in the bulk. Negatively charged phosphate anions have been reported being capable to attract photogenerated holes, thus preventing electron-hole recombination. [250] Too many titanium phosphate sites in dispersed state could play a role of charge recombination centers in TiO_2 because of the lack of general spatial charge separation effect. This is hypothesized to explain the non-activity shown by the dried P-involved TiO_2 samples synthesized in HAc medium ("IL", "PANaF" and "BCPA" series). By contrast, for the calcined P-involved TiO_2 samples, the migration of phosphates from bulk to surface could result in a better spatial separation of phase (TiO_2 *vs* Ti-PO_4 phase). In other words, the titanium phosphate phase would be less dispersed within the TiO_2 crystals. This would result in a better spatial separation of charge carriers. Along with the P-induced smaller size effect for TiO_2 nanocrystals, P-induced (and F-induced) spatial charge separation effect is proposed to be responsible for the strong increase in the photocatalytic activity.

Explanation of the crystal evolution during the calcination of P-derived TiO_2

Beside the phosphate distribution change caused by calcination, crystal shape and size were also changed for all phosphorus-involved TiO_2 samples. Again, taking "PANaF0.03 HAc 6d" sample as example, spindle/rod-like nanocrystals were visualized by TEM images before calcination (Fig 52), with a mean length near 10 nm and a mean width around 3-4 nm, while after calcination at 550 ^oC, the crystals changed of morphology to a larger spherical shape with a mean diameter around 12 nm (Fig 51 B). We can note that the length of the crystal did not grow too much upon calcination compared to the increase in width. This could be seen here as a crystal growth only along the direction of width. Since the crystallinity of the crystal before calcination was already rather good, we do not think that the crystal width could increase so much (up to nearly three times) by converting amorphous TiO_2 in small amount. We propose that the crystal growth during calcination may be caused by the sintering

of several already-crystallized crystals along the direction of the length. As example, this means a final spherical TiO_2 crystal with a diameter of 12 nm could schematically result from the sintering of three rod-like-shape crystals stacked together along their length direction during calcination. Although a decrease in the specific surface area after calcination was inevitable with the sintering, the photocatalytic activity of the TiO_2 nanocrystals was still enhanced due to the change of the phosphate distribution state occurring simultaneously. A proposed complete explanation of the action mode of phosphorous on TiO_2, resulting in the modification of the TiO_2 properties, is illustrated in Fig 66.

III.1.3.4. Proposed combined roles of fluorine and phosphorus on TiO_2 properties and photocatalytic activity

By combining the above separated investigation on the roles played by phosphorus and fluorine elements, a full mechanism of the $BmimPF_6$-assisted TiO_2 sol-gel synthesis in HAc medium can be proposed and described as follows: first, the titanium precursor was hydrolyzed by water to yield $Ti(OR)_{n-x}(OH)_x$ network. Meanwhile the PF_6 ions from $BmimPF_6$ were hydrolyzed as well to yield phosphate and fluoride ions. Quickly thanks to the coordination ability of HAc, small size Ti-O-Ti networks were generated and immediately drew the nearby phosphate ions to form very stable Ti-O-P-O-Ti clusters through strong Ti-O-P bonds, preventing the newly-formed nucleation centers from being re-dissolved in acidic reaction medium. As the room temperature crystallization process began during the aging step, more randomly-arranged Ti-O-Ti networks begin to re-arrange and crystallize into anatase phase, increasing the crystallinity. At the same time, the fluoride ions, released along with the phosphate anions from the hydrolyzed $BmimPF_6$, preferentially interact with the 5-coordinated Ti sites located on the {001} facets of the newly formed anatase TiO_2 nanocrystals. The fluoride ions lowered the surface energy of the {001} facets, resulting in a crystal growth preserving and exposing the {001} facets. This mechanism is taking place till the end of the aging step when nearly all amorphous networks were converted to anatase phase. The anatase TiO_2 crystals after aging remained small and well crystallized thanks to the formation of stable and highly dispersed nucleation seeds in large number. Upon calcination, the migration of phosphates from bulk to surface and/or the phosphate sintering resulted in less dispersed, larger size phosphate phases, while a limited mean crystal size

growth and a possible crystallite stacking were observed. So the TiO_2 photocatalyst could be considered as anatase-titanium phosphate composite.

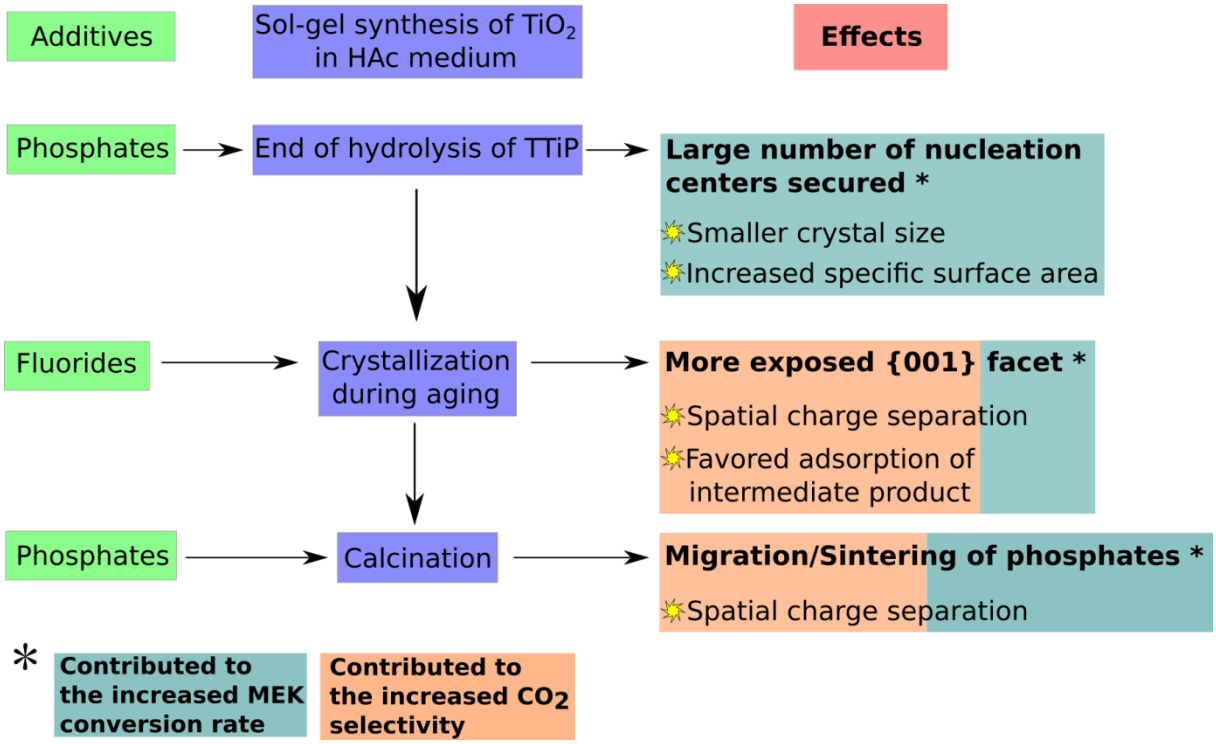

Fig 67 : Schematic explanation of the proposed combined roles of phosphorus and fluorine elements in sol-gel synthesis of TiO_2 in HAc medium, their effects on the TiO_2 properties and on the photocatalytic activity enhancement.

Taking advantage from a small crystal size, expressing thus a large specific surface area, the adsorption of MEK is enhanced. Following this, the hypothesized favored adsorption of intermediate products of MEK degradation on highly exposed TiO_2 {001} facets would increase the probability of TiO_2 to mineralize MEK into CO_2 completely. Also, benefiting from the large total BET surface area and a highly exposure of the highly reactive {001} facets, the total reactive surface area was significantly increased, and the total number of reactive heterogeneous catalytic sites available to produce highly oxidizing radicals increased. Besides, F- and P-induced spatial charge separation could reduce significantly the charge recombination rate for TiO_2 samples. This was proposed to explain why the $BmimPF_6$-derived TiO_2 nanoparticle samples, with a suitable $BmimPF_6$/Ti ratio, achieved much higher photocatalytic activity for the degradation of MEK than the corresponding $BmimPF_6$-free TiO_2 samples and commercial P25 reference. Replacement of $BmimPF_6$ by phosphoric acid and sodium fluoride in an adequate ratio in the sol-gel synthesis in HAc medium can result in similar (or more interesting) TiO_2 materials in terms of properties and photocatalytic activity.

Especially, the phosphate and fluoride anions could be available since the beginning of the aging step because of the direct release and availability of phosphates and fluorides from PA and NaF, which might lead to a faster and better crystallization of the TiO_2 nanomaterials. A schematic explanation of the proposed combined roles of the phosphorus and fluorine elements on the TiO_2 properties, are presented in Fig 67.

III.2. Liquid-phase photocatalytic anti-bacterial activity

In this section, two different TiO_2 photocatalyst nanomaterials have been chosen for the evaluation of the photocatalytic liquid-phase antibacterial activity. One is the commercially available TiO_2 P25, which serves as the reference, the other is the "PANaF0.03 HAc 6d 550" TiO_2 nanomaterial, which has been demonstrated above as the most active for gas-phase photo-degradation of MEK (III.1.2.3). Properties of the TiO_2 photocatalyst nanomaterials are here evaluated as deposits on glass surface, referred to "TiO_2 coatings" in this section. Before results are shown, an introduction of experimental methods and image analysis methods used for evaluating the coatings' photoactivities are detailed. At the end, mechanisms of actions of photocatalysis on different bacteria, including influence of surface topology and impact of dissolved oxygen on photocatalytic efficiency, are discussed.

III.2.1. Experimental methods

Description of the experimental methods begins with the surface topographic analysis of TiO_2 coating samples which have been made to evaluate weather surface topography may influence their photocatalytic anti-bacterial activity. Then, methods used for evaluating photocatalytic anti-bacterial activity are presented in details, following a brief description of different microbiological equipment and the bacterial strains used in this work.

III.2.1.1. Production of TiO_2 nanomaterials coatings

In section III.2, two TiO_2 photocatalyst nanomaterials, *i.e.* "PANaF0.03 HAc 6d 550" ("PANaF" in short) and the commercially available TiO_2 P25 as the reference, have been chosen for the evaluation of the photocatalytic liquid-phase antibacterial activity. The corresponding synthesized powders were evenly deposed on 22x22 mm borosilicate glass cover slips (ROTH Karlsruhe Deckglaser 22 x 22 mm) by using the same technic described in section III.1.1, to obtain a final TiO_2 surface density equal to 1 mg/cm^2. Those immobilized TiO_2-coated glass surface samples are used for the entire studies carried out in section III.2.

III.2.1.2. Topographic analysis of immobilized TiO_2 samples

AFM microscopy has been used to study the surface topographical properties of the TiO_2 nanomaterials immobilized as coatings. AFM experiments have been performed by using a NanoScope IIIa AFM microscope with the following parameter settings: Tapping mode; Tip thickness of 7 µl, length of 225 µm, width of 38 µm; Resonance frequency of 190 KHz; Force constant of 13-77 N/m; Image size of 1 µm x 1 µm for 5 different zones on each sample.

Surface image histograms have been obtained for both TiO_2 P25 and PANaF samples. Surface roughness has been extracted for each micrograph after adequate image treatment and analysis.

III.2.1.3. Bacteria strains and culture methods

Microbiological experiments were conducted with three strains, one for each of three bacteria species, the Gram-negative fluorescent, slime- and GFP producing *Escherichia coli* (*E. coli*) SCC1 strain, [284] the Gram-positive moderate-slime-producing *Staphylococcus epidermidis* (*S. epidermidis*) ATCC 35983 (CIP 106510) strain, [285] and the Gram-negative wild-type *Pseudomonas fluorescens* (*P. fluorescens*) ATCC 13525 (CIP 69.13T) strain. [286]

Previously, −80 ^{o}C frozen bacteria were spread and cultured for two nights at 30 ℃ on LB (Lysogeny broth, Sigma-Aldrich) agar plate for *E. coli*, at 37 ^{o}C on LB agar plate for *S. epidermidis* and at 30 ^{o}C on BHI (Brain-Heart-Infusion, Sigma-Aldrich) agar plate for *P. fluorescens* respectively.

The day before microbiological analysis (J_0), precultures were prepared in liquid medium with one colony of *E. coli* in LB, of *S. epidermidis* in LB and of *P. fluorescens* in BHI, before overnight incubation at 30, 37 and 30 ^{o}C, respectively. At the day J_0, cultures were prepared with 10 % dilution of the overnight cultures in LB for *E. coli* and *S. epidermidis*, and with 33.3 % of the overnight cultures in BHI for *P. fluorescens*. They were then incubated for 4h at the same temperatures as used for precultures, before bacteria were harvested by centrifugation (3000 rpm for 20 min). According to the experiment, bacteria pellets were re-suspended either in physiological NaCl (9 g/L, pH 6.8) solution or in the so-called M63G *E. coli*-selective minimum medium (pH 6.8). [287] Bacterial suspensions were adjusted to an absorbance at 600 nm (A_{600} nm) of 0.1 (5×10^7 CFU mL^{-1}) for being ready to inoculate the previously prepared TiO_2 nanomaterial coatings.

All bacterial manipulations in section III.2 were performed in a biosafety cabinet class II in order to prevent exterior contaminations. All biological containers and lab consumable materials were purchased sterile or sterilized through a standard autoclave procedure prior to use.

III.2.1.4. Microbiological analysis of the photocatalytic anti-bacterial activity of TiO_2 nanomaterial coatings

Evaluating photocatalytic anti-bacterial activity of TiO_2 consists of determining the intact and damaged bacterial population on the coating sample surfaces, and comparing the values obtained before and after UVA illumination, and with possible supplementary delay allowing bacterial regrowth. The degree of loss of viable bacterial population through illumination process is considered the direct reflection of the photocatalytic bactericidal effect.

In this section, anti-bacterial activities of P25 and PANaF TiO_2 coatings were compared. In addition, cleaned borosilicate glass cover slip surface was used as an internal control of bacterial adhesion and sessile population growth. All cleaned borosilicate glass cover slips were sterilized through HCl-EtOH solution immersion treatment followed by standard autoclave procedure. Prior to their use in microbiological experiments, deposition of TiO_2 on glass cover slips were performed under a non-sterilized environment, which imposes to sterilize the prepared TiO_2 coatings prior to make contact with bacterial solutions. This was achieved by a standard 7 min UVC germicide illumination (wavelength 254 nm) with a 2 cm coating-lamp distance.

Analysis of bacterial population on coating samples was achieved by *in situ* observation using a fluorescence mode upright confocal microscope (LSM700, Carl ZEISS) equipped with a X63 water immersion objective (W Plan Apochromat X63/1.0, 2.0 mm). To be visualized in fluorescent mode, bacteria were self-fluorescent or fluorescently stained by different markers depending on the different experimental methods (detailed below).

Briefly, four main populations of bacteria are distinguished:

-Cells considered as intact and called “Live” in the III.2.2 section;

-Cells with damaged membrane, called “Dead”;

-Cells with active enzymatic activity, called “Calcine-AM”;

-Cells with active respiratory activity, called “CTC”.

Images of the bacteria present at coating surface were obtained by stacking micrographs every 0.3 µm, starting from the surface and throughout the whole bacterial layer thickness.

3D micrographs were finally analyzed by using ImageJ 1.47v software to determine the quantity of the colored or stained bacteria, which was expressed as the surface fraction covered by bacteria (in percentage). It is usuful to note that, according to the non-confluent monolayer structure of the bacterial population usually observed after 3h incubation, and the mean bacterial size determined elsewhere, [288] the maximal number measured on the coating samples is about 10^3 of bacterial. Therefore, the highest reduction that can be determined is 3log3, corresponding to one bacteria, *i.e.* <1% coverage.

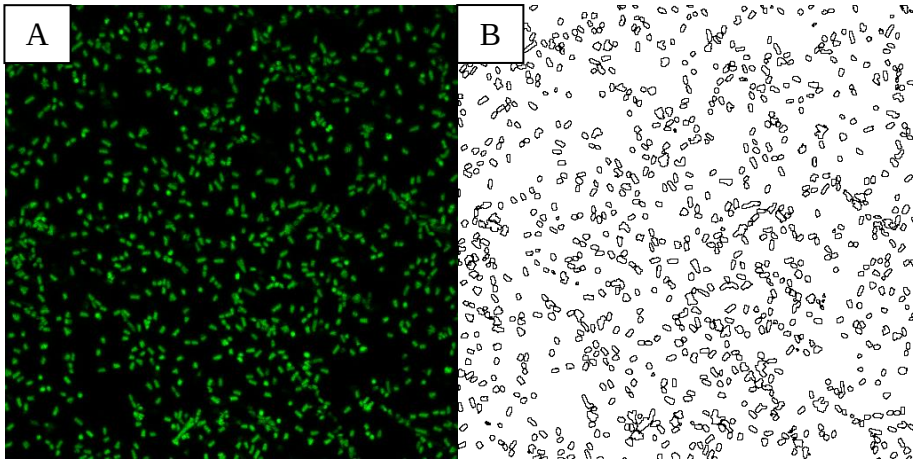

Fig 68 : A typical stacked green fluorescent bacterial image for *E. Coli* SCC1 (A), each green rod is living bacteria; and the processed image by using ImageJ to calculate the surface coverage area in percentage (B), each bacteria is outlined by black edge, then the surface coverage area in percentage is the ratio between the sum of pixels in all outlined area and the whole pixels of the image zone.

UVA radiation of each coating sample surface was performed in a way similar to as described in section III.1.1. The distance between lamp and sample surface was 1.5 cm resulting in an irradiance of 30 W/m^2 under the long axe of the lamp. Due to the large angle related to the small illumination distance, and the small sample surface area, center-to-edge deviation of the received irradiance can be neglected. Comparison of bacterial populations before and after irradiation on reference surface (*i.e.* glass cove slip) provided indications regarding potential toxicity of UVA irradiation on bacteria.

III.2.1.4.a. Analysis of the immediate anti-bacterial effect

Immediate anti-bacterial effect was assessed by comparing bacteria's quantities (intact ad damaged) before and after 10 min, 45 min or 3h (if necessary *i.e.* only for *P. fluorescens*) of UVA irradiation on the different coating samples (P25, PANaF and control). For each illumination duration, experiments were repeated three times. For each experiment, three coating samples of each type (clean glass clip cover control, P25 and PANaF) were analyzed. Two samples were illuminated with UVA while the rest one served as an internal non-illuminated reference. A typical experiment is schematically displayed in Fig 69 for *E. coli*. Briefly, all nine coating samples were sterilized by UVC for 7 min before being immersed in 3 ml of fresh prepared bacterial suspension (described in section III.2.1.2) in Petri dishes (ROTH, standard petri dish, PS, 35 mm diameter, 10 mm height). To study the influence of different inorganic ions on the photocatalytic bactericidal activity, bacterial suspension was either prepared in M63G medium or in physiological NaCl (9 g/L) medium (only in physiological NaCl medium for *S. epidermidis* ATCC 35983 and *P. fluorescens* ATCC 13525 strains). After 3 hours of incubation at 30 ^{o}C, samples were washed three times by 2 ml physiological NaCl without creating surface-air interface to remove most of the planktonic bacteria without driving away any attached ones.

Observations of samples inoculated with *E. coli* SCC1 were conducted under confocal microscope in fluorescence mode with the incident laser set at 488 nm for exciting GFP, while the receiving emission interval set in the range of 420 nm-550 nm to cover the main green part of GFP emission. For the two naturally non-fluorescent *S. epidermidis* ATCC 35983 and *P. fluorescens* ATCC 13525 strains, the fluorescent Syto9® DNA marker (Aldrich-Sigma), which stains cells in green, prepared with a dilution of 0.01 µl/ml for *S. epidermidis* and 0.02 µl/ml for *P. fluorescens*, was used with same excitation and emission settings of the microscope. Microscopie observation was done before and after illumination on the same samples for experiments conducted with *E. coli* SCC1. In contrast, Syto9® staining, being likely to disturb normal bacterial metabolism and viability, it does not allow the comparison on the same sample of cells quantities before and after illumination. This was rather done by comparing cell quantities determined one by one on illuminated coating samples versus non-illuminated coating samples of the same coating type.

In order to assess the potential damage of bacterial membrane induced by UVA and photocatalytic treatment, the membrane integrity was evaluated by staining bacteria with propidium iodide (PI, Aldrich-Sigma). PI only penetrates cells with damaged membranes *via*

dilated pores and stains DNA of those bacteria in red. In case of *E. coli*, 2 ml of diluted PI of 0.67 µl/ml in physiological NaCl solution were used as last washing solution for samples without illumination or as supplementary washing solution right after UVA illumination. In case of *S. epidermidis* ATCC 35983 and *P. fluorescens* ATCC 13525 strains, PI was added to the previously described Syto9® solution (0.67 µl/ml or 0.75 µl/ml in physiological NaCl solution), 2 ml of the so-prepared mixture of early described Syto9® with diluted PI was used as last or supplementary washing solution. The ratio of Syto9®/PI was adjusted in order to ensure color transition from green to red for the damaged cells. Coating samples were incubated for 15 min for allowing staining with PI or Syto9®/PI solution. For observing PI-stained bacteria, the same setting of the incident laser was used as for Syto9® and emitted fluorescence wavelength was received from 610 nm to 750 nm. In order to simultaneously conduct both Syto9® and PI staining observation, emission lights associated to Syto9® and PI respectively were treated by two different photo multiphases. The final images were therefore the composition of 2 separate channels of colors in RGB form (green and red). Each channel were analyzed *via* ImageJ 1.47V® software to access respective quantity of viable bacteria (green) and membrane-damaged bacteria (red).

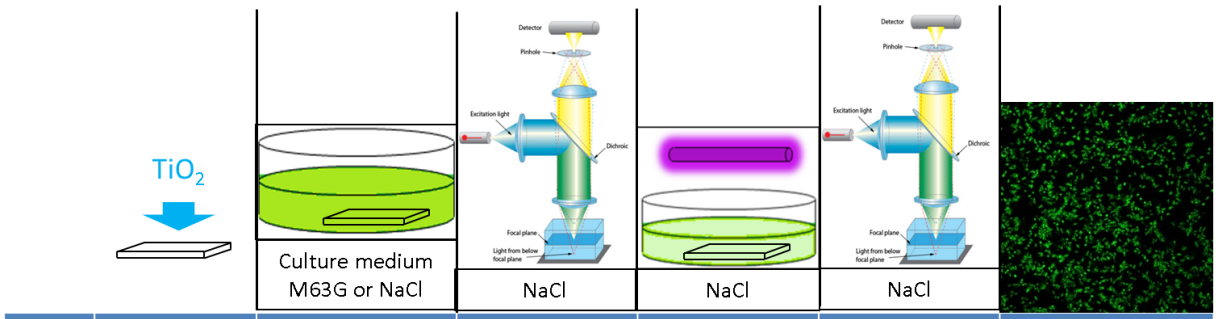

	1	2	3	4	5	6
Steps	Sample preparation	Immersion and incubation	Observations	UVA illumination	Observations After illumination	Evaluation of anti-bacterial effects
Detail	Deposition of TiO_2 on glass sheet & Sterilization by UVC	Bacterial density A_{600} nm = 0.1 Incubation 3h at 30°C Washed by NaCl after incubation	Confocal microscopy (fluorescent) in NaCl medium	30W/m² for 0, 10, 45 min or more Washed by NaCl Addition of PI	Confocal microscopy (fluorescent) in NaCl medium	% Surface covrage by bacteria (comparison before and after illumination)

Time

Fig 69 : Schematic view of the assay aiming at the microbiological evaluation of immediate photocatalytic anti-bacterial effects of TiO_2 coatings on *E. coli*.

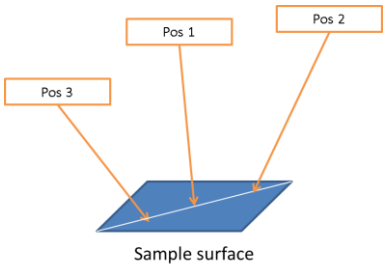

Fig 70 : The three positions taken by confocal microscope to obtain bacterial images for each coating sample, one at the center, two at middle positions between center position and diagonal edge aside of the center one.

Microscopie images were taken on 3 different locations of each coating sample, placed on the diagonal line (Fig 70, one at the center, two at middle positions between center position and diagonal edge aside of the center one). By a consequence, for each illumination duration with each bacteria strain, 18 positions and 9 positions were taken for illuminated and non-illuminated coating respectively for each type of coating. Positions taken for one specific coating were not completely identical before and after illumination, since samples moved in Petri dish during the series of manipulations between two observations.

Significance of the two-by-two differences between averages of bacteria's quantity on the diverse coating surfaces (μ_{P25} and μ_{PANaF}) were evaluated for numbers of adherent bacteria, by bilateral Student's *t* tests with significance thresholds (*p*-value) of 0.05. According to Scherrer, [289] the alternative hypothesis (H_1: $\mu_{P25} \neq \mu_{PANaF}$) was assumed to be true when the main hypothesis (H_0: $\mu_{P25} = \mu_{PANaF}$) was rejected.

III.2.1.4.b. Analysis of the post photocatalytic anti-bacterial effect

Aiming at evaluating the long-term efficiency of the photocatalytic antibacterial treatment, *i.e.* capacity of treated bacteria to recover, post anti-bacterial effect was assessed by comparing bacteria's quantities immediately after UVA illumination and after 18 hours (overnight) of regrowth in nutritive medium (favorable for regrowth). For that purpose, bacteria after UVA illumination were immediately put into an adequate nutritive culture medium for an overnight culture, before the final confocal microscope observation. Typical post photocatalytic anti-bacterial effect analysis for *E. coli* SCC1 is showed in Fig 71. Briefly, the general procedure is similar as for immediate anti-bacterial effect analysis. The only changes are the following:

1. In the "immersion and incubation" step, only NaCl 9 g/L was used as a culture medium.
2. Coating samples were directly illuminated by UVA after incubation. After illumination treatment, physiological NaCl 9 g/L medium was replaced by the same volume of nutritive LB medium, and samples were left in incubator at 30°C for an overnight culture (18 hours).
3. Incubated coating samples were washed twice with 2 ml physiological NaCl 9 g/L medium in order to remove the planktonic bacteria remaining in solution above the biofilm. Finally, 2 ml of a fresh diluted PI of 0.67 µl/ml in physiological NaCl 9 g/L solution was used to wash the coating samples. In case of *S. epidermidis* ATCC 35983 and *P. fluorescens* ATCC 13525 strains, 2 ml of Syto9®/PI solution prepared as described in section III.2.1.3.a was used to wash the coating samples. Then, coatings were incubated for 15 min for before being observed by confocal microscope.
4. For *P. fluorescens* ATCC 13525 strain, an additional 3 hours UVA illumination experiment was performed as the step "UVA illumination"

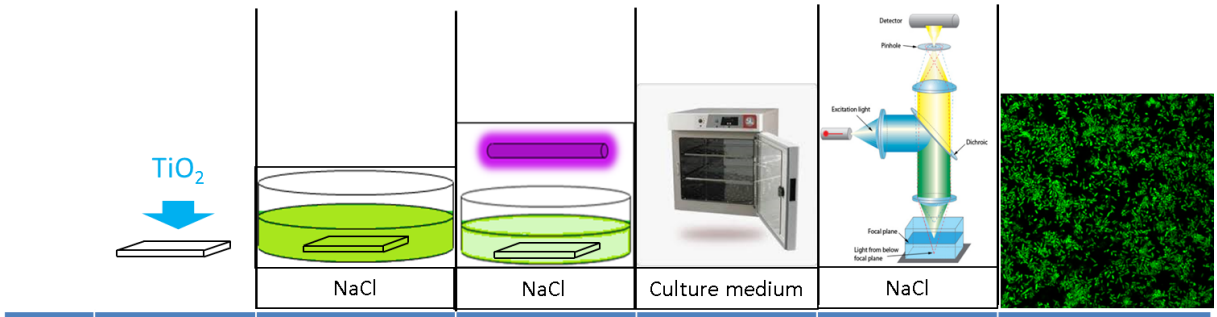

	1	2	3	4	5	6
Steps	Sample preparation	Immersion and incubation	UVA illumination	Regrowth	Observations after regrowth	Evaluation of post anti-bacterial effects
Detail	Deposition of TiO_2 on glass sheet Sterilization by UVC	Bacterial density A_{600} nm = 0.1 Incubation 3h at 30°C Washed by NaCl after incubation	30W/m² For 0, 10, 45 min or more Switched with culture medium	Incubation overnight at 30°C Washed by NaCl Addition of dyes	Confocal microscopy (fluorescent) in NaCl medium	% Surface covrage by bacteria after regrowth

Fig 71 : Schematic view of the assay aiming at the microbiological evaluation of post photocatalytic anti-bacterial effects of TiO_2 coatings on *E. coli*.

Because PI and Syto9® stainings are likely to disturb normal bacterial metabolism and viability, they do not allow direct comparison of cells quantities on the same sample immediately after illumination and after regrowth. This was rather done by comparing cell quantities obtained after regrowth or immediately after illumination on different samples of the same coating type.

III.2.1.4.c. Study of the photocatalytic action mechanism on *E. coli*

Mechanism of the photocatalytic action on bacteria was studied on *E. coli* PHL 628 strain, a biofilm-making K12 MG1655 derivate strain [290] without fluorescence properties. The general objective was to check whether vital functionalities may be sustained after photocatalytic action by TiO_2 and to determine the progress of potential damages occurred in the cells.

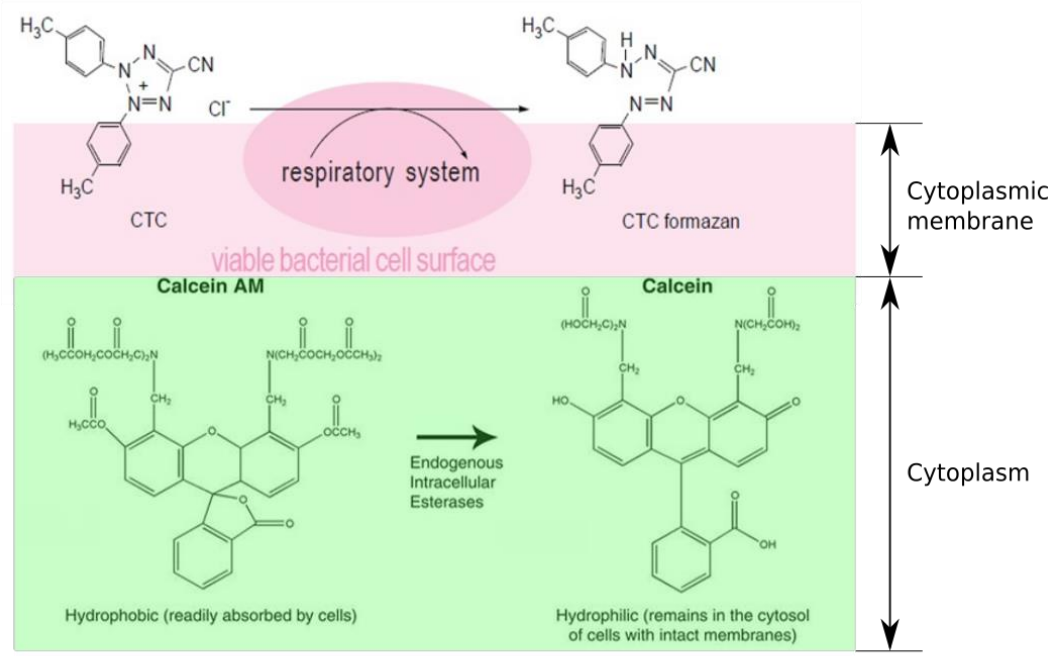

Fig 72 : Schematic representation of bacteria's stainings by Calcein AM (CAM) and 5-cyano-2,3,-ditolyl tetrazolium chloride (CTC).

Two fluorescent dyes were used, Calcein AM (CAM) and 5-cyano-2,3,-ditolyl tetrazolium chloride (CTC) for staining bacteria with intact endogenous intracellular esterase activities and redox respiratory activities respectively. Bacteria with intact metabolic activities

should present esterase activities, which can hydrolyze the ester function of the easily uptaken non-fluorescent CAM to form the green-fluorescent Calcein. Hydrolyzed Calcein can readily bind to metal cations in cytoplasm, which makes them thus too voluminous to get out of bacteria, but allows the ions to accumulate in cell. In addition, the active redox respiratory system, localized in the cytoplasmic membrane, can reduce non-fluorescent CTC to red-fluorescent CTC formazan. As a result, bacteria with active respiratory functions will be stain in red under fluorescence microscope. Principle of staining by CAM and CTC is schematized in Fig 72. Since spectral emissions of the two dyes are different (green and red respectively), they can be used simultaneously on the non-fluorescent *E. coli* PHL 628.

The experimental procedure is almost similar to that used for the analysis of immediate anti-bacterial photocatalytic effect conducted on *E. coli* SCC1. Only changes compared to the Fig 69 are the following:

1. In the step "Immersion and incubation", only NaCl 9 g/L was used as a culture medium.
2. Since CAM and CTC dyes are likely to disturb normal bacterial metabolism and viability, they do not allow direct comparison of enzymatically/respirationally active cells' quantities on the same sample before and after illumination. This was rather done by comparing the results obtained on illuminated coating samples with results obtained on coating samples of same material type nut treated without illumination. As a consequence, the step "observation by confocal microscope before UVA illumination" was removed. Fluorescent dyes were added just before microscope observations.
3. At the end of step "UVA illumination" or after a delay of same duration for control conditions without illumination, 2 ml of a staining solution prepared with 3 mmol/L of CAM and 1 mmol/L of CTC in LB medium was used to replace the last physiological NaCl 9 g/L medium. Coating samples were then incubated for 20 min before a last washing process by 2 ml of physiological NaCl 9 g/L medium before performing the next step. Both dyes were added in LB medium to reactivate the respiration activities of bacteria that were previously starved by 3h of incubation in nutrition-poor physiological NaCl 9 g/L medium. Indeed, poor CTC staining efficiency has been reported on long-time starved bacteria, [291] which we confirmed by measurement of extremely low staining quality by adding physiological NaCl 9

g/L based CTC solution on coating samples with previous 3h incubation in physiological NaCl 9 g/L.

III.2.1.4.d. Study of liquid-phase photocatalytic bactericidal action in confined space and role of oxygen

Oxygen level is an important factor in photocatalytic actions. The immediate anti-bacterial effect of photocatalysis has been therefore also evaluated in a confined space (Fig 73). Bacteria strain was *E. coli* SCC1.

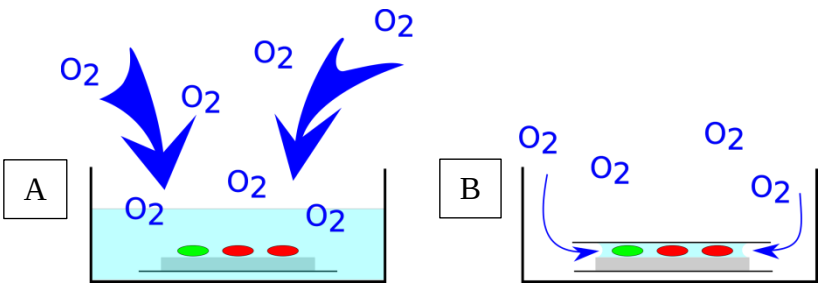

Fig 73 : Microbiological analysis of anti-bacterial effect by photocatalysis in open (A) and confined (B) space. The culture medium was freshly autoclaved and thus lacked oxygen.

UVA illumination irradiance was identical as indicated above, illumination duration was enhanced to 3h since treatment conditions (*i.e.* confined space) were expected to drastically reduce the photocatalytic activity. Two other major differences concern the experimental procedure:

1. For coating sample inoculation, 20 µl of bacterial suspension was dropped on each sample, which was immediately covered by a glass cover slip. Thus bacterial solution drop was pushed between coating sample and cover slip and spread out to the entire surface of samples in a very confined thin space. Culture medium freshly autoclaved and therefore lacking oxygen was used to prepare bacterial suspension. In contrast to the method described above (section III.2.1.4), the air-liquid interface area was here limited at the outer edge of the double glass cover layer, thus very small. Oxygen was therefore expected to remain lacking in the confined conditions, even after long incubation times.
2. Assessment of the sessile bacteria's quantities was determined as previously described by confocal microscope and, additionally by using a classic plate counting method, which specifically evaluates viable bacteria numbers. After photocatalytic

treatment, bacteria were detached from coating samples by a surfactant-assisted ultrasonication. They were then dispersed in physiological NaCl 9g/L solutions with series of dilutions. Each dilution was cultured on agar plate (100 ml plate) and resulted colonies' numbers (CFU) were count if between 30 and 200 CFU. [292] The number of bacteria per bacterial suspension volume obtained right before or after any photocatalysis treatment was then calculated.

Glass cover slip was previously confirmed not to absorb neither UVA nor the fluorescent signals emitted by bacteria.

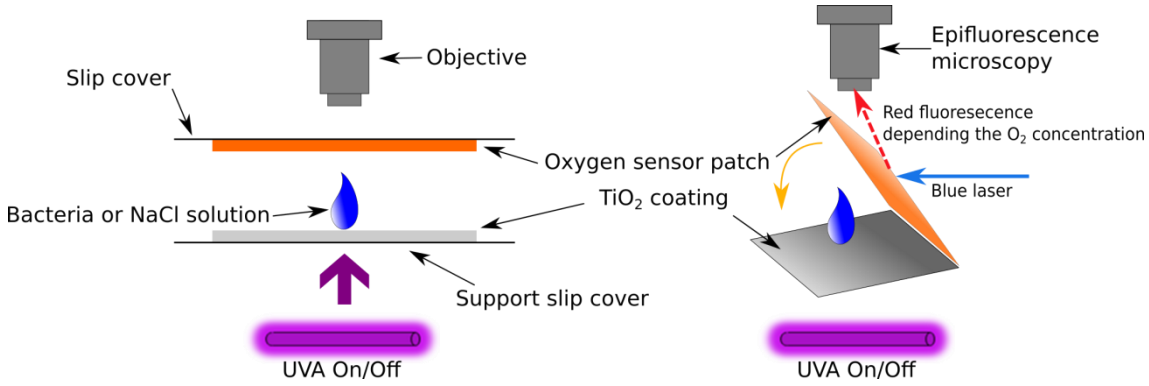

Fig 74 : Setup used for the investigation of oxygen level changes during photocatalysis actions.

To study the oxygen level variation during photocatalysis action in confined space, an oxygen sensor patch (HIOXY Oxygen Sensor patch, IDIL) was stuck on the interior side of the top cover slip, to allow the direct contact of the compressed bacterial suspension with both TiO_2 coating and the top oxygen sensor (Fig 74). In absence of oxygen, the sensor, an oxygen sensitive fluorescent polymer, emits a strong red fluorescence if excited by light with wavelength in blue. In contrast, oxygen leads to quench the sensor fluorescence, which results in a modulation of the fluorescence intensity level according to the oxygen concentration of the medium in contact with sensor. Therefore, oxygen level inside the compressed solution in the confined space can be determined by observing the intensity of sensor fluorescence directly under an up-right epifluorescence microscope (Olypus BX51). UVA illumination was applied on the bottom side of the coating sample and emitted fluorescence was detected by the objective located above. The intensity of UVA irradiance was controlled at the same level as before. To compare oxygen level with and without UVA illumination, micrographs were

taken with both non-illuminated samples and illuminated samples. Both bacteria suspension and fresh, bacteria-free physiological NaCl 9 g/L medium were used as aqueous medium confined between coating and sensor/cover slip. This allowed determining whether the presence of bacteria may change the oxygen level within the confined space.

III.2.2. Results of liquid-phase photocatalytic anti-bacterial effects

Five major parts are reported here. Firstly, topographies of the two main types of TiO_2 coatings are compared. Then, comparisons of immediate and post photocatalytic anti-bacterial effects of these TiO_2 coatings on three different bacteria strains are shown, followed by the results about the photocatalytic action mechanism studied on *E. coli*. Finally, the effects of confined space and of some ions of the M63G culture medium on liquid-phase photocatalysis against bacteria are presented.

III.2.2.1. Topography of prepared sample surfaces

Topographic characteristics of P25 and PANaF TiO_2 coating samples are reported in Fig 75. A significate difference in terms of surface roughness and morphology can be noticed. P25 surface is composed of relatively large grain-form aggregations (Fig 75, B, D) with aggregate size of about 180 ± 35 nm (Fig 75, F) while surface of PANaF is composed of smaller grain-form aggregations (Fig 75, A, C) with mean size of about 42 ± 16 nm (Fig 75, E). The smoother surface and smaller aggregate size of PANaF compared to P25 probably results from the smaller TiO_2 crystal size of PANaF (about 12 nm) compared to P25 (about 22 nm), as reported in chapter II. Even if grains (several tenth or hundredth of nanometers in scale) observed in AFM micrographs do not represent single TiO_2 crystals (several nanometers in scale), smaller single TiO_2 crystals are expected to compact in smaller aggregations than the larger ones, resulting in smoother surface for TiO_2 coatings made of the PANaF crystals.

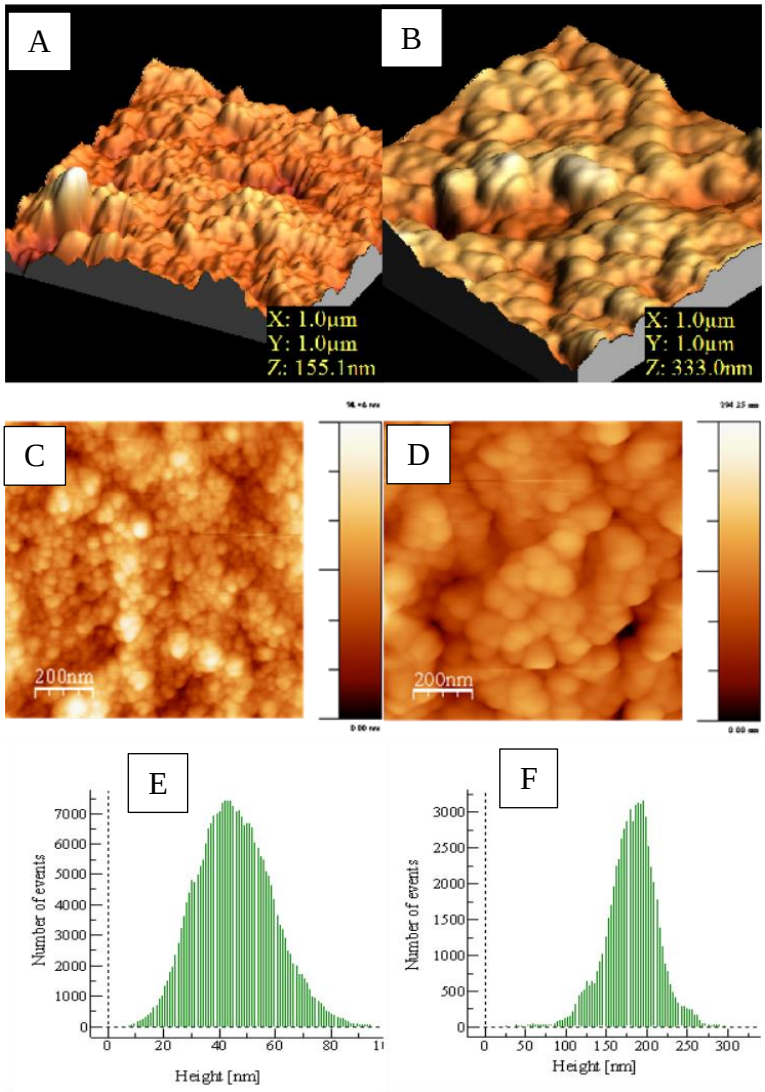

Fig 75 : Topological micrographs (A, C) and height profiles (E) of TiO_2 PANaF and TiO_2 P25 surfaces (B, D, F), analyzed by AFM.

III.2.2.2. Effect of UVA illumination on bacteria

For *E. coli* SCC1, *S. epidermidis* ATCC 35983 and *P. fluorescens* ATCC 13525 strains, after both 10 min (data not shown here) and 45 min of UVA illumination, control samples (glass cover slip) did not show any loss of "live" bacteria quantity (Fig 76). This confirms that 10 min and 45 min of UVA illumination at the irradiance level we used (which is quite high compared to the UVA irradiation level of 2.5 W/m^2 used in the work of Verdier *et al.*, [105] and 9 W/m^2 in that of Bonetta *et al.* [103]) is not able to induce detectable bactericidal effect on sessile bacteria. Even 3h of UVA illumination has resulted in limited bactericidal effect (shown in Fig 104 in annex).

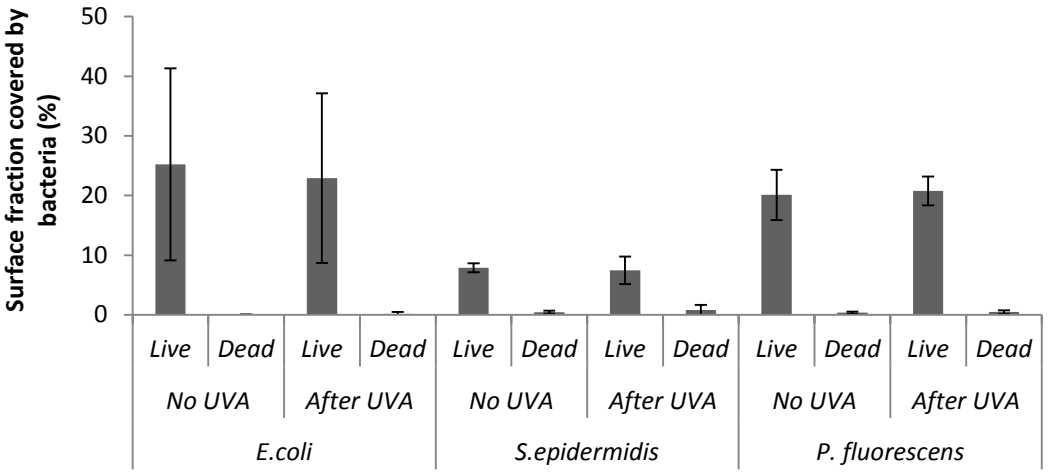

Fig 76 : Immediate photocatalytic bactericidal effect after 45 min of UVA illumination on *E. coli* SCC1 strain, *S. epidermidis* ATCC 35983 strain and *P. fluorescens* ATCC 13525 strains, for control (clean cover slip) (n = 9) samples. 30% of surface fraction covered by bacteria corresponds to $2.0x10^7$ cells per cm^2 for *E. coli*, $2.4x10^7$ cells per cm^2 for *S. epidermidis* and *P. fluorescens*.

III.2.2.3. Comparison of immediate photocatalytic anti-bacterial efficiencies of different TiO_2 samples on different bacteria strains

In this section, the immediate photocatalytic anti-bacterial efficiency after certain durations of UVA illumination on P25 and PANaF TiO_2 coating samples are displayed for *E. coli*, *S. epidermidis* ATCC 35983 and *P. fluorescens* ATCC 13525 bacteria strain. Two different parameters were considered: 1) Surface fraction covered by bacteria with active GFP metabolism (for *E.coli*) or stained in green by Syto9®/PI staining (for *S. epidermidis* and *P. fluorescens*), called "Live" in the following text. 2) Surface fraction covered by bacteria with damaged membrane as demonstrated by the red staining of PI (for all bacteria strains), called "Dead" in the following text. "Live" quantity is displayed before illumination as a control of a normal growth of the sessile population, while both "Live" and "Dead" quantities are displayed after the given duration of illumination, or without illumination but after a delay corresponding to the given duration of illumination.

For the *E. coli* SCC1 strain, two UVA illumination times were tested, 10 and 45 min. Surface fraction covered by *E. coli* SCC1 before and after illumination are shown in Fig 77. Before illumination, colonizations of all three types of samples (glass control, P25 and PANaF) are similar, which indicates that the TiO_2 coatings do not present any noticeable attraction or repel properties for bacteria compared to control. After 10 min or 45 min without illumination, coatings and control also revealed similar colonization as before illumination. This means that, as expected for NaCl 9 g/L medium, no significant bacterial growth occurred

on control or TiO_2 coating samples during this period. In addition, this proves that no toxicity effect resulted from either cover slip or TiO_2 coatings if not illuminated by UVA. This is confirmed by the very few "Dead" bacteria's quantity observed on all samples in absence of illumination.

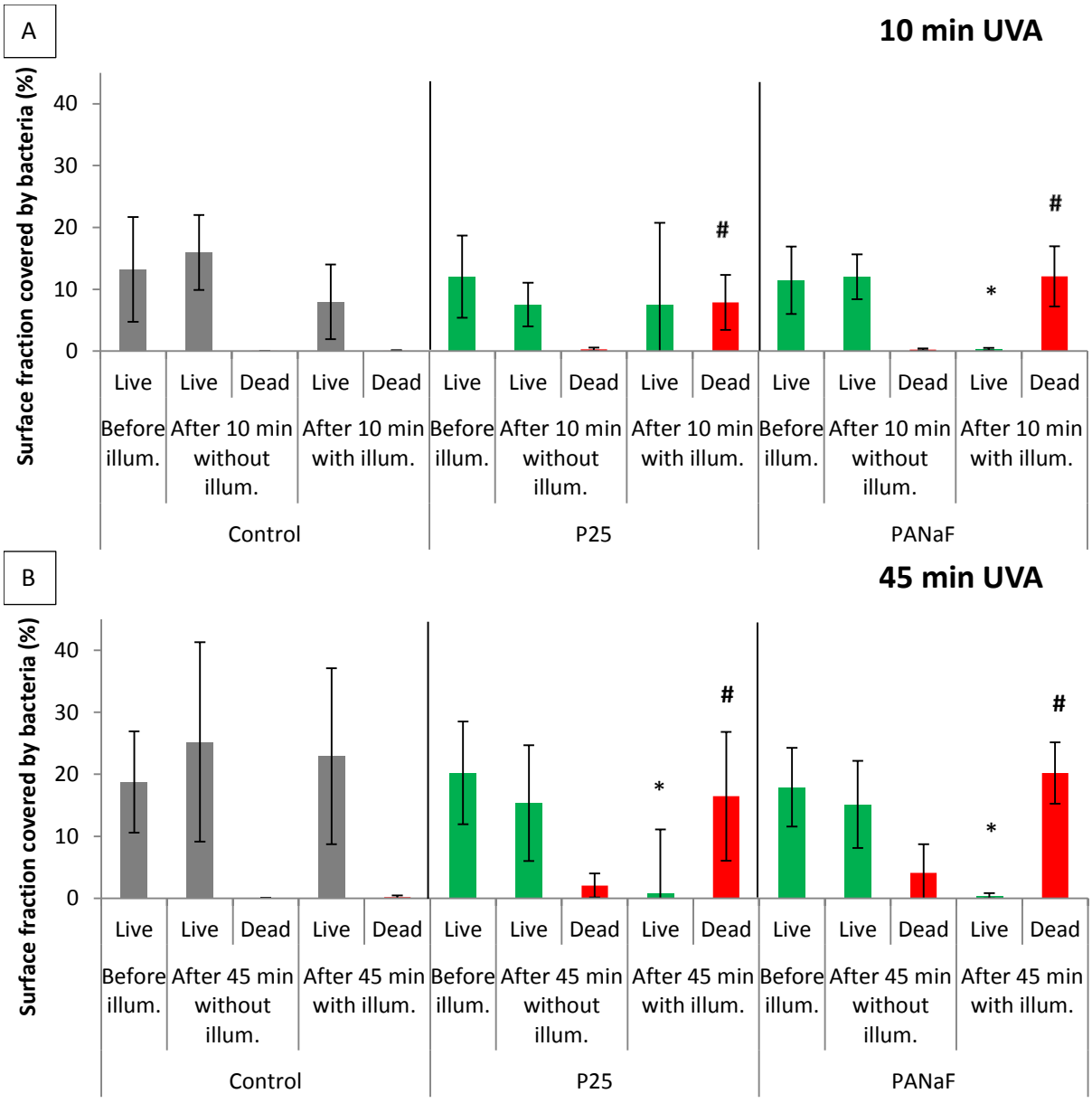

Fig 77 : Immediate photocatalytic bactericidal effect after 10 (A) and 45 (B) min of UVA illumination on *E. coli* SCC1 strain adhered on control (clean cover slip) (n = 9), P25 (n = 18) and PANaF (n = 18) TiO_2 coating samples. 30% of surface fraction covered by bacterial generally corresponds to $2.0x10^7$ cells/cm^2. *: Significant differences (*p*-value = 0.05) compared to "Live" after 10min without illumination for the corresponding coatings. #: Significant differences (*p*-value = 0.05) compared to "Dead" after 10min without illumination for the corresponding coatings.

10 min of UVA treatment resulted in a sharp bactericidal effect on PANaF samples, even reaching nearly negligible sessile population. In contrast, results on P25 samples through 10 min UVA treatment only provided about 50% of decrease, with a high variability of the "Live"

bacterial quantity, *i.e.* a quasi-absence of "Live" bacteria quantity loss of some of the P25 coating samples but high efficiency of the treatment on some others. This is illustrated by confocal micrographs taken after 10 min of illumination, which display different of P25 regions with very different ratios of "Live" to "Dead" bacteria numbers (Fig 79 A, B, C).

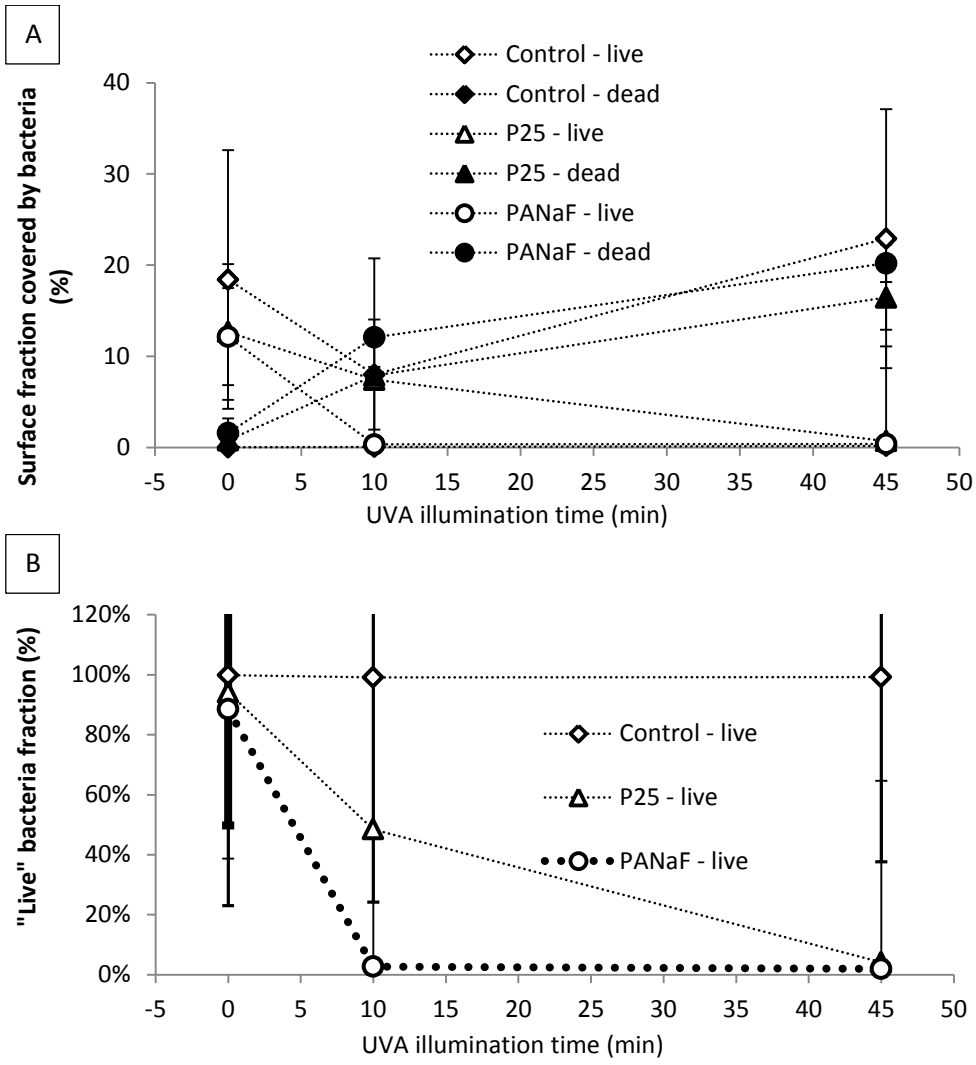

Fig 78 : Surface fraction covered by bacteria (A) and fraction of "Live" bacteria (B) of *E. coli* SCC1 in function of illumination time on control, P25 and PANaF coating samples.

After 45 min of UVA illumination however, a great reduction of "Live" bacteria quantity was observed on both P25 and PANaF coating samples. The enhanced bactericidal activity for both coating types through 45 min of illumination is confirmed by the fact that, on both coating types, "Live" bacteria quantity decreased to nearly zero while the "Dead" bacteria quantity reached the controls level. In general, a good correlation between loss of the "Live" bacteria quantity and gain of the "Dead" bacteria quantity was found for all coating samples

and all illumination time conditions. In other words, each decrease in "Live" bacteria quantity accompanied an increase of "Dead" bacteria quantity (Fig 78 A), and the highest "Dead" bacteria quantity was similar to the bacteria quantity measured before illumination. This indicates that the use of PI in association with the natural GFP production was suitable for the evaluation of bacterial intact/damaged states. Since toxicity for bacteria of non-illuminated TiO_2 and of UVA illumination in our experimental conditions have been excluded above, these significant losses of "Live" bacteria observed on TiO_2 coating samples after illumination of 10 min or 45 min for both P25 and PANaF can be only attributed to photocatalytic actions of TiO_2. In particular, cell membrane damages highlighted by PI staining should have been caused by photocatalysis.

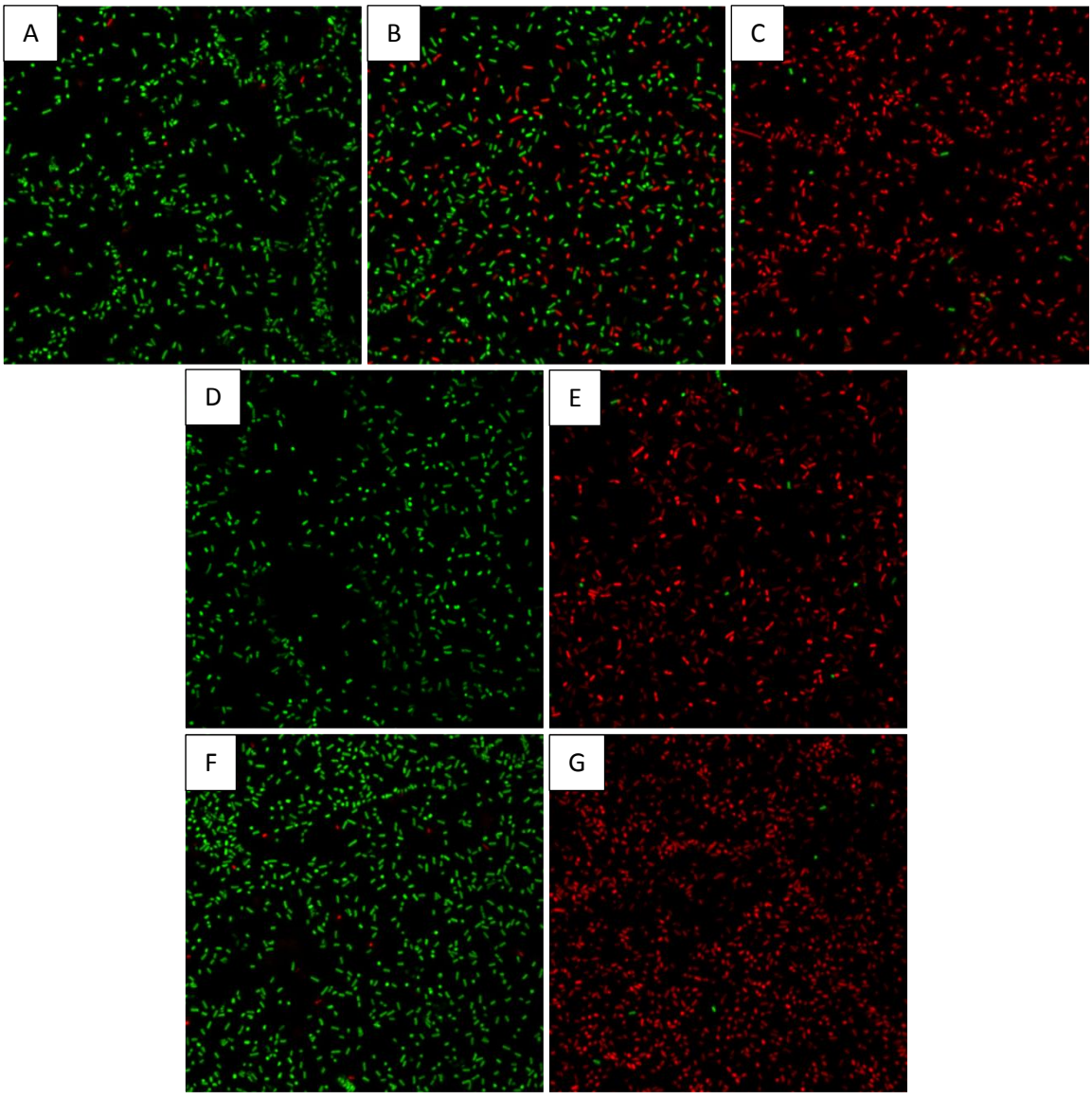

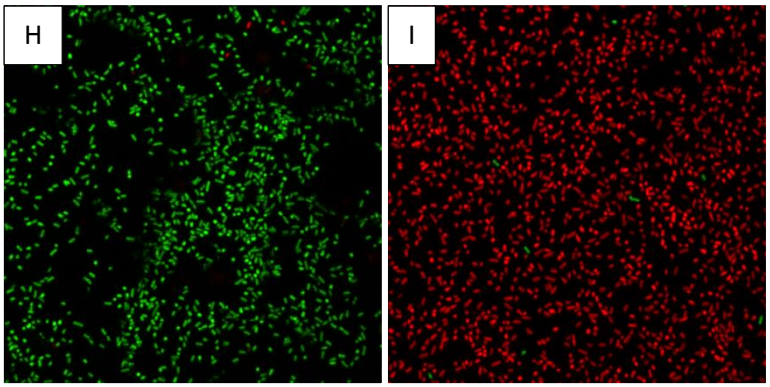

Fig 79 : *E coli* SCC1 bacteria images taken by confocal microscope. (A) P25 left for 10 min without illumination, (B) Region 1 of P25 after 10 min illumination, (C) Region 2 of P25 after 10 min illumination, (D) PANaF after 10 min without illumination, (E) PANaF after 10 min illumination, (F) P25 after 45 min without illumination, (G) P25 after 45 min illumination, (H) PANaF after 45 min without illumination, (I) PANaF after 45 min illumination.

For *S. epidermidis* ATCC 35983 strain, two UVA illumination times were tested, 10 and 45 min. Surface fraction covered by *S. epidermidis* ATCC 35983 before and after illumination are shown in Fig 80.

Before illumination, colonizations of all three types of samples (glass control, P25 and PANaF) are similar, which indicates as for *E. coli* that the TiO_2 coatings do not present any noticeable attraction or repel properties for bacteria compared to control. After 10 min or 45 min without illumination, coatings and control also revealed similar colonization as before illumination, as expected for NaCl 9 g/L medium and already noticed for *E. coli* SCC1 strains. As for *E. coli* SCC1 strain, this proves that no toxicity effect resulted from either cover slip or TiO_2 coatings if not illuminated by UVA. This is confirmed by the very few "Dead" bacteria quantity observed on all samples in absence of illumination.

10 min of UVA treatment failed to cause any significant bactericidal effect neither on P25 nor on PANaF coating samples. "Live" bacteria quantity was unchanged after photocatalytic treatment for the P25 samples, and "Dead" bacteria quantity was near to zero. About 80 % of "Live" bacteria fraction survived on PANaF coating samples, and slightly higher but very variable "Dead" bacteria quantity was stained by PI. Thus, a slight advantage in terms of photocatalytic bactericidal effect for PANaF over P25 coating samples was evidenced.

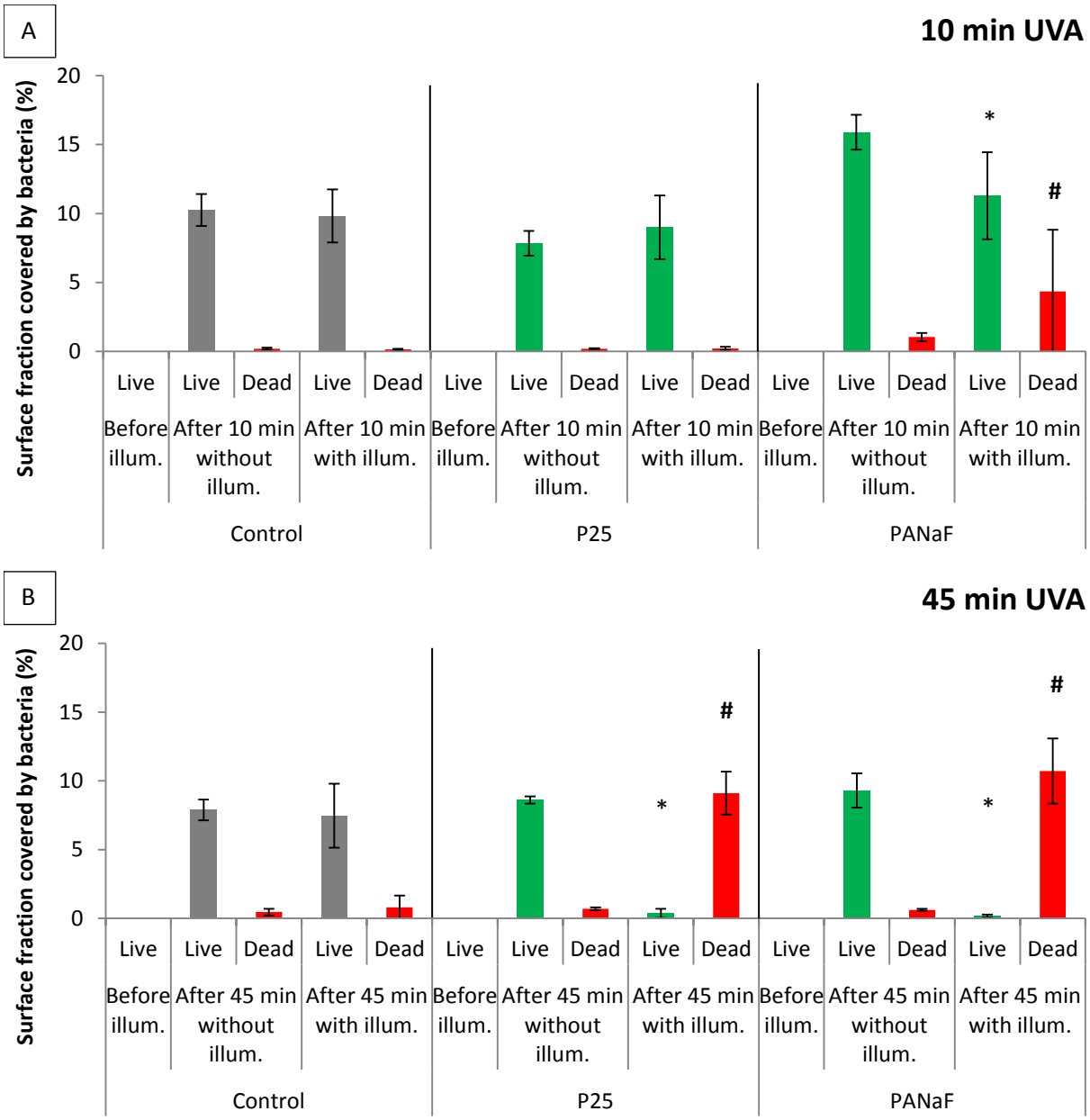

Fig 80 : Immediate photocatalytic bactericidal effect after 10 and 45 min of UVA illumination on *S. epidermidis* ATCC 35983 strain adhered on control (clean cover slip) (n = 9), P25 (n = 18) and PANaF (n = 18) TiO_2 coating samples. 15% of surface fraction covered by bacterial generally corresponds to $1.2x10^7$ cells/cm^2. *: Significant differences (*p*-value = 0.05) compared to "Live" after 10min or 45min without illumination for corresponding coatings. #: Significant differences (*p*-value = 0.05) compared to "Dive" after 10min or 45min without illumination for corresponding coatings.

After 45 min of UVA illumination however, a great reduction of "Live" bacteria quantity was observed on both P25 and PANaF coating samples. The enhanced bactericidal activity for both PANaF and P25 coating samples with 45 min of illumination is confirmed by the fact that "Live" bacteria quantity decreased to nearly zero while "Dead" bacteria quantity reached the control's level. In general and as expected for Syto9®/PI combination, a good correlation between loss of the "Live" bacteria quantity and gain of the "Dead" bacteria quantity was

found for all coating samples and all illumination time conditions (Fig 78 A). Finally, since toxicity for bacteria of non-illuminated TiO_2 and of UVA illumination in our experimental conditions have been excluded above, the significant losses of "Live" bacteria observed on TiO_2 coating samples after illumination of 45 min for both P25 and PANaF can be only attributed to photocatalytic actions of TiO_2. In particular, cell membrane damages highlighted by PI staining should have been caused by photocatalysis, as already demonstrated for *E. coli* SCC1 strain.

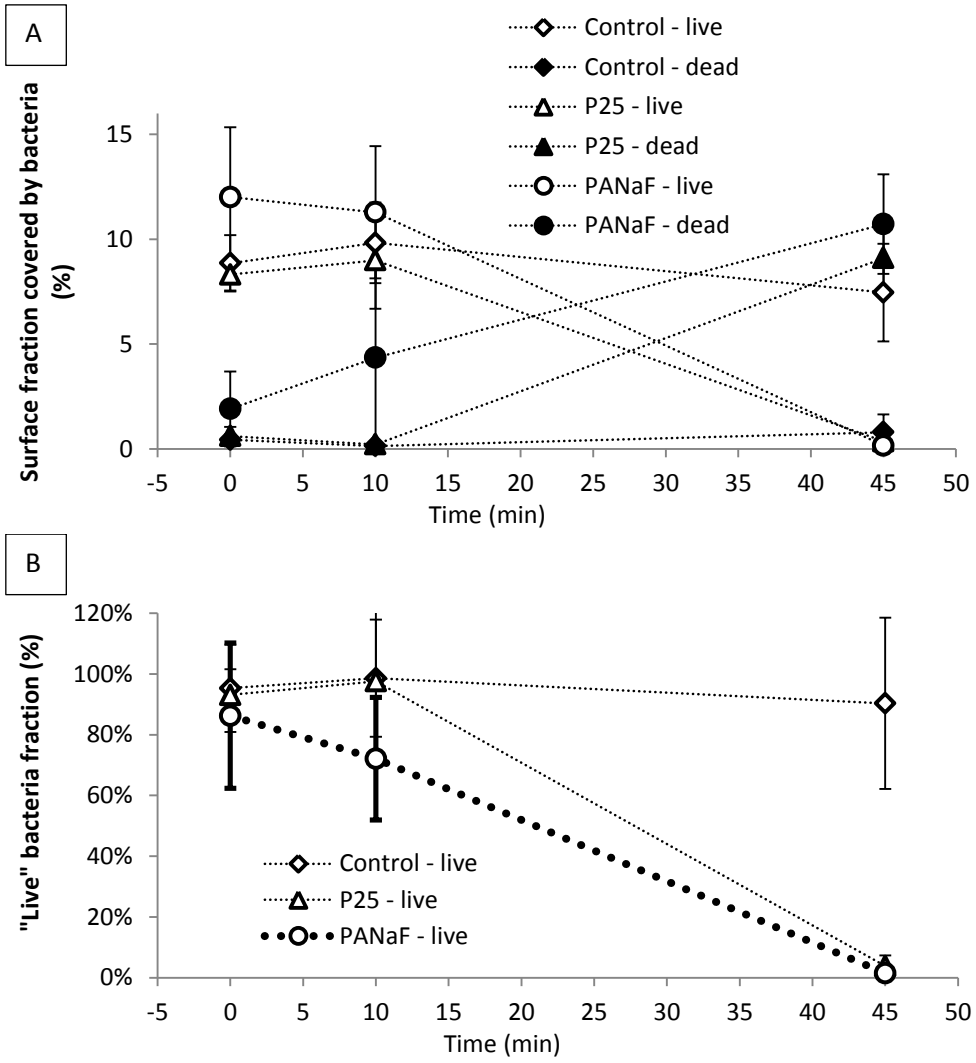

Fig 81 : Surface fraction covered by bacteria (A) and "Live" bacterial fraction (B) of *S. epidermidis* ATCC 35983 strain in function of illumination time on control, P25 and PANaF coating samples.

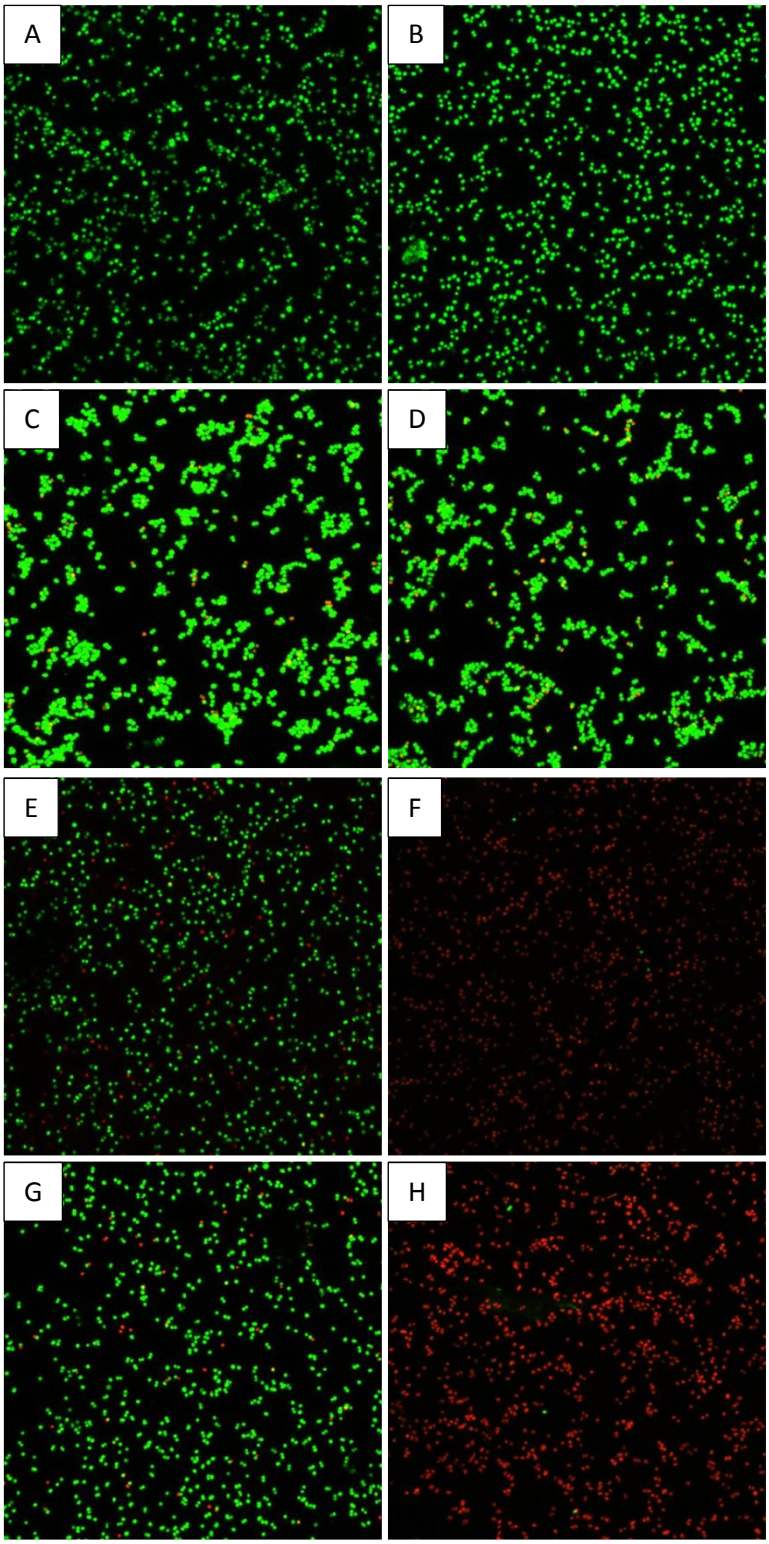

Fig 82 : *S. Epidermidis* ATCC 35983 bacteria images taken by confocal microscope. (A) P25 after 10 min without illumination, (B) P25 after 10 min illumination, (C) PANaF after 10 min without illumination, (D) PANaF after 10 min illumination, (E) P25 after 45 min without illumination, (F) P25 after 45 min illumination, (G) PANaF after 45 min without illumination, (H) PANaF after 45 min illumination.

For *P. fluorescens* ATCC 13525 (CIP 69.13T) strain, surface fraction covered by bacteria on control, P25 and PANaF coating samples was determined before and after illumination. Three UVA illumination time were tested: 10, 45 min and 3h. Results are shown in the following Fig 83.

Before illumination, colonizations of all three types of samples (glass control, P25 and PANaF) were similar, which, as for the other bacterial strains, indicates that the TiO_2 coatings do not present any noticeable attraction or repel properties for bacteria compared to control. After 10, 45 min or 3h without illumination, coatings and control also revealed similar colonization as before illumination, as expected for NaCl 9 g/L medium, also confirming that no toxicity effect resulted from either cover slip or TiO_2 coatings if not illuminated by UVA. The very few "Dead" bacteria quantity observed on all samples in absence of illumination.

As for *S. epidermidis*, 10 min of UVA treatment failed to provide any bactericidal effect on both P25 and PANaF samples. "Live" bacteria quantity was unchanged after photocatalytic treatment, and "Dead" bacteria quantity was near zero. No advantage in terms of photocatalytic bactericidal effect for PANaF over P25 coating samples was evidenced here.

In contrast, 45 min of UVA illumination led to about 50% of reduction of "Live" bacteria quantity on P25 coating samples and about 70% on PANaF coating samples. However, "Dead" bacteria quantity on both TiO_2 coating samples was similar to the bacteria quantity measured before illumination. This may result from the double staining by red PI and green Syto9® of a certain amount of bacteria. In a group of confocal micrographs taken after 45 min of illumination on P25 and PANaF coating samples, presented in Fig 85, we can see some regions where bacteria were stained as dark orange instead of complete red, resulted from combination of green and red colors. 3h of UVA treatment resulted in no further increase in terms of bactericidal effect. Although "Live" bacteria quantities for both PANaF and P25 samples were very variable as displayed by large standard derivation bars, we can notice a moderate bactericidal activity. "Live" bacteria fraction was only decreased to as low as 20% but "Dead" bacteria quantity almost reached the "Live" level measured before illumination. Here but again, as shown in Fig 85, a double-color staining phenomenon leading to orange bacteria was observed on both coating samples for 3h of UVA treatment.

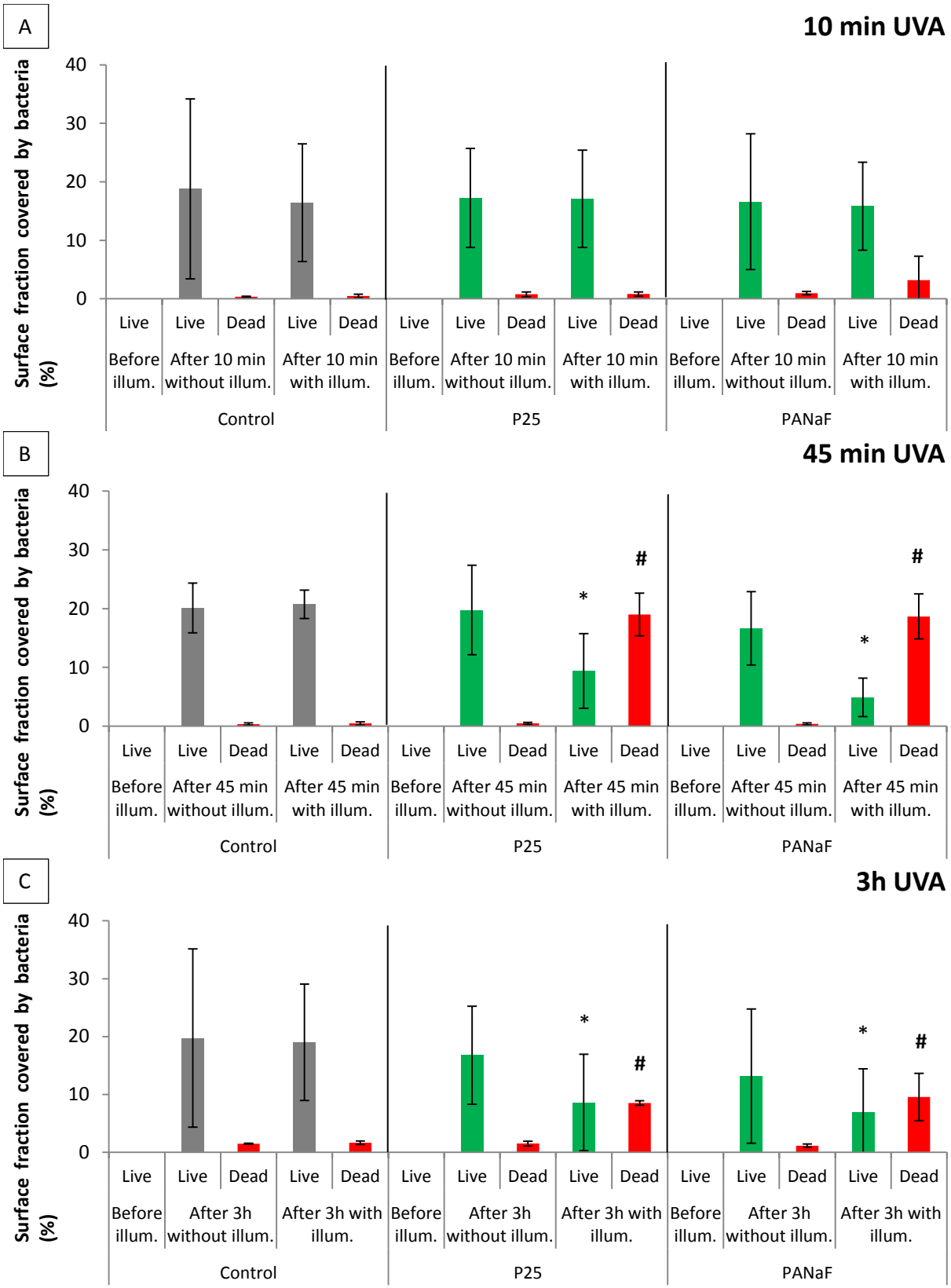

Fig 83 : Immediate photocatalytic bactericidal effect after 10, 45 min and 3h of UVA illumination on *P. fluorescens* ATCC 13525 strain adhered on control (clean cover slip), (n = 9), P25 (n = 18) and PANaF (n = 18) TiO_2 coating samples. 15% of surface fraction covered by bacterial generally corresponds to $1.2x10^7$ cells/cm^2. *: Significant differences (*p*-value = 0.05) compared to "Live" after 45min and 3h without illumination for corresponding coatings. #: Significant differences (*p*-value = 0.05) compared to "Dead" after 10min without illumination for corresponding coatings.

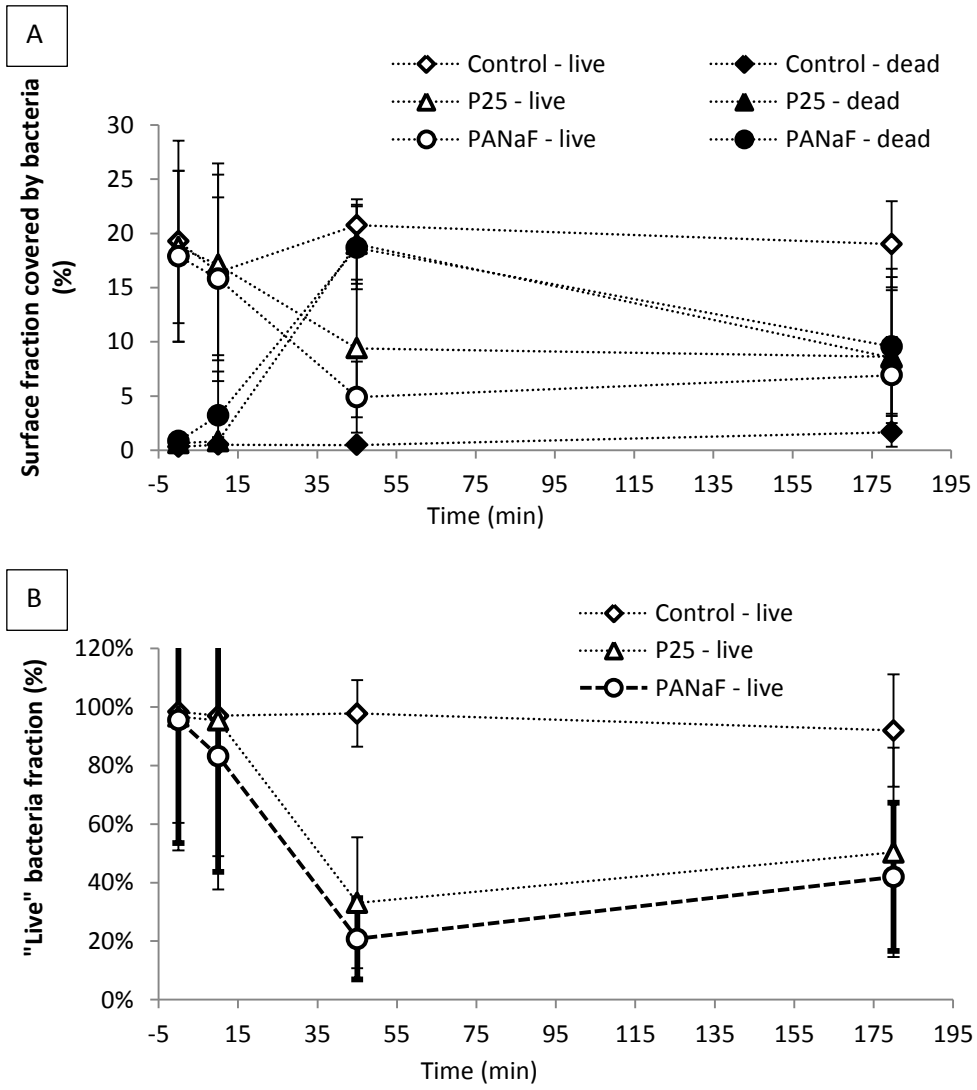

Fig 84 : Surface fraction covered by bacteria (A) and "Live" bacteria fraction (B) of *P. fluorescens* ATCC 13525 strain in function of illumination time on control, P25 and PANaF coating samples.

In general, no good correlation between loss of "Live" bacteria quantity and gain of "Dead" bacteria quantity is found for 45min and 3h of illumination conditions, the sum of "Live" and "Dead" bacteria quantity being superior to that of the non-illuminated samples. This indicates an intermediate Live/Dead state of the involved cells (*i.e.* viable but cell-membrane-damaged bacteria). Since toxicity for bacteria of non-illuminated TiO_2 and of UVA illumination in our experimental conditions have been excluded above, significant losses of "Live" bacteria and increases of "Dead" bacteria observed on TiO_2 coating samples after illumination of 45 min or 3h for both P25 and PANaF are attributed to photocatalytic actions of TiO_2. In particular, cell membrane damages highlighted by PI staining should have been caused by photocatalysis. Nevertheless, no significant efficiency of the bacterial

treatment could be highlighted for the shortest UVA illumination duration. In addition, no significant differences in terms of photocatalytic bactericidal activity are observed between P25 and PANaF coating samples whatever the illumination duration.

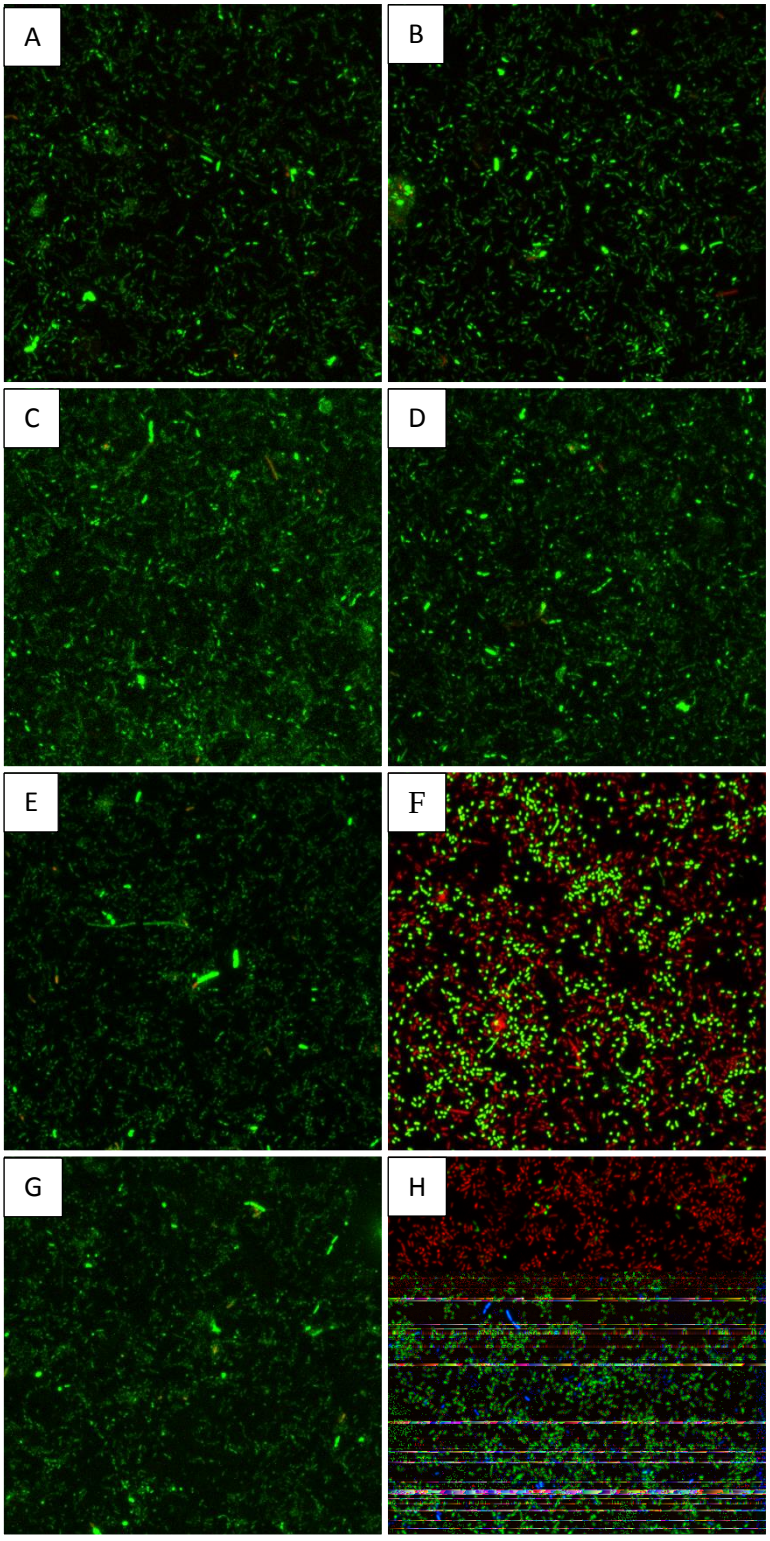

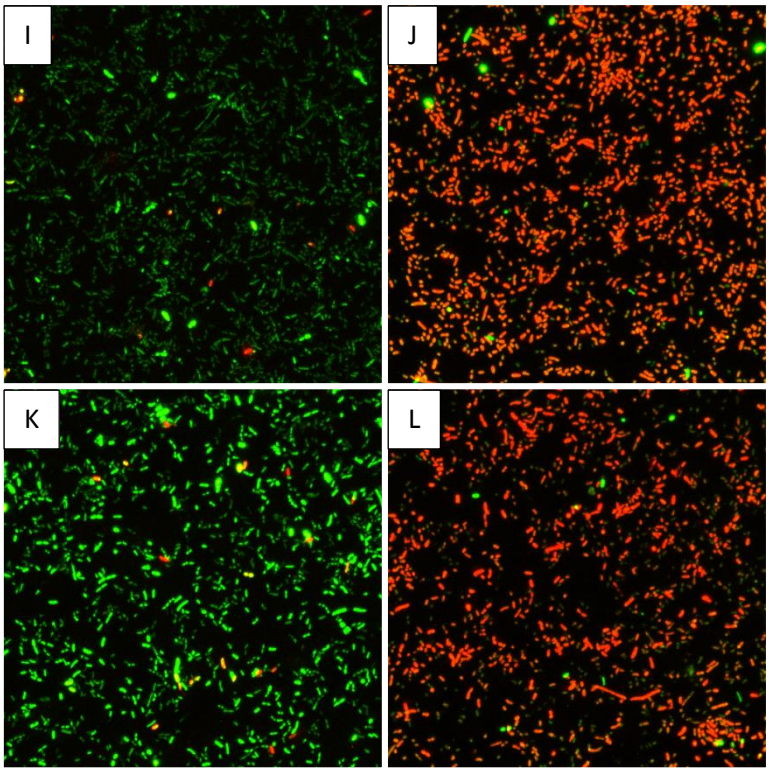

Fig 85 : *P. fluorescens* ATCC 13525 bacteria images taken by confocal microscope. (A) P25 left for 10 min without illumination, (B) P25 after 10 min illumination, (C) PANaF after 10 min without illumination, (D) PANaF after 10 min illumination, (E) P25 after 45 min without illumination, (F) P25 after 45 min illumination, (G) PANaF after 45 min without illumination, (H) PANaF after 45 min illumination, (I) P25 after 3h without illumination, (J) P25 after 3h illumination, (K) PANaF after 3h without illumination, (L) PANaF after 3h illumination.

III.2.2.4. Post photocatalytic anti-bacterial effect

In this section, surface fraction covered after overnight regrowth for the three types of samples (control, P25, PANaF) previously treated with or without UVA illumination are shown. The goal is to assess the post photocatalytic *i.e.* long-term anti-bacterial efficiencies after increasing durations of UVA illumination. *E. coli* SCC1, *S. epidermidis* ATCC 35983 and *P. fluorescens* ATCC 13525 strains were used as before. Two different parameters were considered: 1) Surface fraction covered by bacteria with active GFP metabolism (for *E.coli*) or stained in green by Styo9® staining (for *S. epidermidis* and *P. fluorescens*); they are called "Live" in the following text. 2) Surface fraction covered by bacteria with damaged membrane as demonstrated by the red staining with PI resulting from Styo9®/PI or PI (for *E. coli*) staining; they are called "Dead" in the following text. "Live" quantity is displayed before illumination as a control of a normal growth of the sessile population, while both "Live" and "Dead" quantities are displayed after the given duration of illumination, or without illumination but after a delay corresponding to the given duration of illumination.

For *E. coli* SCC1 strain, results are depicted in Fig 86. As in section III.2.2.3, "Live" bacteria are cells having normal GFP production activity, and "Dead" bacteria are cells having allowed PI molecules to penetrate cell and to mark DNA, *i.e.* having suffered membrane damages.

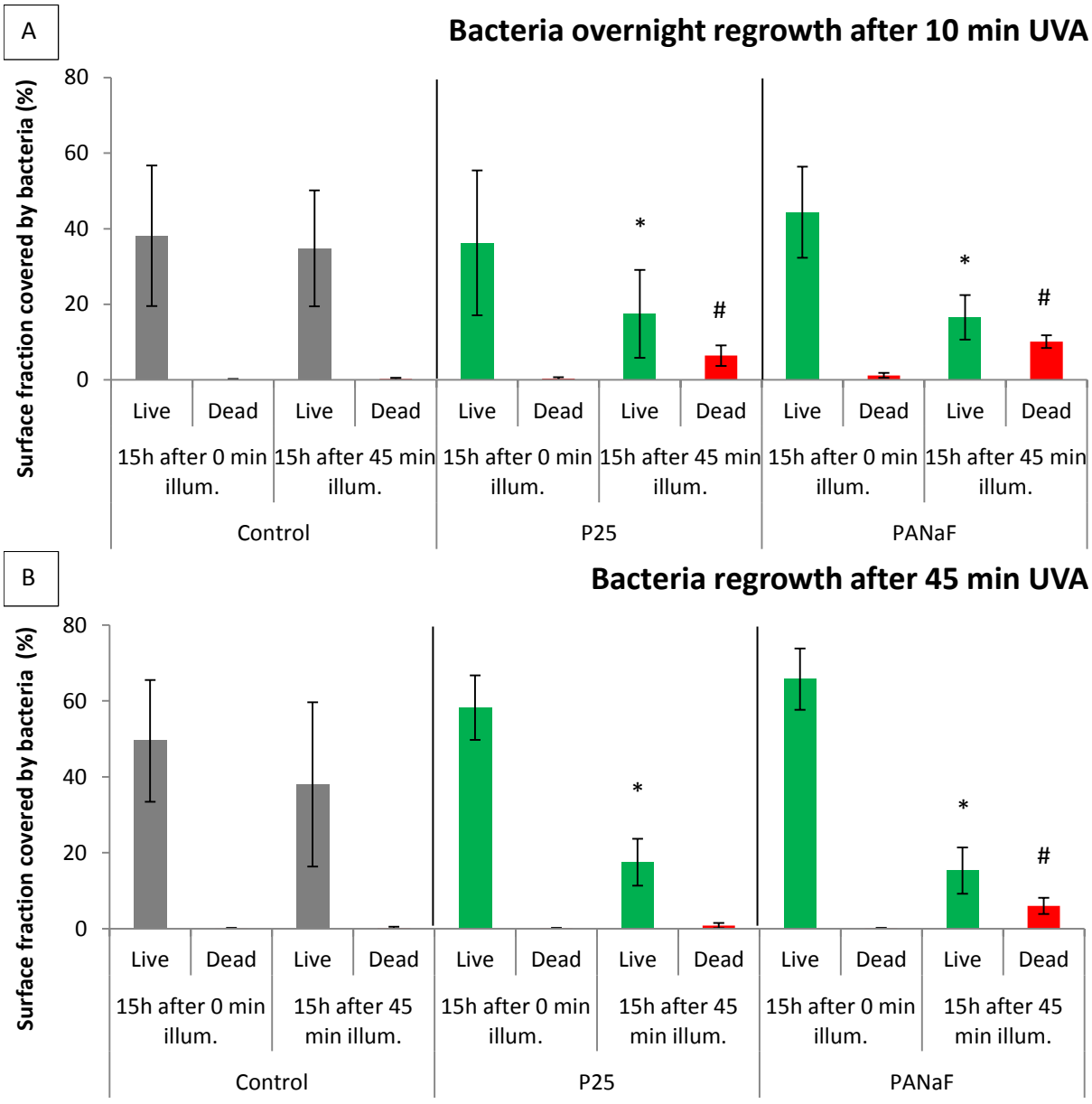

Fig 86 : Post photocatalytic bactericidal effect on overnight bacteria regrowth after 10 (A) and 45 min (B) of UVA illumination on *E. coli* SCC1 strain adhered on control (clean cover slip), P25 and PANaF TiO_2 coating samples. *: Significant differences (p-value = 0.05) compared to "Live" after regrowth without illumination for corresponding coatings. #: Significant differences (p-value = 0.05) compared to "Dead" after regrowth without illumination for corresponding coatings.

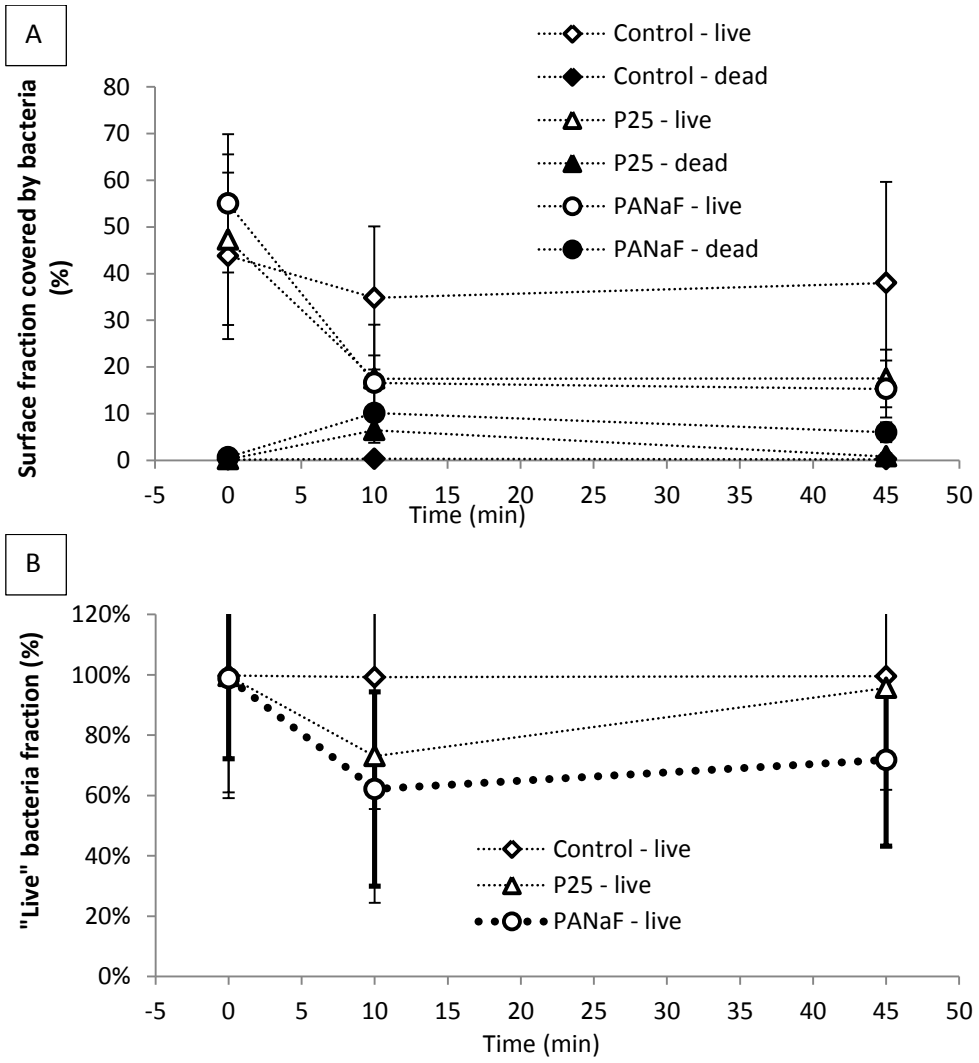

Fig 87 : Surface fraction covered by bacteria (A) and "Live" bacteria fraction (B) of *E. coli* SCC1 after overnight regrowth in function of the illumination time on control, P25 and PANaF samples.

For non-illuminated TiO_2 coating and control samples, the "Live" surface fraction increased from 15-20 % before regrowth (Fig 77 in III.2.2.2) to over 40-50 % after overnight regrowth. In contrast, 10 min of UVA treatment resulted in a significant reduction of "Live" bacteria quantity, reaching nearly half of the non-treated population for both P25 and PANaF sample. 45 min of UVA treatment led to even more inhibition of bacteria population regrowth for these TiO_2 samples. This was accompanied by a higher active bacteria fraction on both two TiO_2 samples compared to the corresponding immediate illuminated samples, which might be caused by the fact that some initially red-stained bacteria were able to recover and reproduce during the overnight period in a nutrition-riche culture medium. [293] However, in general, the inhibition of bacteria population growth on post-illuminated TiO_2 samples allowed to maintain significant decreases of sessile bacteria population thanks to photocatalytic treatment even after recovery of favorable conditions of bacterial growth.

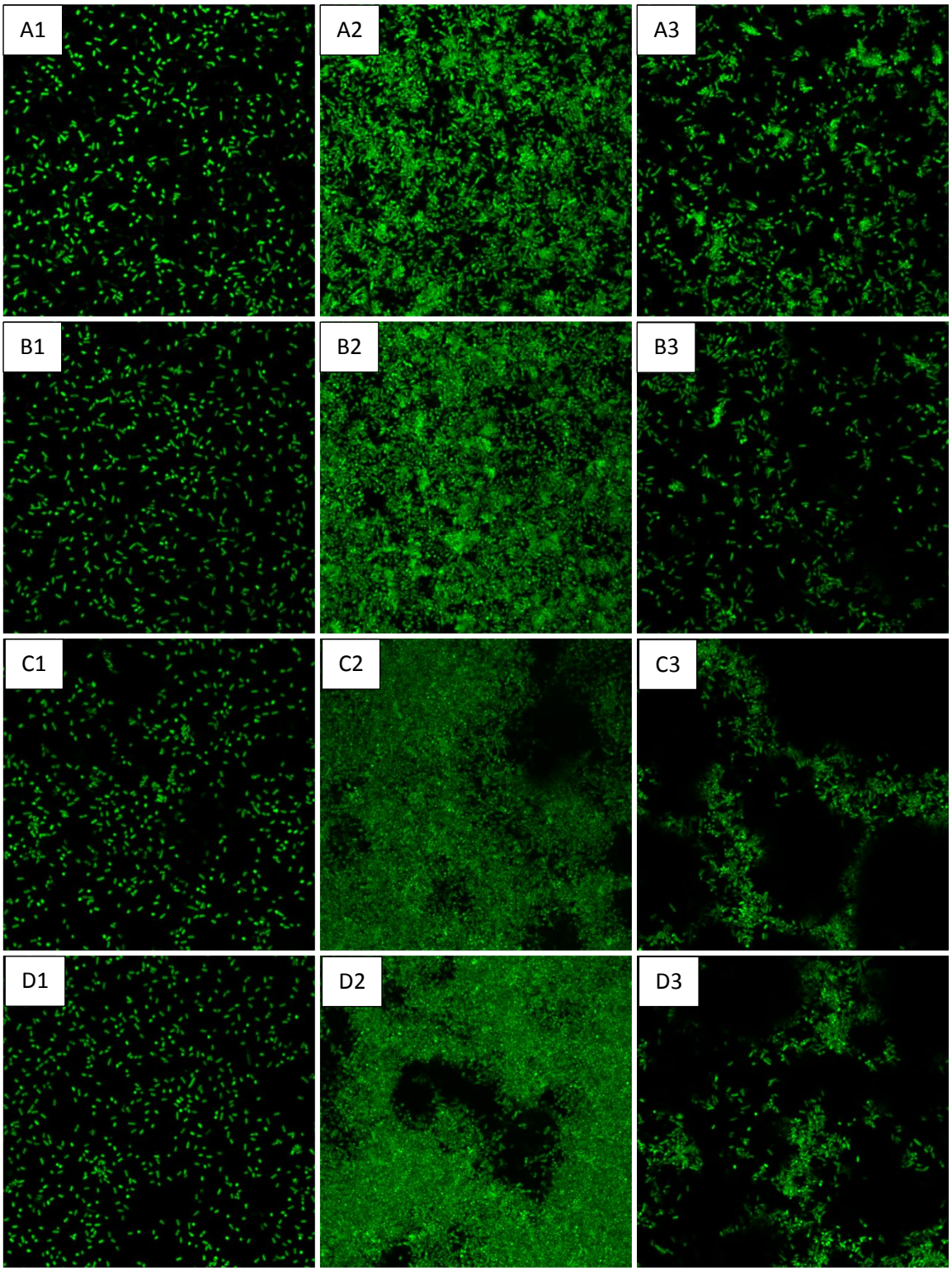

Fig 88 : *E coli* SCC1 bacteria images taken by confocal microscope. Column 1 represents bacteria before UVA illumination; column 2 represents bacteria after regrowth on non-illuminated TiO_2 samples; column 3 represents bacteria after regrowth on illuminated TiO_2 samples. (A) line corresponds to P25 with 10 min of illumination or not; (B) line corresponds to PANaF with 10 min of illumination or not; (C) line corresponds to P25 with 45 min of illumination or not; (D) line corresponds to PANaF with 45 min of illumination or not.

The "Live" bacteria quantity after overnight regrowth only reached to 20 % for 10 or 45 min of photocatalytic treatment on both P25 and PANaF coating samples, while the "Live" bacteria quantity after overnight regrowth without any treatment was around 40-50 % (Fig 87). Illumination times longer than 45 min were not tested. They may lead to enhance the regrowth inhibition effect, not by reducing the "Live" bacteria quantity that already was near to zero immediately after illumination. But rather by reducing the damaged but still living bacterial population measured immediately after illumination.

For *S. epidermidis* ATCC 35983 (CIP 106510) strain, results are depicted in Fig 90. As in section III.2.2.3, "Live" bacteria are cells stained by Syto9® marking DNA, *i.e.* having intact membrane integrity, while "Dead" bacteria are cells having allowed PI molecules to penetrate cell and mark DNA, *i.e.* having suffered membrane damages.

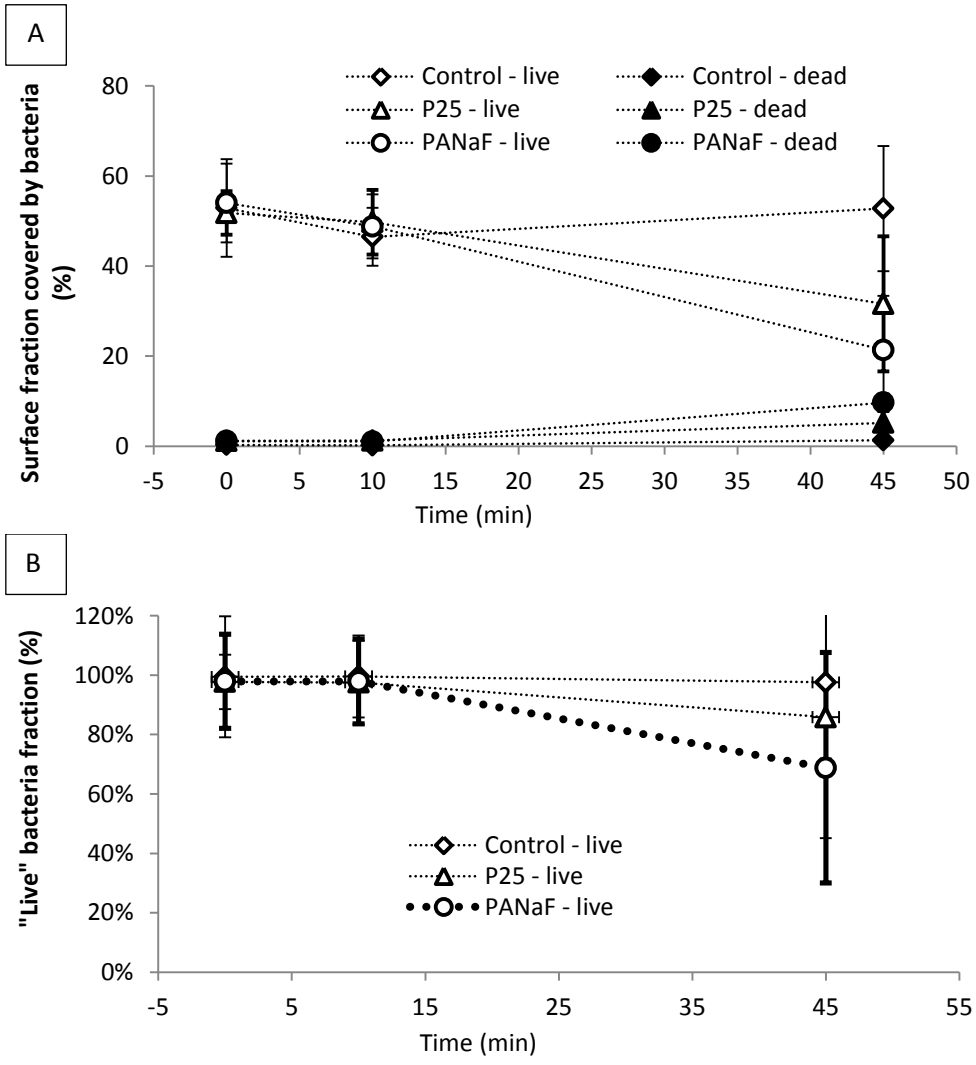

Fig 89 : Bacteria surface coverage fraction (A) and "Live" bacteria fraction (B) of *S. epidermidis* ATCC 35983 (CIP 106510) after overnight regrowth in function of the illumination time on control, P25 and PANaF coating samples.

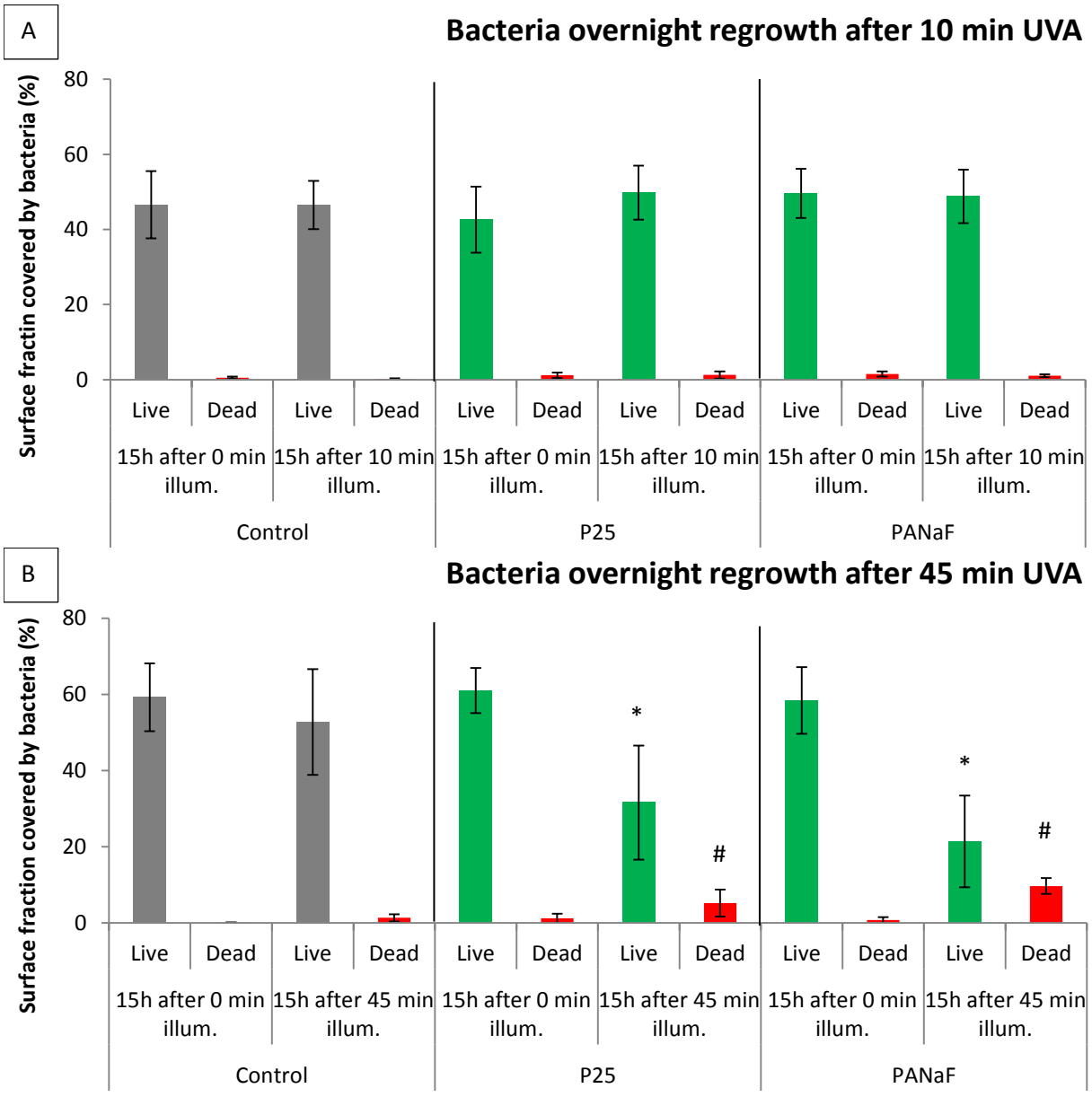

Fig 90 : Post photocatalytic bactericidal effect after 10 (A) and 45 min (B) of UVA illumination on *S. epidermidis* ATCC 35983 (CIP 106510) strain adhered on control (clean cover slip), P25 and PANaF TiO_2 coating samples. *: Significant differences (*p*-value = 0.05) compared to "Live" after regrowth without illumination for corresponding coatings. #: Significant differences (*p*-value = 0.05) compared to "Dead" after regrowth without illumination for corresponding coatings.

For non-illuminated TiO_2 coating and control samples, "Live" bacteria quantity increased from near 10% before regrowth (Fig 80 in III.2.2.3) to over 50-60 % after overnight regrowth. A higher bacteria population regrowth is noticed for this strain compared to that of *E. coli* SCC1 strain. This is probably due to specificities of the strains, but this may be also caused, for a part, by the use of LB medium for culturing *S. epidermidis* instead of M63G medium for culturing *E. coli*, since the non-selective LB medium is more nutrition-riche than

the selective minimum M63G medium. 10 min of UVA treatment has shown no significant reduction of "Live" bacteria quantity after overnight regrowth for both P25 and PANaF coating samples. However, 45 min of UVA illumination resulted in more inhibition of bacteria's regrowth for both the coating types. "Live" bacteria quantity after overnight regrowth reached to 40% after 45 min of photocatalytic treatment of P25 coating but only near 30% for PANaF coating, while "Live" bacteria quantity after overnight regrowth without such treatment was around 50 %.

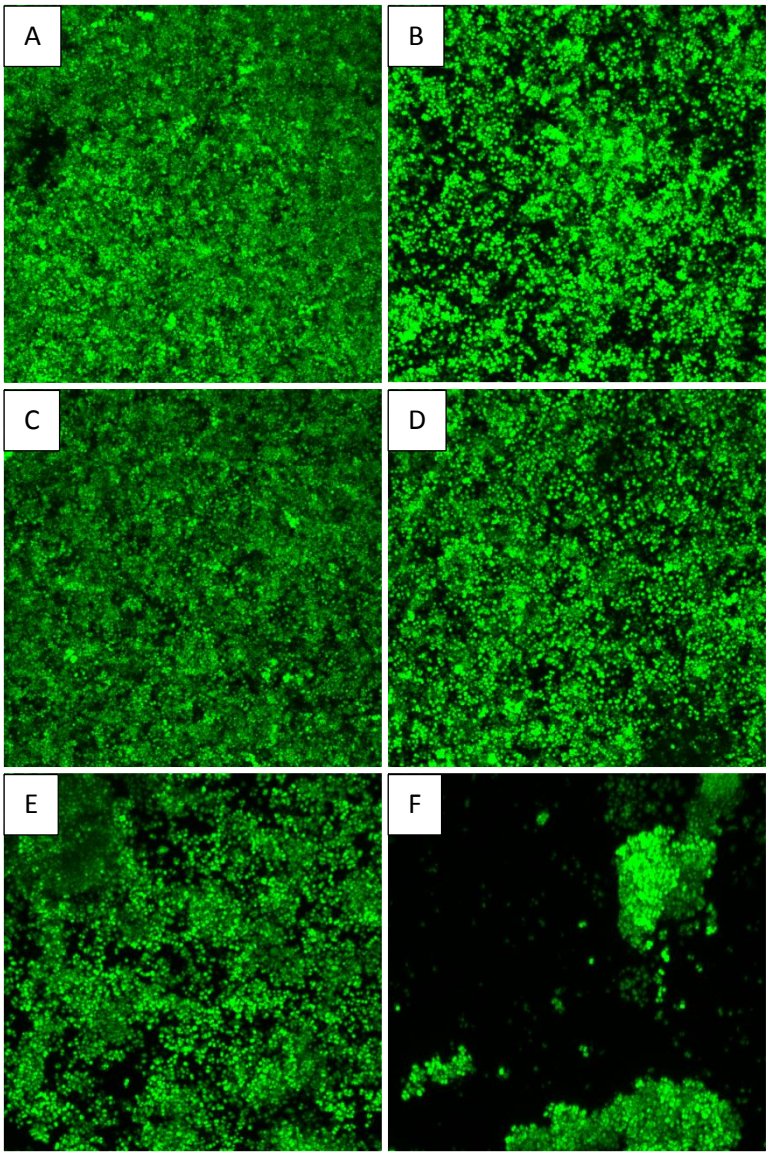

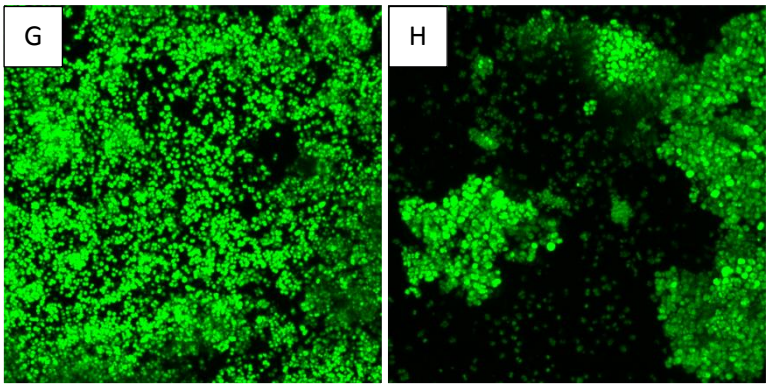

Fig 91 : *S. epidermidis* ATCC 35983 live bacteria images taken after overnight regrowth by confocal microscope. (A) P25 after 10 min without illumination; (B) P25 with 10 min illumination; (C) PANaF after 10 min without illumination; (D) PANaF with 10 min illumination; (E) P25 after 45 min without illumination; (F) P25 with 45 min illumination; (G) PANaF after 45 min without illumination; (H) PANaF with 45 min illumination.

Less "Dead" bacteria quantity is noticed after regrowth on both two TiO_2 coating samples compared to that of corresponding immediate illuminated samples, which might be caused by the fact that some initially red-stained bacteria were able to recover and reproduce during overnight period in a nutrition-riche culture medium. Nevertheless, in general, the inhibition of the bacterial population growth on post-illuminated TiO_2 coating samples allowed the maintenance of significant decreases of sessile bacteria population thanks to the photocatalytic treatment (45 min UVA) even after recovery in favorable conditions of bacterial growth.

For *P. fluorescens* ATCC 13525 (CIP 69.13T) strain, the "Live" bacteria quantity after overnight regrowth could not be determined for the three types of coatings (control, P25, PANaF) with and without illumination. Since bacteria's quantity after regrowth forms a biofilm too thick to be imaged with the confocal microscope with a reasonable time of analysis (Fig 92). Thick biofilms were observed for all three types of coating samples after overnight regrowth even with 45 min of UVA illumination. The high thickness of biofilm even prevents staining by dyes of bacteria in depth, thus making the observation of the whole bacterial population within biofilm impossible. Without deep bacteria stained successfully, any bacteria surface coverage calculated on the basis of the superficial stained bacteria would be biased, preventing thus any quantification of the bacteria's populations.

However, 3D images of the whole biofilms if possible or of a part if not can provide quantitative comparison of bacteria's quantities on the TiO_2 coating samples in terms of visual aspects (Fig 93). From the results, we can notice a moderate inhibition of biofilm

regrowth after 45 min of illumination for both P25 and PANaF samples. If the illumination time was extended to 3h, a better inhibition effect was evidenced by the much less dense "Live" bacterial mass observed in biofilm. The increased red stained bacteria may be due to for a part the photocatalytic treatment, but also to UVA illumination.

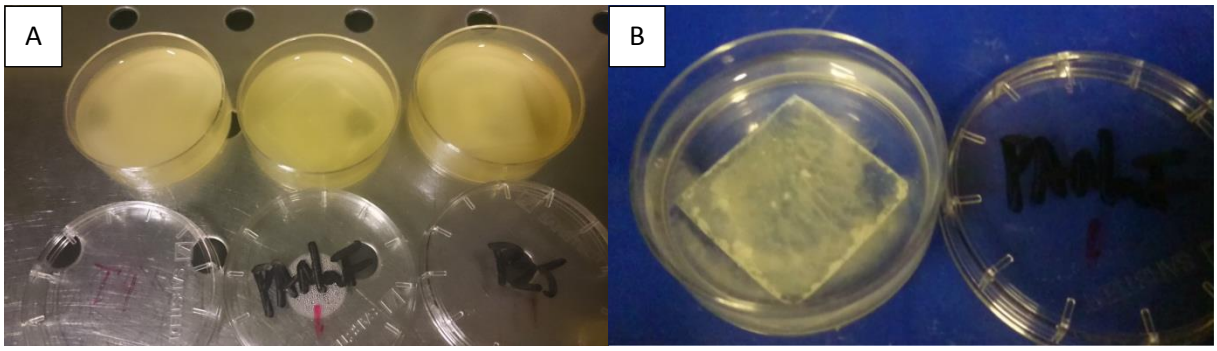

Fig 92 : (A) Control, PANaF and P25 (from left to right) samples after regrowth with 45 min of illumination. (B) Thick biofilm of *P. fluorescens* on the PANaF coating sample of (A), even after rinsing three times with physiological NaCl medium.

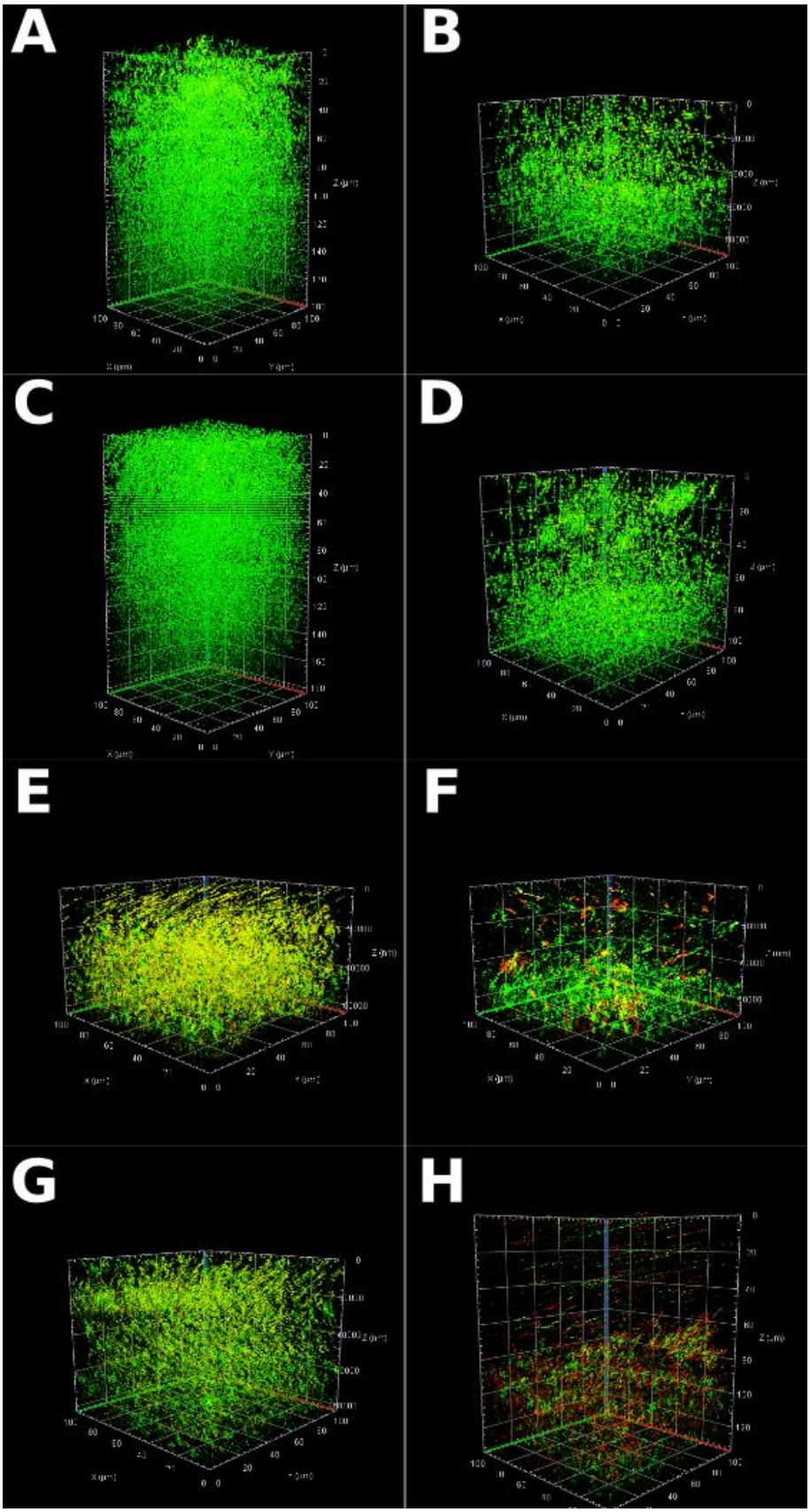

Fig 93 : 3D views of the bacterial biofilms of *P. fluorescens* after overnight regrowth after (A) 45 min without illumination on P25; (B) 45 min with illumination on P25; (C) 45 min without illumination on PANaF; (D) 45 min with illumination on PANaF; (E) 3h without illumination on P25; (F) 3h with illumination on P25; (G) 3h without illumination on PANaF; (H) 3h with illumination on PANaF.

III.2.2.5. Action mechanism of photocatalysis on *Escherichia coli*

Propidium iodide staining of *E. coli*, *S. epidermidis* and *P. fluorescens* provided evidence of cell membrane degradation following photocatalytic treatment of bacteria. To complete the information concerning the mechanism of action of photocatalysis on bacteria, enzymatic and respiratory activities were also studied. For that prupose, *E .coli* PHL 628 strain was stained by CAM and CTC dyes. The corresponding surface fractions covered by bacteria determined on non-illuminated and illuminated samples immediately after the given illumination time (10 min and 45 min) are shown in Fig 94 for each coating type (control, P25, PANaF). Results are presented as CAM or CTC positive bacteria's quantity before and immediately after the given time of illumination (bacterial images are shown in Fig 105 and Fig 106 in annex).

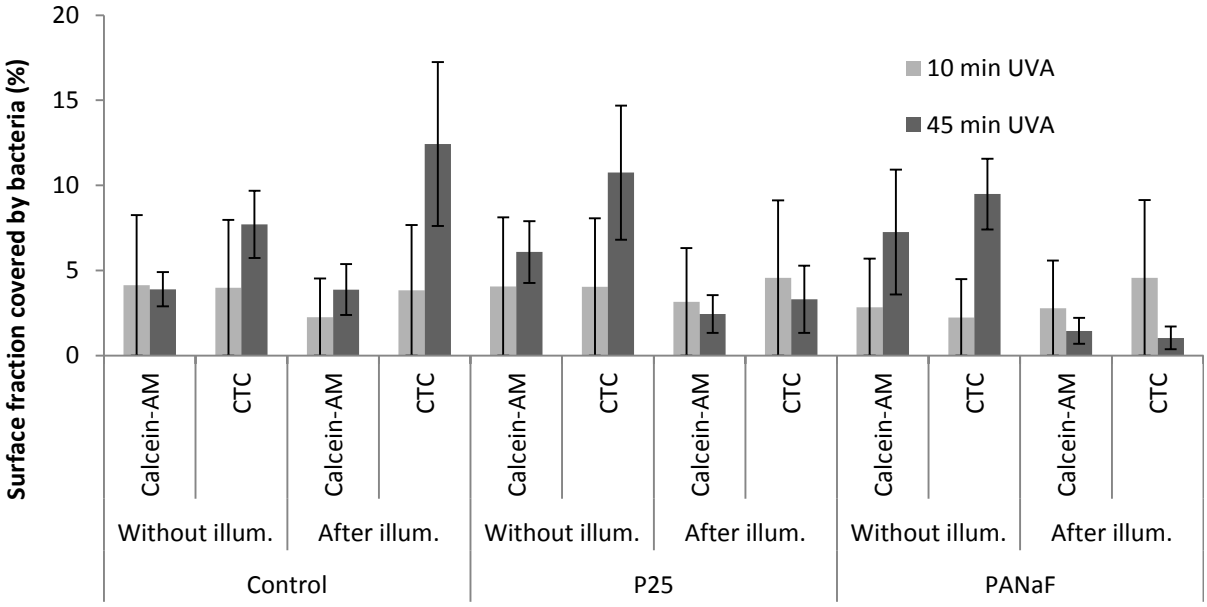

Fig 94 : CAM/CTC positive bacteria surface coverage fraction before and immediately after certain time of illumination on control, P25 and PANaF coating samples.

CAM or CTC positive bacteria's quantity are generally at a similar level as controls, with or without illumination, and as non-illuminated TiO_2 coating samples for the respective illumination time. This indicates that neither toxicity of TiO_2 nor bactericidal effect of UVA illumination significantly influenced the enzymatic and respiratory activities of bacteria. This confirms the results reported above for *E. coli* SCC1 strain stained with PI, and is in accordance with the cell membrane integrity demonstrated by this staining.

10 min of UVA illumination did not result in significant differences between CAM or CTC positive bacteria's quantities measured before and immediately after illumination. In

contrast, 45 min of illumination has resulted in a great reduction of CTC positive bacteria's quantity on P25, even greater on PANaF coating samples. 45 min of illumination has also resulted in a moderate loss of CAM positive bacteria's quantity on P25, which was also even greater on PANaF coating samples. For clearer comparison, Fig 95 resumes the mean CAM and CTC stained bacteria quantities on control, P25 and PANaF coatings for 10 and 45 min of photocatalytic treatment.

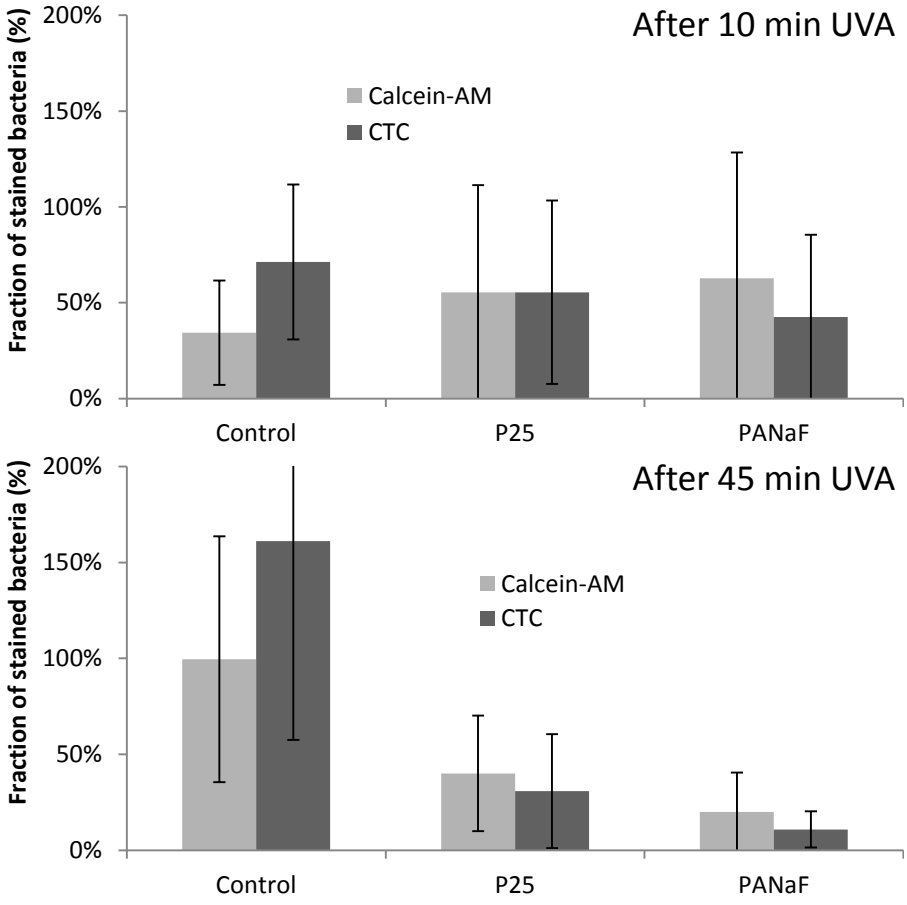

Fig 95 : CAM and CTC stained bacteria quantities for control, P25 and PANaF coatings after 10 and 45 min of UVA illumination. The bacterial strain used was *E. coli* PHL 628.

It should be noticed that, compared to the near total inactivation of GFP production and the membrane degradation of the quasi-complete cell population as shown by PI staining after 45 min of UVA treatment (0.1 %/17 % and 0.1 %/21 % of surface fraction covered by bacteria with GFP/PI labelling for P25 and PANaF coating samples respectively), bacteria with enzymatic and respiratory activities are in higher quantities (2.5 %/3.2 % and 2.0 %/1.8 % of surface fraction covered by bacteria with CAM/CTC labelling for P25 and PANaF coatings respectively).

III.2.2.6. Role of O_2 and of different ions on photocatalytic anti-bacterial activity

Role of O_2 and confined space

Immediate photocatalytic anti-bacteria effect has been evaluated in confined *i.e.* O_2-poor, space, knowing the impact of O_2 in the photocatalytic mechanism. Results on *E. coli* SCC1 strain in confined space for both P25 and PANaF coating samples with or without 45 min of illumination are shown in Fig 96. Surface fraction covered by bacteria was low (between 1% and 5%), because of the few bacteria's quantity present for the inoculation inside the confined space (20 µl of bacteria suspension). After 45 min of UVA treatment, neither P25 nor PANaF coating samples has shown significant reduction in "Live" bacteria quantity, while immediate photocatalytic tests results in "open" system has shown nearly 100% of bactericidal efficiency (Fig 77 B in III.2.2.3).

We also tested 3h hours of UVA illumination with however another method of bacteria's quantification (plate counting method). No immediate photocatalytic anti-bacteria effect was visible in such confined space conditions on both P25 and PANaF coating samples. The loss of CFU was only about 1log, which is considered as not significant.

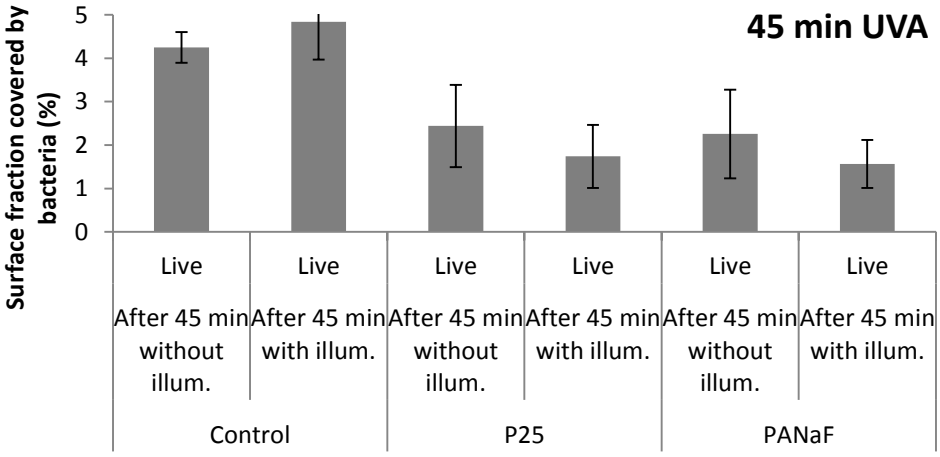

Fig 96 : Immediate photocatalytic anti-bacteria effect on *E. coli* CSS1 strain in confined space for both P25 and PANaF coatings with or without 45 min of UVA illumination.

In order to assess whether the confined space was responsible for the reduction of photocatalytic bactericidal effect, similar conditions have been reproduced with and without bacteria, with special consideration regarding color changes of the TiO_2 nanomaterials of the

coatings. Indeed, TiO_2 in various crystalline phase does not absorb visible light, showing white color, while reduced TiO_2 is blue due to the existence of oxygen vacancies. [294, 295] Results in Fig 97 show that color of the PANaF coating sample in open air did not change after illumination, while all the samples placed in confined space have shown color changes of various degrees. The most dramatic changes occurred with the three samples covered with physiological NaCl 9 g/L medium, regardless of the concentration of bacteria used for the inoculation. This was attributed to a reducing environment created by the lack of dissolved oxygen in the solution in contact with the TiO_2 coating samples.

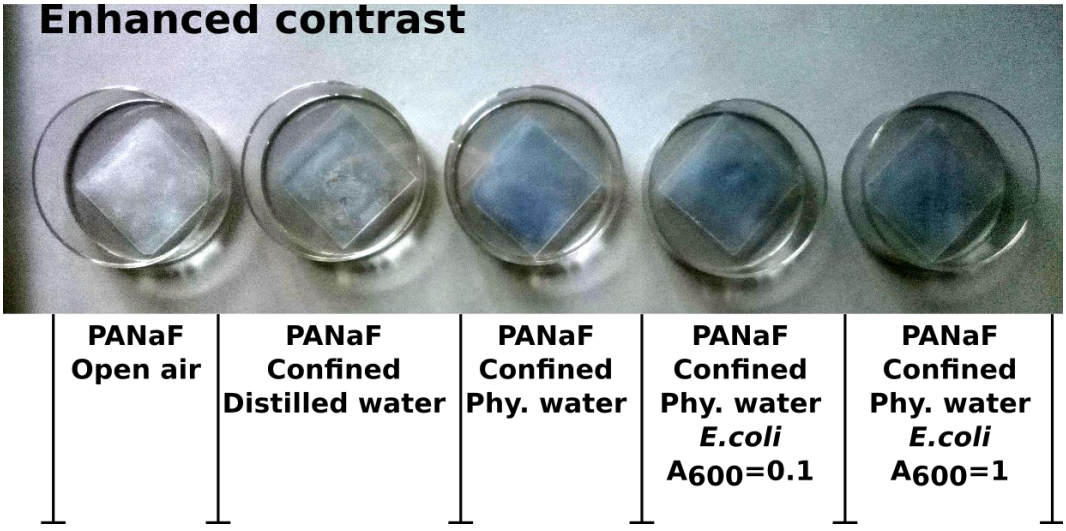

Fig 97 : Contrast-enhanced photographs (contrast-reajusted by ImageJ 1.47v®) of PANaF coating samples after UVA illumination of 45 min. From left to right: sample in open air ; sample in confined space filled with distilled water ; sample in confined space filled with physiological water (NaCl 9g/L); sample in confined space filled with bacterial solution (A_{600}=0.1) in physiological water (NaCl 9g/L); sample in confined space filled with bacterial solution (A_{600}=1) in physiological water (NaCl 9g/L).

To confirm the variation of O_2 concentration, an oxygen level sensor patch was used. Oxygen concentration changes were investigated with and without UVA illumination in a confined space filled with physiological NaCl 9 g/L medium in contact with PANaF coating samples. Results are shown in Fig 98. Both in open air or in confined space, without illumination, fluorescence intensity measured on coating samples is low, indicating that the patch was exposed to an oxygen-rich environment (Fig 98 A and B). In contrast, as soon as UVA illumination is applied, a sharp boost of fluorescence intensity is observed (Fig 98 C). Since fluorescence intensity increased immediately upon UVA turned on, UVA irradiation is thought to have reached PANaF coating instantly, greatly decreasing the concentration of dissolved oxygen in the confined space. Background fluorescence of the patch alone without

exciting laser but with only UVA illumination shows black color (Fig 98 D), which excludes any UVA illumination-induced fluorescence emission from the patch. Reduction of the dissolved oxygen concentration on PANaF with UVA illumination in confined space will be discussed in the next section.

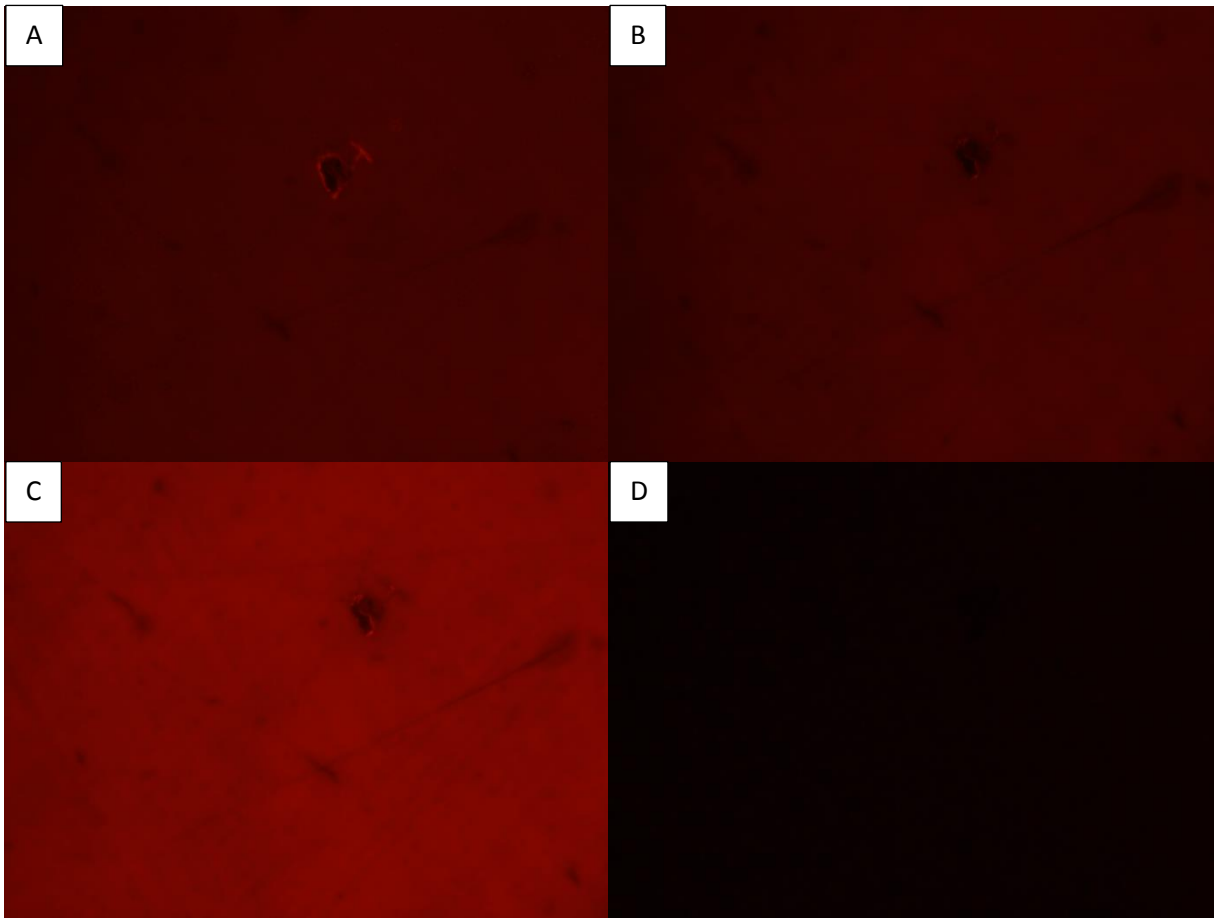

Fig 98 : Fluorescent images of oxygen sensor patch in contact with a PANaF sample. (A) In open air; (B) In confined space within physiological NaCl 9 g/L medium before UVA illumination; (C) In confined space within physiological NaCl 9 g/L medium during UVA illumination; (D) Background fluorescence without exciting laser but with only UVA illumination. The four photographs were taken at the same location.

Role of ions

Immediate photocatalytic effect of TiO_2 samples on *E. coli* SCC1 strain was also evaluated in a more complex medium than physiological NaCl 9 g/L solution in order to determine any potential variation of the treatment efficiency due to the medium. For that purpose, experiments were conducted in M63G medium. The resulting immediate photocatalytic anti-bacteria effect on *E. coli* SCC1 strain for both P25 and PANaF coating samples, with or without 1h of UVA illumination is shown in Fig 99.

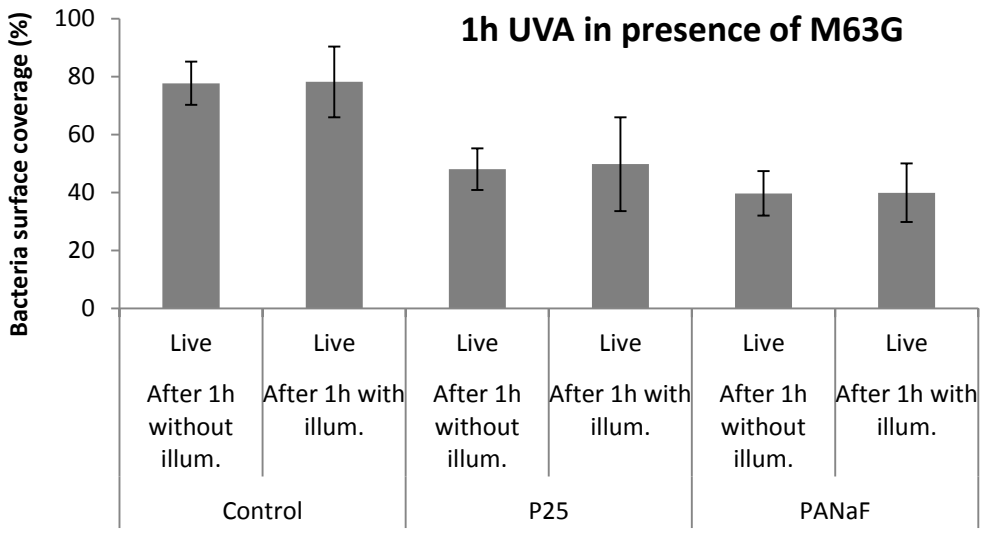

Fig 99 : Immediate photocatalytic anti-bacteria effect on *E. coli* SCC1 strain for both P25 and PANaF coatings with or without 1h of illumination. Samples were cultivated with bacterial suspension prepared in M63G medium. [88]

1h of photocatalytic treatment failed to result in any significant reduction in "Live" bacteria's quantity, which is very different to the results obtained with samples incubated in NaCl 9 g/L medium. The reason might be the presence of some M63G components at the surface of the coating samples, which may block reactions or play as charge recombination centers when samples were illuminated by UVA, even if M63G medium was washed 3 times with NaCl 9 g/L solution before illumination. To study and confirm the influence of M63G presence on photocatalytic activity, liquid-phase photocatalytic degradation of methylene blue (MB) by PANaF nanomaterials sample was studied in the presence or absence of M63G medium. Evaluation of MB degradation efficiency was done by measuring the light absorbance of the reaction medium at 677 nm, which is the main characteristic absorption peak of MB. Results are shown in Fig 100.

The presence of M63G medium was shown to completely stop the photocatalytic degradation reaction of MB, even with 100 times of dilution of M63G medium, which still greatly inhibited the photocatalytic activity of TiO_2 nanomaterial samples. This result supports the fact that even the small quantity of M63G medium remaining in bacteria NaCl 9 g/L suspension during the photocatalytic treatment has a great negative impact on the bactericidal efficiency for TiO_2 coating samples.

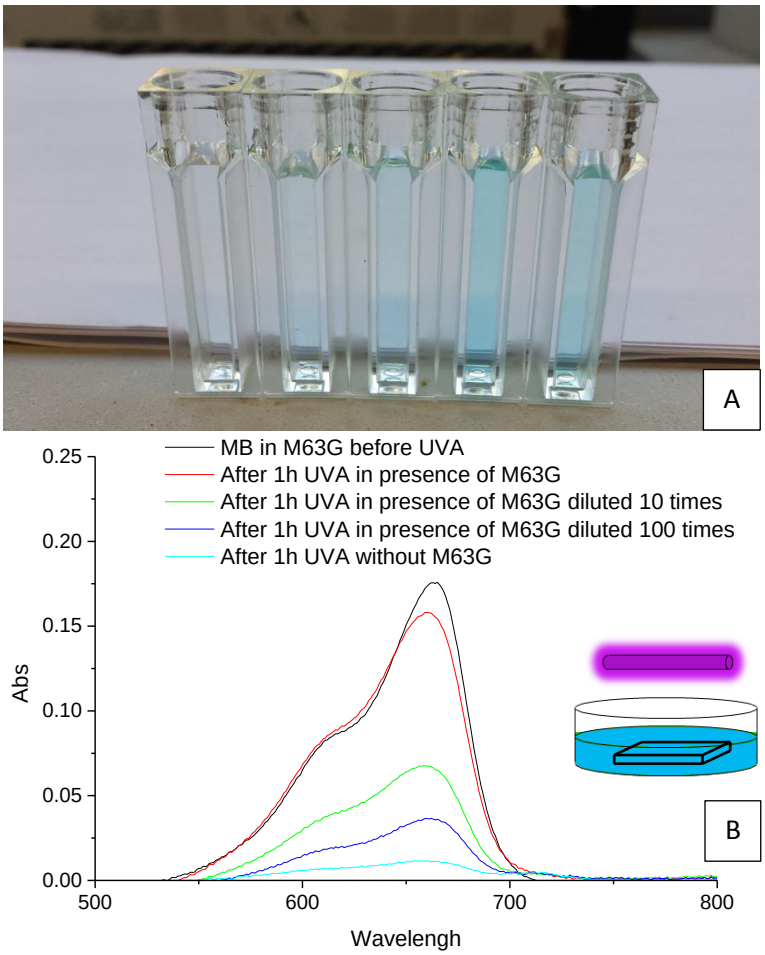

Fig 100 : (A) Photographs of cuvettes containing methylene blue (MB) before illumination or after 1h of illumination on PANaF coating samples in presence of various M63G concentrations. The order from the right to left corresponds to the order from black to cyan explained in (B). (B) UV-absorbance of methylene blue (MB) of the 5 samples in (A). The right middle insert schematizes the experimental setup.

XPS analysis of TiO_2 coating samples with or without being previously immersed in M63G medium provided the atomic ratios of C, O, Ti and P elements (Table 29). The phosphorus level was shown to increase after immersion in M63G medium, which was attributed to the phosphorus present as phosphate form in M63G medium (composition of M63G is shown in annex), while the phosphorus present in PANaF before immersion was attributed to phosphorus-containing addtive (H_3PO_4) used during the synthesis of PANaF TiO_2 nanomaterials, as described in section II.2.4. The increase of phosphate deposition on TiO_2 coating surface is thought to be responsible for the decreased photocatalytic bactericidal effect. More detail of the inhibition effect of M63G medium will be discussed in the next section.

Atomic ratio (%) / Atoms	P25		PANaF	
	Reference	Immersed in M63G	Reference	Immersed in M63G
C_{1s}	19.32	20.25	15.07	12.73
O_{1s}	56.28	59.93	59.94	63.74
Ti_{2p}	24.41	15.85	22.42	17.8
P_{2p}	0	3.97	2.58	5.72

Table 29 : C, O, Ti and P atomic ratios obtained by XPS analysis for P25 and PANaF coating samples before and after immersion in M63G medium.

III.2.3. Discussion

Immediate and post-photocatalytic bactericidal effects were evaluated on P25 and PANaF TiO_2 coatings with several bacterial species and different illumination durations. We have also studied the photocatalytic action mechanism of TiO_2 on *E. coli*, and we have investigated the roles of dissolved oxygen and of the various ions present in M63G culture medium on the efficiency of the photocatalytic activity.

The results clearly displayed a strong anti-bacterial efficiency of the photocatalytic treatment related to the TiO_2 coating, better for PANaF TiO_2 coatings, as well as significant differences of sensitivity of the bacterial species. Since efficiency is expected to depend on both coating and bacterial strain, we will firstly discuss the potential deviation of the anti-bacterial efficiency related to coating properties, especially surface topography for different TiO_2 coatings if bacteria strain is fixed. Then we will discuss the bacteria strain-related anti-bacterial efficiency deviations for TiO_2 coatings, if the TiO_2 material type is fixed. The last section will concern the role of oxygen and M63G medium in the photocatalysis treatment.

III.2.3.1. Relation between samples surface properties and photocatalytic bactericidal activities

We have seen above that PANaF TiO_2 coatings revealed a higher photocatalytic activity than P25 in terms of immediate or post catalytic bactericidal effects on all the various bacterial strains, if other parameters such as illumination time are fixed. Physical and chemical surface properties may play important roles in the alteration of the TiO_2 coating's photocatalytic activity. Among physical properties, surface topography might be a crucial factor affecting photocatalytic bactericidal effect. Indeed, in contrast to VOC molecules, bacteria have too large size to diffuse into the tiny pores between the TiO_2 particles

immobilized on the coating surface. They can therefore only lie on the top of the surface created by TiO_2 nanoparticles aggregates, and have limited number of contact points and valleys between contact points with the surface. [296] Those contact points and the depth of valleys between contact points are very crucial for anti-bacterial effect: [297] if the number of contact points is high and the depths of valleys between contact points are shallow, reactive ROSs generated by TiO_2 can thus reach bacteria cell wall without diffusion on a long distance, which may induce the loss of a large part of ROSs. [162] This is thought to be one reason why PANaF performed enhanced photocatalytic bactericidal effect, as illustrated in Fig 101. Indeed, in accordance to the size of grain-like aggregations as reported in section III2.2.1, PANaF coating has higher number of contact points with a bacterium, and valleys between grains are less deep than that of P25 coating. Thus even if the total contact surface area between a bacterium with two TiO_2 coatings is difficult to compare, we can assure that PANaF coating reveals a higher surface area from which ROSs can be released closer to the bacterium membrane. PANaF coating surface is therefore likely to have more advantage for photocatalytic action than P25 coating surface.

Surface charge is another physical property likely to affect bacterial adhesion to the coating surface. [55] Nevertheless, since isoelectric point (IEP) of both TiO_2 coatings are expected to be much lower than the pH of bacterial culture media (pH = 6.8-7.0), surface charges of P25 and PANaF coatings are both expected to be negative. [298] Therefore, and despite potential weak variation of repulsion between bacteria and coating surfaces that might result from the small difference in negative charge of P25 and PANaF coating surfaces, surface charge is here unlikely to be a factor able to visibly modulate bacterial adhesion strength or photocatalytic activity of P25 and PANaF coatings. [299]

Chemical properties may also be responsible for variations in photocatalytic bactericidal activity. We have concluded in section III.1 that PANaF coating exhibits better activity in degrading MEK compared to P25 because of the effects of fluorine and phosphorous elements used for its synthesis. This may also be the case here, since ROS production can here also benefit from the lower charge recombination phenomena offered by PANaF TiO_2 nanocrystals compared to P25 ones.

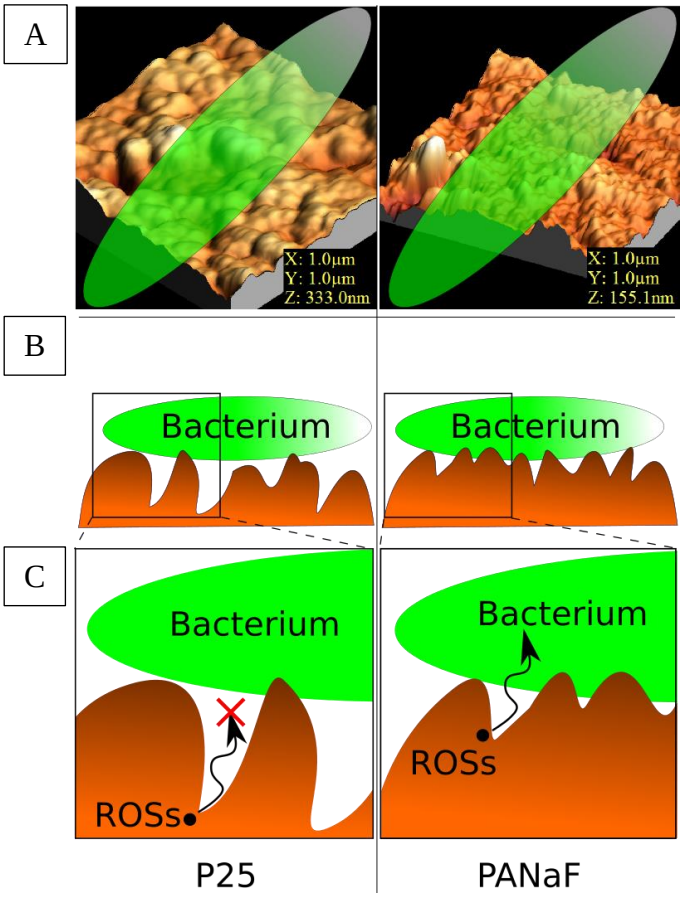

Fig 101 : A) 3D surface topography of P25 (left) or PANaF (right) TiO_2 coatings, the green eclipse represent single bacterium in relative scale size. B) Schematic presentation of the contact between one bacterium and the TiO_2 coatings. Diffusion patterns of ROSs are illustrated in zooming parts for corresponding TiO_2 coatings (C).

Finally, the superior photocatalytic anti-bacterial activity of PANaF coating compared to P25 one is probably the result of the combination of two factors: 1) the oxidative activity of each single PANaF TiO_2 crystal that is higher than single P25 crystal thanks to the use of fluorine and phosphorus element during the synthesis of PANaF TiO_2 coating; 2) the smaller size of PANaF TiO_2 particle that produces a higher surface area that can produce more ROSs and a closer contact modality with the adhered bacteria

III.2.3.2. Anti-bacterial efficiencies of TiO_2 coatings and difference between bacteria species

In section III.2.2, the photocatalytic anti-bacterial performance was shown to depend not only on material properties such as those addressed in section III.2.3.1, but also on bacterial species used in the tests. If TiO_2 material is fixed, results of sections III.2.2.2 and III.2.2.3

show that some bacterial species were more sensitive to photocatalytic treatment than others, both in terms of immediate and post bactericidal efficiency. The general order from the most sensitive to the least sensitive bacteria strain is as following: *E. coli* SCC1 > *S. epidermidis* ATCC 35983 > *P. fluorescens* ATCC 13525. More precisely, *E.coli* SCC1 was the only strain that was near-totally inactivated with only 10 min of UVA illumination time on PANaF coatings, while non-negligible quantity of *P. fluorescens* survived after 3h of UVA illumination treatment. This order of sensitivity is also confirmed by tests of overnight regrowth after the same duration of illumination: Regrowth of *E.coli* was greatly inhibited after being illuminated for 10 min on PANaF coatings, while still dense biofilm of *P. fluorescens* could formed even after being illuminated for 3h.

Three bacterial species-related factors are suspected to be involved in the photocatalytic anti-bacterial efficiency: 1) The production of extracellular matrix (ECM), 2) The structure properties of bacteria cell wall and 3) The defense mechanism countering ROSs.

ECM is expected to prevent both efficient illumination of TiO_2 [300] and diffusion of some ROSs. For example, extracellular polysaccharides (EPSs) have been demonstrated to form a protective layer that prevents the entry of toxic hydrogen peroxide (H_2O_2). [301] However, since all illumination procedures were carried out for TiO_2 coating samples immersed in physiologic saline solution rather than in nutritive culture medium, biofilms are not expected to form in a significant manner. [56] Thus, the possible influence of ECM on the efficiency of photocatalysis, and therefore on differences of efficiency between species, which may protect cells from ROSs by interrupting their diffusion, is here expected to be unlikely.

Cell wall, and especially cytoplasmic membrane of bacterial cell, is the last and the most vital defensive line against any attack from the environment, not only because it keeps the cell structure integrity intact [68] but also because it contains systems performing vital metabolic functions, as for example the respiratory system. [291] In particular, enzymatic activities generally occur in cytoplasm, [302] while the respiratory system is located in the cytoplasmic membrane layer. Consequently, ROSs are expected to need reaching the cytoplasmic layer as first before starting to degrade the enzymes. Results in section III.2.2.4 for Gram-negative *E. coli* SCC1 bacterial strain are in agreement with such attack order of bacterium by ROSs: they have shown that the reduction of respiratory activity was in correlation with an increase of the physical damage of membrane integrity. In addition, the enzymatic activity decreased when

the physical membrane damage increased, even though enzymatic activity was less sensitive to membrane damage than respiration activity.

Cell wall type might be also expected to vary the bacterial susceptibility to ROSs, knowing that *E. coli* and *P. fluorescens* are Gram-negative species while *S. epidermidis* is a Gram-positive species. Indeed, even if ROSs need to reach the cytoplasmic membrane of cell wall, allowing inner vital components of the cell to leak out, to irreversibly damage bacteria. The outer membrane (in the case of Gram-negative bacteria) and the peptidoglycan (PGN) layer are the main barriers for ROSs before reaching this depth (see Fig 12 in bibliographic section). [66] The liposaccharides and lipid layer of the outer membrane of Gram-negative bacteria have been demonstrated to be degradable under photocatalysis treatment. [13, 165] In contrast, the PGN layer was shown to be the most resistant component of cell wall. [104] However, pores in PGN layer are large enough for allowing diffusion of ROSs. [66] Thus, ROSs easily bypass PGN layer and reach the cytoplasmic membrane, which is the location of vital functions like regulation of material exchanges and the electron transfer activities of the bacterial respiration. Considering that the PGN layer does not need to be degraded, we hypothesize the following attack orders of the photogenerated ROSs on *E. coli*, *S. epidermidis* and *P. fluorescens*:

For the Gram-positive *S. epidermidis* ATCC 35983 strain

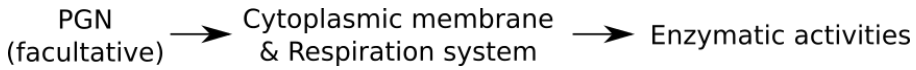

For the Gram-negative *E. coli* SCC1 and *P. fluorescens* ATCC 13525 strains

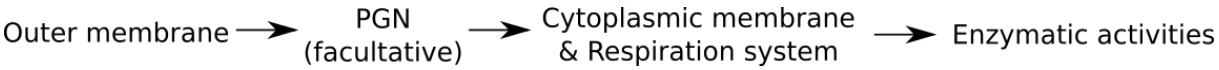

These different interaction steps of ROSs with bacterial cell wall might explain that the Gram-positive *S. epidermidis* ATCC 35983 strain having thick PGN layer was shown to be much more sensible to photocatalysis treatment than the Gram-negative *P. fluorescens*. Nevertheless, in agreement with literature, [303] no direct correlation has been found here between the photocatalytic bactericidal efficiency and the cell wall type, with for example, very different sensitivities of the both Gram-negative *E. coli* SCC1 and *P. fluorescens* ATCC 13525 strains.

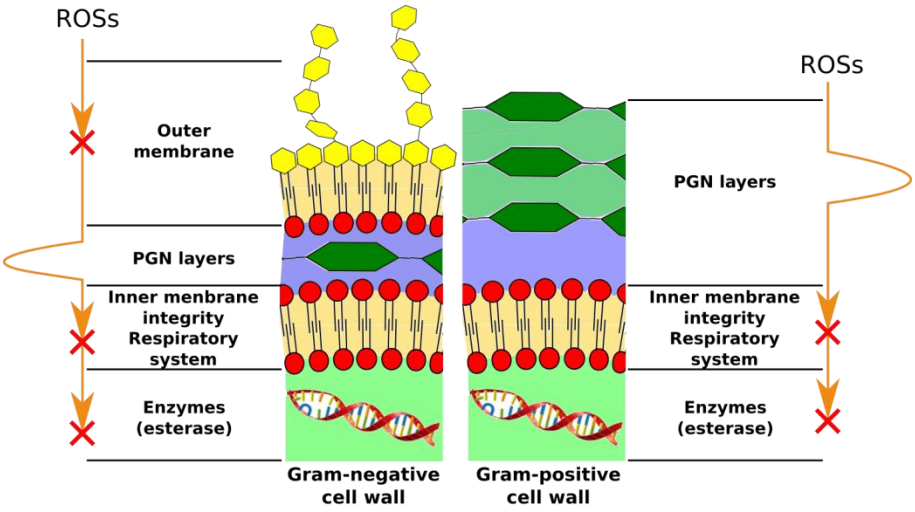

Fig 102 : Illustration of attack order of ROSs on a Gram-positive and Gram-negative bacteria cell wall.

Better resistance of some bacterial strains to photocatalytic treatment may be also related to **defense mechanisms able to counter ROSs**. Several enzymes such as catalase, SOD and others are efficient means of survival possessed by bacteria to provide defenses against oxidative stresses that originate from the external environment (solar UV irradiation, oxygen, etc) or from inner metabolic activities (degradation of biopolymers, respiration, etc). [304] Attack by ROSs is usually located at the cytoplasmic membrane, both for attacks coming from outside- or inside-produced ROSs. The defense mechanisms are therefore thought to also act inside the cytoplasmic membrane. [305] All three bacteria strains used in the present work are catalase and SOD positive, but the efficiency of detoxification of ROSs depends specifically on each strain. [306] Aerobic organisms are exposed to more frequent oxidative stresses than anaerobic or facultative anaerobic organisms and have evolved intricate mechanisms to neutralize ROSs. [307] Alhasawi *et al.* have demonstrated that *P. fluorescens*, as obligate aerobic bacterial specie (non-mutant), can survive in media containing 500µm H_2O_2 by generating NADPH, ATP and glyoxylate in an effort to fend off ROSs, showing its ability to defend against ROSs. [304] In contrast, the anaerobically grown *E .coli* K12 strain, which additionally lacks one SOD type compared to environmental *E. coli* B strain, has been shown sensitive to oxygen exposure in culture media, if being anaerobically treated previously. [308] This main difference against ROSs is a probable cause of the significant difference of sensitivity to the photocatalytic treatment that we observed between *E. coli* and *P. fluorescens*. For its part, *S. epidermidis* bacteria are facultative anaerobes, but they also need oxygen to synthesize cytochromes required for nitrate reduction, [309] allowing to expect an intermediate

resistance level to ROSs. As a conclusion, difference between *E. coli*, *S. epidermidis* and *P. fluorescens* in terms of respiration type may then explain some diversity in the intensity of the photocatalytic anti-bacteria effect here. *P. fluorescens*, obligate aerobe, develops versatile mechanisms to defend oxygen stresses in oxygen-rich environments, thus being expected the most-resistant to ROSs. *S. epidermidis*, facultative anaerobe that could need oxygen to growth, might develop moderate anti-ROS mechanisms, while anaerobic *E. coli* K12 strain probably does not tolerate oxygen-rich conditions, thus being expected to be the least resistant to ROSs from releases by TiO_2 materials.

III.2.3.3. Role of O_2 and effects of ions in solution on photocatalytic anti-bacterial activity

Strong reduction and even suppression of the photocatalytic bactericidal efficiency has been shown when TiO_2 coating samples were placed in a confined space, filled with physiological saline (see results in section III.2.2.6). It was also observed that color of the illuminated TiO_2 coating samples in confined space turned from white into shades of blue without any connection with the bacterial presence. We have attributed this result to the reduction of Ti^{4+} into the lower oxidation state Ti^{3+}, and we have confirmed by using an oxygen sensor patch [310] that a loss of oxygen instantly occurred upon the UVA illumination treatment. We can therefore propose that the reduction of Ti^{4+} into the blue colored Ti^{3+} [295] happened immediately upon UVA illumination, due to an instantaneous drop of the concentration of oxygen dissolved in solution, leading to change TiO_2 structure and thus photocatalytic properties. [295] Instant loss of O_2 is attributed to the following phenomena during photocatalytic reactions: TiO_2 material captures and consumes O_2 by giving away one photogenerated electron to O_2 molecules, leading to the formation of superoxide radical anions. [112] The reason for such electron transfer to occur is the conduction band of anatase TiO_2 (reduction potential of photogenerated electron) which is higher than the redox potential of the molecular oxygen. [112] Nevertheless, if photocatalytic reactions happen in oxygen deficient environment, electrons cannot be all transferred and accumulate in the TiO_2 material. In this case (shown in Fig 103), electrons can also reduce Ti^{4+} presented in TiO_2 material since the redox potential level of Ti^{3+} species are just lower than the conduction band of the anatase TiO_2 (about 0.3 to 0.8 eV lower). [295] Due to small accessibility of O_2 in air to TiO_2 coatings in confined space, O_2 supply was limited. Thus the photo-reduced Ti^{3+} may be stable.

When the formation of Ti^{3+} expands over a relative large area of TiO_2 coating surface, visual observation of color change would be possible. Accordingly, samples in confined space (in physiological saline or distilled water) all showed color change, as expected due to limited O_2 supply. However, it should be noticed that in contrast to as expected, physiological saline has resulted in a more severe blue color than distilled water did. Our hypothesis is that the physiological saline solution used in these experiments was initially poor in dissolved oxygen due to the autoclave sterilization that may have resulted in chasing out the initial dissolved oxygen from the container.

In contrast to what happened with samples in confined spaces, sample exposed in open air remains its white color under illumination, meaning that no left-over electrons were available for the formation of Ti^{3+} centers. This was here expected, as the limitless supply of O_2 in open system can prevent electrons from reducing Ti^{4+} centers.

The presence of bacteria did not have any influence on the color change, although bacteria can uptake O_2 for respiration activities. [311] We hypothesize that O_2 uptake by the bacterial population used in this test was too low compared to the consumption of O_2 by photocatalysis to result in any visible change. This may be further enhanced by the use of a non-nutritive medium, in which bacteria have weak respiratory activities. [291]

Regarding the consequence for the efficiency of the photocatalytic treatment, lack of oxygen can prevent any free-radical-involved polymer or biopolymer chain scission as presented in "bibliography" chapter. [312] As a result, bacteria may have high chance of surviving photocatalytic treatment in confined space. It is worth to mention that inhibition of the photocatalytic effect on degrading MEK, manifested by PANaF materials in O_2-poor environment have been also demonstrated: we have conducted supplementary experiments, in collaboration with the Laboratoire Catalyse et Spectrochimie (LCS UMR 6506, Caen). They consisted of varying the oxygen amount in the inlet air flow during gas-phase photocatalytic reaction of MEK degradation. The results (shown in Fig 107 in annex) show a strong reduction of the photocatalytic activity with decrease of oxygen concentration, leading to the complete inhibition when oxygen concentration reached zero.

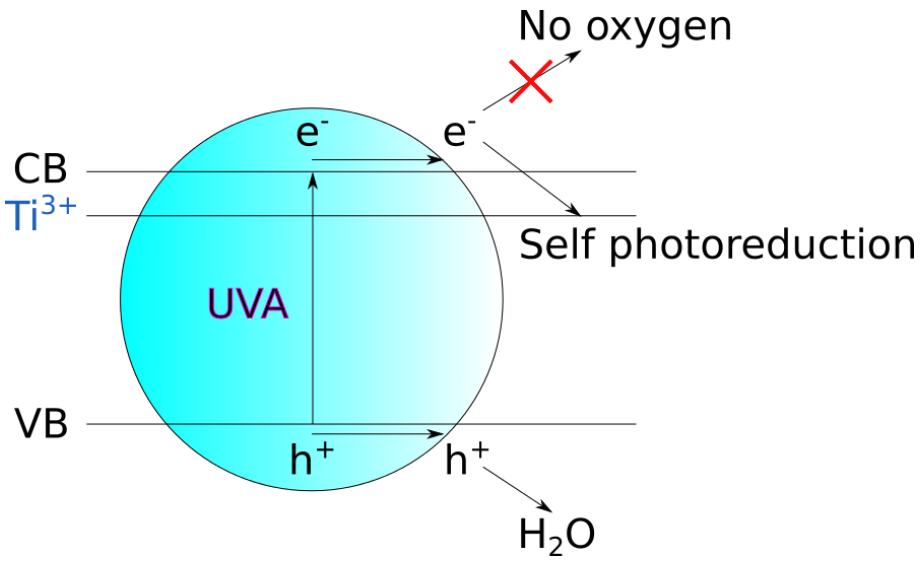

Fig 103 : Self-photocatalytic reduction of Ti^{4+} to Ti^{3+} for TiO_2 placed in oxygen deficient conditions.

Effect of the presence of specific ions in the liquid media has been also investigated. We have compared the immediate photocatalytic bactericidal effect on *E. coli* on TiO_2 coating samples inoculated with M63G or physiological saline-based bacterial suspension before the UVA illumination treatment. In addition, MB degradation through photocatalytic treatment conducted in M63G media or not was tested. The results have shown the very noticeable inhibition effect of M63G on the photocatalytic activity even with M63G in tiny quantity. XPS analysis confirmed the large quantity of phosphate ions present in M63G, which may be responsible for the inhibition effect, since phosphate ions can be easily absorbed onto TiO_2 surface. Thus they block the reactive sites for the targeted molecules or they play as charge recombination centers (*i.e.* poisoning of the photocatalyst). In agreement with this hypothesis, it has been reported that phosphate ions are the most detrimental ones, amount other common ions presented in waste water, to reduced photocatalytic efficiency in liquid phase. [159] This result is of great importance to specify the best conditions for reaching efficient photocatalytic treatment in applications of photocatalysis in aqueous environments.

IV. General conclusion and perspectives

In response to the objectives of this PhD thesis, we have accomplished three main tasks:

1) Inspired by the synthesis of a $BmimPF_6$-ionic-liquid-derived anatase TiO_2 nanomaterial through a modified sol-gel route in HAc media, we reported the first synthesis (to our knowledge) of an anatase TiO_2 nanomaterial by a modified sol-gel route in HAc media using cheap H_3PO_4 and NaF as additives and controllable substitutes to $BmimPF_6$ (referred as PANaF), followed by calcination.

When compared to TiO_2 P25 reference and additive-free TiO_2 materials, interesting physico-chemical properties have been evidenced for both $BmimPF_6$- and PANaF-derived TiO_2 materials. They possess a high specific surface area, a small mean crystallite size, and display fast crystallization during aging at room temperature together with a strongly inhibited size growth of crystals during calcination. The role of each of the additives during synthesis has been investigated. Beside the $BmimPF_6$ ionic liquid, BmimCl, HPF_6, H_3PO_4 and NaF (constituent elements of the ionic liquid $BmimPF_6$) have been added as single or paired additive in the TiO_2 sol-gel syntheses using HAc or HCl as acid catalyst. The P-involved TiO_2 materials (P/Ti ratio of 0.03) showed the main characteristics above-described than the IL-derived TiO_2 materials. Furthermore, a high P content resulted in a strong modification of the surface chemical state, and the formation of titanium phosphate phase has been evidenced. Although this phenomenon was less observed with a low P content in HAc media, we have evidenced the presence and the influence of P preferentially at the surface of TiO_2 material, and a migration of P from bulk to surface or a surface sintering was proposed to occur during calcination. We hypothesize that, thanks to the presence of P, the formation of Ti-PO_4 could stabilize a large number of nucleation seeds before aging thus leading to a faster crystallization rate and smaller anatase TiO_2 crystals; already well crystallized TiO_2 before calcination results in a growth of small mean size particles during calcination.

F has been observed to cause the formation of anisotropic spindle/rod-like TiO_2 crystals during aging. We believe that this could result from the capping ability of fluoride ions, which can favor easier growth of {001} facet of TiO_2 crystal. In contrast to the existence of P within the TiO_2 photocatalyst, F has been removed after calcination.

The role of $Bmim^+$ was not investigated in this work.

2) Evaluation of the photocatalytic activity of the TiO_2 photocatalysts in the degradation of a model VOC as well as in the elimination of bacteria has been performed.

First, the gas-phase photocatalytic activity of the additive-derived TiO_2 photocatalysts for degrading a common VOC, the Methyl Ethyl Ketone (MEK), under UVA irradiation was tested and compared to TiO_2 P25 reference. Among photocatalysts synthesized in HAc media, high MEK conversion was observed for P-derived TiO_2 materials and high CO_2 selectivity was observed for F-derived TiO_2 materials. Only P- and F-derived TiO_2 materials synthesized in HAc media (PANaF TiO_2 material with low P and F content) have shown the highest activity in terms of CO_2 mineralization yield, which was superior to that of P25 and comparative (even higher) to that of $BmimPF_6$-derived TiO_2 materials. This material presents high industrial interest since the additive used (H_3PO_4 and NaF) are much cheaper than $BmimPF_6$. High P content or in absence of calcination resulted in total inhibition of photocatalytic activity.

Also, replacing HAc by HCl in the sol-gel synthesis of additive-derived TiO_2 was valuable for gaining more information on the properties of modified TiO_2. However, TiO_2 synthesis in HCl exhibited lower activity in the MEK degradation than the HAc-analogue.

Liquid-phase photocatalytic anti-bacterial tests (in terms of both immediate and post effects) against several bacterial strains (*E. coli* SCC1, *S. epidermidis* ATCC 35983 and *P. fluoresences* ATCC 13525) under UVA irradiation was also performed for PANaF TiO_2 material deposited on surface, and compared to that of P25. The results showed a material type-, illumination time- and bacterial strain-dependency. In general, PANaF material presents higher bactericidal effect than that of P25. 10 min of illumination can already induce near-total elimination of *E. coli,* for PANaF TiO_2 material, while moderated efficiency has been observed for P25. 45 min of illumination can induce near-total elimination of *E. coli* SCC1 and *S. epidermidis* ATCC 35983 bacterial strain on both two TiO_2 materials, while non-negligible *P. fluoresences* fraction still survived after 3h of illumination for both two TiO_2 materials. Along with few studies reported before, we have evidenced a post photocatalytic anti-bacterial effect for *E. coli* SCC1 and *S. epidermidis* ATCC 35983 strains. The results showed good correlation with that of immediate photocatalytic anti-bacterial tests. *P. fluoresences* ATCC 13525 is the most resistant bacterial strain to post-photocatalytic effect. Cytoplasmic membrane is believed to be the most vital cell component target of photogenerated ROS and a good correlation between inactivated respiratory activity and damaged cell membrane integrity has been deserved. The order of cell components to be attacked was proposed for both Gram-negative and Gram-positive bacterial cell wall type. Order of bacterial strain in function of resistance against ROS-induced oxygen stress was

proposed as *P. fluorescens* ATCC 13525 > *S. epidermidis* ATCC 35983 > *E. coli* SCC1, with no correlation to the bacterial cell wall type. The stronger oxygen stress defense mechanism in aerobic *P. fluorescens* ATCC 13525 strain was hypothesized to be the factor here. Presence of PO_4^{3-} ions or absence of dissolved oxygen in the reaction medium can strongly inhibit the photocatalytic bactericidal activity.

3) Finally, a correlation between the high performance in the photocatalytic degradation of MEK and the photocatalytic bactericidal properties, and with the properties of PANaF-derived TiO_2 materials was established. To our knowledge, this is the first time that a combined role of P and F during aging in sol-gel synthesis has been proposed.

High MEK conversion was observed in gas phase for P-derived TiO_2 materials, which benefit mainly from high specific surface area and small mean crystallite size. High CO_2 selectivity was observed for F-derived TiO_2 materials, which might benefit mainly from the favored adsorption of intermediate degradation products of MEK on the highly exposed {001} facets of TiO_2 crystals. Furthermore, benefiting from the large total BET surface area and the exposure of the highly reactive {001} facet for each of the crystal, the total reactive surface area was significantly increased, so that the total number of reactive heterogeneous catalytic sites available to produce highly oxidizing radicals are greatly increased. P- and F-induced spatial charge separation phenomenon was also proposed to play a role for achieving a higher overall photocatalytic activity.

The enhanced liquid-phase photocatalytic bactericidal efficiency of PANaF TiO_2 material over P25 can also benefit from the above-mentioned explanations. Furthermore, smaller particles of PANaF material results in a smoother surface topology, which was thought to reduce the necessary diffusion length of variable photogenerated ROSs to reach and attack the bacterial membrane. Adsorption of PO_4^{3-} anions on the TiO_2 material was detrimental to the photocatalytic activity, as they can block the reactive sites or favor charge recombination. Further, oxygen has been evidenced as an indispensable factor for photocatalytic bactericidal efficiency. Indeed, in the absence of oxygen, TiO_2 material is proposed to undergo self-reduction and to turn into blue color, eventually leading to a loss of photocatalytic activity.

This interdisciplinary PhD thesis combines material science with photocatalysis and microbiology. Some new hypotheses have been put forward to explain the results obtained

during our work. Although some of them are hypothetic, we think however that they can open new ways in understanding the synthesis of tunable TiO_2 nanomaterials for increasing photocatalytic activity, and the interface with microbiology will continue to be a research topic of high interest. In this work, we have obtained important information on the reaction of bacteria through photocatalysis, and on the influence of some environmental conditions on photocatalysis. **So here we would like to list some perspectives**, for both chemical and microbiological aspects:

1) Crystallization of TiO_2 during aging in low-temperature sol-gel synthesis in the presence of P and F is fairly a new topic, and it was not fully studied in this work. We think that there are three parameters worth to be studied to get more understanding on the rate and yield of PANaF TiO_2 crystallization, for optimizing synthesis protocols and targeting higher efficiency materials: temperature (0^oC-60^oC), P/Ti ratio and F/Ti ratio (0.01- 0.1).

2) The role of F in exposing {001} facet was not fully understood in our work. Specific studies on NaF(solely)-derived TiO_2 material synthesized in HAc media would be appreciated.

3) The studies on the crystallization progress during aging and on the migration of P during calcination, as well as the relation between the dispersion state of P within dried and calcined TiO_2 and the photocatalytic activity can be further extended, with varying the calcination temperature and/or the P content. On one hand, since the aged TiO_2 crystals were already well crystallized, it is always worth to implement a less-energy-consuming calcination process; on another hand, a too low calcination temperature could unfavor P-migration. So, ideally, we should perhaps target a well crystallized TiO_2 material after aging with already a low dispersion of P.

4) Since hypotheses have been made to explain the higher resistance of aerobic strains towards ROSs over anaerobic strains, investigations using genetically modified bacterial strains (both aerobic and anaerobic) and PCR as gene-express analysis method would be needed to confirm such a theory.

5) The anti-bacterial efficiency against biofilm has never been truly studied in this work, notably because of the concern due to the presence of PO_4 in the culture medium. A search for a suitable culture medium with no inhibition of photocatalytic activity would be needed. If poly(phosphate)-polymer (in contrast to free monophosphate anions) would show no influence on the photocatalytic activity, tryptone broth may be a good candidate.

6) The blue color change of TiO_2 in confined space would be another topic to study, and the total inhibition of photocatalytic activity need to be more understood. A time resolved microwave conductivity characterization would be adapted to follow charge-carrier lifetime of the corresponding TiO_2 material, and to evidence the relationship between the color intensity and the photocatalytic performance.

In the future, another one of the interesting perspectives of this work may be the incorporation of these photocatalytic powdered nanomaterials into optimized paint formulation to yield photocatalytic coatings, efficient for both bactericidal and air cleaning applications. Some very preliminary tests have been performed and showed higher efficiency in the degradation of MEK than commercial paints from KEIM and STO companies.

Citations

1. EPA, Exposure factors handbook. *US Environment protection agency, Washington, DC* 1997, Chapter 15, Table 15-176.

2. Jones, A. P., Indoor air quality and health. *Atmospheric Environment* 1999, 4535}4564.

3. Schöpp, W.; Amann, M.; Cofala, J.; Heyes, C.; Klimont, Z., Integrated assessment of European air pollution emission control strategies. *Environmental Modelling & Software* 1998, 14, 1-9.

4. D'Amato, G.; Liccardi, G.; D'Amato, M., Environment and development of respiratory allergy. II. Indoors. *Monaldi archives for chest disease, Fondazione clinica del lavoro, IRCCS [and] Istituto di clinica tisiologica e malattie apparato respiratorio, Universita di Napoli, Secondo ateneo* 1994, 49, 412-20.

5. Husman, T., Health effects of indoor-air microorganisms. *Scandinavian journal of work, environment & health* 1996, 5-13.

6. Monteiro, R. A. R.; Lopes, F. V. S.; Silva, A. M. T.; Ângelo, J.; Silva, G. V.; Mendes, A. M.; Boaventura, R. A. R.; Vilar, V. J. P., Are TiO_2-based exterior paints useful catalysts for gas-phase photooxidation processes? A case study on n-decane abatement for air detoxification. *Applied Catalysis B: Environmental* 2014, 147, 988-999.

7. Gandolfo, A.; Bartolomei, V.; Gomez Alvarez, E.; Tlili, S.; Gligorovski, S.; Kleffmann, J.; Wortham, H., The effectiveness of indoor photocatalytic paints on NOx and HONO levels. *Applied Catalysis B: Environmental* 2015, 166-167, 84-90.

8. Folli, A.; Pade, C.; Hansen, T. B.; De Marco, T.; Macphee, D. E., TiO_2 photocatalysis in cementitious systems: Insights into self-cleaning and depollution chemistry. *Cement and Concrete Research* 2012, 42, 539-548.

9. Huang, Y.; Ho, S. S.; Lu, Y.; Niu, R.; Xu, L.; Cao, J.; Lee, S., Removal of indoor volatile organic compounds via photocatalytic oxidation: A short review and prospect. *Molecules* 2016, 21.

10. Keller, N.; Pham-Huu, C.; Ledoux, M. J., Continuous process for selective oxidation of H_2S over SiC-supported iron catalysts into elemental sulfur above its dewpoint. *Applied Catalysis a-General* 2001, 217, 205-217.

11. Kühn, K. P.; Chaberny, I. F.; Massholder, K.; Stickler, M.; Benz, V. W.; Sonntag, H.-G.; Erdinger, L., Disinfection of surfaces by photocatalytic oxidation with titanium dioxide and UVA light. *Chemosphere* 2003, 53, 71-77.

12. Weschler, C. J., Ozone in indoor environments: Concentration and chemistry. *Indoor Air-Int. J. Indoor Air Qual. Clim.* 2000, 10, 269-288.

13. Maness, P. C.; Smolinski, S.; Blake, D. M.; Huang, Z.; Wolfrum, E. J.; Jacoby, M. A., Bactericidal activity of photocatalytic TiO_2 reaction toward an understanding of its killing mechanism. *Applied and Environmental Microbiology* 1999, 65, 4094-4098.

14. Shields, H. C.; Fleischer, D. M.; Weschler, C. J., Comparisons among VOCs measured in three types of US commercial buildings with different occupant densities. *Indoor Air-Int. J. Indoor Air Qual. Clim.* 1996, 6, 2-17.

15. Begerow, J.; Jermann, E.; Keles, T.; Ranft, U.; Dunemann, L., Passive sampling for volatile organic compounds (VOCs) in air at environmentally relevant concentration levels. *Fresenius Journal of Analytical Chemistry* 1995, 351, 549-554.

16. Sahlberg, B.; Gunnbjornsdottir, M.; Soon, A.; Jogi, R.; Gislason, T.; Wieslander, G.; Janson, C.; Norback, D., Airborne molds and bacteria, microbial volatile organic compounds (MVOC), plasticizers and formaldehyde in dwellings in three North European cities in relation to sick building syndrome (SBS). *Science of the Total Environment* 2013, 444, 433-440.

17. WHO, Air quality guidelines for europe. *World Health Organisation* 2014.

18. WHO, Air quality guidelines for europe. *World Health Organisation* 2010.

19. Huang, Y.; Ho, S. S. H.; Ho, K. F.; Lee, S. C.; Gao, Y.; Cheng, Y.; Chan, C. S., Characterization of biogenic volatile organic compounds (BVOCs) in cleaning reagents and air fresheners in Hong Kong. *Atmospheric Environment* 2011, 45, 6191-6196.

20. Clobes, A. L.; Ananth, G. P.; Hood, A. L.; Schroeder, J. A.; Lee, K. A., Human activities as sources of volatile organic compounds in residential environments. *Annals of the New York Academy of Sciences* 1992, 641, 79-86.

21. Maroni, M.; Axelrad, R.; Bacaloni, A., NATO's efforts to set indoor air quality guidelines and standards. *American Industrial Hygiene Association Journal* 1995, 56, 499-508.

22. Abraham, M. H.; Gola, J. M. R.; Cometto-Muniz, J. E.; Cain, W. S., The correlation and prediction of VOC thresholds for nasal pungency, eye irritation and odour in humans. *Indoor Built Environ.* 2001, 10, 252-257.

23. Brooks, B. O.; Utter, G. M.; Debroy, J. A.; Schimke, R. D., Indoor air pollution - An edifice complex. *J. Toxicol.-Clin. Toxicol.* 1991, 29, 315-374.

24. Wang, S.; Ang, H. M.; Tade, M. O., Volatile organic compounds in indoor environment and photocatalytic oxidation: State of the art. *Environment International* 2007, 33, 694-705.

25. Lee, S. C.; Lam, S.; Fai, H. K., Characterization of VOCs, ozone, and PM10 emissions from office equipment in an environmental chamber. *Building and Environment* 2001, 36, 837-842.

26. Reiss, R.; Ryan, P. B.; Tibbetts, S. J.; Koutrakis, P., Measurement of organic acids, aldehydes, and ketones in residential environments and their relation to ozone. *Journal of the Air & Waste Management Association* 1995, 45, 811-822.

27. Masson, R.; Keller, V.; Keller, N., β-SiC alveolar foams as a structured photocatalytic support for the gas phase photocatalytic degradation of methylethylketone. *Applied Catalysis B: Environmental* 2015, 170-171, 301-311.

28. NIOSH, *Manual of Analytical Methods (NMAM): Method 2500* 1996, 1-4.

29. Mills, W. J.; Grigg, B. J.; Offermann, F. J.; Gustin, B. E.; Spingarn, N. E., Toluene and methyl ethyl ketone exposure from a commercially available contact adhesive. *Journal of Occupational and Environmental Hygiene* 2012, 9, D95-D102.

30. Welch, L.; Kirshner, H.; Heath, A.; Gilliland, R.; Broyles, S., Chronic neuropsychological and neurological impairment following acute exposure to a solvent mixture of toluene and methyl ethyl ketone (MEK). *J. Toxicol.-Clin. Toxicol.* 1991, 29, 435-445.

31. Noh, K.-C.; Oh, M.-D., Variation of clean air delivery rate and effective air cleaning ratio of room air cleaning devices. *Building and Environment* 2015, 84, 44-49.

32. Yu, C. H.; Yiin, L.-M.; Fan, Z.-H.; Rhoads, G. G., Evaluation of HEPA vacuum cleaning and dry steam cleaning in reducing levels of polycyclic aromatic hydrocarbons and house dust mite allergens in carpets. *Journal of Environmental Monitoring* 2009, 11, 205-211.

33. EPA, Exposure factors handbook. *US Environment protection agency, Washington, DC* 2009.

34. Guieysse, B.; Hort, C.; Platel, V.; Munoz, R.; Ondarts, M.; Revah, S., Biological treatment of indoor air for VOC removal: potential and challenges. *Biotechnology advances* 2008, 26, 398-410.

35. Rong, H. Q.; Ryu, Z. Y.; Zheng, J. T.; Zhang, Y. L., Influence of heat treatment of rayon-based activated carbon fibers on the adsorption of formaldehyde. *Journal of colloid and interface science* 2003, 261, 207-212.

36. Okachi, T.; Onaka, M., Formaldehyde encapsulated in zeolite: A long-lived, highly activated one-carbon electrophile to carbonyl-ene reactions. *Journal of the American Chemical Society* 2004, 126, 2306-2307.

37. Bellat, J. P.; Bezverkhyy, I.; Weber, G.; Royer, S.; Averlant, R.; Giraudon, J. M.; Lamonier, J. F., Capture of formaldehyde by adsorption on nanoporous materials. *Journal of hazardous materials* 2015, 300, 711-7.

38. Saeung, S.; Boonamnuayvitaya, V., Adsorption of formaldehyde vapor by amine-functionalized mesoporous silica materials. *J. Environ. Sci.* 2008, 20, 379-384.

39. Atkinson, R.; Arey, J., Atmospheric degradation of volatile organic compounds. *Chemical reviews* 2003, 103, 4605-4638.

40. Zhong, L. X.; Haghighat, F.; Ashrae, Ozonation air purification technology in HVAC applications. In *Ashrae Transactions 2014, Vol 120, Pt 1*, Amer Soc Heating, Refrigerating and Air-Conditioning Engs: Atlanta, 2014; Vol. 120.

41. Quiroz Torres, J.; Royer, S.; Bellat, J.-P.; Giraudon, J.-M.; Lamonier, J.-F., Formaldehyde: catalytic oxidation as a promising soft way of elimination. *ChemSusChem* 2013, 6, 578-92.

42. Shiraishi, F.; Ishimatsu, T., Toluene removal from indoor air using a miniaturized photocatalytic air purifier including a preceding adsorption/desorption unit. *Chemical Engineering Science* 2009, 64, 2466-2472.

43. Luengas, A.; Barona, A.; Hort, C.; Gallastegui, G.; Platel, V.; Elias, A., A review of indoor air treatment technologies. *Reviews in Environmental Science and Bio/Technology* 2015, 14, 499-522.

44. Huang, Y. C.; Luo, C. H.; Yang, S. H.; Lin, Y. C.; Chuang, C. Y., Improved removal of indoor volatile organic compounds by activated carbon fiber filters calcined with copper oxide catalyst. *Clean-Soil Air Water* 2010, 38, 993-997.

45. Soreanu, G.; Dixon, M.; Darlington, A., Botanical biofiltration of indoor gaseous pollutants - A mini-review. *Chem. Eng. J.* 2013, 229, 585-594.

46. Lu, Y.; Liu, J.; Yoshino, H.; Lu, B.; Jiang, A.; Li, F., Use of biotechnology coupled with bake-out exhaust to remove indoor VOCs. *Indoor Built Environ.* 2011, 21, 741-748.

47. Holzer, F.; Roland, U.; Kopinke, F. D., Combination of non-thermal plasma and heterogeneous catalysis for oxidation of volatile organic compounds Part 1. Accessibility of the intra-particle volume. *Appl. Catal. B-Environ.* 2002, 38, 163-181.

48. Zhu, L.; Chen, J.-Q.; Zhang, B.-S.; Wang, J.-H., Experimental research of oil vapor pollution control for gas station with membrane separation technology. *Huan jing ke xue= Huanjing kexue / [bian ji, Zhongguo ke xue yuan huan jing ke xue wei yuan hui "Huan jing ke xue" bian ji wei yuan hui.]* 2011, 32, 3704-9.

49. D'Amato, G.; Liccardi, G.; Cazzola, M., Environment and development of respiratory allergy: I. Outdoors. *Monaldi archives for chest disease, Fondazione clinica del lavoro, IRCCS [and] Istituto di clinica tisiologica e malattie apparato respiratorio, Universita di Napoli, Secondo ateneo* 1994, 49, 406-11.

50. Salerno, M.; Huss, K.; Huss, R. W., Allergen avoidance in the treatment of dust-mite allergy and asthma. *The Nurse practitioner* 1992, 17, 53-65.

51. Kaliner, M. A.; White, M. V., Asthma: causes and treatment. *Comprehensive therapy* 1994, 20, 645-50.

52. Peat, J.; Bjorksten, B., Primary and secondary prevention of allergic asthma. *The European respiratory journal. Supplement* 1998, 27, 28s-34s.

53. Serene, F.; Bedford, K. J.; Gould, M. E. L.; Coward, W. R.; Hewitt, C. R. A., Respiratory syncytial virus infection and virus-induced inflammation are modified by contaminants of indoor air. *Immunology* 2003, 108, 109-15.

54. Donlan, R. M.; Costerton, J. W., Biofilms: Survival mechanisms of clinically relevant microorganisms. *Clin. Microbiol. Rev.* 2002, 15, 167-+.

55. Garrett, T. R.; Bhakoo, M.; Zhang, Z., Bacterial adhesion and biofilms on surfaces. *Progress in Natural Science* 2008, 18, 1049-1056.

56. Costerton, J. W., Introduction to biofilm. *International Journal of Antimicrobial Agents* 1999, 11, 217-221.

57. Costerton, J. W.; Cheng, K. J.; Geesey, G. G.; Ladd, T. I.; Nickel, J. C.; Dasgupta, M.; Marrie, T. J., Bacterial biofilms in nature and disease. *Annual Review of Microbiology* 1987, 41, 435-464.

58. Ploux, L.; Ponche, A.; Anselme, K., Bacteria/Material interfaces: Role of the material and cell wall properties. *Journal of Adhesion Science and Technology* 2010, 24, 2165-2201.

59. Laxarova, V.; Savoye, P.; Janex, M. L., Advanced wastewater disinfection technologies State of the art and perspectives. *Wat. Sci. Tech.* 1999, 40, 203-213.

60. Chin, M. Y.; Sandham, A.; de Vries, J.; van der Mei, H. C.; Busscher, H. J., Biofilm formation on surface characterized micro-implants for skeletal anchorage in orthodontics. *Biomaterials* 2007, 28, 2032-40.

61. Boyce, J. M.; Potter-Bynoe, G.; Chenevert, C.; King, T., Environmental contamination due to methicillin-resistant Staphylococcus aureus: Possible infection control implications. *Infection Control and Hospital Epidemiology* 1997, 18, 622-627.

62. Hota, B., Contamination, disinfection, and cross-colonization: Are hospital surfaces reservoirs for nosocomial infection? *Clinical Infectious Diseases* 2004, 39, 1182-1189.

63. Benvenuti, C.; Canil, G.; Chiggiato, P.; Collin, P.; Cosso, R.; Guerin, J.; Ilie, S.; Latorre, D.; Neil, K. S., Surface cleaning efficiency measurements for UHV applications. *Vacuum* 1999, 53, 317-320.

64. Hoenigsberg, H., Non-Darwinian and Darwinian prokaryotic and eukaryotic evolution--an enigma in cell biology conservation. *Genetics and molecular research : GMR* 2003, 2, 279-87.

65. Beveridge, T. J., Use of the Gram stain in microbiology. *Biotechnic & Histochemistry* 2001, 76, 111-118.

66. Vollmer, W.; Blanot, D.; de Pedro, M. A., Peptidoglycan structure and architecture. *FEMS microbiology reviews* 2008, 32, 149-67.

67. Nikaido, H., Molecular basis of bacterial outer membrane permeability revisited. *Microbiology and Molecular Biology Reviews* 2003, 67, 593-656.

68. Ofek, I.; Beachey, E. H.; Jefferson, W.; Campbell, G. L., Cell membrane-binding properties of group-A Streptococcal lipoteichoic acid. *Journal of Experimental Medicine* 1975, 141, 990-1003.

69. Deza, M.; Araujo, M.; Garrido, M., Inactivation of Escherichia coli, Listeria monocytogenes, Pseudomonas aeruginosa and Staphylococcus aureus on stainless steel and glass surfaces by neutral electrolysed water. *Letters in applied microbiology* 2005, 40, 341-346.

70. Bos, R.; van der Mei, H. C.; Busscher, H. J., Physico-chemistry of initial microbial adhesive interactions - its mechanisms and methods for study. *FEMS microbiology reviews* 1999, 23, 179-230.

71. Mitik-Dineva, N.; Wang, J.; Truong, V. K.; Stoddart, P.; Malherbe, F.; Crawford, R. J.; Ivanova, E. P., Escherichia coli, Pseudomonas aeruginosa , and Staphylococcus aureus Attachment Patterns on Glass Surfaces with Nanoscale Roughness. *Current Microbiology* 2009, 58, 268-273.

72. Gaboriaud, F.; Dague, E.; Bailet, S.; Jorand, F.; Duval, J.; Thomas, F., Multiscale dynamics of the cell of Shewanella putrefaciens as a response to pH change. *Colloids & Surfaces B Biointerfaces* 2006, 52, 108-16.

73. Shannon, M. A.; Bohn, P. W.; Elimelech, M.; Georgiadis, J. G.; Marinas, B. J.; Mayes, A. M., Science and technology for water purification in the coming decades. *Nature* 2008, 452, 301-10.

74. Linden, K. G.; Darby, J. L., Ultraviolet disinfection of marginal effluents: determining ultraviolet absorbance and subsequent estimation of ultraviolet intensity. *Water Environ. Res.* 1998, 70, 214-223.

75. Warriner, R.; Kostenbader, K. D.; Cliver, D. O.; Ku, W. C., Disinfection of advanced wastewater treatment effluent by chlorine, chlorine dioxide and ozone: Experiments using seeded poliovirus. *Water research* 1985, 19, 1515-1526.

76. Morones, J. R.; Elechiguerra, J. L.; Camacho, A.; Holt, K.; Kouri, J. B.; Ramirez, J. T.; Yacaman, M. J., The bactericidal effect of silver nanoparticles. *Nanotechnology* 2005, 16, 2346-2353.

77. Kang, S.; Herzberg, M.; Rodrigues, D. F.; Elimelech, M., Antibacterial effects of carbon nanotubes: Size does matter. *Langmuir : the ACS journal of surfaces and colloids* 2008, 24, 6409-6413.

78. Guillard, C.; Bui, T.-H.; Felix, C.; Moules, V.; Lina, B.; Lejeune, P., Microbiological disinfection of water and air by photocatalysis. *Comptes Rendus Chimie* 2008, 11, 107-113.

79. McDonnell, G.; Russell, A. D., Antiseptics and disinfectants: Activity, action, and resistance. *Clin. Microbiol. Rev.* 1999, 12, 147-+.

80. Hahn, M.; Bonkovsky, H. L., Multiple chemical sensitivity syndrome and porphyria - A note of caution and concern. *Arch. Intern. Med.* 1997, 157, 281-285.

81. Stibich, M.; Stachowiak, J.; Tanner, B.; Berkheiser, M.; Moore, L.; Raad, I.; Chemaly, R. F., Evaluation of a pulsed-xenon ultraviolet room disinfection device for impact on hospital operations and microbial reduction. *Infection Control & Hospital Epidemiology* 2011, 32, 286-288.

82. Hall, L.; Otter, J. A.; Chewins, J.; Wengenack, N. L., Use of hydrogen peroxide vapor for deactivation of Mycobacterium tuberculosis in a biological safety cabinet and a room. *Journal of clinical microbiology* 2007, 45, 810-815.

83. Tsibouklis, J.; Stone, M.; Thorpe, A. A.; Graham, P.; Peters, V.; Heerlien, R.; Smith, J. R.; Green, K. L.; Nevell, T. G., Preventing bacterial adhesion onto surfaces: the low-surface-energy approach. *Biomaterials* 1999, 20, 1229-1235.

84. Weber, D. J.; Rutala, W. A., Self-disinfecting surfaces: review of current methodologies and future prospects. *American journal of infection control* 2013, 41, S31-5.

85. Krsko, P.; McCann, T. E.; Thach, T.-T.; Laabs, T. L.; Geller, H. M.; Libera, M. R., Length-scale mediated adhesion and directed growth of neural cells by surface-patterned poly (ethylene glycol) hydrogels. *Biomaterials* 2009, 30, 721-729.

86. Katsikogianni, M.; Missirlis, Y., Concise review of mechanisms of bacterial adhesion to biomaterials and of techniques used in estimating bacteria-material interactions. *Eur Cell Mater* 2004, 8.

87. Cheng, G.; Zhang, Z.; Chen, S.; Bryers, J. D.; Jiang, S., Inhibition of bacterial adhesion and biofilm formation on zwitterionic surfaces. *Biomaterials* 2007, 28, 4192-4199.

88. Veuillet, M.; Ploux, L.; Roucoules, V.; Courbeyre, Y.; Gaudichet-Maurin, E., Bacterial adhesion driven by mechanical properties of DMAEMA plasma polymer coatings. *22nd International Symposium on Plasma Chemistry; July 5-10, 2015; Antwerp, Belgium* 2015.

89. Snyder, A.; Siedlecki, C.; Milner, K., Anti-adhesive surface treatments. Google Patents: 2005.

90. Washburn, N. R.; Yamada, K. M.; Simon, C. G.; Kennedy, S. B.; Amis, E. J., High-throughput investigation of osteoblast response to polymer crystallinity: influence of nanometer-scale roughness on proliferation. *Biomaterials* 2004, 25, 1215-1224.

91. Rutala, W. A.; Weber, D. J., New disinfection and sterilization methods. *Emerging infectious diseases* 2001, 7, 348.

92. Crudden, J. J., Disinfecting methods and compositions. Google Patents: 2010.

93. Gibbins, B. L., SilvaGard technology summary. Beaverton, OR, USA: AcryMed, Inc: 2005.

94. Møretrø, T.; Høiby-Pettersen, G. S.; Habimana, O.; Heir, E.; Langsrud, S., Assessment of the antibacterial activity of a triclosan-containing cutting board. *International journal of food microbiology* 2011, 146, 157-162.

95. Baxa, D.; Shetron-Rama, L.; Golembieski, M.; Golembieski, M.; Jain, S.; Gordon, M.; Zervos, M., In vitro evaluation of a novel process for reducing bacterial contamination of environmental surfaces. *American journal of infection control* 2011, 39, 483-487.

96. Hegstad, K.; Langsrud, S.; Lunestad, B. T.; Scheie, A. A.; Sunde, M.; Yazdankhah, S. P., Does the wide use of quaternary ammonium compounds enhance the selection and spread of antimicrobial resistance and thus threaten our health? *Microbial drug resistance* 2010, 16, 91-104.

97. Bedran, T. B. L.; Grignon, L.; Spolidorio, D. P.; Grenier, D., Subinhibitory concentrations of triclosan promote Streptococcus mutans biofilm formation and adherence to oral epithelial cells. *PloS one* 2014, 9, e89059.

98. Hoffman, L. R.; D'Argenio, D. A.; MacCoss, M. J.; Zhang, Z.; Jones, R. A.; Miller, S. I., Aminoglycoside antibiotics induce bacterial biofilm formation. *Nature* 2005, 436, 1171-1175.

99. Glinel, K.; Thebault, P.; Humblot, V.; Pradier, C. M.; Jouenne, T., Antibacterial surfaces developed from bio-inspired approaches. *Acta biomaterialia* 2012, 8, 1670-84.

100. Mills, A.; Le Hunte, S., An overview of semiconductor photocatalysis. *Journal of photochemistry and photobiology A: Chemistry* 1997, 108, 1-35.

101. Jacoby, W. A.; Maness, P. C.; Wolfrum, E. J.; Blake, D. M.; Fennell, J. A., Mineralization of bacterial cell mass on a photocatalytic surface in air. *Environmental Science & Technology* 1998, 32, 2650-2653.

102. Sunada, K.; Kikuchi, Y.; Hashimoto, K.; Fujishima, A., Bactericidal and detoxification effects of TiO_2 thin film photocatalysts. *Environmental Science & Technology* 1998, 32, 726-728.

103. Bonetta, S.; Bonetta, S.; Motta, F.; Strini, A.; Carraro, E., Photocatalytic bacterial inactivation by TiO_2 coated surface. *AMB Express* 2013, 3, 59.

104. Kiwi, J.; Nadtochenko, V., Evidence for the mechanism of photocatalytic degradation of the bacterial wall membrane at the TiO_2 interface by ATR-FTIR and laser kinetic spectroscopy. *Langmuir : the ACS journal of surfaces and colloids* 2005, 21, 4631-4641.

105. Verdier, T.; Coutand, M.; Bertron, A.; Roques, C., Antibacterial activity of TiO_2 photocatalyst alone or in coatings on E. coli: The influence of methodological aspects. *Coatings* 2014, 4, 670-686.

106. Wei, X.; Yang, Z.; Tay, S. L.; Gao, W., Photocatalytic TiO_2 nanoparticles enhanced polymer antimicrobial coating. *Applied Surface Science* 2014, 290, 274-279.

107. Rtimi, S.; Pulgarin, C.; Sanjines, R.; Nadtochenko, V.; Lavanchy, J.-C.; Kiwi, J., Preparation and mechanism of Cu-decorated TiO_2–ZrO_2 films showing accelerated bacterial inactivation. *ACS applied materials & interfaces* 2015, 7, 12832-12839.

108. Herrmann, J. M., Titania-based true heterogeneous photocatalysis. *Environmental science and pollution research international* 2012, 19, 3655-65.

109. Lichtin, N. N.; Avudaithai, M.; Berman, E.; Dong, J., Photocatalytic oxidative degradation of vapors of some organic compounds over TiO2. *Research on Chemical Intermediates* 1994, 20, 755-781.

110. Turchi, C. S.; Ollis, D. F., Photocatalytic degradation of organic water contaminants: mechanisms involving hydroxyl radical attack. *Journal of catalysis* 1990, 122, 178-192.

111. Carre, G., Understanding the molecular mechanisms of photocatalysis applied to the degradation of microorganisms : application to air treatment and self-decontaminating textiles. 2013.

112. Linsebigler, A. L.; Lu, G. Q.; Yates, J. T., Photocatalysis on TiO2 surfaces: principles, mechanisms, and selected results. *Chemical reviews* 1995, 95, 735-758.

113. Wu, W.; Changzhong, J.; Roy, V. A., Recent progress in magnetic iron oxide-semiconductor composite nanomaterials as promising photocatalysts. *Nanoscale* 2015, 7, 38-58.

114. Nishimoto, S.; Ohtani, B.; Kajiwara, H.; Kagiya, T., Correlation of the crystal structure of titanium dioxide prepared from titanium tetra-2-propoxide with the photocatalytic activity for redox reactions in aqueous propan-2-ol and silver salt solutions. *Journal of the Chemical Society-Faraday Transactions I* 1985, 81, 61-68.

115. Hoffmann, M. R.; Martin, S. T.; Choi, W. Y.; Bahnemann, D. W., Environmental applications of semiconductor photocatalysis. *Chemical reviews* 1995, 95, 69-96.

116. Pehkonen, S., Determination of the oxidation states of iron in natural waters. A review. *Analyst* 1995, 120, 2655-2663.

117. Khodja, A. A.; Sehili, T.; Pilichowski, J.-F.; Boule, P., Photocatalytic degradation of 2-phenylphenol on TiO_2 and ZnO in aqueous suspensions. *Journal of Photochemistry and Photobiology A: Chemistry* 2001, 141, 231-239.

118. Maldotti, A.; Andreotti, L.; Molinari, A.; Varani, G.; Cerichelli, G.; Chiarini, M., Photocatalytic properties of iron porphyrins revisited in aqueous micellar environment: oxygenation of alkenes and reductive degradation of carbon tetrachloride. *Green Chemistry* 2001, 3, 42-46.

119. Rhydderch, S.; Howe, R. F., In Situ EPR Studies of Reaction Pathways in Titania Photocatalyst-Promoted Alkylation of Alkenes. *Molecules* 2015, 20, 4055-4070.

120. Talebi, R.; Khademolhoseini, S.; Rahnamaeiyan, S., Preparation and characterization of the magnesium aluminate nanoparticles via a green approach and its photocatalyst application. *J. Mater. Sci.-Mater. Electron.* 2016, 27, 1427-1432.

121. Jafari, S. J.; Moussavi, G.; Hossaini, H., Degradation and mineralization of diazinon pesticide in UVC and UVC/TiO_2 process. *Desalination and Water Treatment* 2016, 57, 3782-3790.

122. Hasmath Farzana, M.; Meenakshi, S., Photocatalytic aptitude of titanium dioxide impregnated chitosan beads for the reduction of Cr(VI). *International journal of biological macromolecules* 2015, 72, 1265-71.

123. Yue, D.; Qian, X.; Zhao, Y., Photocatalytic remediation of ionic pollutant. *Science Bulletin* 2015, 60, 1791-1806.

124. Swamy, V.; Gale, J. D.; Dubrovinsky, L. S., Atomistic simulation of the crystal structures and bulk moduli of TiO_2 polymorphs. *J. Phys. Chem. Solids* 2001, 62, 887-895.

125. Keller, N.; Barraud, E.; Bosc, F.; Edwards, D.; Keller, V., On the modification of photocatalysts for improving visible light and UV degradation of gas-phase toluene over TiO_2. *Applied Catalysis B: Environmental* 2007, 70, 423-430.

126. Kandiel, T. A.; Robben, L.; Alkaim, A.; Bahnemann, D., Brookite versus anatase TiO_2 photocatalysts: phase transformations and photocatalytic activities. *Photochemical & photobiological sciences : Official journal of the European Photochemistry Association and the European Society for Photobiology* 2013, 12, 602-9.

127. Voznyakovskii, A. P.; Ponimatkin, V. P.; Timkin, V. V., Environmental problems of finely dispersed titanium dioxide production. *Russ. J. Gen. Chem.* 2013, 83, 2651-2662.

128. Wei, K. S.; Adelman, A. H., The photooxidation of toluene. The role of an excited charge transfer complex. *Tetrahedron Letters* 1969, 10, 3297-3300.

129. Fujishima, A.; Honda, K., Electrochemical photolysis of water at a semiconductor electrode. *Nature* 1972, 238, 37-8.

130. Anpo, M.; Takeuchi, M., The design and development of highly reactive titanium oxide photocatalysts operating under visible light irradiation. *Journal of Catalysis* 2003, 216, 505-516.

131. Evtushenko, Y. M.; Romashkin, S. V.; Davydov, V. V., Synthesis and properties of TiO_2-based nanomaterials. *Theoretical Foundations of Chemical Engineering* 2011, 45, 731-738.

132. Koppenol, W. H.; Liebman, J. F., The oxidizing nature of the hydroxyl radical - A comparison with the ferryl ion (FEO^{2+}). *Journal of Physical Chemistry* 1984, 88, 99-101.

133. Wood, P. M., The potential diagram for oxygen at pH 7. *Biochem. J.* 1988, 253, 287-289.

134. Schindler, K. M.; Kunst, M., Charge carrier dynamics in TiO_2 powders. *Journal of Physical Chemistry* 1990, 94, 8222-8226.

135. Maeda, M.; Watanabe, T., Effects of crystallinity and grain size on photocatalytic activity of titania films. *Surface & Coatings Technology* 2007, 201, 9309-9312.

136. Almquist, C. B.; Biswas, P., Role of synthesis method and particle size of nanostructured TiO_2 on its photoactivity. *Journal of Catalysis* 2002, 212, 145-156.

137. Wu, N.; Wang, J.; Tafen, D. N.; Wang, H.; Zheng, J.-G.; Lewis, J. P.; Liu, X.; Leonard, S. S.; Manivannan, A., Shape-enhanced photocatalytic activity of single-crystalline anatase TiO_2 (101) nanobelts. *Journal of the American Chemical Society* 2010, 132, 6679-6685.

138. Verbruggen, S. W.; Masschaele, K.; Moortgat, E.; Korany, T. E.; Hauchecorne, B.; Martens, J. A.; Lenaerts, S., Factors driving the activity of commercial titanium dioxide powders towards gas phase photocatalytic oxidation of acetaldehyde. *Catalysis Science & Technology* 2012, 2, 2311.

139. Lu, G.; Linsebigler, A.; Yates Jr, J. T., Ti^{3+} defect sites on TiO_2 (110): production and chemical detection of active sites. *The Journal of Physical Chemistry* 1994, 98, 11733-11738.

140. Tachikawa, T.; Yamashita, S.; Majima, T., Evidence for crystal-face-dependent TiO_2 photocatalysis from single-molecule imaging and kinetic analysis. *Journal of the American Chemical Society* 2011, 133, 7197-7204.

141. Liu, Z.; Zhang, X.; NISHIMOTO, S.; MURAKAMI, T.; Fujishima, A., Efficient photocatalytic degradation of gaseous acetaldehyde by highly ordered TiO_2 nanotube arrays. *Environ. Sci. Technol.* 2008, 8547–8551.

142. Ameen, M. M.; Raupp, G. B., Reversible catalyst deactivation in the photocatalytic oxidation of dilute o-xylene in air. *Journal of Catalysis* 1999, 184, 112-122.

143. Raillard, C.; Héquet, V.; Cloirec, P. L.; Legrand, J., TiO_2 coating types influencing the role of water vapor on the photocatalytic oxidation of methyl ethyl ketone in the gas phase. *Applied Catalysis B: Environmental* 2005, 59, 213-220.

144. Vincent, G.; Queffeulou, A.; Marquaire, P. M.; Zahraa, O., Remediation of olfactory pollution by photocatalytic degradation process: Study of methyl ethyl ketone (MEK). *Journal of Photochemistry and Photobiology A: Chemistry* 2007, 191, 42-50.

145. Foster, H. A.; Ditta, I. B.; Varghese, S.; Steele, A., Photocatalytic disinfection using titanium dioxide: spectrum and mechanism of antimicrobial activity. *Applied microbiology and biotechnology* 2011, 90, 1847-68.

146. Benabbou, A.; Derriche, Z.; Felix, C.; Lejeune, P.; Guillard, C., Photocatalytic inactivation of Escherischia coli: Effect of concentration of TiO_2 and microorganism, nature, and intensity of UV irradiation. *Applied Catalysis B: Environmental* 2007, 76, 257-263.

147. Nakahashi, M.; Mawatari, K.; Hirata, A.; Maetani, M.; Shimohata, T.; Uebanso, T.; Hamada, Y.; Akutagawa, M.; Kinouchi, Y.; Takahashi, A., Simultaneous irradiation with different wavelengths of ultraviolet light has synergistic bactericidal effect on Vibrio parahaemolyticus. *Photochem Photobiol* 2014, 90, 1397-403.

148. Santos, A. L.; Oliveira, V.; Baptista, I.; Henriques, I.; Gomes, N. C.; Almeida, A.; Correia, A.; Cunha, Â., Wavelength dependence of biological damage induced by UV radiation on bacteria. *Archives of microbiology* 2013, 195, 63-74.

149. Tyrrell, R. M., Induction of pyrimidine dimers in bacterial DNA by 365 nm radiation. *Photochemistry and photobiology* 1973, 17, 69-73.

150. Berney, M.; Weilenmann, H. U.; Egli, T., Gene expression of Escherichia coli in continuous culture during adaptation to artificial sunlight. *Environmental microbiology* 2006, 8, 1635-47.

151. Sondi, I.; Salopek-Sondi, B., Silver nanoparticles as antimicrobial agent: a case study on E. coli as a model for Gram-negative bacteria. *Journal of colloid and interface science* 2004, 275, 177-182.

152. Stoimenov, P. K.; Klinger, R. L.; Marchin, G. L.; Klabunde, K. J., Metal oxide nanoparticles as bactericidal agents. *Langmuir : the ACS journal of surfaces and colloids* 2002, 18, 6679-6686.

153. Azam, A.; Ahmed, A. S.; Oves, M.; Khan, M. S.; Habib, S. S.; Memic, A., Antimicrobial activity of metal oxide nanoparticles against Gram-positive and Gram-negative bacteria: a comparative study. *Int J Nanomedicine* 2012, 7, 6003-6009.

154. Huang, Z.; Zheng, X.; Yan, D.; Yin, G.; Liao, X.; Kang, Y.; Yao, Y.; Huang, D.; Hao, B., Toxicological effect of ZnO nanoparticles based on bacteria. *Langmuir : the ACS journal of surfaces and colloids* 2008, 24, 4140-4144.

155. Brayner, R.; Ferrari-Iliou, R.; Brivois, N.; Djediat, S.; Benedetti, M. F.; Fiévet, F., Toxicological impact studies based on Escherichia coli bacteria in ultrafine ZnO nanoparticles colloidal medium. *Nano Letters* 2006, 6, 866-870.

156. Auffan, M.; Achouak, W.; Rose, J.; Roncato, M.-A.; Chanéac, C.; Waite, D. T.; Masion, A.; Woicik, J. C.; Wiesner, M. R.; Bottero, J.-Y., Relation between the redox state of iron-based nanoparticles and their cytotoxicity toward Escherichia coli. *Environmental science & technology* 2008, 42, 6730-6735.

157. Simon-Deckers, A.; Loo, S.; Mayne-L'hermite, M.; Herlin-Boime, N.; Menguy, N.; Reynaud, C.; Gouget, B.; Carrière, M., Size-, composition-and shape-dependent toxicological impact of metal oxide nanoparticles and carbon nanotubes toward bacteria. *Environmental science & technology* 2009, 43, 8423-8429.

158. Aruoja, V.; Dubourguier, H. C.; Kasemets, K.; Kahru, A., Toxicity of nanoparticles of CuO, ZnO and TiO_2 to microalgae Pseudokirchneriella subcapitata. *The Science of the total environment* 2009, 407, 1461-8.

159. Rincon, A., Effect of pH, inorganic ions, organic matter and H_2O_2 on E. coli K12 photocatalytic inactivation by TiO_2 Implications in solar water disinfection. *Applied Catalysis B: Environmental* 2004, 51, 283-302.

160. Li, Y.; Zhang, W.; Niu, J.; Chen, Y., Mechanism of photogenerated reactive oxygen species and correlation with the antibacterial properties of engineered metal-oxide nanoparticles. *Acs Nano* 2012, 6, 5164-5173.

161. Ireland, J. C.; Klostermann, P.; Rice, E. W.; Clark, R. M., Inactivation of Escherichia coli by titanium dioxide photocatalytic oxidation. *Applied and environmental microbiology* 1993, 59, 1668-1670.

162. Pryor, W. A., Oxy-radicals and related species: their formation, lifetimes, and reactions. *Annual Review of Physiology* 1986, 48, 657-667.

163. Kikuchi, Y.; Sunada, K.; Iyoda, T.; Hashimoto, K.; Fujishima, A., Photocatalytic bactericidal effect of TiO_2 thin films: dynamic view of the active oxygen species responsible for the effect. *Journal of Photochemistry and Photobiology A: chemistry* 1997, 106, 51-56.

164. Fridovich, I., Superoxide radical an endogenous toxicant. *Ann. Rev. Pharmacol. Toxcicol.* 1983, 23, 239.

165. Sunada, K.; Watanabe, T.; Hashimoto, K., Studies on photokilling of bacteria on TiO_2 thin film. *Journal of Photochemistry and Photobiology A: Chemistry* 2003, 156, 227-233.

166. Kiwi, J.; Nadtochenko, V., New evidence for TiO_2 photocatalysis during bilayer lipid peroxidation. *The Journal of Physical Chemistry B* 2004, 108, 17675-17684.

167. Hu, C.; Guo, J.; Qu, J.; Hu, X., Photocatalytic degradation of pathogenic bacteria with AgI/TiO_2 under visible light irradiation. *Langmuir : the ACS journal of surfaces and colloids* 2007, 23, 4982-4987.

168. Bock, C.; Dittmar, H.; Gemeinhardt, H.; Bauer, E.; Greulich, K.-O., Comet assay detects cold repair of UV-A damages in a human B-lymphoblast cell line. *Mutation Research/DNA Repair* 1998, 408, 111-120.

169. Cabiscol, E.; Tamarit, J.; Ros, J., Oxidative stress in bacteria and protein damage by reactive oxygen species. *International Microbiology* 2010, 3, 3-8.

170. Carré, G.; Hamon, E.; Ennahar, S.; Estner, M.; Lett, M.-C.; Horvatovich, P.; Gies, J.-P.; Keller, V.; Keller, N.; Andre, P., TiO_2 photocatalysis damages lipids and proteins in Escherichia coli. *Applied and environmental microbiology* 2014, 80, 2573-2581.

171. Pablos, C.; van Grieken, R.; Marugán, J.; Moreno, B., Photocatalytic inactivation of bacteria in a fixed-bed reactor: mechanistic insights by epifluorescence microscopy. *Catalysis today* 2011, 161, 133-139.

172. Kubacka, A.; Diez, M. S.; Rojo, D.; Bargiela, R.; Ciordia, S.; Zapico, I.; Albar, J. P.; Barbas, C.; Martins dos Santos, V. A.; Fernandez-Garcia, M.; Ferrer, M., Understanding the antimicrobial mechanism of TiO_2-based nanocomposite films in a pathogenic bacterium. *Scientific reports* 2014, 4, 4134.

173. Gumy, D.; Rincon, A.; Hajdu, R.; Pulgarin, C., Solar photocatalysis for detoxification and disinfection of water: different types of suspended and fixed TiO_2 catalysts study. *Solar Energy* 2006, 80, 1376-1381.

174. Bowler, C.; Montagu, M. v.; Inze, D., Superoxide dismutase and stress tolerance. *Annual review of plant biology* 1992, 43, 83-116.

175. Ross, D.; Moldeus, P., Antioxidant defense systems and oxidative stress. *Membrane lipid oxidation* 1991, 2, 151-170.

176. Koizumi, Y.; Yamada, R.; Nishioka, M.; Matsumura, Y.; Tsuchido, T.; Taya, M., Deactivation kinetics of Escherichia coli cells correlated with intracellular superoxide dismutase activity in photoreaction with titanium dioxide particles. *Journal of Chemical Technology and Biotechnology* 2002, 77, 671-677.

177. Gogniat, G.; Dukan, S., TiO_2 photocatalysis causes DNA damage via Fenton reaction-generated hydroxyl radicals during the recovery period. *Applied and environmental microbiology* 2007, 73, 7740-7743.

178. Rincón, A.; Pulgarin, C., Photocatalytical inactivation of E. coli: effect of (continuous–intermittent) light intensity and of (suspended–fixed) TiO_2 concentration. *Applied Catalysis B: Environmental* 2003, 44, 263-284.

179. Coeyman, M., TiO_2 industry faces a tightening market. *Chem. Week* 1994, 155, 6-6.

180. Tian, C.; Huang, S.; Yang, Y., Anatase TiO_2 white pigment production from unenriched industrial titanyl sulfate solution via short sulfate process. *Dyes and Pigments* 2013, 96, 609-613.

181. Alonso-Tellez, A.; Masson, R.; Robert, D.; Keller, N.; Keller, V., Comparison of Hombikat UV100 and P25 TiO_2 performance in gas-phase photocatalytic oxidation reactions. *Journal of Photochemistry and Photobiology A: Chemistry* 2012, 250, 58-65.

182. Ohno, T.; Sarukawa, K.; Tokieda, K.; Matsumura, M., Morphology of a TiO_2 Photocatalyst (Degussa, P-25) Consisting of Anatase and Rutile Crystalline Phases. *Journal of Catalysis* 2001, 203, 82-86.

183. Ohtani, B.; Prieto-Mahaney, O. O.; Li, D.; Abe, R., What is Degussa (Evonik) P25? Crystalline composition analysis, reconstruction from isolated pure particles and photocatalytic activity test. *Journal of Photochemistry and Photobiology A: Chemistry* 2010, 216, 179-182.

184. Yang, H. G.; Zeng, H. C., Preparation of hollow anatase TiO2 nanospheres via Ostwald ripening. *The Journal of Physical Chemistry B* 2004, 108, 3492-3495.

185. Chen, C.; Cai, W.; Long, M.; Zhang, J.; Zhou, B.; Wu, Y.; Wu, D., Template-free sol-gel preparation and characterization of free-standing visible light responsive C,N-modified porous monolithic TiO2. *Journal of hazardous materials* 2010, 178, 560-565.

186. Dai, G. P.; Yu, J. G.; Liu, G., Synthesis and enhanced visible-light photoelectrocatalytic activity of p− n junction BiOI/TiO_2 nanotube arrays. *J. Phys. Chem. C* 2011, 115, 7339-7346.

187. Dutta, S.; Patra, A. K.; De, S.; Bhaumik, A.; Saha, B., Self-assembled TiO_2 nanospheres by using a biopolymer as a template and its optoelectronic application. *ACS applied materials & interfaces* 2012, 4, 1560-1564.

188. Haouemi, K.; Touati, F.; Gharbi, N., Characterization of a new TiO_2 nanoflower prepared by the sol–gel process in a reverse microemulsion. *Journal of Inorganic and Organometallic Polymers and Materials* 2011, 21, 929-936.

189. Kwon, S.; Fan, M.; Cooper, A. T.; Yang, H., Photocatalytic applications of micro- and Nano-TiO_2 in environmental engineering. *Critical Reviews in Environmental Science and Technology* 2008, 38, 197-226.

190. Luo, L.; Cooper, A. T.; Fan, M., Preparation and application of nanoglued binary titania-silica aerogel. *Journal of hazardous materials* 2009, 161, 175-182.

191. Mali, S. S.; Betty, C. A.; Bhosale, P. N.; Devan, R. S.; Ma, Y.-R.; Kolekar, S. S.; Patil, P. S., Hydrothermal synthesis of rutile TiO_2 nanoflowers using bronsted acidic ionic liquid BAIL : Synthesis, characterization and growth mechanism. *Crystengcomm* 2012, 14, 1920-1924.

192. Yang, M.; Ding, B.; Lee, S.; Lee, J.-K., Carrier transport in dye-sensitized solar cells using single crystalline TiO_2 nanorods grown by a microwave-assisted hydrothermal reaction. *J. Phys. Chem. C* 2011, 115, 14534-14541.

193. Hench, L. L.; Wang, S. H., The sol-gel glass transformation of silica. *Phase Transitions* 1990, 24-6, 785-834.

194. Wang, Y.; He, Y.; Lai, Q.; Fan, M., Review of the progress in preparing nano TiO_2: an important environmental engineering material. *Journal of environmental sciences* 2014, 26, 2139-77.

195. Livage, J.; Beteille, F.; Roux, C.; Chatry, M.; Davidson, P., Sol-gel synthesis of oxide materials. *Acta Mater* 1998, 46, 743-750.

196. Livage, J., Sol-gel synthesis of heterogeneous catalysts from aqueous solutions. *Catalysis Today* 1998, 41, 19.

197. Livage, J.; Sanchez, C.; Henry, M.; Doeuff, S., The chemistry of the sol-gel process. *Solid state ionics* 1988, 32/33, 633-638.

198. Kamal, M. S. K.; Mohamed, I. Z., Synthesis of high surface area titania powders via basic hydrolysis of titanium isopropoxide. *Powder technology* 1997, 92, 233-239.

199. Gupta, S. M.; Tripathi, M., A review on the synthesis of TiO_2 nanoparticles by solution route. *Central European Journal of Chemistry* 2012, 10, 279-294.

200. Li, W.; Yang, J.; Wu, Z.; Wang, J.; Li, B.; Feng, S.; Deng, Y.; Zhang, F.; Zhao, D., A versatile kinetics-controlled coating method to construct uniform porous TiO_2 shells for multifunctional core–shell structures. *Journal of the American Chemical Society* 2012, 134, 11864-11867.

201. Tseng, T. K.; Lin, Y. S.; Chen, Y. J.; Chu, H., A review of photocatalysts prepared by sol-gel method for VOCs removal. *International Journal of Molecular Sciences* 2010, 11, 2336-2361.

202. Isley, S. L.; Lee Penn, R., Titanium dioxide nanoparticles: effect of sol-gel pH on phase composition, particle size, and particle growth mechanism. *J.Phys.Chem.C* 2008, 112, 4469-4474.

203. Eiden-Assmann, S.; Widoniak, J.; Maret, G., Synthesis and characterization of porous and nonporous monodisperse colloidal TiO_2 particles. *Chemistry of Materials* 2004, 16, 6-11.

204. Lee, S.; Cho, I.-S.; Lee, J. H.; Kim, D. H.; Kim, D. W.; Kim, J. Y.; Shin, H.; Lee, J.-K.; Jung, H. S.; Park, N.-G.; Kim, K.; Ko, M. J.; Hong, K. S., Two-Step Sol-Gel Method-Based TiO_2 Nanoparticles with Uniform Morphology and Size for Efficient Photo-Energy Conversion Devices. *Chemistry of Materials* 2010, 22, 1958-1965.

205. Grandcolas, M.; Karkmaz-Le Du, M.; Bosc, F.; Louvet, A.; Keller, N.; Keller, V., Porogen template assisted TiO_2 rutile coupled nanomaterials for improved visible and solar light photocatalytic applications. *Catalysis Letters* 2008, 123, 65-71.

206. Bosc, F.; Ayral, A.; Albouy, P.-A.; Guizard, C., A simple route for low-temperature synthesis of mesoporous and nanocrystalline anatase thin films. *Chem Mater* 2003, 15, 2463-2468.

207. Bosc, F.; Ayral, A.; Albouy, P.-A.; Datas, L.; Guizard, C., Mesostructure of anatase thin films prepared by mesophase templating. *Chem Mater* 2004, 16, 2208-2214.

208. Loryuenyong, V.; Angamnuaysiri, K.; Sukcharoenpong, J.; Suwannasri, A., Sol–gel derived mesoporous titania nanoparticles: Effects of calcination temperature and alcoholic solvent on the photocatalytic behavior. *Ceramics International* 2012, 38, 2233-2237.

209. Malinger, K. A.; Maguer, A.; Thorel, A.; Gaunand, A.; Hochepied, J.-F., Crystallization of anatase nanoparticles from amorphous precipitate by a continuous hydrothermal process. *Chem. Eng. J.* 2011, 174, 445-451.

210. Rosseler, O.; Shankar, M. V.; Du, M. K. L.; Schmidlin, L.; Keller, N.; Keller, V., Solar light photocatalytic hydrogen production from water over Pt and Au/TiO_2(anatase/rutile) photocatalysts: Influence of noble metal and porogen promotion. *Journal of Catalysis* 2010, 269, 179-190.

211. Loryuenyong, V.; Buasri, A.; Srilachai, C.; Srimuang, H., The synthesis of microporous and mesoporous titania with high specific surface area using sol-gel method and activated carbon templates. *Materials Letters* 2012, 87, 47-50.

212. Elder, S. H.; Gao, Y.; Li, X.; Liu, J.; McCready, D. E.; Windisch, C. F., Zirconia-stabilized 25-angstrom TiO_2 anatase crystallites in a mesoporous structure. *Chemistry of Materials* 1998, 10, 3140-3145.

213. Yu, J. C.; Zhang, L.; Zheng, Z.; Zhao, J., Synthesis and characterization of phosphated mesoporous tianium dioxide with high photocatalytic activity. *Chem. Mater.* 2003, 15, 2280-2286.

214. Tian, N.; Zhou, Z.-Y.; Sun, S.-G.; Ding, Y.; Wang, Z. L., Synthesis of tetrahexahedral platinum nanocrystals with high-index facets and high electro-oxidation activity. *Science* 2007, 316, 732-735.

215. Burda, C.; Chen, X. B.; Narayanan, R.; El-Sayed, M. A., Chemistry and properties of nanocrystals of different shapes. *Chemical reviews* 2005, 105, 1025-1102.

216. Chen, C.; Hu, R.; Mai, K.; Ren, Z.; Wang, H.; Qian, G.; Wang, Z., Shape evolution of highly crystalline anatase TiO_2 nanobipyramids. *Crystal Growth & Design* 2011, 11, 5221-5226.

217. Fang, W. Q.; Gong, X.-Q.; Yang, H. G., On the unusual properties of anatase TiO_2 exposed by highly reactive facets. *Journal of Physical Chemistry Letters* 2011, 2, 725-734.

218. Li, Y. F.; Liu, Z. P.; Liu, L. L.; Gao, W. G., Mechanism and activity of photocatalytic oxygen evolution on titania anatase in aqueous surroundings. *Journal of the American Chemical Society* 2010, 132, 13008-13015.

219. Yang, H. G.; Sun, C. H.; Qiao, S. Z.; Zou, J.; Liu, G.; Smith, S. C.; Cheng, H. M.; Lu, G. Q., Anatase TiO_2 single crystals with a large percentage of reactive facets. *Nature* 2008, 453, 638-41.

220. Jun, Y. W.; Casula, M. F.; Sim, J. H.; Kim, S. Y.; Cheon, J.; Alivisatos, A. P., Surfactant-assisted elimination of a high energy facet as a means of controlling the shapes of TiO_2 nanocrystals. *Journal of the American Chemical Society* 2003, 125, 15981-15985.

221. Vioux, A.; Viau, L.; Volland, S.; Le Bideau, J., Use of ionic liquids in sol-gel; ionogels and applications. *Comptes Rendus Chimie* 2010, 13, 242-255.

222. Yoo, K. S.; Lee, T. G.; Kim, J., Preparation and characterization of mesoporous TiO_2 particles by modified sol–gel method using ionic liquids. *Microporous and Mesoporous Materials* 2005, 84, 211-217.

223. Wang, Y.; Maksimuk, S.; Shen, R.; Yang, H., Synthesis of iron oxide nanoparticles using a freshly-made or recycled imidazolium-based ionic liquid. *Green Chemistry* 2007, 9, 1051.

224. Xie, Z.-L.; Feng, M.-L.; Tan, B.; Huang, X.-Y., The multifunctional roles of the ionic liquid [Bmim][BF_4] in the creation of cadmium metal–organic frameworks. *CrystEngComm* 2012, 14, 4894.

225. Lee, C. M.; Jeong, H. J.; Lim, S. T.; Sohn, M. H.; Kim, D. W., Synthesis of iron oxide nanoparticles with control over shape using imidazolium-based ionic liquids. *ACS applied materials & interfaces* 2010, 2, 756-9.

226. Choi, E. H.; Hong, S.-I.; Moon, D. J., Preparation of thermally stable mesostructured nano-sized TiO_2 particles by modified sol–gel method using ionic liquid. *Catalysis Letters* 2008, 123, 84-89.

227. Zhao, X. W.; Jin, W. Z.; Cai, J. G.; Ye, J. F.; Li, Z. H.; Ma, Y. R.; Xie, J. L.; Qi, L. M., Shape- and size-controlled synthesis of uniform anatase TiO_2 nanocuboids enclosed by active {100} and {001} facets. *Adv Funct Mater* 2011, 21, 3554-3563.

228. Freire, M. G.; Neves, C. M. S. S.; Marrucho, I. M.; Coutinho, J. A. P.; Fernandes, M., Hydrolysis of tetrafluoroborate and hexafluorophosphate counter ions in imidazolium-based ionic liquids. *J. Phy. Chem. A* 2010, 114, 3744-3749.

229. Keidel, E., Influence of titanium white on the fastness to light of coal-tar days. *Farben-Zeitung* 1929, 34, 1242-1243.

230. Goodeve, C.; Kitchener, J., Photosensitisation by titanium dioxide. *Transactions of the Faraday Society* 1938, 34, 570-579.

231. Murphy, G. M., Sunblocks: Mechanisms of action. *Photodermatol. Photoimmunol. Photomed.* 1999, 15, 34-36.

232. Allen, N. S.; Edge, M.; Verran, J.; Stratton, J.; Maltby, J.; Bygott, C., Photocatalytic titania based surfaces: Environmental benefits. *Polymer Degradation and Stability* 2008, 93, 1632-1646.

233. Auvinen, J.; Wirtanen, L., The influence of photocatalytic interior paints on indoor air quality. *Atmospheric Environment* 2008, 42, 4101-4112.

234. Leofanti, G.; Tozzola, G.; Padovan, M.; Petrini, G.; Bordiga, S.; Zecchina, A., Catalyst characterization: characterization techniques. *Catalysis Today* 1997, 34, 307-327.

235. Mikhail, R. S.; Brunauer, S., Surface-area measurements by nitrogen and argon adsorption. *Journal of colloid and interface science* 1975, 52, 572-577.

236. Sing, K. S., Reporting physisorption data for gas/solid systems with special reference to the determination of surface area and porosity (Recommendations 1984). *Pure and applied chemistry* 1985, 57, 603-619.

237. Storck, S.; Bretinger, H.; Maier, W. F., Characterization of micro and mesoporous solids by physisorption methods and poresize analysis. *Applied Catalysis A: General* 1998, 147, 137-146.

238. Scofield, J. H., Hartree-Slater subshell photoionization cross-sections at 1254 and 1487 eV. *Journal of Electron Spectroscopy and Related Phenomena* 1976, 8, 129-137.

239. Doniach, S.; Sunjic, M., Many-electron singularity in X-ray photoemission and X-ray line spectra from metals. *Journal of Physics C: Solid State Physics* 1970, 3, 285.

240. Kowalczyk, S.; Ley, L.; Martin, R.; McFeely, F.; Shirley, D., Relaxation and final-state structure in XPS of atoms, molecules, and metals. *Faraday Discussions of the Chemical Society* 1975, 60, 7-17.

241. Yang, X. H.; Li, Z.; Sun, C.; Yang, H. G.; Li, C., Hydrothermal stability of {001} faceted anatase TiO_2. *Chemistry of Materials* 2011, 23, 3486-3494.

242. Alfaya, A. A. S.; Gushikem, Y.; de Castro, S. C., Highly dispersed phosphate supported in a binary silica-titania matrix: Preparation and characterization. *Chemistry of Materials* 1998, 10, 909-913.

243. Splinter, S. J.; Rofagha, R.; McIntyre, N. S.; Erb, U., XPS characterization of the corrosion films formed on nanocrystalline Ni-P alloys in sulphuric acid. *Surf. Interface Anal.* 1996, 24, 181-186.

244. Bortun, A. I.; Khainakov, S. A.; Bortun, L. N.; Poojary, D. M.; Rodriguez, J.; Garcia, J. R.; Clearfield, A., Synthesis and characterization of two novel fibrous titanium phosphates $Ti_2O(PO_4)_2.2H_2O$. *Chemistry of Materials* 1997, 9, 1805-1811.

245. Sudarsan, V.; Muthe, K. P.; Vyas, J. C.; Kulshreshtha, S. K., PO_4^{3-} tetrahedra in $SbPO_4$ and $SbOPO_4$: a 31P NMR and XPS study. *Journal of Alloys and Compounds* 2002, 336, 119-123.

246. Liu, S.; Yu, J.; Cheng, B.; Jaroniec, M., Fluorinated semiconductor photocatalysts: tunable synthesis and unique properties. *Advances in colloid and interface science* 2012, 173, 35-53.

247. Hanaor, D. A. H.; Sorrell, C. C., Review of the anatase to rutile phase transformation. *Journal of Materials Science* 2010, 46, 855-874.

248. Reinauer, F.; Glaum, R., Ideal and real structure of $Ti_5O_4(PO_4)_4$: X-ray and HRTEM investigations. *Acta Cryst.* 1998, B54, 722-731.

249. Han, Z.; Wang, J.; Liao, L.; Pan, H.; Shen, S.; Chen, J., Phosphorus doped TiO_2 as oxygen sensor with low operating temperature and sensing mechanism. *Applied Surface Science* 2013, 273, 349-356.

250. Zhao, D.; Chen, C.; Wang, Y.; Ji, H.; Ma, W.; Zang, L.; Zhao, J., Surface modification of TiO_2 by phosphate: effect on photocatalytic activity and mechanism implication. *The Journal of Physical Chemistry C* 2008, 112, 5993-6001.

251. Gasik, M.; Gladkikh, V., The investigation of phosphorus chemical bond in the manganese-ore materials. 2015.

252. Lyakishev, N. P.; Gladkikh, V. A.; Gasik, M. I., The nature of chemical bonding of phosphorus in monomineral fractions and concentrates of manganese ores. *Russ. Metall.* 1994, 1-9.

253. Korosi, L.; Oszko, A.; Galbacs, G.; Richardt, A.; Zollmer, V.; Dekany, I., Structural properties and photocatalytic behaviour of phosphate-modified nanocrystalline titania films. *Appl. Catal. B-Environ.* 2007, 77, 175-183.

254. Bourbigot, S.; Le Bras, M.; Gengembre, L.; Delobel, R., XPS study of an intumescent coating application to the ammonium polyphosphate/pentaerythritol fire-retardant system. *Applied surface science* 1994, 81, 299-307.

255. Lebugle, A.; Sallek, B., XPS study of apatites and related calcium phosphates. *Hydroxyapatite and related materials, ed. P. Brown and B. Constanz, CRC Press, Boca Raton, FL* 1994, 319-324 á

256. Bhaumik, A.; Inagaki, S., Mesoporous titanium phosphate molecular sieves with ion-exchange capacity. *Journal of the American Chemical Society* 2001, 123, 691-696.

257. Ribeiro, C. C.; Barbosa, M. A., Affinity of hydroxyapatite to metal cations - A study on the composition and structure of phosphates formed in the presence of titanium and aluminium. In *Bioceramics*, Giannini, S.; Moroni, A., Eds. Trans Tech Publications Ltd: Zurich-Uetikon, 2000; Vol. 192-1, pp 55-58.

258. Li, G.; An, T.; Chen, J.; Sheng, G.; Fu, J.; Chen, F.; Zhang, S.; Zhao, H., Photoelectrocatalytic decontamination of oilfield produced wastewater containing refractory organic pollutants in the presence of high concentration of chloride ions. *Journal of hazardous materials* 2006, 138, 392-400.

259. Yu, S.; Liu, B.; Wang, Q.; Gao, Y.; Shi, Y.; Feng, X.; An, X.; Liu, L.; Zhang, J., Ionic liquid assisted chemical strategy to TiO_2 hollow nanocube assemblies with surface-fluorination and nitridation and high energy crystal facet exposure for enhanced photocatalysis. *ACS applied materials & interfaces* 2014, 6, 10283-10295.

260. 22197-2, I., Fine ceramics (advanced ceramics, advanced technical ceramics) -- Test method for air-purification performance of semiconducting photocatalytic materials -- Part 2: Removal of acetaldehyde. 2011.

261. Hurum, D. C.; Agrios, A. G.; Gray, K. A.; Rajh, T.; Thurnauer, M. C., Explaining the enhanced photocatalytic activity of Degussa P25 mixed-phase TiO_2 using EPR. *The Journal of Physical Chemistry B* 2003, 107, 4545-4549.

262. Sofianou, M.-V.; Psycharis, V.; Boukos, N.; Vaimakis, T.; Yu, J.; Dillert, R.; Bahnemann, D.; Trapalis, C., Tuning the photocatalytic selectivity of TiO_2 anatase nanoplates by altering the exposed crystal facets content. *Applied Catalysis B: Environmental* 2013, 142-143, 761-768.

263. Fan, X.; Yu, T.; Wang, Y.; Zheng, J.; Gao, L.; Li, Z.; Ye, J.; Zou, Z., Role of phosphorus in synthesis of phosphated mesoporous TiO_2 photocatalytic materials by EISA method. *Applied Surface Science* 2008, 254, 5191-5198.

264. Seo, D. S.; Lee, J. K.; Lee, E. G.; Kim, H., Effect of aging agents on the formation of TiO_2 nanocrystalline powder. *Materials Letters* 2001, 51, 115-119.

265. Qi, K.; Xin, J. H., Room-temperature synthesis of single-phase anatase TiO_2 by aging and its self-cleaning properties. *ACS applied materials & interfaces* 2010, 2, 3479-85.

266. Wu, N.-L.; Wang, S.-Y.; Rusakova, I., Inhibition of crystallite growth in the sol-gel synthesis of nanocrystalline metal oxides. *Science* 1999, 285, 1375-1377.

267. Wachs, I. E., Recent conceptual advances in the catalysis science of mixed metal oxide catalytic materials. *Catalysis Today* 2005, 100, 79-94.

268. Zhang, Q.; Liu, S.-J.; Yu, S.-H., Recent advances in oriented attachment growth and synthesis of functional materials: concept, evidence, mechanism, and future. *J. Mater. Chem.* 2009, 19, 191-207.

269. Su, C.; Hong, B. Y.; Tseng, C. M., Sol–gel preparation and photocatalysis of titanium dioxide. *Catalysis Today* 2004, 96, 119-126.

270. Polleux, J.; Pinna, N.; Antonietti, M.; Hess, C.; Wild, U.; Schlögl, R.; Niederberger, M., Ligand functionality as a versatile tool to control the assembly behavior of preformed titania nanocrystals. *Chemistry–A European Journal* 2005, 11, 3541-3551.

271. Tian, F.; Zhang, Y.; Zhang, J.; Pan, C., Raman spectroscopy: A new approach to measure the percentage of anatase TiO_2 exposed (001) facets. *The Journal of Physical Chemistry C* 2012, 116, 7515-7519.

272. Wang, Y.; Sun, H.; Tan, S.; Feng, H.; Cheng, Z.; Zhao, J.; Zhao, A.; Wang, B.; Luo, Y.; Yang, J.; Hou, J. G., Role of point defects on the reactivity of reconstructed anatase titanium dioxide (001) surface. *Nature communications* 2013, 4, 2214.

273. Luan, Y.; Jing, L.; Wu, J.; Xie, M.; Feng, Y., Long-lived photogenerated charge carriers of 001-facet-exposed TiO_2 with enhanced thermal stability as an efficient photocatalyst. *Applied Catalysis B: Environmental* 2014, 147, 29-34.

274. Gong, X.-Q.; Selloni, A., Reactivity of anatase TiO_2 nanoparticles: the role of the minority (001) surface. *The Journal of Physical Chemistry B* 2005, 109, 19560-19562.

275. Zhang, H.; Wang, Y.; Liu, P.; Han, Y.; Yao, X.; Zou, J.; Cheng, H.; Zhao, H., Anatase TiO_2 crystal facet growth: mechanistic role of hydrofluoric acid and photoelectrocatalytic activity. *ACS applied materials & interfaces* 2011, 3, 2472-8.

276. Swatloski, R. P.; Holbrey, J. D.; Rogers, R. D., Ionic liquids are not always green: hydrolysis of 1-butyl-3-methylimidazolium hexafluorophosphate. *Green Chemistry* 2003, 5, 361.

277. Murakami, N.; Kurihara, Y.; Tsubota, T.; Ohno, T., Shape-controlled anatase titanium (IV) oxide particles prepared by hydrothermal treatment of peroxo titanic acid in the presence of polyvinyl alcohol. *The Journal of Physical Chemistry C* 2009, 113, 3062-3069.

278. Han, Y.; Liu, C.-j.; Ge, Q., Interaction of Pt clusters with the anatase TiO_2 (101) surface: A first principles study. *The Journal of Physical Chemistry B* 2006, 110, 7463-7472.

279. Xiang, Q.; Lv, K.; Yu, J., Pivotal role of fluorine in enhanced photocatalytic activity of anatase TiO_2 nanosheets with dominant (001) facets for the photocatalytic degradation of acetone in air. *Applied Catalysis B: Environmental* 2010, 96, 557-564.

280. Lv, K.; Cheng, B.; Yu, J.; Liu, G., Fluorine ions-mediated morphology control of anatase TiO_2 with enhanced photocatalytic activity. *Physical chemistry chemical physics : PCCP* 2012, 14, 5349-62.

281. Zhou, P.; Zhu, X.; Yu, J.; Xiao, W., Effects of adsorbed F, OH, and Cl ions on formaldehyde adsorption performance and mechanism of anatase TiO_2 nanosheets with exposed {001} facets. *ACS applied materials & interfaces* 2013, 5, 8165-72.

282. Liu, H.; Wang, X.; Pan, C.; Liew, K. M., First-principles study of formaldehyde adsorption on TiO_2 rutile (110) and anatase (001) surfaces. *The Journal of Physical Chemistry C* 2012, 116, 8044-8053.

283. Elghniji, K.; Saad, M. E.; Araissi, M.; Elaloui, E.; Moussaoui, Y., Chemical modification of TiO_2 by $H_2PO_4^-/HPO_4^{2-}$ anions using the sol-gel route with controlled precipitation and hydrolysis: enhancing thermal stability. *Mater. Sci.* 2014, 32, 617-625.

284. Miao, H.; Ratnasingam, S.; San Pu, C.; Desai, M. M.; Sze, C. C., Dual fluorescence system for flow cytometric analysis of Escherichia coli transcriptional response in multi-species context. *Journal of microbiological methods* 2009, 76, 109-119.

285. Méndez-Vilas, A.; Gallardo-Moreno, A. M.; González-Martín, M. L.; Calzado-Montero, R.; Nuevo, M. J.; Bruque, J. M.; Pérez-Giraldo, C., Surface characterisation of two strains of Staphylococcus epidermidis with different slime-production by AFM. *Applied Surface Science* 2004, 238, 18-23.

286. Alhasawi, A.; Auger, C.; Appanna, V.; Chahma, M.; Appanna, V., Zinc toxicity and ATP production in Pseudomonas fluorescens. *Journal of applied microbiology* 2014, 117, 65-73.

287. Vidal, O.; Longin, R.; Prigent-Combaret, C.; Dorel, C.; Hooreman, M.; Lejeune, P., Isolation of an Escherichia coli K-12 mutant strain able to form biofilms on inert surfaces: involvement of a new ompR allele that increases curli expression. *Journal of bacteriology* 1998, 180, 2442-2449.

288. Böhmler, J.; Haidara, H.; Ponche, A.; Ploux, L., Impact of chemical heterogeneities of surfaces on colonization by bacteria. *ACS Biomaterials Science & Engineering* 2015, 1, 693-704.

289. Scherrer, B., Biostatistique, vol. 1. *Gaëtan Morin éditeur (816 pp.)* 2007.

290. Junker, L. M.; Toba, F. A.; Hay, A. G., Transcription in Escherichia coli PHL628 biofilms. *FEMS microbiology letters* 2007, 268, 237-43.

291. Schaule, G.; Flemming, H.; Ridgway, H., Use of 5-cyano-2, 3-ditolyl tetrazolium chloride for quantifying planktonic and sessile respiring bacteria in drinking water. *Applied and Environmental Microbiology* 1993, 59, 3850-3857.

292. LeChevallier, M. W.; Seidler, R. J.; Evans, T., Enumeration and characterization of standard plate count bacteria in chlorinated and raw water supplies. *Applied and Environmental Microbiology* 1980, 40, 922-930.

293. Yeager, J. G.; Ward, R., Effects of moisture content on long-term survival and regrowth of bacteria in wastewater sludge. *Applied and environmental microbiology* 1981, 41, 1117-1122.

294. Qiu, J.; Li, S.; Gray, E.; Liu, H.; Gu, Q.-F.; Sun, C.; Lai, C.; Zhao, H.; Zhang, S., Hydrogenation synthesis of blue TiO_2 for high-performance lithium-ion batteries. *The Journal of Physical Chemistry C* 2014, 118, 8824-8830.

295. Di Valentin, C.; Pacchioni, G.; Selloni, A., Reduced and n-type doped TiO_2: nature of Ti^{3+} species. *The Journal of Physical Chemistry C* 2009, 113, 20543-20552.

296. Anselme, K.; Davidson, P.; Popa, A. M.; Giazzon, M.; Liley, M.; Ploux, L., The interaction of cells and bacteria with surfaces structured at the nanometre scale. *Acta biomaterialia* 2010, 6, 3824-46.

297. Tong, T.; Shereef, A.; Wu, J.; Binh, C. T.; Kelly, J. J.; Gaillard, J. F.; Gray, K. A., Effects of material morphology on the phototoxicity of nano-TiO_2 to bacteria. *Environ Sci Technol* 2013, 47, 12486-95.

298. Suttiponparnit, K.; Jiang, J.; Sahu, M.; Suvachittanont, S.; Charinpanitkul, T.; Biswas, P., Role of surface area, primary particle size, and crystal phase on titanium dioxide nanoparticle dispersion properties. *Nanoscale Res Lett* 2011, 6, 27.

299. Li, B.; Logan, B. E., Bacterial adhesion to glass and metal-oxide surfaces. *Colloids and surfaces. B, Biointerfaces* 2004, 36, 81-90.

300. Takeuchi, H.; Gomi, T.; Shishido, M.; Watanabe, H.; Suenobu, N., Neutrophil elastase contributes to extracellular matrix damage induced by chronic low-dose UV irradiation in a hairless mouse photoaging model. *Journal of dermatological science* 2010, 60, 151-158.

301. D'Haeze, W.; Glushka, J.; De Rycke, R.; Holsters, M.; Carlson, R. W., Structural characterization of extracellular polysaccharides of Azorhizobium caulinodans and importance for nodule initiation on Sesbania rostrata. *Molecular microbiology* 2004, 52, 485-500.

302. Kashket, E. R., Bioenergetics of lactic acid bacteria: cytoplasmic pH and osmotolerance. *FEMS microbiology reviews* 1987, 3, 233-244.

303. Pal, A.; Pehkonen, S. O.; Yu, L. E.; Ray, M. B., Photocatalytic inactivation of Gram-positive and Gram-negative bacteria using fluorescent light. *Journal of Photochemistry and Photobiology A: Chemistry* 2007, 186, 335-341.

304. Alhasawi, A.; Castonguay, Z.; Appanna, N. D.; Auger, C.; Appanna, V. D., Glycine metabolism and anti-oxidative defence mechanisms in Pseudomonas fluorescens. *Microbiological research* 2015, 171, 26-31.

305. Bruno-Bárcena, J. M.; Azcárate-Peril, M. A.; Hassan, H. M., Role of antioxidant enzymes in bacterial resistance to organic acids. *Applied and environmental microbiology* 2010, 76, 2747-2753.

306. Zeller, T.; Klug, G., Detoxification of hydrogen peroxide and expression of catalase genes in Rhodobacter. *Microbiology* 2004, 150, 3451-3462.

307. Groves, M. R.; De Orue Lucana, D. O., Adaptation to oxidative stress by Gram-positive bacteria: the redox sensing system HbpS-SenS-SenR from *Streptomyces reticuli*. *Appl Microbiol Microb Biotechnol* 2010.

308. Hassan, H. M.; Fridovich, I., Enzymatic defenses against the toxicity of oxygen and of streptonigrin in Escherichia coli. *Journal of Bacteriology* 1977, 129, 1574-1583.

309. Jacobs, N.; Conti, S., Effect of hemin on the formation of the cytochrome system of anaerobically grown Staphylococcus epidermidis. *Journal of bacteriology* 1965, 89, 675-679.

310. Amao, Y., Probes and polymers for optical sensing of oxygen. *Microchimica Acta* 2003, 143, 1-12.

311. Devol, A. H., Bacterial oxygen uptake kinetics as related to biological processes in oxygen deficient zones of the oceans. *Deep Sea Research* 1978, 25, 137-146.

312. Singh, B.; Sharma, N., Mechanistic implications of plastic degradation. *Polymer Degradation and Stability* 2008, 93, 561-584.

Annex

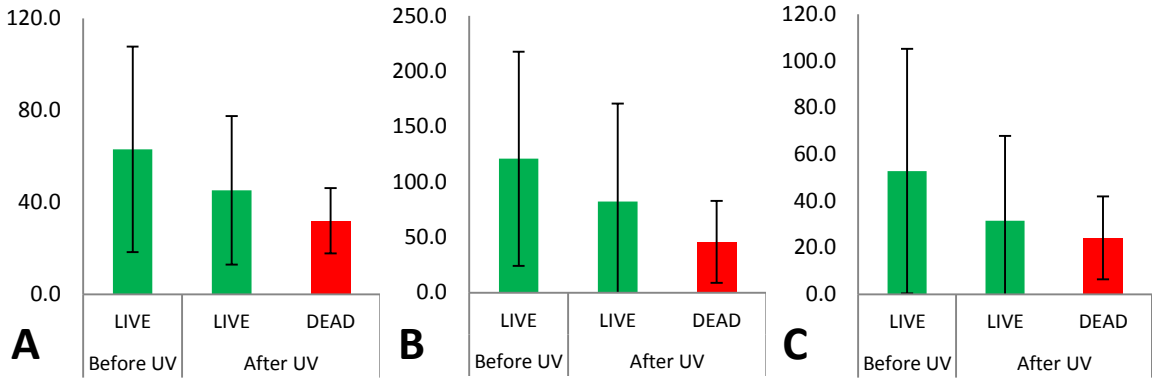

Fig 104 : Effect of 3h of UVA illumination on the population (in number) of *E. coli* (A), *S. epidermidis* (B) and *P. fluorescens* (C) bacterial strains.

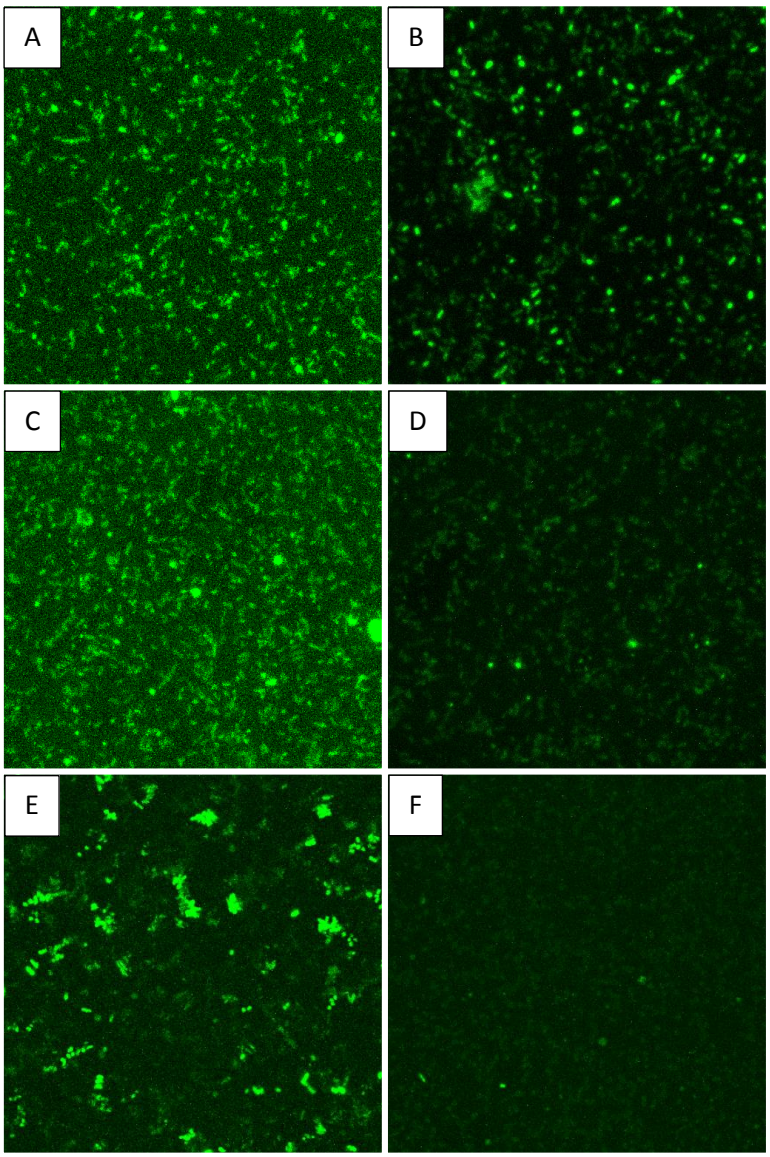

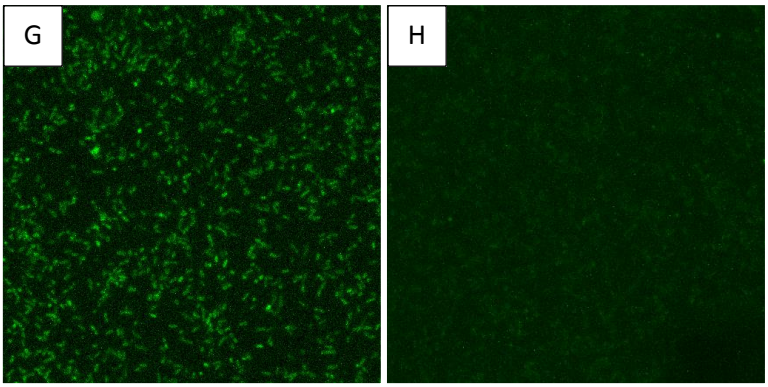

Fig 105 : *E coli* PHL 628 bacteria images taken by confocal microscope. Bacteria of positive enzymatic activity are stained by green color. (A) P25 after 10 min without illumination; (B) P25 after 10 min illumination; (C) PANaF after 10 min without illumination; (D) PANaF after 10 min illumination; (E) P25 after 45 min without illumination; (F) P25 after 45 min illumination; (G) PANaF after 45 min without illumination; (H) PANaF after 45 min illumination.

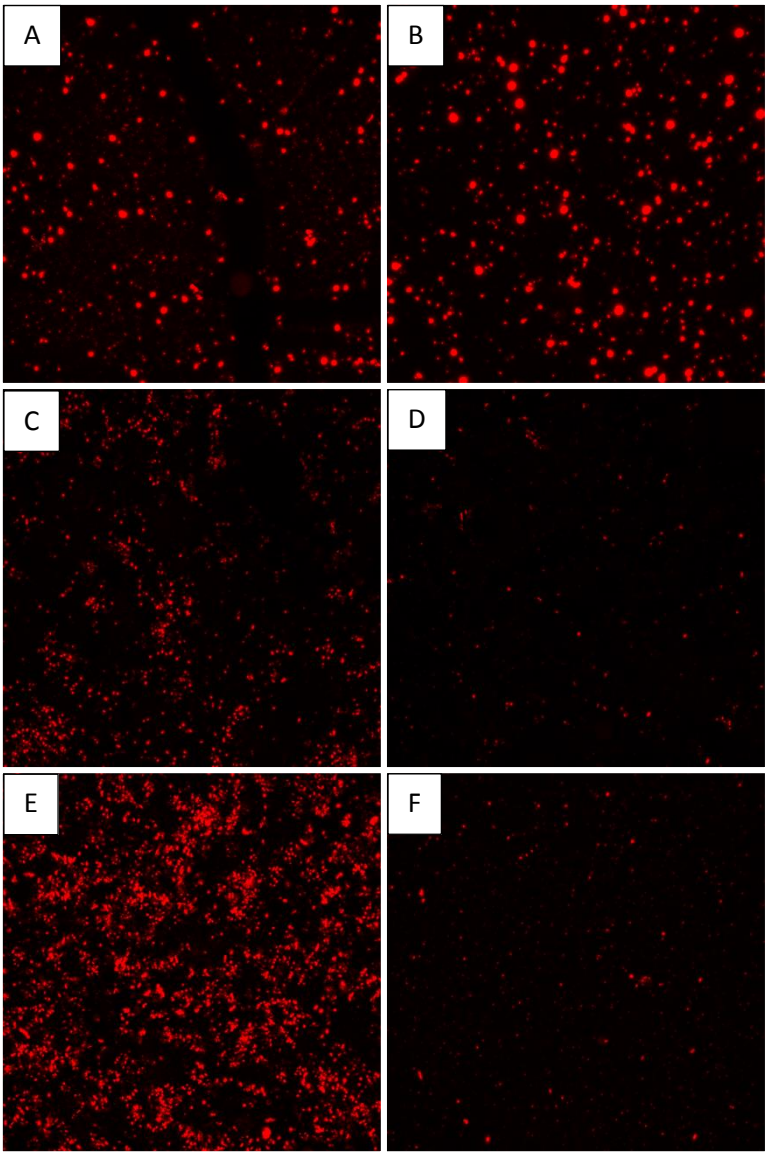

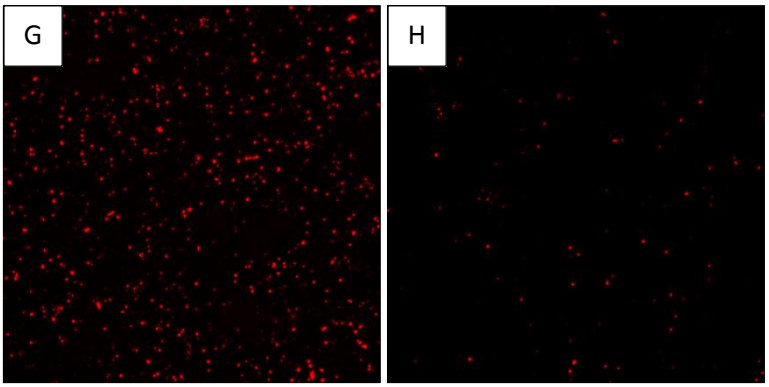

Fig 106 : *E coli* PHL 628 bacteria images taken by confocal microscope. Bacteria of positive respiratory activity are stained by red color. (A) P25 after 10 min without illumination; (B) P25 after 10 min illumination; (C) PANaF after 10 min without illumination; (D) PANaF after 10 min illumination; (E) P25 after 45 min without illumination; (F) P25 after 45 min illumination; (G) PANaF after 45 min without illumination; (H) PANaF after 45 min illumination.

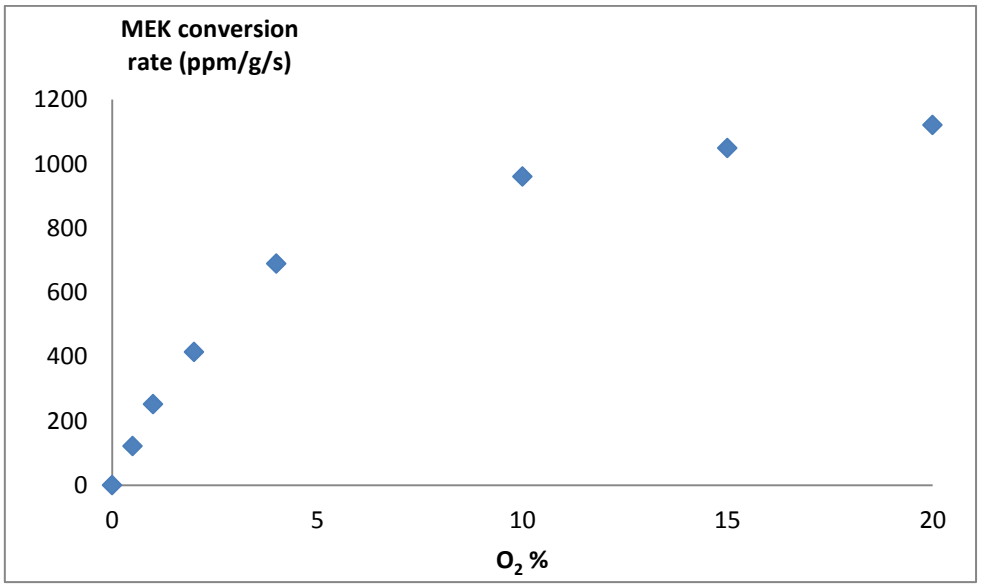

Fig 107 : Effect of O_2 concentration on gas-phase photocatalytic MEK conversion rate (calculated and presented as ppm/g/s).

Institut de Science des Matériaux de Mulhouse

Medium M63G for *Escherichia coli*: liquid medium

Composition

	For 1 liter
KH_2PO_4	13.6g
$(NH_4)_2SO_4$ 20%wt.	10 ml or 2g
$FeSO_4$ 0.1%wt.	0.5 ml
$MgSO_4$ 20%wt.	1mL or 0.2g
KOH 6Mwt	11.7 ml adjusted to pH 6.8
Vitamin B1 0.05%wt.	1ml
Glucose 10% wt.	0.5ml for 25ml of medium

Preparation:

- Water in Erlenmeyer flask
- In order : dissolve under agitation KH_2PO_4, $(NH_4)_2SO_4$, $MgSO_4$ (be careful the order is important because of precipitation)
- Add KOH , don't forget to adjust pH to 6.8
- Autoclave at 120°C
- Add under PSM sterile vitamin B1, 0,1mL per 100mL of medium

In all cases add D-Glucose for culture just before the use for bacteria re-inoculation.

Yige YAN

TiO_2 photocatalysts prepared *via* a sol-gel route assisted by P- and F-containing additives. Application to the degradation of MEK and to the elimination of bacteria on surfaces.

Résumé

L'objectif de ce travail est de synthétiser des nanomatériaux de TiO_2 pour la dégradation des COV et pour l'élimination des bactéries en surface. Tout d'abord, basé sur une synthèse des matériaux de TiO_2 avec la présence d'un liquide ionique $BmimPF_6$ par une voie sol-gel modifiée, les rôles de deux éléments constitutifs de $BmimPF_6$ (P et F) ont été étudiés en faisant remplacer $BmimPF_6$ par des additives contenant P et F. Par rapport à la référence P25 et aux matériaux de TiO_2 synthétisés sans additif, le TiO_2 synthétisé en présence de P a déjà montré une meilleure cristallinité en phase anatase avant la calcination, et une surface spécifique élevée et une petite taille moyenne des cristaux étaient maintenus même après calcination. Ces propriétés étaient similaires aux échantillons TiO_2 synthétisés en présence de $BmimPF_6$; Tandis que les cristaux de TiO_2 en présence de F ont montré une forme anisotrope pendant le murissement de la synthèse. Les évaluations de l'activité photocatalytique des photocatalyseurs ont ensuite été réalisées. Par rapport au TiO_2 synthétisé sans additif et au TiO_2 P25, les matériaux de TiO_2 à faible teneur en P et F ("PANaF") ont présenté une activité plus élevée sous irradiation UVA à la dégradation d'un COV modèle, Méthyléthylcétone (MEK) en phase gazeuse. Le même matériau a également montré une activité anti-bactérienne en surface plus élevée sous UVA contre plusieurs souches de différentes espèces bactériennes dans liquide par rapport à celles de P25. Une corrélation entre la performance photocatalytique élevée et les propriétés des matériaux pour TiO_2 "PANaF" a été finalement proposée. Les influences de la présence de PO_4^{3-} en bulk ou en surface de TiO_2, de la concentration d'O2 dissous dans le milieu et de la topologie de surface des photocatalyseurs sur l'activité photocatalytique éteint également sujets de discussion. Le produit "PANaF" présente un intérêt pour l'élaboration industrielle à cause des réactifs pas cher et son performance élevée.

Résumé en anglais

The objective of this work consists in synthesizing TiO_2 nanomaterials designed for the degradation of VOCs and for the elimination of bacteria on surface. Firstly, based on a synthesis of a $BmimPF_6$-ionic liquid-derived TiO_2 material through a modified sol-gel route, the roles of two constituent elements of $BmimPF_6$ (P and F) have been investigated by replacing $BmimPF_6$ with P- and F-contained additives. Comparing to the reference P25 and additive-free-derived TiO_2 materials, P-derived TiO_2 showed already well crystallized anatase phase before calcination and a high surface area along with a small mean crystal size even after calcinations. Those properties were similar to that synthesized with the presence of $BmimPF_6$; while F-derived TiO_2 crystals showed anisotropic shape during the aging step of the synthesis. Evaluation of the photocatalytic activity of the photocatalysts has been performed then. Compared to additive-free derived TiO_2 and the TiO_2 P25, P- and F- derived TiO_2 materials with low P and F content ("PANaF") showed higher activity under UVA in terms of gas-phase degradation of a model VOC, Methl Ethyl Ketone (MEK). The same material also showed higher surface anti-bacterial activity under UVA in liquid against several strains of different bacterial species over that of P25. A correlation between the high photocatalytic performances with the material properties for "PANaF" TiO_2 materials was finally proposed. The influences of the presence of bulk or surface PO_4^{3-}, dissolved O_2 concentration and surface topology on photocatalytic activity were also discussed. The cheap replacement additives used and the resulted high activity of "PANaF" TiO_2 nanomaterials presents interest for industrial elaboration